MEASUREMENT OF THE LONGITUDINAL SINGLE-SPIN ASYMMETRY FOR $W^{\pm}$ BOSON PRODUCTION IN POLARIZED PROTON-PROTON COLLISIONS AT $\sqrt{S} = 510$ GEV AT RHIC

A Dissertation
Submitted to
the Temple University Graduate Board

In Partial Fulfillment
of the Requirements for the Degree
DOCTOR OF PHILOSOPHY

---

by
Devika Gunarathne
Diploma Date August 2017

Examining Committee Members:

Prof. Bernd Surrow, Advisory Chair, Physics Department, Temple University

Prof. Andreas Metz, Physics Department, Temple University

Prof. Zein-Eddine Meziani , Physics Department, Temple University

Dr. Leslie C. Bland, Physics Department, BNL

©
Copyright
2017

by

Devika Gunarathne

All Rights Reserved

Wonderful, indeed, it is to subdue the mind, so difficult to subdue, ever swift, and seizing whatever it desires. A tamed mind brings happiness.

-The Dhammapada, Pali Tripitaka
Gautama Buddha

"Sariputta, there are these four kinds of generation. What are the four? Egg-born generation, womb-born generation, moisture-born generation and spontaneous generation. What is egg-born generation? There are these beings born by breaking out of the shell of an egg; this is called egg-born generation. What is womb-born generation? There are these beings born by breaking out from the caul; this is called womb-born generation. What is moisture-born generation? There are these beings born in a rotten fish, in a rotten corpse, in rotten dough, in a cesspit, or in a sewer; this is called moisture-born generation. What is spontaneous generation? There are gods and denizens of hell and certain human beings and some beings in the lower worlds; this is called spontaneous generation. These are the four kinds of generation."

-Maha-Sihanada Sutta: The Great Discourse on the Lion's Roar

Gautama Buddha

ABSTRACT

Understanding the spin structure of the nucleon can be considered as one of the fundamental goals in nuclear physics. Following the introduction of the quark model in 1964, the spin of the proton was naively explained by the alignment of spins of the valence quarks. However, in our current understanding, the valence quarks, sea quarks, gluons, and their possible orbital angular momentum are all expected to contribute to the overall spin of the proton. Despite this significant progress, our understanding of the individual spin contributions of quarks and antiquarks to the proton is not yet complete.

Measurements of $W^{\pm}$ single spin asymmetries in longitudinally polarized proton-proton collisions at RHIC provides unique and clean access to the individual helicity distributions of light quarks and antiquarks of the proton. $W^{+(-)}$ boson are produced through the annihilation of $u + \bar{d}$ ($\bar{u} + d$) and can be detected through their leptonic decays, $e^{+} + \nu_e$ ($e^{-} + \bar{\nu}_e$). Due to maximal violation of parity during the production, W bosons couple to left-handed quarks and right-handed anti-quarks and hence offer direct probes of their respective helicity distributions in the nucleon. The STAR experiment at RHIC is well equipped to measure $W \rightarrow e + \nu$ in longitudinally polarized $p + p$ collisions, where only the charged lepton is observed in the final state with a large missing transverse energy opposite in azimuth due to the undetected neutrino.

In this dissertation, the details of the analysis and the results of the longitudinal single spin asymmetry, A_L, for W boson production at RHIC are presented. The total integrated luminosity of the data analyzed is 246 pb^{-1} with an average beam polarization of $\sim$54%. The data are collected during 2013 in longitudinally polarized proton-proton collisions at $\sqrt{s} = 510$ GeV by the STAR experiment at

RHIC. The analysis includes the procedure, the results and the evaluation of the systematic uncertainty of the calibration of the STAR Barrel Electromagnetic Calorimeter which was performed coincident with the primary W A_L analysis. The W A_L analysis is discussed in terms of data QA, the reconstruction of W bosons via decayed $e^{\pm}$, and the estimation of the electroweak and QCD type background contributions. The reconstruction of $W \rightarrow e + \nu$ events includes the use of the Time Projection Chamber for the tracking purposes and the Barrel Electromagnetic Calorimeter for the identification and isolation of $e^{\pm}$ candidates by measuring their transverse energies in the calorimeter towers. Finally the results of A_L for $W^+(W^-)$ are reported as a function of decay positron (electron) pseudo-rapidity η, between -1 and +1. The theoretical predictions for the spin asymmetries calculated using recent polarized and unpolarized parton distribution functions, are compared with the measured values.

To My Family.

ACKNOWLEDGMENTS

I would like to thank my advisor, Prof. Bernd Surrow, for the guidance, encouragement, and continuous support during my graduate career at Temple University. Thanks Bernd for understanding my personality as a student and providing me with appropriate guidance throughout my studies. Thanks for being patient and understanding at my flaws. Thanks for allowing me to think and work in a pressure free environment so that I could discover my own potential to reach the final goal. Thanks for being the most friendly and the greatest advisor in the world.

I would like to thank the rest of my thesis committee: Prof, Andreas Metz, Prof. Zein-Eddine Meziani, and Dr. Leslie C. Bland, for their insightful comments on this dissertation and encouragements.

My sincere thanks to all the members of the SPIN physics working group at the STAR collaboration for their valuable comments, suggestions, and motivations during this research work. I would like to thank fellow members of "STAR Run 13 W A_L group", Jinlong Zhang and Qinghua Xu for all the meaningful discussions during the analysis. I would also like to thank all the members of STAR EMC^2 group for all their comments and suggestions during the calibration of the STAR Barrel Electromagnetic Calorimeter. Special thanks to all the members of the STAR software and computing team, in particular, Jerome Lauret and Gene Van Buren for all the technical support and helpful discussions.

I would like to thank all my teachers at the department of physics at Temple University. Special thanks to former graduate chair, Dr. Burkhardt for all the help and support he had provided during my enrollment at the university, current graduate chair, Prof. Metz for providing all the details and timeline regarding the graduation process, and the department chair for providing all the grad students (including me) with numerous opportunities to broaden our knowledge of physics.

I would like to thank all the members of my research group for being great supportive colleagues. Thanks to Amani, Amilkar, Matt, and Nick for agreeing to read my thesis and providing me with various comments and suggestions. Special thanks to Amani for being a great friend and keep reminding me to complete my thesis on time. Thanks to Matt, Nick from my group and Danielle Berish from the physics department for agreeing to proofread my thesis. I really appreciate the time you have spent for me.

Last but not the least, I would like to thank my family. My parents, Mr. and Mrs. Gunarathne (Amma and Pappa), thanks for being the greatest parents in the world. Thanks for giving me and my sister, the most valuable wealth of this universe, the great teachings of Lord Buddha. Thanks for teaching us that great learning of the wisdom and humanity through the "Triple Gem" in Buddhism. Thank you for equally teaching us the importance of the education and how that can be used to the great service of the mankind. We both are only lucky to be born as your children. Thanks and love to my lovely sister, Roshika Gunarathne for being the best and the most supportive sibling I could ever ask for. Thanks to my brother-in-law, Pawan for all you support and care for the family. Thanks to my little nephew who brought the love and smile to me during this writing. Finally, thanks to my husband Aruna Wijesinghe, for all the sacrifices you have made for me. Thanks for being the kindest person I ever met in my life. Thanks for being patient and understanding at my short tempers. Thanks for giving me an unconditional love, support, and protection. Thanks for being always there for me at every step of our journey of life since the day we met. I would not be where I am today without you.

TABLE OF CONTENTS

Page

LIST OF TABLES

LIST OF FIGURES

Figure | Page

Figure Page

CHAPTER 1
INTRODUCTION

The protons and neutrons together called nucleons can be considered as the basic building blocks of matter which the visible universe is primarily made up of[1]. Nucleons themselves are composed of fundamental constitutes called quarks, that are bound together by the strong interaction, which is mediated by a fundamental gauge boson known as the gluon. Additionally, quarks also interact with other fundamental particles, known as leptons, through weak and electromagnetic interactions. In order to understand the basic structure of matter, a precise knowledge of the structure and underlying dynamics of nucleons is required. Experimentally, the structure of nucleons are studied primarily using protons due to their non zero charge in contrast to neutrons. The proton is a composite particle made up of quarks and gluons, and thus it is very important to understand how the basic properties of the proton such as the charge, the mass, and the spin emerge from the underlying quarks, gluons and their dynamics.

Among all the basic properties of the proton the spin is an important aspect, as it is an essential property of all the subatomic particles, atoms and molecules. Since the proton was understood as a composite particle, the origin of it's spin was extensively studied both theoretically and experimentally. With the development of QCD the current understanding of the spin of the proton is described as a sum of contributions from the total quark and antiquark polarizations, total gluon polarizations and their corresponding orbital angular momentum. Over the past several decades dedicated experiments to estimate these contributions,

[1] The standard model of cosmology indicates that the 95.1% of total mass-energy content of the universe is not made up of ordinary matter that are visible, but unidentified type of matter known as dark matter and unidentified form of energy known as dark energy.

in particular the total quark and gluon contributions have been conducted all over the world. Despite much progress, our understanding of the individual spin contributions of quarks, antiquarks and gluons to the proton is not yet complete. Through the measurements of inclusive Deep Inelastic Scattering (DIS) and semi-inclusive DIS (SIDIS) experiments the total quark and antiquark contribution was well constrained and accounted for about 30% to the spin of the proton. However, the flavor separated, individual polarizations of the antiquarks were poorly constrained.

The main objective of the research discussed in this dissertation, is to study the individual quark and antiquark contributions to the spin of the proton through the measurement of the longitudinal single-spin asymmetries, A_L, for the $W^{\pm}$ bosons production in polarized proton-proton collisions at RHIC. The measurement of A_L for W bosons at RHIC and therefore the research discussed in this thesis has been primarily motivated by the following reasons. Over the years, SIDIS experiments have provided a significant contribution to the extraction of helicity-dependent (polarized) Parton Distribution Functions (PDF) of the proton. However, large uncertainties were seen in the extracted polarized antiquark PDFs, which was largely attributed to the large uncertainties in the fragmentation functions that were used. In comparison to SIDIS, the W boson production in proton-proton collisions has unique advantages in terms of their direct sensitivity to the anti-quarks of interest and non-fragmentation in the final state when decayed through the leptonic decay modes. Therefore the measurement of A_L for W boson production in proton-proton collisions have been recognized as a unique tool to study the quark and antiquark polarizations of the proton.

The sensitivity of W A_L to individual quark and antiquark helicity distributions at forward and backward pseudorapidity of decay leptons has provided a unique opportunity to study the flavor asymmetry ($\Delta\bar{u} - \Delta\bar{d}$) in the polarized nucleon sea. Experimentally established non-perturbative asymmetric nature of the unpolarized nucleon sea is explained via several non-perturbative models such as the chiral-quark soliton model [1]. A similar asymmetry in the polarized nucleon sea, large positive $\Delta\bar{u}-\Delta\bar{d}$, was as well predicted by these models. Consequently, the experimental extraction of $\Delta\bar{u}-\Delta\bar{d}$ was largely demanded in order to test these various model predictions and to understand the non-perturbative nature of the polarized nucleon sea. The extraction of $\Delta\bar{u}-\Delta\bar{d}$, at leading order based on SIDIS data, are suggestive of a positive asymmetry in the polarized sea. However, the uncertainties of these extractions are significantly large. The measurement of W A_L provides an important measurement of $\Delta\bar{u}-\Delta\bar{d}$ via its sensitivity to individual quark and antiquark polarized distribution, and therefore an independent test of non-perturbative model predictions.

In this thesis work, single-spin asymmetries are measured for $W^{\pm}$ boson production through the collisions of longitudinally polarized protons at a center of mass energy equal to 510 GeV at RHIC located at Brookhaven National Laboratory (BNL) in the US. The measurement of W A_L was carried out at the STAR experiment at RHIC. The produced $W^{\pm}$ bosons at the STAR interaction region were reconstructed by detecting their decay electrons and positrons. The single-spin asymmetries of decay electrons and positrons from W^- and W^+ respectively, were measured as a function of electron's and positron's pseudorapidity, η. The pseudorapidity dependance of measured asymmetries was understood as follows. As shown in the illustration in Fig 1.1, at the backward region, the A_L for W^- is sensitive to the anti-up quark helicity distribution ($\Delta\bar{u}$) and at the forward region, the A_L is sensitive to the down quark helicity distribution (Δd). In the mid-rapidity region, the A_L is sensitive to the combination of both the quark (Δd) and the antiquark ($\Delta\bar{u}$) helicity distributions.

The dissertation is organized as follows. Chapter 2 provides a summary of historical and theoretical background of this research. Chapter 3 describe the experimental apparatus, the RHIC and the STAR detector. Some relevant analysis prerequisites are discussed in Chapter 4. Chapter 5 details the calibration

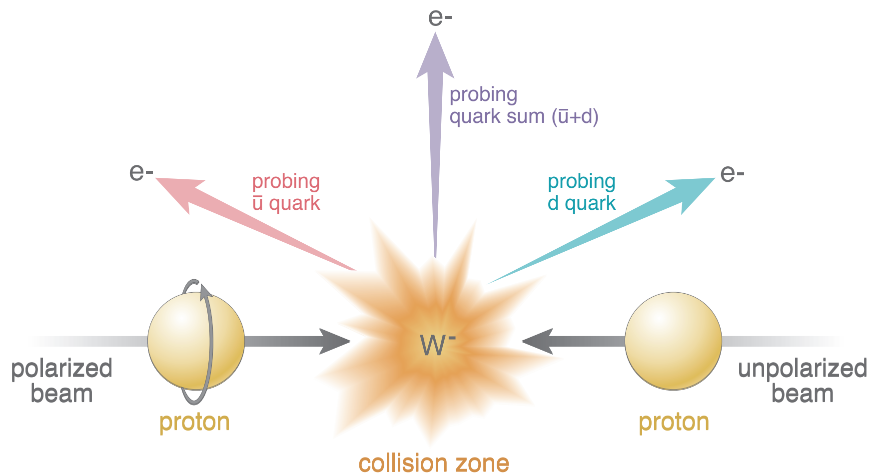

Figure 1.1.: Illustration of probing the quark (d) and the antiquark ($\bar{u}$) helicity through the single-spin asymmetry of the decay electrons from the produced W^- boson.

of the Barrel Electromagnetic Calorimeter at the STAR experiment. The data and the production of simulation samples are discussed in Chapter 6. Chapter 7 details the analysis of data, and the procedure of reconstructing W boson form decay electrons and positrons. The background estimation procedure is discussed in Chapter 8. The path to the final results and the results are discussed and presented in Chapter 9. Finally, Chapter 10 presents the conclusion and outlook.

CHAPTER 2
THEORETICAL ASPECT

2.1 Historical Background

For better or worse, we as humans are born with a deep curious nature. Just like our species, our curiosity has evolved with time. If it wasn't for this curiosity, quite possibly our ancestors could have died imagining that the earth is flat and the sun revolves around it. However, this was not the case and we have come further than we ever could have imagined in our exploration of the universe. Naturally, our ancestors first began to question the macroscopic world around them. Whether it was the sky with its stars or the surrounding nature or another kind of life form, they questioned, "What's everything we see made up of ?". This question was often followed by "How?", "Why?", and "When?". The period when deep thinking went into these basic questions marks the era of ancient philosophy. With time, these questions were broadened and point of views changed. Gradually people came to the understanding that the visible world is not all that exists and began to suspect the existence of a microscopic world not visible to the naked eye. Some speculated that studying the microscopic world could bring answers to the questions that they were unable to understand.

First, the idea of an atomic world, where matter is made up of discrete units, was introduced. In the beginning, atomic theory was left unheeded due to the lack of experimental evidence. However, with a growing number of discoveries of chemical elements between the 16th and 18th centuries, chemists began to use the word "atoms" and subsequently began to study atomic physics. Transition from the atomic world to the particle world occurred about two centuries later, when the first elementary particle was discovered. The discovery of the electron by J. J Thomson in 1896 can be considered as the birth of particle physics. Around the same time, the discovery of radioactivity by Henri Becquerel gave birth to nuclear physics, which studies the atomic nuclei and their interactions. Since then these two branches of physics, particle and nuclear, have evolved into particle physics studying the nature of fundamental particles and their interactions, and nuclear physics studying the properties of the atomic nucleus, nuclei, and their interactions.

2.1.1 The Simple Picture : What ?

It would not be an overstatement to say that three experimental minds, among all of the great physicists that lived during late 19th and early 20th centuries, found the simplest answer possible to the question, "What is matter made up of?". The discoveries of the electron, the proton, and the neutron can be considered as the classical era of nuclear and particle physics. First, J. J Thomason discovered the electron using deflected cathode rays in a cathode ray tube [2]. While contradicting prior explanations of cathode rays as negatively charged waves, atoms or molecules, he indicated that cathode rays, in fact, were unique, negatively charged particles with a mass predicted to be one thousandth of the mass of the least massive ion known at the time, hydrogen. Next, Ernest Rutherford, who came to be known as the father of nuclear physics, discovered the second particle of the simple picture, the proton. Rutherford's discovery of the proton was influenced by his initial work on the radioactive decay of atomic nuclei and the discovery of the atomic nucleus. In 1911, following the recent discoveries of alpha (α) and beta (β) radiations of radioactive elements, Rutherford and his students discovered the atomic nucleus as a small, concentrated point of positive charge inside the atom [3]. They discovered the nucleus while conducting an alpha particle scattering experiment, now known as the Rutherford gold foil experiment, in an attempt to test Thomson's "plum pudding model"[1] of the atom. Following the discovery of the atomic nucleus, Rutherford conducted a series of experiments in 1917 (where he shooted alpha particles into air which is largely consisted of nitrogen gas) and discovered that the hydrogen nucleus is present in all other nuclei. Therefore, he concluded that the hydrogen nucleus is a fundamental building block of the nucleus and named it the "proton" [4].

The discovery of the proton allowed physicists to understand atomic properties better, in particular the relation between atomic mass and atomic number[2]. As long as elements were light, the atomic mass-number relation was found to be in agreement. However, complications occurred when this relation was used to justify the larger mass of heavy elements[3]. In order to explain the observed disparity between the atomic mass-number relation of heavy elements, Rutherford proposed the existence of a massive particle with a neutral charge in the atomic nucleus and named the hypothetical particle the "neutron". However, how neutrons were localized inside the atomic nucleus was not clearly understood. Therefore it's experimental discovery was highly demanded. James Chadwick[4], who had been conducting unsuccessful experiments for about a decade to find the suggested neutron by Rutherford, was triggered by the discovery of an emission of an unknown type of radiation when high energetic alpha particles fall on certain light elements. Inspired further by a follow up experiment on these particular radiations, which claimed that high energetic protons were ejected when those

[1] Knowing that atoms were electrically neutral and, in order to justify the negatively charged electrons, Thomson described the atom as a positively charged region of space where negatively charged electrons are distributed in it as plumps in a pudding.

[2] The atomic mass in units of charge of elements is equal to twice the atomic number: only true for lighter elements.

[3] The atomic mass of heavy elements was found be larger than twice the atomic number and the discrepancy increased with increasing atomic number.

[4] What truly fascinating is the fact that Chadwick happened to be a doctoral student of Rutherford and Rutherford himself was happened to be a doctoral student of J. J. Thomason.

incident on hydrogen rich compounds, Chadwick conducted a major experiment in 1932 [5] to find the neutron and subsequently concluded that the unknown radiations were in fact Rutherford's neutrons. He also measured the mass of the neutron and found it to be the same as that of the proton. With the discovery of the neutron, the simple three particles picture answered "What is matter made up of?", only to be followed with the serious question of "How" ?

2.1.2 Simple to Complex : How ?

With the simple picture of the atom established, it was only a matter of time until physicists realized that something was wrong. As neutrons have no charge, how could positively charged protons be held together in a tiny volume inside the nucleon without repelling each other? After all, the coulomb force between the protons should break the nucleus apart. Since that was not happening, the only reasonable explanation that physicists of the time could put forward was that some type of "strong" force, much stronger than the coulomb force, between the protons was keeping them stuck together. Since electrons did not seem to be affected by such a strong force, the force was understood as short range, implying that its influence drops to zero rapidly beyond the region of the nucleus. This force was named the "nuclear force", which was later identified as the residual force of one of the fundamental forces that we understand today, the strong force.

The "theory of the meson" [6], proposed by Hideki Yukawa in 1934, can be considered as the earliest attempt to explain the nature of the nuclear force. By using electromagnetic fields as a model, he theorized a new field inside the nuclei which corresponds to the nuclear force. According to quantum field theory, each field of forces should be accompanied by a new quantum (some type of carrier particle) similar to the photon which is associated with the electromagnetic field. Therefore, Yukawa introduced a new particle accompanied by his field and predicted the mass of this new particle to be about 200 times heavier than that of the electron. As the mass falls in between the mass of the electron and the proton he named the particle "meson"[1]. According to Yukawa's theory, the nuclear force was understood as the force acting between the nucleons which is exchanged by mesons. In 1936, a particle was discovered with an intermediate mass between the electron and the proton. Immediately, it was identified as the Yukawa's meson. Then, in 1947, a second type of particle with an intermediate mass and properties of a meson was discovered. Subsequently, the first one was named "mu meson" (μ), and the second one was named "pi meson" (π). For decades, the μ was considered the first discovered meson particle. However, it was later found that μ did not participate in nuclear interactions in the same way as other mesons. In reality, it was similar to the electron, but with a larger mass, and was eventually re-categorized as a lepton and given the name muon.[2] Following the discovery of the π meson, many different types of mesons (ex, "Kaon (K)", "eta (η)") were discovered over several decades. In 1950, a new type of particle called "Lambda (Λ)", which decays into a proton and a light meson, was discovered [7]. As the properties of Λ differed from that of the mesons, Λ was grouped into a different category known as "baryons". Subsequently more baryons ("Delta (Δ)", "Sigma (Σ)" , "Xi (Ξ)")were discovered.

2.1.3 Strange in an Eightfold Way

Further studies on both mesons and baryons revealed that some of them (K, Λ, etc.,) behaved strangely, in that they decayed extremely slower than expected for their higher mass and large production cross section. Therefore, these parti-

[1] The Greek word for "intermediate" is "mesos". However, following the similar fashion of naming other particles, the "electron", the "proton" and the "neutron", the name was ended with the term "on" instead of "os".

[2] As no another particle like μ was found for some time, physicists had no idea how to explain its properties or how to fit it in the meson group. The discovery of the muon caused so much chaos during the time, Nobel laureate I. I. Rabi famously quoted, "Who ordered that?"

cles were categorized as "strange particles",[1] which exhibit the property called "strangeness". As more and more particles with different properties were discovered, they were referred to as "zoo of particles".[2] In order to handle all of these particles and organize them, an idea known as "Eightfold way"[3] was proposed [9] by Murray Gell-Mann in 1961. He organized known particles at the time into multiplets of SU(3) representation. The mesons are organized into an octet (8-member family) and the baryons are organized into both an octet and a decuplet (10-member family) based on their spin, integer charge value (Q = -1, 0, 1, 2), and strangeness (S= -3, -2, -1, 0, 1), as shown in Figure 2.1. The

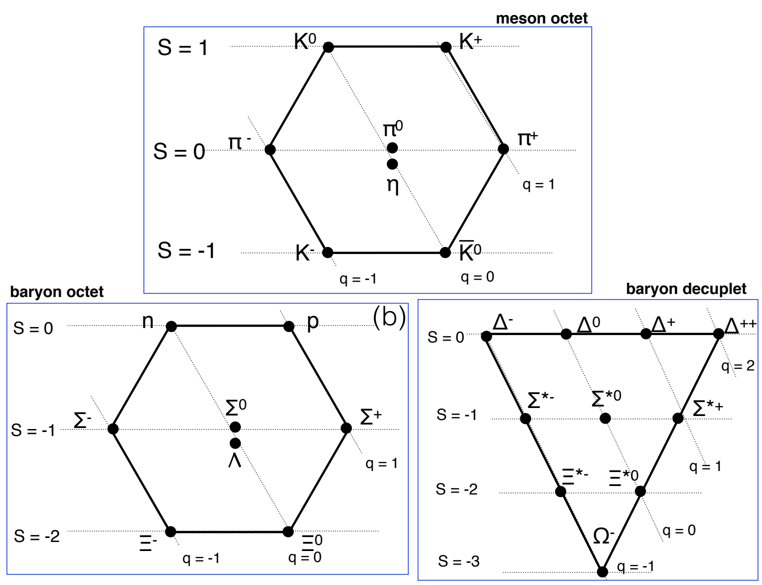

Figure 2.1.: Eight fold way classification of meson octet, baryon octet and baryon decuplet. Particles along the same horizontal line share the same strangeness, S, while those on the same diagonals share the same charge, q.

[1] The study of strange particles subsequently led to the understanding of the parity violation in the weak interaction [8].

[2] Due to the increasing number of discoveries of new particles physicist had hard time of keeping track of them. Some has famously quote: (Wolfgang Pauli) "Had I foreseen that, I would have gone into botany".

[3] Eightfold way was named alluding to the Noble Eightfold Path of Buddhism.

known mesons at the time fit perfectly into their octet and one of the missing members (η meson) was discovered two years after the theory was proposed. The omega baryon (Ω) was postulated by theory to complete the baryon decuplet and subsequently discovered [10] at Brookhaven National Laboratory (BNL) with a mass predicted by theory. Therefore, the eightfold way was successfully accepted and subsequently led to the introduction of the quark model.

2.1.4 The Quark Model

While trying to understand symmetry breaking [9] in the strong interaction in 1964, Gell-Mann [11], and independently, George Zweig [12, 13], proposed the quark model introducing new fundamental particles named "quarks",[1] which made up mesons and baryons. In the quark model, three members, "u (up)", "d (down)" and "s (strange)" from three fundamental representations of SU(3) ($3 \times 3 \times 3$)[2] and their antiparticles were introduced. The mass of the s quark was predicted to be roughly 1/9 of that of the proton while u and d quarks were predicted to have masses roughly $1/50^{th}$ and $1/20^{th}$ of that of the s quark. In addition, calculations implied that each member would have fractional charges. The u-quark would have a charge 2/3 of the elementary charge while d and s quarks would have charge -1/3 of the elementary charge and their antiparticles would have opposite charges.

All the mesons in their octet and all the baryons in their octet and decuplet were successfully constructed using these three fundamental quarks. However, as fractional charges had never been observed in experiments, physicists were ini-

[1] Zweig proposed four such particles (Gell Mann proposed only three) named "aces", [14] refereeing to four aces in a pack of cards.

[2] The unitary triplet t in $SU(3)$ consists of members (u, d), which are an isotopic doublet with charge $z, z+1$, and s, an isotopic singlet with charge z.

tially reluctant to accept[1] the quark model, although Gell Mann insisted that one of the quarks, u or d, would be absolutely stable. Nevertheless, many opposed the idea of fractional charges. Adding fire to the existing chaos, the violation of Pauli's exclusion principle by the quarks with spin 1/2 was raised.[2] The introduction of "color charge"[3] for quarks by O. W. Greenberg provided a way around this quandary. The color charge was proposed as a hidden property that quarks carry, implying that quarks not only come in different flavors, as in u, d, and s, but they can also come in three different colors, red, blue and green. Thus, quarks with the same flavor can coexist, as long as they have different colors, without violating the exclusion principle.

By the time the quark model was proposed, four leptons were already discovered, the electron (e), electron-neutrino (ν_e), muon (μ), and muon-neutrino (ν_μ). The idea of lepton-quark symmetry of the universe suggested the existence of a fourth quark in addition to the three quarks introduced by the quark model. This was first introduced as a new quantum number in mid 1964, called "charm" [16], for mesons and baryons, with the prediction of the existence of many "charmed" particles. In the quark model these predicted charmed particles were explained by introducing a new quark [17] named "charm". By this time, the discovery of such charmed particles was crucial for the establishment of the quark model. However, a single charmed particle was not discovered for another decade, forcing the quark model to exist vaguely.

In 1969 Feynman proposed a new model called the "parton model" [18] in order to explain the very high energetic collisions of hadrons. In the parton model

[1] Instead physicist tended to use an earlier model, the "Sakata model" [15] based on the p, n and Λ baryon as fundamental constituents, rather than accepting quarks with fractional charges.

[2] For example, the Δ^{++} baryon was postulated to consist of three u quarks in the same spin state, and the Ω baryon constituted of three strange quarks which cannot occupy the same state.

[3] Quark color is introduced as a new degree of freedom like charge, but does not refer to color we use in everyday life.

he treated hadrons in an infinite momentum frame (for example, a proton with very large momentum) as a composition of a number of point like constituents called "partons"[1]. Results from early high energy Inelastic Electron-Proton Scattering experiments [19] performed at SLAC (Stanford Linear Accelerator Center), were successfully explained [20] using Feynman's parton model. The results, however, did not agree very well with the quark model and subsequently led to the concept of confinement[2]. By the late 60's and early 70's the state of theoretical and experimental efforts to understand the structure of the nucleon and strong interaction were as follows. Rapidly developing high energy scattering experiment results around the world began to show a very complex structure of the nucleon. Various theoretical models were proposed to explain these results. However, the very models which successfully explained high energy scattering did a bad job explaining the bound state of the hadrons and the ones which explained the bound state well hardly explained the high energy results well. Therefore a single theory to explain both of these states of the strong interaction was badly needed. Apart from all of this, nothing was seemingly "right" as the universe was so "odd" with 4 experimentally discovered leptons, 3 theorized quarks with known hadrons successfully explained as bound states, but one hypothetical quark whose bound state hadron was not discovered.

2.1.5 The revolutionary J/ψ and beyond

One of the revolutionary experimental discoveries in the history of nuclear-particle physics is the discovery of the J/ψ meson. The discovery of this meson, independently by two research groups, one at SLAC [21] and one at BNL [22], in November 1974, brought the much needed quark-lepton symmetry back to the

[1] Partons were subsequently understood as the same quarks in the quark model and gluons, which act as point like constituents at very high energies.

[2] The phenomenon that color charged particles (such as quarks) cannot be isolated singularly, and therefore cannot be directly observed.

universe. The J/ψ meson was explained as a bound state of a charm quark and its antiquark, $J/\psi = c\bar{c}$, [23] with a mass roughly equal to that of a proton. Thus, the discovery of the J/ψ confirmed the existence of the charm quark, adding a 4^{th} quark to the quark model. After the discovery of the J/ψ, more such particles were discovered and were all categorized into a subset called "charmonium", meaning particles containing charm quarks. Following the discovery of the charm quark a fifth lepton, "tau" (τ), was discovered [24] at SLAC, which immediately implied the existence of its associated neutrino. A total of six leptons implied the existence of two more quarks, named "bottom" and "top". The existence of the bottom quark was confirmed with the discovery of the upsilon (Y) meson at Fermilab in 1977 [25]. Upsilon was explained as a bound state of a bottom quark and its antiquark ($Y = b\bar{b}$). The bottom quark was found to be roughly four times heavier than the proton. The discovery of the top quark was soon anticipated through a hadronic bound state of it despite knowing it would be the heaviest of them all and thus would require much larger energy to create in a particle collision. However, it was only discovered [26] two decades after the discovery of the bottom quark, in 1995, following many experimental efforts at the Tevatron at Fermilab while keep increasing collision energy to very larger values. The mass of the top quark was found to be ~ 40 times heavier than that of the bottom quark, which was an extraordinary mass than what anticipated for the quark family.

2.1.6 Fundamental Interactions & The Standard Model

Alongside the discoveries of fundamental quarks and leptons, the interactions between these particles were studied as well. By the 1970's theoretical and mathematical models had been put forward to understand four fundamental interactions (fundamental forces) responsible for the interactions between fundamental particles. These are known as the gravitational, electromagnetic, strong, and weak forces [27]. Each interaction is described mathematically as a field which is explained in terms of a gauge theory[1]. The gravitational force is modeled as a classical gauge field while the other three interactions are modeled as discrete quantum gauge fields. In addition, the gravitational is the weakest[2] among the four forces and thus has no influence on the properties of everyday matter. As the other three interactions are explained by quantized gauge fields, each is associate with a quanta of its gauge field which is known as a gauge boson. These gauge bosons are identified as fundamental boson particle which acts as the force carrier of its respective interaction.

The theory of electromagnetic interaction, which acts between charged particles, is known as Quantum Electrodynamics (QED) with the associated mediators, photons. This theory was well established in the 50's before the introduction of the quark model. The first indication of the weak interaction, which acts between all fermions[3] came from the discovery of beta decay in late 1920's. A unified quantum theory, known as the "Electro Weak Theory (EWT)" [28], to explain the weak interaction was proposed in the 60's together with the electromagnetic interaction as a unified force, by Sheldon Glashow, Abdus Salam, and Steven Weinberg. Three new associated gauge bosons ($W^{\pm}$ and Z bosons) were introduced by EWT in addition to the photon. The strong interaction, which acts between quarks, was explained by a theory known as "Quantum Chromodynamics (QCD)", with its associated gauge boson the "gluon"[4]. The theory of QCD began to develop with the introduction of the quarks in the quark model

[1] A type of field theory in which the Lagrangian is invariant under a continuous group of local transformations.

[2] It is 10^{29} times weaker than the second weakest, the weak force.

[3] Quarks and leptons together are called fermions.

[4] As the quarks (anti-quarks) come in three color states, red, blue, and green (anti-red, anti-blue, anti-green) and they bound together to form colorless states such as hadrons, gluons can come in eight independent color states (gluon octet), by linearly combining different possible quark color and anti-color states. Due to this property gluon can interact between themselves in contrast to the photons in QED.

and was firmly established decades later after many high energy experiments in the 60's and 70's.

As it is rather complex and difficult to understand interactions in mathematical forms, Feynman introduced diagrams to visually represent interactions as simply as possible, known as Feynman diagrams. Feynman diagrams of an elementary process in QED, a weak interaction and a elementary process in QCD are shown in Figure 2.2. The QED vertex can be interpreted as a charged particle, q, entering and emitting (or absorbing) a photon, γ, and exiting, q'. The annihilation of a down (d) and anti-up ($\bar{u}$) quarks producing a W^- boson, which decays through the leptons is shown in the middle diagram, and a simple QCD vertex of quarks annihilation to a gluon is shown in the right diagram. Following the

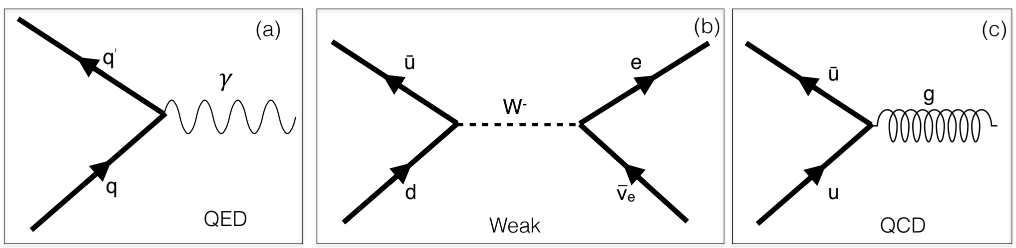

Figure 2.2.: Feynman diagrams of a simplest QED vertex, quarks annihilation (pion decay) via weak interaction and a simplest QCD vertex.

establishment of gauge theories for the fundamental interactions, a single model, known as the "Standard Model (SM)", which represents the current understanding of all the fundamental fermions, gauge bosons, and their interactions [27] was introduced. The SM implies that matter is made up of fundamental particles: quarks, leptons and carrier bosons. Figure 2.3 shows the current understanding of the SM. Both the leptons and quarks can be classified into three generations based on their properties as shown in the figure. The SM contains six leptons and six anti-leptons making 12 total leptons. There are six flavors of quarks and each come in three colors making 18 quarks. Together with the corresponding 18

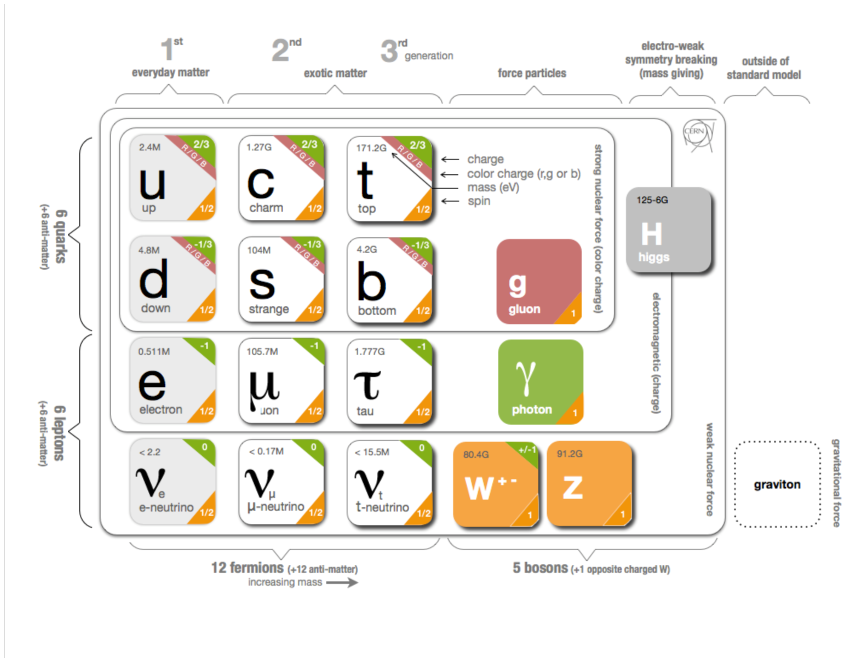

Figure 2.3.: The Standard Model [29]

anti-quarks the SM has 36 total quarks. Finally, there are force carries: 8 gluons, 3 weak bosons ($W^{\pm}$ and Z), 1 photon and 1 Higgs boson, the gauge boson of the Higgs field.

2.2 Weak Interaction and W & Z Bosons

The W bosons discussed in this thesis are the force carries of the weak interaction in the SM. Therefore the properties of the weak interaction are briefly discussed here. In contrast to the other forces, the weak force acts between all the fermions in the standard model [28]. It is the only force capable of changing the flavor of a quark, thus is responsible for radioactive decays, such as β decay, which change a neutron into a proton by changing the flavor of d quarks into a u quarks. Typically, the decay of particles through the weak interaction occur slower than those through the electromagnetic or strong interaction due to the heavy masses of the W ($\sim$ 80 GeV / c^2) and Z ($\sim$ 91 GeV / c^2) bosons. However, due to the same reason, the decay of the W and Z bosons themselves occur rapidly. The weak interaction violates many conservation laws, such as parity and charge symmetry, which are conserved by the other two forces in the standard model. In the theory of the weak interaction, EWT, W and Z bosons are originally introduced as three massless gauge bosons, (W^+, W^- and W^0). However, they acquire masses through the Higgs mechanism [30]. After acquiring masses W^+, W^- become the regular W boson that are observed experimentally. However, the W^0 boson (and B boson corresponding to the photon) does not immediately implies the observed Z^0 boson (and the photon). The vector fields that correspond to W^0 and B bosons are mixed by a characteristic angle known as the weak mixing angle, to subsequently produce the observed Z^0 and the photon [27].

The weak interaction is not conserved under the parity transformation. The parity transformation is defined as a flip in the sign of one spatial coordinate. In three dimensions it can be described as the simultaneous flip in the sign of all three spatial coordinates, ($x \to -x$, $y \to -y$, $z \to -z$). Therefore, under parity transformation, a phenomenon transforms into its mirror image. For example, parity transforms a right handed system to its corresponding left handed system. The weak interaction mediated by $W^{\pm}$ bosons is known as the charge current interaction while the weak interaction mediated by the Z^0 bosons is known as the neutral current interaction. Due to the violation of parity symmetry, the weak interaction is describe by a vector minus axial vector (V-A) or left handed Lagrangian. This theory implies that the weak interaction acts only on left-handed particles and right-handed antiparticles. Therefore, the W bosons that are produced in the $p+p$ collision discussed in this thesis work, only couple to the left handed quarks and right handed antiquarks in the polarized proton. However, this is not entirely true for the case of neutral current (Z^0) as right handed fields as well enters it's Lagrangian.

2.3 Structure of the Proton

Since the discovery of the atomic nucleus using α particle scattering experiments, scattering experiments has been used as a primary tool to explore the internal structure of particles. Elastic scattering using low energy electrons was used extensively to study the electronic configuration of the atom. However, in order to explore the structure of the nucleons (protons and neutrons) high energy electrons were required[1]. The low energy ($\sim$ MeV) elastic electron-proton scattering experiments that were performed during the late 1950's to early 1960's defined the proton as a soft (mushy) object that could have an extended structure, possibly with a hard core surrounded by a cloud of mesons [31]. In order to see the structure of this hard core, one needed to go "deep" inside of the proton and therefore required higher energy electron beams to scattered off of it. With this motivation the SLAC (fixed target) and subsequently many fixed target and collider accelerator facilities were commissioned and various hard scattering experiments such as Deep Inelastic Scattering (DIS), lepton-hadron scattering, and hadron-hadron scattering were performed to study the structure of the nucleon.

2.3.1 Deep Inelastic Scattering (DIS)

Figure 2.4 shows the Feynman diagram of an inclusive DIS scattering of a lepton (e or μ) off a proton target at rest. The lepton interacts with the proton via an exchange of a virtual photon, γ^*.[2] If the momentum transfer, Q^2 to the virtual photon is large enough so that its wavelength, λ, is less than the proton charge radius the internal structure of the proton can be probed.

In order to understand this, the kinematics of a DIS process [31] must be

[1] As the energy increased the wavelength of particles becomes shorter and therefore by scattering off high energy particles one can probe internal structure of composite particles with relatively smaller radii.

[2] A virtual particle is a type of temporary particle that is short lived and carry non-zero mass in contrast to real photon which carry zero mass.

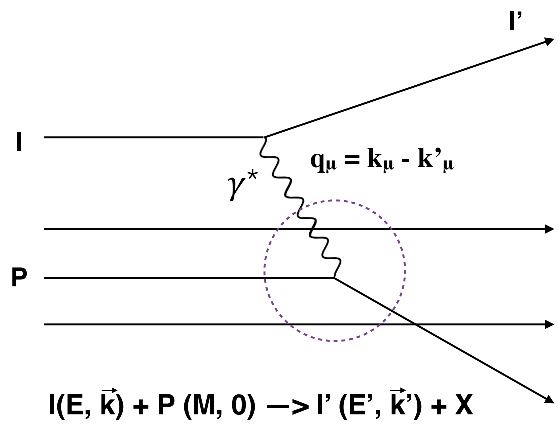

Figure 2.4.: Feynman diagram of DIS scattering of electron off a fixed proton target.

understood. In the case where only the scattered electron is detected in the final state, we call it an inclusive process. If k^μ, k'^μ and p^μ are four-momenta of the incoming electron, outgoing scattered electron and target proton respectively, the four momentum transfer to the virtual photon, q^μ, can be written as,

$$q^\mu = k^\mu - k'^\mu. \tag{2.1}$$

The q^μ is often characterized by the quantity known as resolution scale, Q^2, which is the square of q^μ,

$$Q^2 = -q_\mu q^\mu = -q^2 = 2EE' \sin^2(\theta/2) \tag{2.2}$$

where θ is the scattering angle of the scattered lepton, $l'(E', \vec{k'})$, in the lab frame. The energy loss, ν, of the scattered electron,

$$\nu = q \cdot p = M(E - E'), \tag{2.3}$$

and a measure of the inelasticity which can be obtained as the fraction of the energy loss by the scattered electron,

$$y = \frac{q \cdot p}{l \cdot p} = \frac{\nu}{E} = 1 - \frac{E}{E'}. \tag{2.4}$$

The invariant or missing mass, W, of the final hadronic system can be obtained as,

$$W^2 = (2M\nu + M^2 - q^2), \tag{2.5}$$

where M is the mass of the target (proton). On the assumption of a single photon exchange the differential cross section, $d^2\sigma/d\Omega dE'(E, E', \theta)$, can be written in terms of two structure functions W_1, W_2,[1]

$$\frac{d^2\sigma}{d\Omega dE'}(E, E', \theta) = \sigma_M \Big(W_2(\nu, Q^2) + 2W_1(\nu, Q^2) tan^2(\theta/2) \Big) \tag{2.6}$$

where $\sigma_M = \frac{4\alpha^2 E'^2}{Q^4} cos^2(\theta/2)$ is the Mott cross section for elastic scattering from a point proton and $\alpha = 1/137$ is the QED coupling constant. By measuring the differential cross section for several values of θ for fixed ν and q^2 two structure functions can be extracted.

In 1969 Bjorken proposed [32] that in the limit of q^2 and ν approaching infinity ("Bjorken limit") ($q^2 \to \infty$, $\nu \to \infty$) and with the ratio, $\omega = 2M\nu/q^2$[2], held fixed, the two quantities W_1 and νW_2 becomes functions of ω only. This implies that one can write new structure functions, F_1 and F_2, as functions of x as,

$$F_1(x) = 2MW_1(\nu, q^2) \; and \; F_2(x) = \nu W_2(\nu, q^2). \tag{2.7}$$

This property is referred to as "Bjorken scaling" in the Bjorken limit. In simple terms, what Bjorken implied by structure functions being largely independent from q^2 is that the virtual photon is scattered from a particle (quark) with no further substructure. If a substructure exists, then one should see changes (increment) in the structure functions as q^2 is increased. The structure functions obtained from early inclusive DIS results [19, 33] from the SLAC experiments

[1] The structure functions summarize all the information of the target particles, analog to elastic and magnetic form factors in a elastic scattering.

[2] The inverse of this quantity is now referred to as x, which is the fraction of momentum that each patron inside a hadron takes from the hadron's total momentum.

showed the scaling behavior as proposed by Bjorken. As a result, the behavior of the structure functions was understood as due to scattering off charged point like particles, "partons", in the proton [34–36] as explained in Feynman's Parton model [18]. The Parton model assumed the infinite momentum frame of the proton, where partons mostly have collinear momentum[1] and carry a fraction of momentum, $x = 1/\omega = Q^2/2\nu = Q^2/2M(E - E')$, from the proton.

In late 1968, Curt Callan and David Gross proposed [37] that if partons were spin 1/2 particles then in the Bjorken limit $F_2 = xF_1$. The experimental results agreed with the Callan-Gross relation in the Bjorken limit, concluding that partons were indeed spin 1/2 particles. Over the years extensive DIS experiments were conducted for large variations of Q^2 and it was found that for certain Q^2 and for certain x values the structure functions show dependance on Q^2. This was then referred to as "scaling violation". During this time, the proton was understood on the basis of both the quark model and the parton model interpretations ("quark-parton model") as a constitute of three quarks, which carry larger fractions of the proton's momentum ("valence" quarks), and a collection of quark-antiquark pairs ("sea" quarks), which accounted for the large DIS cross section observed at low Bjorken x values. However, calculations reveled that quarks carry only about 50% of the proton momentum, and therefore, "gluons", which bind the quarks together were introduced to accommodate the remaining momentum of the proton [38]. Extensive theoretical studies were performed in order to explain the experimental DIS results, in particular the scaling violation which resulted in the development of QCD theory [39].

QCD theory explains the DIS results as follows. At large values of x ($0.3 \leq x < 1$), according to the uncertainty principle, a quark with momentum x is more likely to dissociate into a quark and a gluon making a bound state of a hadron.

[1] Partons were assumed not to interact with one another while the virtual photon was exchanged, thus having negligible transverse momentum. This assumption of a near-vanishing of the parton-parton interaction during lepton scattering, in the Bjorken limit, was subsequently shown to be a consequence of QCD, the asymptotic freedom.

And for small x values the population of both quarks and anti-quarks enhanced by gluon breaking into quark and anti-quark pairs (sea quarks). This implies that as Q^2 increases the structure function should fall at large values of x and rise at small values of x ("QCD scaling violation"). As the very early DIS results were limited by a small $x - Q^2$ span region the behavior predicted by QCD was not seen clearly. However, when larger kinematic ranges became accessible in experiments and energies of scattering beams were increased[1] scaling violation in QCD was confirmed. A summary [40] of DIS experiments results, from all over the world, of the F_2 structure function which covers large parameter space in both x and Q^2, is shown in Figure 2.5. A clear Q^2 dependance of F_2 can be seen. F_2 increases with increasing Q^2 at small $x < 0.3$, and decreases at large $x > 0.3$ values, showing strong agreement with QCD scaling violation.

2.3.2 Parton Distribution Functions

The structure functions from the previous section can be constructed from the probability density, $q_i(x)$, of finding a parton with flavor q carrying a momentum fraction x in the proton, the "parton distribution function" (PDF) [31], as,

$$F_2(x) = 2xF_1(x) = \Sigma_i e_i^2 x q_i(x) \tag{2.8}$$

where the sum on i is over the quark flavors and e_i is the electric charge of that flavor quark. Since the gluons are electrically neutral the DIS structure functions are not directly sensitive to the gluon distributions. The PDFs are extremely important for predictions of cross sections for processes that involve hadrons. Due to the non-perturbative nature of the tightly bound partons in the bound state of hadrons, the PDFs can not be calculated by the first principle of perturbative

[1] In 1991, HERA electron-proton and positron-proton collider increased lepton beam energy to 30 GeV and protons to 920 GeV.

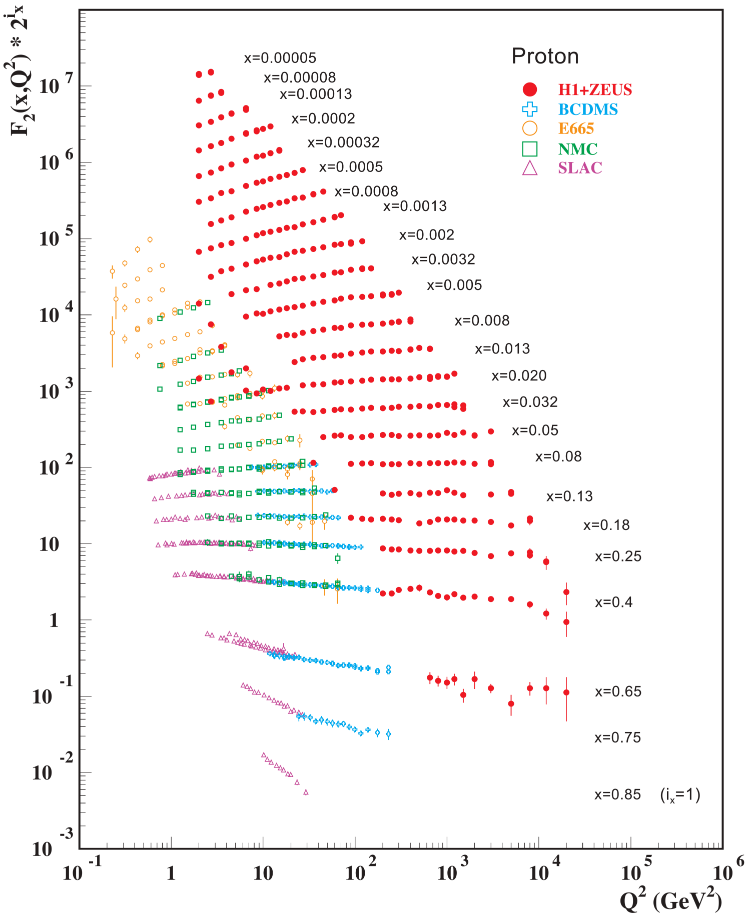

Figure 2.5.: The structure function $F_2(x)$ measurements from DIS world data. [40]

QCD and are thus required to be extracted from experiment.[1] The theoretical foundation which allows one to extract PDFs from various particle processes in wide kinematic ranges is provided by three principles, QCD factorization, universality, and QCD evolution [42]. QCD factorization allows the cross sections for hard scattering processes in hadron-hadron or lepton-hadron collisions to be factorized into two (or more) components: short ranges and long ranges. The

[1] Calculations in Lattice QCD can be applied to some of the non-perturbative effects of bound states in QCD, however various restrictions limit providing complete calculations for all kinematic ranges, see [41] for a recent review.

short range component can be computed in perturbative QCD due to the weak coupling asymptotic behavior of partons at short ranges. The long-range components, however, are not calculable perturbatively and are instead described using distribution functions of partons in a hadron, Parton Distribution Functions (PDF). The factorization theorem provides the basis for the universality of PDFs at leading twist. This implies that when a parton participate in a partonic process of a hard scattering, the PDF that describes its distribution amplitude in the bound state of the hadron would be same when it participates in another partonic process in a different hard scattering. Therefore, PDF of a parton does not depend on the type of the hadron. The QCD evolution equation (DGALP [31]) provides the scale dependance (Q^2) of PDFs. Based on this theoretical framework, one can use universal PDFs that are calculated at one scale to predict the cross section of a hadron scattering process that occurred at a different scale.

The process of extracting PDFs from data requires a large amount of data from many different types of hard scattering experiments (such as fixed target DIS, fixed target Drell-Yan (DY)[1], and hadron/ lepton/ jet[2] production in collider scattering). This data is incorporated into a certain type of "global analysis" method which subsequently extracts PDFs. The general concept of such a global analysis is to start with a reasonable functional form for the expected x dependance of an individual PDF with some adjustable parameters. The experimental data is compared with perturbative QCD calculations based on factorization which uses the established functional form of the PDFs in the first step as input. Then, one can make a global fit of these input PDFs to the world data by adjusting the free parameters. Such global analyses are performed by many collaborations in the world and Figure 2.6 shows the PDFs extracted by the MSTW collaboration [43]. The valence structure of the proton is evident from the rise of the u and d quark PDFs at high x values. As the sea quarks

[1] Pair of oppositely charge lepton production from a virtual photon or Z boson that was produced through an annihilation of a quark and anti-quark

[2] stream of roughly collinear hadrons from a hard scattering in hadron-hadron collisions.

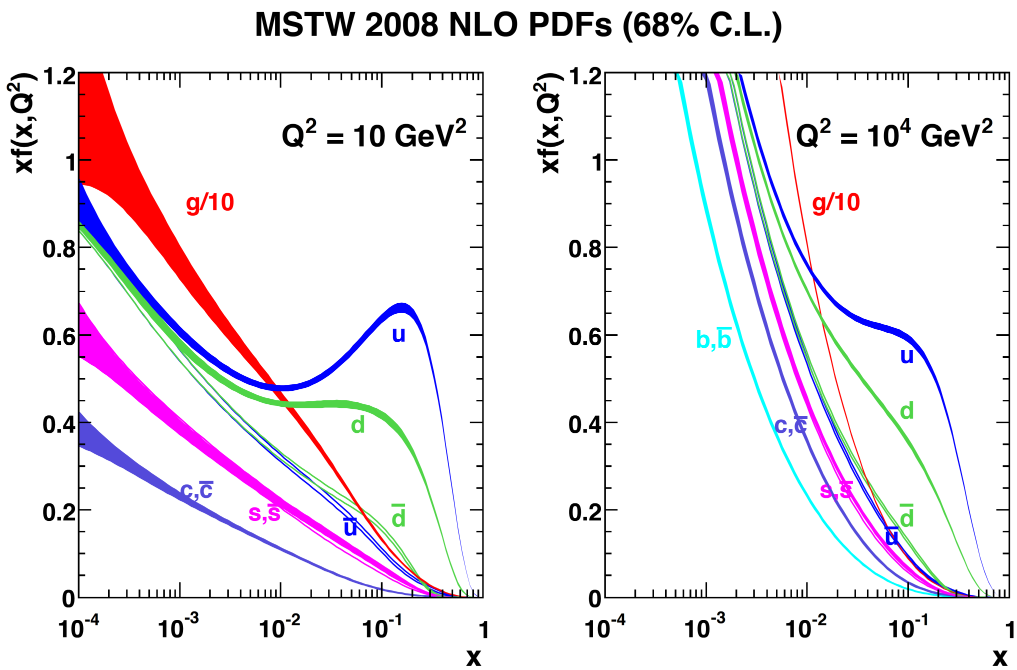

Figure 2.6.: PDFs as a function of x from the MSTW 2008 [43] set evaluated at $Q^2 = 10$ GeV^2 and $Q^2 = 10^4$ GeV^2 up to next-to-leading order (NLO).

carry a very small fraction of the proton's momentum the PDFs of sea quarks dominate at low x values.

2.4 Spin Structure of the Proton

Spin[1] is a fundamental property of all elementary particles, composite particles and atomic nuclei. Since the proton was discovered as a spin 1/2 fermion, which consists of quarks and gluons with their own internal spin the question immediately is raised, how does the spin of internal particles combine to make the spin of the proton? The quark-parton model assumed that the spin of the proton is simply the vector sum of the intrinsic spins of its valence quarks, similar to the charge of the proton which is explained by summing up the electric

[1] A type of angular momentum which can induces a magnetic dipole moment.

charges of its valence quarks [44]. In order to test this, polarized deep inelastic scattering (polDIS) experiments were performed. The kinematics of polDIS is similar to that of the unpolarized DIS that we have discussed so far. However, in polDIS polarized beams and targets are used. Therefore, one can study the spin dependent structure of the nucleon by scattering polarized beams off polarized targets (or another polarized beam in the case of colliders).

During the late 60's and early 70's several sum rules were proposed with integral values for a spin dependent structure function, $g_1(x)$, over all x values. One sum rule, that was subjected to the testing of early polarized DIS experiments, was known as the Ellis-Jaffe sum rule [45]. This sum rule was based on exact SU(3) flavor symmetry and assumed the strange sea quark polarization to be zero.[1] In order to test these sum rules, polarized DIS experiments were performed at SLAC [46] [47]. The results were limited by a small kinematic range and small Q^2 values ($x > 0.1, Q^2 < 10$GeV) and they agreed with the existing sum rules such as Ellis-Jaffe sum rule which were based on the quark-parton model, suggesting that the majority of the proton spin was carried by the valance quarks of the proton.

In 1989 the CERN EMC collaboration presented new polarized DIS results [48] of g_1^p based on a polarized muon scattering off of a polarized proton target. The results were in disagreement with the Ellis-Jaffe sum rule for g_1^p. The disagreements were significant and the results suggested that total quarks contribute very little (∼20%) to the spin of the proton. This was a big surprise and physicists realized they did not know how to justify the spin of the proton, a crisis which is referred to as the "proton spin crisis". After many theoretical and experimental efforts, new sum rules were produced indicating that the spin of the proton is contributed by quarks and anti-quarks polarization, gluon polarization, and their respective orbital angular momenta.

[1] As SU(3) does not have exact flavor symmetry and the polarization of strange quarks is not exactly zero Ellis-Jaffe sum rule was violated.

2.4.1 Helicity Parton Distribution Functions

Equation 2.9 shows the difference in the cross sections for polarized DIS when the helicities[1] of the polarized beam and the polarized target are anti-aligned and aligned,

$$\left(\frac{d^2\sigma^{+-}}{dQ^2 d\nu}\right) - \left(\frac{d^2\sigma^{++}}{dQ^2 d\nu}\right) = \frac{4\pi\alpha^2}{E^2 Q^2}[M(E + E'\cos\theta)G_1(Q^2,\nu) - Q^2 G_2(Q^2,\nu)] \quad (2.9)$$

where the first superscript and the second superscript of the cross section, σ, indicate the helicity of the beam and the target respectively. Symbols E, E', ν, θ, and M have the same meaning as in Equation 2.6. Similar to the unpolarized case, spin-dependent structure functions, $G_1(Q^2,\nu)$ and $G_2(Q^2,\nu)$, approach $g_1(x)$ and $g_2(x)$ structure functions at the Bjorken limit. In quark-parton model, $g_1(x)$ is defined as,

$$g_1 = \frac{1}{2}\Sigma_q e_q^2[q^+(x) - q^-(x)] = \frac{1}{2}\Sigma_q e_q^2 \Delta q(x), \quad (2.10)$$

where $q_i^{+(-)}(x)$, is the PDF of quark of flavor i, whose helicity is parallel (antiparallel) to that of the nucleon and $\Delta q_i(x)$ is the helicity PDF, which can interpreted as the probability density of finding a quark of flavor q with a proton momentum fraction x which has helicity parallel to that of the proton. Both $g_1(x)$ and $g_2(x)$ can be extracted from polarized DIS scattering experiments where polarized lepton beams scattered from polarized target nucleons. In this case, the spin asymmetry of the scattered lepton, A, is measured as the primary observable and it is related to the asymmetries of the virtual photon, A_1, and A_2.[2] The asymmetry A_1 can be written as [48],

$$A_1 = \frac{\sigma_{1/2} - \sigma_{3/2}}{\sigma_{1/2} + \sigma_{3/2}} \quad (2.11)$$

[1] The helicity of a particle is positive if it's spin vector and momentum vector parallel to each other and it is negative if their are anti-parallel.

[2] A_2 is related to total transverse photo absorption cross section and experimentally is neglected due to the small contribution.

where $\sigma_{1/2(3/2)}$ is the photoabsorption cross section of virtual photons whose spin is antiparallel (parallel) to that of target nucleon. According to angular momentum conservation, in an infinite momentum frame, a spin 1/2 parton cannot absorb a spin 1 photon when their two helicities are parallel (+). Therefore, a parton can only contribute to $\sigma_{1/2(3/2)}$, when it's helicity is parallel (antiparallel) to that of the target nucleon. This implies that,

$$A_1 = \frac{\Sigma_i e_i^2 (q^+(x) - q^-(x))}{\Sigma_i e_i^2 (q^+(x) + q^-(x))} = \frac{\Sigma_i e_i^2 \Delta q_i(x)}{\Sigma_i e_i^2 q_i(x)}, \tag{2.12}$$

where $q^{+(-)}(x)$ has the same meaning as in Equation 2.10, and $\Delta q_i(x)(q_i(x))$ is the polarized (unpolarized) PDF. Therefore, according to Equations 2.10 and 2.8, one can see that A_1 is equal to the ratio of the polarized structure function, $g_1(x)$, to the unpolarized structure function, $F_1(x)$ [48]. Similar to the unpolarized case, $g_1(x)$ was extracted from spin asymmetries which provided the information of polarized PDFs of nucleons.

Following the spin crisis, a modern sum rule was proposed by Jaffe and Manohar in 1990 [49] where proton spin is decomposed into contributions from intrinsic quark and antiquark polarization ($\Delta\Sigma$), intrinsic gluon polarization (ΔG), and orbital angular momenta of quarks (L_q) and gluons (L_g) as,

$$\langle S_p \rangle = \frac{1}{2} = \frac{1}{2}\Delta\Sigma + \Delta G + L_q + L_g, \tag{2.13}$$

where,

$$\Delta\Sigma = \int dx(\Delta u(x) + \Delta\bar{u}(x) + \Delta d(x) + \Delta\bar{d}(x) + \Delta s(x) + \Delta\bar{s}(x) \tag{2.14}$$

is the total quark and antiquark contribution written as the sum of polarized (helicity-dependent) PDFs of individual flavors (neglecting heavy flavors). Similar to the unpolarized case, helicity PDFs must also be extracted from the measurements of polarized DIS experiments. Through the measurements of inclusive DIS experiments the total quarks and antiquarks contribution was constrained and found to be $\sim 30\%$[1]. The polarized proton-proton collision program at the

[1] As total quarks contribution to the spin was relatively small, gluons and orbital angular momentum together are expected to contribute a significant fraction.

Relativistic Heavy Ion Collider (RHIC) and other facilities in the world conduct dedicated experiments to constrain ΔG[1]. Studying about ΔG or the orbital angular momentum are not the interest of the research work discussed in thesis, thus, no further discussion on those are made in this text.

Inclusive polarized DIS is only sensitive to the square of the charge of the struck parton which the virtual photon has been transferred, thus it is not sensitive to the flavor of the quark or capable of distinguishing between quarks and antiquarks. In order to constrain individual quark and anti-quark flavors new means were required. One such method is polarized semi-inclusive DIS (SIDIS) experiments [51]. In SIDIS, a charged hadron[2] (π, kaon, proton) is detected in the final state in coincidence with the scattered lepton. Based on the type of hadron that formed in the final state, one can obtain the information of the flavor of the individual struck quark or antiquark in the initial state. For example, if a π^+ is tagged in the final state, it would indicate that likely a u quark or $\bar{d}$ quark was struck in the scattering since $\pi^+ = u\bar{d}$. In SIDIS, the analogous expression for the g_1 structure function becomes,

$$g_1^h(x, Q^2, z) = \frac{1}{2}\Sigma_i e_i^2[\Delta q_i(x) D_q^h(z, Q^2) + \Delta \bar{q}_i(x) D_{\bar{q}}^h(z, Q^2)] \tag{2.15}$$

where $D_{q,\bar{q}}^h(z, Q^2)$ is the fragmentation function (FF) of the quark and z is the fractional energy of the hadron. The FF characterizes the scattered parton that fragmented into the part of a hadronic final state. Due to the non-perturbative nature in the fragmentation process, the FFs cannot be primarily calculated in perturbative QCD. Therefore, similar to the PDFs, the FFs are extracted from experimental data. They are determined primarily from precision data on hadron production in e^+ e^- annihilation through perturbative QCD analyses [52, 53].

Over the years, several global analyses were performed to extract the helicity PDFs of individual quarks and antiquarks using DIS, SIDIS, and early RHIC

[1] Recent results from the RHIC suggest a sizable contribution from gluons [50]

[2] This hadron is a result of the fragmentation of the struck parton, which the virtual photon has been transferred.

$pp \to jets$ data. These analyses that were performed by the groups, DSSV, LSS [54] and NNPDF [55] are referred to in this text. Figure 2.7 shows the helicity PDFs from the DSSV08 [56] global analysis by the DSSV group. These

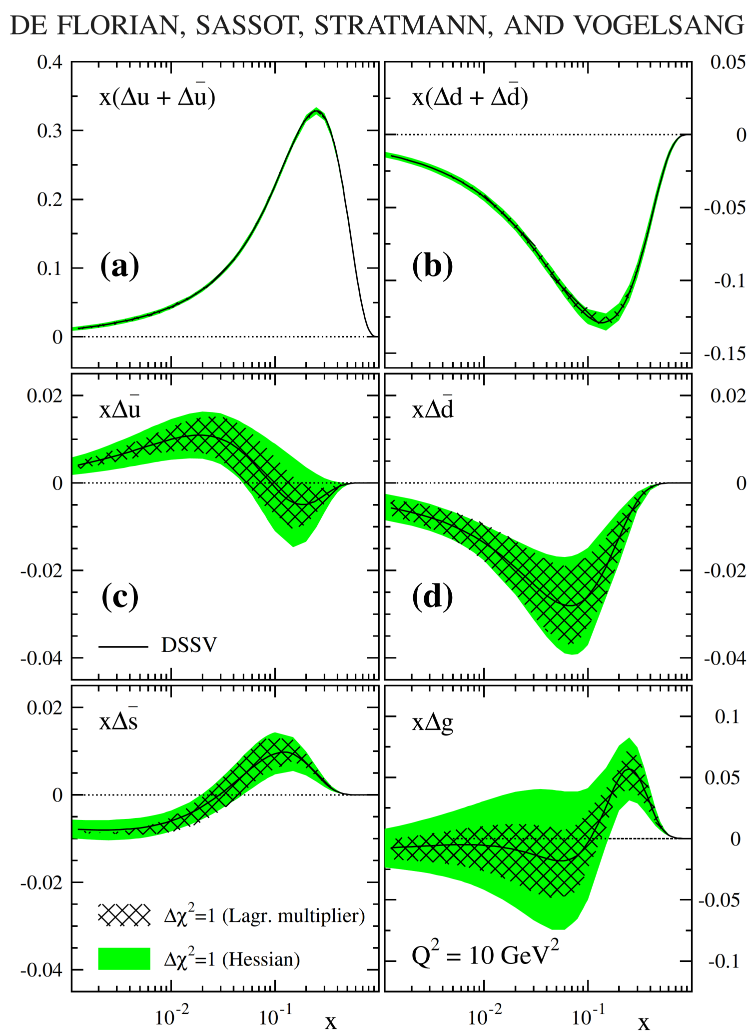

Figure 2.7.: Helicity PDFs of the proton at $Q^2 = 10$ GeV from [56]

PDFs are extracted using world data of DIS and SIDIS experiments that were performed over the years by many collaborations (EMC, SMC, CLAS, HERMES, COMPASS). Some of the early RHIC pp ($pp \to jets$, $pp \to \pi^0$) data as well is also included (see [56] for more details). One can see that the total quark and antiquark distributions of u and d, (panel (a) and (b)) are well constrained with small uncertainties. However, the individual $\bar{u}$ and $\bar{d}$ distributions (panel (c) and (d)) show larger uncertainties. As these were constrained primarily from SIDIS data, the resulted larger uncertainties were attributed to the uncertainties of the FF that were used [56].

As the SIDIS capability of constraining anti-quark helicity distributions was less precise, a need of a more precise method was demanded. In addition, precise understanding of the polarized sea was also motived by evidence of a broken flavor symmetry in the unpolarized sea. In 1998, Fermi Lab E866 DY [57] experiments confirmed the existence of an unpolarized asymmetric sea ($\bar{d} > \bar{u}$ at $x < 0.3$).[1] Several non-perturbative models have explained the behavior of the $\bar{d}/\bar{u}$ that was observed in E866 experiments. These models, which qualitatively reproduce the features of the data includes, Meson cloud models [58], Chiral quark soliton models [1], Instanton models [59], and Statistical models [60].

Meson cloud models explain the excess of $\bar{d}$ quarks in the proton as a result of a sizable contribution from the neutron π^+ state, due to the larger nucleon/delta mass difference. Chiral quark soliton models explain the behavior of excess $\bar{d}$ based on the valance quark structure of the proton and existence of virtual pions. They indicate that virtual pions couples to constituent quarks, and due to the excess of u quarks than d quarks in the proton more virtual π^+ exist than virtual π^-. Therefore more $\bar{d}$ results through the dissociation of excess virtual π^+ into u and $\bar{d}$ than π^- into d and $\bar{u}$. Instanton models implies the helicity flip of a incoming quark through the quark-instanton interaction, producing quark anti-quark pair of a different flavor. Then again, due to more u quarks than d quarks in the proton more $d\bar{d}$ pairs are produced than $u\bar{u}$ pairs by the quark-instanton interaction. Statistical models consider nucleons as a gas of massless quarks and gluons in equilibrium. In this approach both $d\bar{d}$ and $u\bar{u}$ pairs are produced from

[1] Since the mass difference of up and down quarks is small, equal numbers of up and down quark-antiquark pairs are expected to be produced perturbatively in the nucleon sea from gluon splitting.

gluon splitting with roughly equal probability, but because there are more u quarks than d quarks in the valance structure of the proton the $\bar{u}$ quarks in the sea are more likely to annihilate with a valence quark, and thus an excess of $\bar{d}$ quarks remains. These non-perturbative models also predict an asymmetry in the polarized nucleon sea. Some models such as the chiral quark soliton model predicts a large positive asymmetry between $\Delta\bar{u}$ and $\Delta\bar{d}$ ($\Delta\bar{u} > \Delta\bar{d}$). Figure 2.8 shows leading order extraction of x($\Delta\bar{u}-\Delta\bar{d}$) from SIDIS experimental data along with various model predictions. One can see for example, meson cloud model

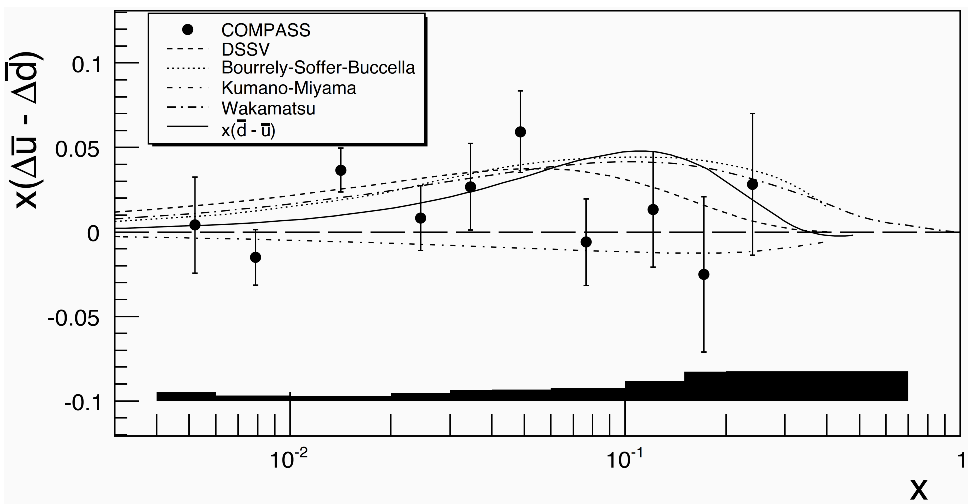

Figure 2.8.: Flavor asymmetry of the polarized sea, x($\Delta\bar{u} - \Delta\bar{d}$). The data points are LO extraction from COMPASS SIDIS data [61]. The other curves includes model predictions from chiral quark soliton (Wakamatsu [62]), meson cloud model (Kumano and Miyama [63]), and statistical (Bourrely, Soffer and Buccella [64]).

predicts a small negative value for x($\Delta\bar{u} - \Delta\bar{d}$), while the statistical model and chiral quark model predict a large positive value. However, this extraction from SIDIS data are not sufficiently precise for one to differentiate among the models. Evidently, one needs more precise measurements of sea quark polarizations in order to understand the asymmetric nature of the polarized sea and to compare among the model predictions.

2.5 W Boson Production in Polarized Proton-Proton Collisions

Searching for a new tool, the production of W and Z bosons in a polarized proton-proton collision was recognized as a unique tool to study the quark and antiquark helicity distributions of the proton. As they are produced through the annihilation of quarks and antiquarks, both W and Z bosons have direct sensitivity to quark and antiquarks of interest. The collision of polarized protons began at RHIC in 2001 [65], creating an opportunity to study the quark antiquark polarization through the production of W and Z bosons [66]. However, one needed to use high energies (CM mass energy $\sim$ 500 GeV, twice the maximum energy RHIC operated at the time). The RHIC was built with potential for such an energy increment, which subsequently resulted in the commissioning of pp collision at $\sqrt{s}$= 500 GeV in 2009, starting the W program. Two dedicated physics analyses, measurement of unpolarized[1] cross section for W boson production to study the unpolarized flavor structure of the sea and measurement of single-spin asymmetries for W boson production to study the quark and antiquark polarization and flavor asymmetry of the polarized sea, began.

At RHIC, W bosons are produced with maximal parity violation[2] [67]. Therefore, W bosons couple to the left handed quarks and right handed antiquarks only. At leading order the $W^+(W^-)$ is produced by an annihilation of a $u(d)$ quark and $\bar{d}$ $(\bar{u})$ quarks. There is negligible contamination from the s, c and $\bar{s}$, $\bar{c}$ quarks

[1] Although the collisions and the kinematics are polarized, by spin averaging the final state one can make a unpolarized measurement.

[2] As the V-A structure of the charge current interaction acts only on left handed particles (right handed anti-particles) and since the mirror reflection of a left-handed particle is right-handed, this give rise to a maximal violation of parity.

due to the flavor mixing explained by the CKM matrix[1], but those ("Cabibbo suppressed transitions") are largely suppressed and therefore neglected for this discussion [68]. Figure 2.9 shows Feynman diagrams for $u+\bar{d} \to W^+$ (the analogs diagram for $d + \bar{u} \to W^-$ is not shown) [67]. Because of the heavy mass ($\sim$ 80

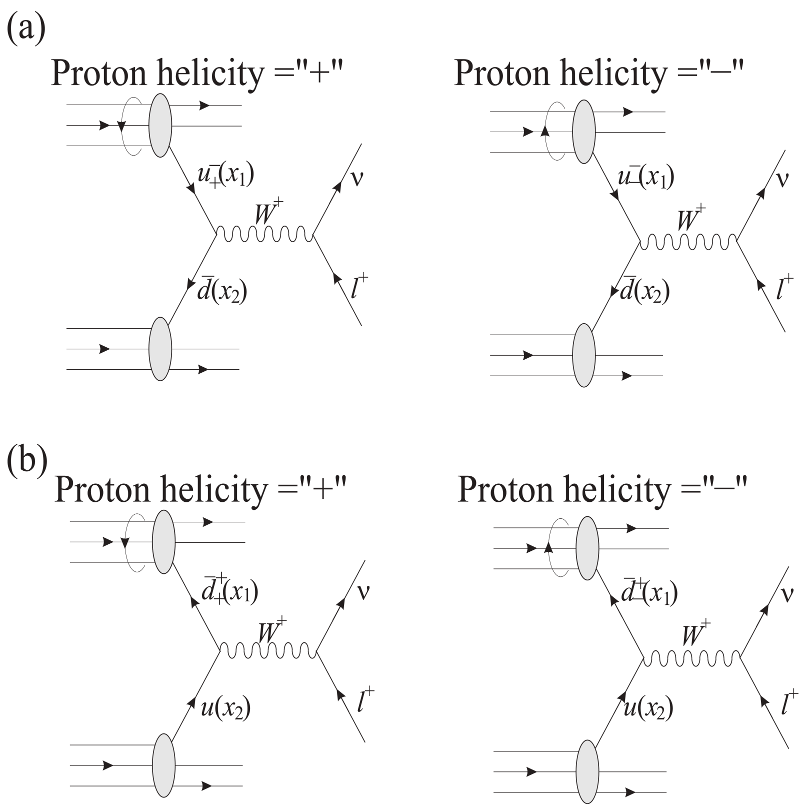

Figure 2.9.: Feynman diagrams for W^+ boson production in polarized pp collision[67]. In (a) the polarized proton provides the u quark, while in (b) the $\bar{d}$ quark is a constituent of the polarized proton. The helicity of the proton (quark) is indicated by the subscript (superscript) on the quark coming from the polarized proton.

GeV) the produced W bosons quickly decay into leptons or hadrons. In this work, we are interested in the W decay into electrons and positrons ($W^+ \to e^+ + \nu_e$,

[1] The CKM matrix provides information on the strength of the qurks flavor changing in the weak interaction.

$W^- \rightarrow e^- + \bar{\nu}_e$), thus they are reconstructed through the detection of decay electrons and positrons. Although the lepton decay mode of W bosons is characterized by a smaller branching ratio ($\sim 10\%$) than that of the hadronic decay mode ($\sim 67\%$), decay leptons from Ws are easy to identify experimentally at the STAR in comparison to the hadronic mode decay products that are hardly separable from the high multiplicity QCD type processes ($pp \rightarrow jets$).

2.5.1 Single-Spin Asymmetry

Spin asymmetries in proton-proton scattering are measured as the primary observable at the RHIC. In this analysis we focus on the production of W bosons and their subsequent decay into leptons ($e^{\pm}$). The longitudinal spin asymmetry, A_L for the process $\vec{p}\vec{p} \rightarrow W^{\pm}X$ can be written as,

$$A_L \equiv \frac{d\sigma^{++} + d\sigma^{+-} - d\sigma^{-+} - d\sigma^{--}}{d\sigma^{++} + d\sigma^{+-} + d\sigma^{-+} + d\sigma^{--}} \tag{2.16}$$

where, σ^{++}, etc. denote the cross section for producing a W boson with superscripts indicating the fixed helicities of the colliding protons. One can see that the helicities of the second proton are summed over, leading to the single-inclusive process $\vec{p}p \rightarrow W^{\pm}X$ where a longitudinally polarized proton collides with an unpolarized proton. Thus the above equation is reduced to the single-spin asymmetry, A_L which can be written as,

$$A_L \equiv \frac{d\Delta\sigma}{d\sigma} = \frac{\sigma^+ - \sigma^-}{\sigma^+ + \sigma^-} \tag{2.17}$$

where, $\sigma^{+(-)}$ is the cross section for producing a W boson when the helicity of the longitudinally polarized proton beam is positive (negative). Due to the pure V-A structure of the coupling in the charged current weak interaction, the helicity of the participating quark and antiquark are fixed. The parity-violating A_L can be expressed in terms of the parton helicity asymmetries, $\Delta q(x, Q^2)$, as shown in Equation 2.10. If a W^+ boson is produced only through the diagram in Figure 2.9 (a), where the u (left handed) quark is provided by the polarized proton, the A_L would be directly sensitive to the u quark longitudinal polarized PDF, Δu. This implies that for the simple lowest order (LO) process of $u\bar{d} \to W^+$, the A_L becomes[1],

$$A_L^{W^+} = \frac{u_+^-(x_1)\bar{d}(x_2) - u_-^-(x_1)\bar{d}(x_2)}{u_+^-(x_1)\bar{d}(x_2) + u_-^-(x_1)\bar{d}(x_2)} = -\frac{\Delta u(x_1)}{u(x_1)} \tag{2.18}$$

where the helicity of the quark (proton) is indicated by the superscript (subscript) and $x_1(x_2)$ is the fraction of momentum that the parton takes from the polarized (unpolarized) proton. When the polarized proton provides the antiquark (right handed), as shown in Figure 2.9 (b), A_L provide the sensitivity to $\bar{d}$ polarized PDF, $\Delta\bar{d}$ which can be written as,

$$A_L^{W^+} = \frac{\bar{d}_+^+(x_1)u(x_2) - \bar{d}_-^+(x_1)u(x_2)}{\bar{d}_+^+(x_1)u(x_2) + \bar{d}_-^+(x_1)u(x_2)} = \frac{\Delta\bar{d}(x_1)}{d(x_1)}. \tag{2.19}$$

As the polarized proton can provide either the quark or the antiquark, the general expression for A_L is a superposition of Figure 2.9 (a) and (b), given by,

$$A_L^{W^+} = \frac{-\Delta u(x_1)\bar{d}(x_2) + \Delta\bar{d}(x_1)u(x_2)}{u(x_1)\bar{d}(x_2) + \bar{d}(x_1)u(x_2)} \tag{2.20}$$

Similarly, for W^- one can write the analogues expression of $A_L^{W^-}$ by switching u with d and $\bar{u}$ with $\bar{d}$ as,

$$A_L^{W^-} = \frac{\Delta\bar{u}(x_1)d(x_2) - \Delta d(x_1)\bar{u}(x_2)}{\bar{u}(x_1)d(x_2) + d(x_1)\bar{u}(x_2)} \tag{2.21}$$

The partonic momentum fraction $x_1(x_2)$ can be related to the rapidity (see Sec. 4.1 for more details) of W, y_W, and the center of mass energy, $\sqrt{s}$, of the

[1] Note that $\Delta q(x) = q^+(x) - q^-(x)$ where the superscript + (-) indicates that the parton helicity is parallel (anti-parallel) to that of the proton.

hadronic system as [69],

$$x_{1,2} = \frac{M_W}{\sqrt{s}} e^{\pm y_W}. \tag{2.22}$$

One can see that at large positive (forward) rapidities, $y_W \gg 0$, $x_1 \sim 1$ and $x_2 \ll 1$. At the center of mass energy available at the RHIC, it is highly likely that the quark is coming from the valence region, carrying a significantly larger momentum fraction of its parent proton than the antiquark. By combining the above two arguments one can see that in the case of W^- at forward rapidities, the asymmetry will be dominated by the valence distribution probed at x_1 and gives direct access to $-\Delta d(x_1, M_W^2)/d(x_1, M_W^2)$ [1]. Likewise, at large negative (backward) rapidities, where $y_W \ll 0$, $x_1 \ll 1$ and $x_2 \sim 1$, the $A_L^{W^-}$ primarily probes the anti-u quark distribution, giving sensitivity to $\Delta\bar{u}(x_1, M_W^2)/\bar{u}(x_1, M_W^2)$. The situation for W^+ follows analogously [69].

The excellent sensitivity of the single-spin asymmetry to individual quark and antiquark helicity distributions at large positive and negative rapidities is a simple picture. However, at RHIC the application of this understanding is relatively hard due to limitation in the reconstruction of full W kinematics in the lab frame. Originally, the kinematics of the W in the lab frame, including the rapidity, was suggested to be reconstructed from its leptonic decay products. One could achieve this by measuring the kinematics of the decay products of the W bosons in the final state which is $e^+(e^-)$ and $\nu_e(\bar{\nu}_e)$ for $W^+(W^-)$. Since the neutrino escapes detection, one must use missing-momentum techniques[2] based on momentum conservation to reconstruct its kinematics. However, as the STAR detector (and also the PHENIX[3]) is not hermetic, such techniques cannot be used to reconstruct total kinematics in the final state and therefore the rapidity of W

[1] The resolution scale, Q^2, is defined by the mass of the W, M_W^2.

[2] This involves reconstructing the momentum of all other final state objects and using conservation of momentum and energy to calculate the kinematics of the undetected particles.

[3] The other large detector at RHIC.

bosons. One can however use MC model techniques to reconstruct W rapidity in the lab frame[1].

Due to the difficulty of reconstructing full kinematics of W, the strategy adopted by STAR (and also by PHENIX) experiment at RHIC is to measure the longitudinal single spin asymmetry for decay leptons as a function of their pseudorapidity, η_l. The relevant process therefore becomes the single-inclusive process, $\vec{p}p \to l^{\pm}X$, instead of $\vec{p}p \to W^{\pm}X$. Thus, one needs to understand the decay kinematics through the scattering angle, θ, of detected leptons. Figure 2.10 illustrates the θ dependance of the scattered $e^{\pm}$ that decay from W bosons. The incoming quarks and anti-quarks are illustrated with their helicities (left handed and right handed respectively). As mentioned before, W's tend to boost in the

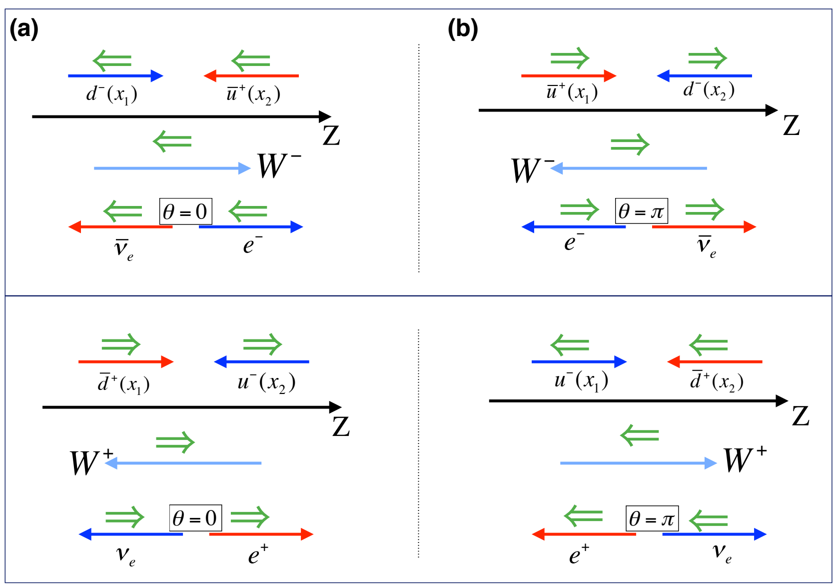

Figure 2.10.: The helicity configuration of W^+ (top) and W^- (bottom) for $\theta = 0$ (a) and $\theta = \pi$ (b). The single arrows ($\rightarrow$) indicates the particle direction of motion while double arrows ($\Rightarrow$) indicate the spin direction.

direction of the incoming valence quark with higher x. As the spin must be con-

[1] This method was applied to W A_N measurement at STAR [70]

served in the process, left handed Ws are produced and, due to the handedness of the decay neutrinos (in the visible universe only left handed neutrinos and right handed anti neutrinos exist), electrons are preferentially emitted parallel to W^-, being left handed, and positrons are emitted anti-parallel to W^+, being right handed.

In addition to the relationship between the scattering angle of the leptons and the helicity of incoming quarks, one must study the impact of higher order QCD correction of W's to the lepton level kinematics. In an ideal situation where W bosons are produced at rest, the W production cross section as a function of decay leptons transverse momentum, p_T, shows a clear peak ("Jacobian peak") at half of the W mass, $M_W/2$, with a very sharp drop at large p_T values. However, in reality the Jacobian peak is smeared out due to the non zero transverse momentum of the W boson arising from higher order QCD radiations[1] [68, 69]. Therefore, in order to properly relate lepton level kinematics with partonic level kinematics, these higher level smearing effects must be considered. A full theoretical framework which studied these effects is available at [71] .

These studies showed that the pseudorapidity dependance of the lepton asymmetry is sensitive to partonic helicity distributions in a similar way as the rapidity dependance of W asymmetry holds the same sensitivity. An excellent sensitivity was found between the average of partonic momentum fraction, $\langle x_1 \rangle$, $\langle x_2 \rangle$, and electron pseudorapidity as,

$$\langle x_{1,2} \rangle \sim \frac{M_W}{\sqrt{s}} e^{\pm \eta_l / 2}. \tag{2.23}$$

The above relation is graphically shown [69] in Fig 2.11 for $|\eta| < 2$, which is the rapidity reach at RHIC (thus, $0.05 \leq x \leq 0.4$, the kinematic reach at RHIC). One can see that the above relation shows the same approximations at the limit of forward and backward η_e that was seen at the limit of forward and backward y_W as shown in Equation 2.22. This implies that at large forward η_e, $x_1 \gg x_2$

[1] Such as quark-gluon scattering, NLO real gluon emissions.

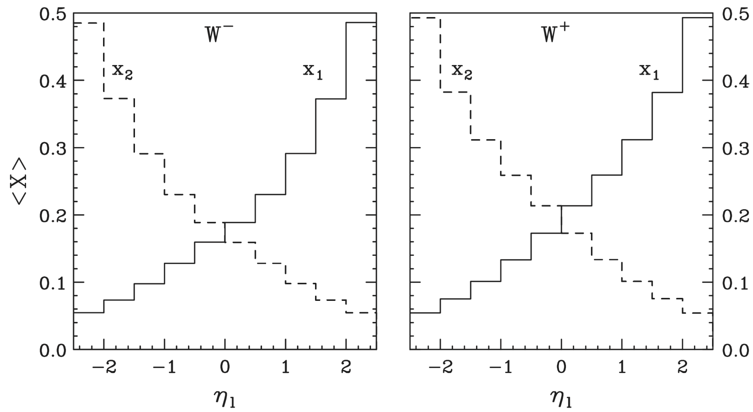

Figure 2.11.: $\langle x_1, x_2 \rangle$ as a function of η_l for W^- (left) and for W^+ (right) [69]

and at large backward η_e, $x_1 \ll x_2$. Similar to Equations 2.20 and 2.21 the lepton asymmetries can be written as a function of θ. In the partonic center of mass system $\theta > 0$ is in the forward direction of the polarized parton. As the kinematics of leptons in the final state does not completely determine the momentum fractions of the partons in the initial state, integration over the momentum fractions appear in the asymmetry formulas for $W^- \to e^- \bar{\nu}_e$ as,

$$A_L^{e^-} \approx \frac{\int_{\otimes(x_1,x_2)}[\Delta\bar{u}(x_1)d(x_2)(1-\cos\theta)^2 - \Delta d(x_1)\bar{u}(x_2)(1+\cos\theta)^2]}{\int_{\otimes(x_1,x_2)}[\bar{u}(x_1)d(x_2)(1-\cos\theta)^2 + d(x_1)\bar{u}(x_2)(1+\cos\theta)^2]} \tag{2.24}$$

and for $W^+ \to e^+ \nu_e$ as,

$$A_L^{e^+} \approx \frac{\int_{\otimes(x_1,x_2)}[\Delta\bar{d}(x_1)u(x_2)(1+\cos\theta)^2 - \Delta u(x_1)\bar{d}(x_2)(1-\cos\theta)^2]}{\int_{\otimes(x_1,x_2)}[\bar{d}(x_1)u(x_2)(1+\cos\theta)^2 + u(x_1)\bar{d}(x_2)(1-\cos\theta)^2]}. \tag{2.25}$$

The relation between θ and η_e expressed in Equation 2.23 implies the following approximations: At large forward η_e, ($\eta_e \gg 0, x_1 \gg x_2$) $\theta \to 0$ and at large backward η_e, ($\eta_e \ll 0, x_1 \ll x_2$) $\theta \to \pi$. Then, from Equation 2.24 of $A_L^{e^-}$, one can see that at large positive η_e the second term in the numerator and denominator dominate based on both the partonic kinematic term ($-\Delta d(x_1)\bar{u}(x_2)$) and the angle factor $(1-\cos\theta)$. Therefore, at relatively large x_1, $A_L^{e^-}$ give accesses to $-\Delta d(x_1)/d(x_1)$, thus probing the d quark helicity distribution. By similar reasoning, at large backward η_e, the first term in both the denominator and the numerator dominate, thus asymmetry gives direct sensitivity to the anti-u quark helicity distribution. At $\eta_e \sim 0$ one can see from Equation 2.23, $x_1 \sim x_2$ and $\theta \rightarrow \pi/2$, thus asymmetry probes the combination of the quark and anti-quark polarization. In the case of $W^+ \rightarrow e^+$, the asymmetry $A_L^{e^+}$, in Equation 2.25, does not make a clear separation between the quark and the antiquark based on the above arguments. This is caused by the fact that both terms contribute at all rapidity ranges. For example, at large forward rapidities one can see in the second term that the partonic term $\Delta u(x_1)\bar{d}(x_2)$ is large. However, it is suppressed due to the vanishing angular factor, $1-\cos\theta$, as $\theta \rightarrow 0$. At the same time the angular factor in the first term is large while the partonic term is not. Therefore both terms are essentially contributing to the W^+ asymmetry at all rapidities. The same is true for large negative rapidities as well.[1]

Various theoretical groups have predicted $W^\pm$ decaying into leptonic asymmetries based on two theoretical frameworks know as RHICBOS [71] and CHE [56, 72] using various PDF sets (which were extracted from DIS / SIDIS) as the input PDFs. The RHICBOS framework is primarily designed for the W Boson production at RHIC and is based on a calculation for resummation of large logarithmic contribution originating from multiple soft gluon radiation. The CHE[2] is a NLO (Next-to Leading Order) framework based on calculations of NLO QCD corrections. Technically, it is a Monte-Carlo like code which provides access to the full kinematics of the final state particles. Several predictions of single-spin asymmetry based on these two frameworks are shown in Figure 2.12. Here, three predictions based on RHICBOS framework by three groups who use PDF sets DNS-K, DNS-KKP, and DSSV08 [56] respectively and one prediction based on

[1] Due to this, the W^+ cross section could be smaller than the W^- cross section at large rapidities [69].

[2] Stands for “Collisisons at High Energies”.

CHE framework by DSSV group who uses PDF set DSSV08 can be seen. The

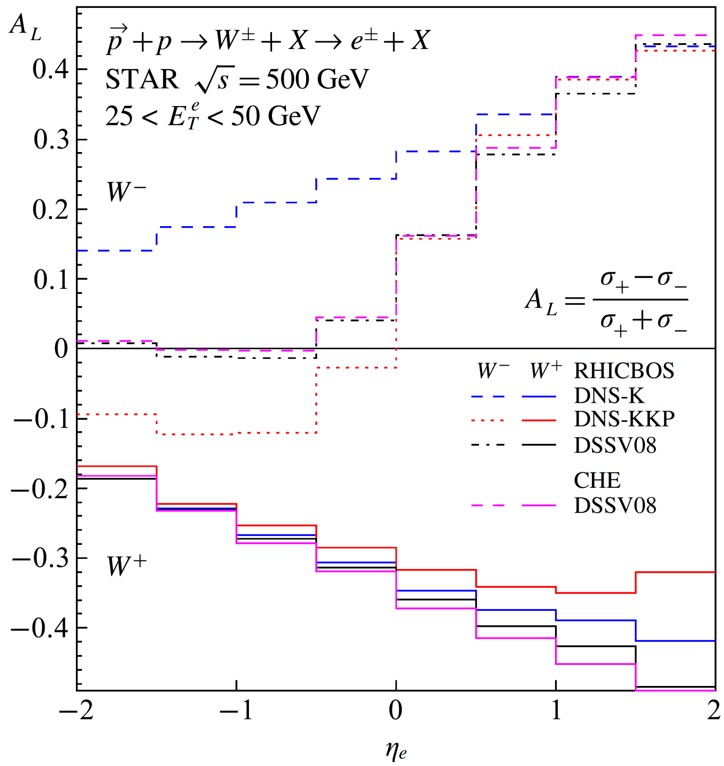

Figure 2.12.: Predictions for the longitudinal single spin asymmetry A_L for $W^{\pm}$ production at $\sqrt{500}$ GeV, as a function of $e^{\pm}$ pseudorapidity. The curves from different helicity PDFs and unpolarized PDFs are discussed in [69]

features explained above are well reflected in the predicted asymmetries from different theoretical calculations using different sets of PDFs. One can see that the W^- asymmetry becomes large and positive towards large forward rapidities, reflecting that the helicity of the d quarks remains negative as expected (noting that at large x $A_L^{e^-}$ probes $-\Delta d/d$). The large dispersion between the curves at large backward rapidities reflect the large uncertainty in the helicity distribution of the anti-u quark. One can see that these predictions based on DIS / SIDIS favor negative anti-u quark polarization in the kinematic range specified above. However, recent results from W A_L analyses at the RHIC show (also in this thesis) a positive and larger anti-u quark polarization than predicted from the theory. As for the W^+, one can see that the asymmetry is largely negative suggesting a large positive u quark polarization as expected and is also observed from DIS / SIDIS experiments. The dispersion between curves seen at large positive rapidities for $A_L^{e^+}$ was found to be correlated with the helicity PDFs of Δd (at $0.15 \leq x \leq 0.3$) [69].

CHAPTER 3
EXPERIMENTAL ASPECT

The analysis discussed in this dissertation is a part of the research performed at the Relativistic Heavy Ion collider (RHIC) at Brookhaven National Laboratory (BNL). The RHIC is a high energy particle collider that is capable of colliding hadrons and heavy ions. It is one of the two operating heavy-ion colliders in the world and[1] is the first and only polarized proton-proton collider in the world. The RHIC can collide polarized protons with center of mass energies up to $\sqrt{s_{pp}} = 510$ GeV and heavy ions species at varying energies from $\sqrt{s_{NN}} = 7.7$ GeV up to 200 GeV. The Solenoidal Tracker At RHIC (STAR) is one of the two large acceptance, multi-purpose detectors at the RHIC. This chapter will provide description of RHIC and STAR which is relevant for the analysis presented in this dissertation.

3.1 RHIC

A layout of the RHIC accelerator complex is shown in Figure 3.1. Several components which are critical for its operation of polarized proton-proton collision will be described briefly below. A full overview of the capabilities of RHIC is available at [73].

3.1.1 Polarized H^- Ion Source

An optically-pumped polarized H^- ion source (OPPIS) starts the accelerator chain of the RHIC complex [74]. The OPPIS replaced the existing BNL atomic

[1] Large Hadron Collider (LHC) at CERN is the other and the largest heavy-ion collider in the world.

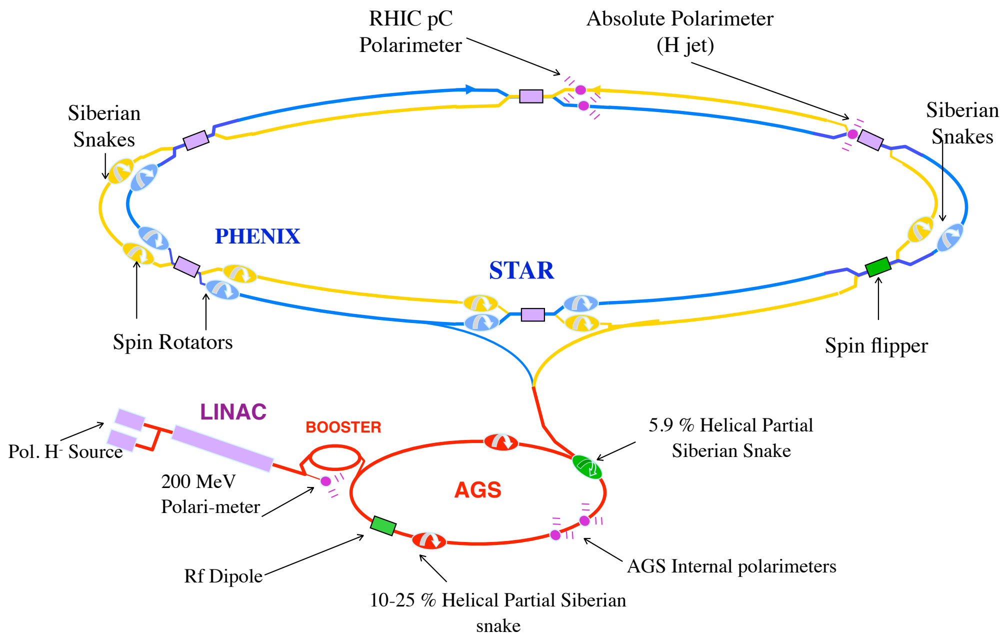

Figure 3.1.: A layout of the RHIC Complex [73]

beam source[1] to provide the required luminosity of $2 \times 10^{32} cm^{-2} s^{-1}$ by the RHIC spin physics program. In order to meet this anticipated luminosity an intensity of 2×10^{11} polarized protons per bunch must be achieved. The OPPIS is able to produce a more than sufficient bunch intensity from a single source pulse. It is capable of producing 500 μA current in a single 300 μs pulse providing 9×10^{11} polarized H^- ions with 80-85% polarization. A layout of the RHIC OPPIS is shown in Figure 3.2.

The OPPIS produces polarized H^- ions as follows[74, 75]. First, an Electron Cyclotron Resonance (ECR) proton source produces a primary proton beam of energy 2.8 - 3.0 keV. It then enters a hydrogen gas (H_2) region where it goes through a neutralization that converts it to a high brightness 6.0-10.0 KeV atomic hydrogen H^0 beam. Following the neutralization, the atomic H^0 beam enters a superconducting solenoid, where a He ionizer cell and an optically-pumped

[1] OPPIS intensity was 30 times higher than that of the atomic beam source.

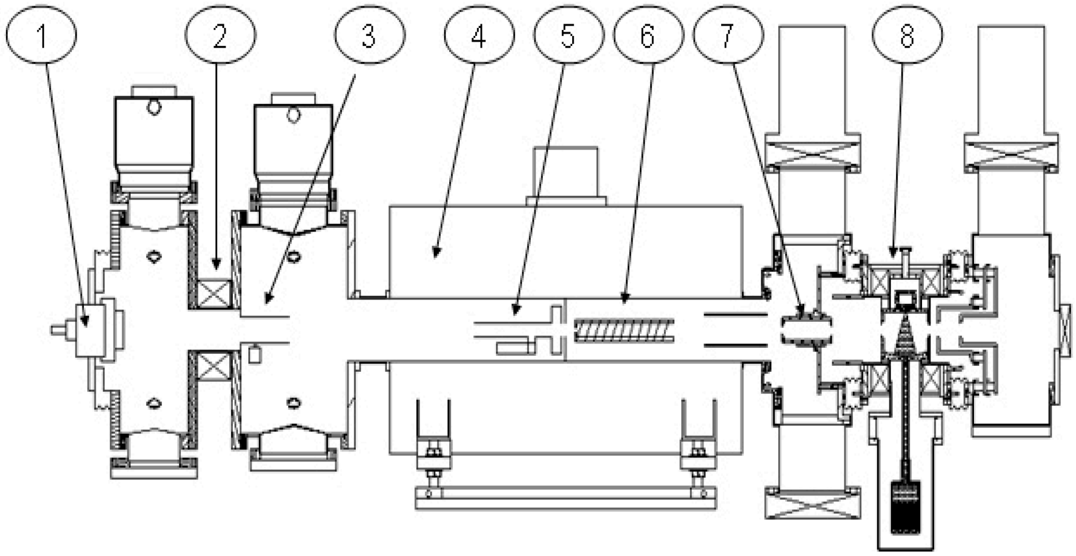

Figure 3.2.: Layout of the OPPIS with atomic hydrogen injector: 1 - high-brightness proton source; 2 - focusing solenoid; 3 - pulsed hydrogen neutralization cell; 4 - super conducting solenoid 30 kG; 5 - Pulsed He ionizer cell; 6 - optically-pumped Rb cell; 7 - Sona shield; 8 - sodium-jet ionizer cell.

polarized Rb cell are situated in a 25-30 kG solenoid field. Inside the He cell the H^0 atoms undergo ionization with $\sim 80\%$ efficiency to form a low emittance intense proton beam. Next, this proton beam enters the polarized Rb vapor cell to become a beam of electron-spin polarized H^0 atoms by picking up electrons from optically pumped polarized Rb atoms. The neutralization efficiency of the Rb is in the order of 50 - 70%, therefore, only about half of the beam intensity survives this stage. The electron-spin polarized H atom beam then enters a magnetic field reversal region in order to transfer their electron polarization to protons in the nucleus, via sona transition technique[1]. The polarized H atoms then enter a sodium-jet (Na-jet) vapor cell, which has a fairly constant ionizing efficiency, to become negatively ionized by taking electrons from the sodium

[1] A method of transferring polarization from electrons to the nucleus using a magnetic field gradient.

vapor forming nuclear polarized H^- ions[75]. Finally, these polarized H^- ions at 35 keV energy exit the OPPIS to be further accelerated by a 200 MHz radio frequency quadrupole (RFQ) and a 200 MeV linear accelerator (LINAC). The OPPIS technique is a multi-step polarization-transfer process. At each step some of the beam polarization is lost, resulting in about 80-85% polarization for the exiting H^- ions pulses.

3.1.2 RFQ preinjector, LINAC, BOOSTER and AGS

After exiting the source the H^- ion beam (OPPIS beam) travels along a 1.9 m long low energy beam transport line (35 KeV transport line) to enter a 1.6 m long RFQ, which is operating at the LINAC frequency of 201.25 MHz[76, 77]. While traversing the transport line the initial longitudinal polarization of the OPPIS beam is converted to the vertical direction by a 23.7^0 bending magnet and a spin rotator solenoid. The beam is energized to 753 KeV at the RFQ and then travels along the mid energy beam transport line (753 KeV transport line), that is 6 m long, to enter the LINAC. Several Radio Frequency (RF) cavities[1] along the way maintain the transverse matching and longitudinal bunch structure of the beam.

The LINAC at RHIC was built in 1971 as a major upgrade to the Alternating Gradient Synchrotron (AGS) complex[78]. The purpose of LINAC is to provide accelerated protons to the AGS and to the Brookhaven Linac Isotope Producer (BLIP). The basic components of the LINAC include ion sources, a RFQ, and nine accelerator RF cavities spanning the length of a 459 foot tunnel. At its maximum energy limit, 200 MeV, beam currents of ∼37 mA can be accelerated in 500 μs pulses. The normalized beam emittance is extremely small ($\sim 2\pi$mm mrad) for 95% of the beam and the beam energy spread is about ±1.2 MeV[79]. The

[1] A type of chamber that contains an electromagnetic field and is used to accelerate charged particles.

accelerated H^- ions of a 400 μs pulse exit the LINAC by being strip-injected[1] into the AGS Booster as a single bunch of 4×10^{11} polarized protons, which is about half of the total efficiency from the source.

The purpose of the AGS Booster at RHIC is to pre-accelerate particles entering the AGS ring, increasing the energy of the proton beams. The circumference of the AGS Booster is one quarter of the circumference of the AGS, which allows four Booster beam pulses to be stacked in the AGS at its injection energy. Each proton bunch is accelerated to 2.4 GeV in the Booster and transferred to AGS for further acceleration.

The AGS accelerates protons in a single bunch, which are inherited from the Booster, up to 24.3 GeV. During this process the speed of the protons are increased up to 99.7% of the speed of light, compared to in the Booster where they were traveling at only 37% of the speed of light.[80] The AGS consists of 240 magnets which are successively alternated inward and outward[2], permitting particles to be focused in the horizontal and vertical plane at the same time. Once the beam acquires the maximum energy of 24.3 GeV it is extracted from the AGS and transferred via the AGS-to-RHIC (ATR) transfer line to be injected into the RHIC for further acceleration and storage[81].

The ATR transfer line has been designed to transport proton beams in a limited energy range in order to preserve the polarization of the beam[82][3]. It is divided into four sections and each section is designed to limit the horizontal and vertical dispersion of the beam as it travels along the way to RHIC[83]. The first section, the Fast Extracted Beam (FEB) line, extracts the beam from the AGS. A switching magnet is placed in this line in order to control the independent operation of AGS when RHIC is not operating. During the second section the beam

[1] The process of stripping electrons out of ions using so-called stripping foils.

[2] indicates how the name of AGS was derived.

[3] Studies has shown that the if ATR transfers beam in an energy window from 23.1 GeV to 24.2 GeV, it can maintain a stable spin direction that would closely matches the stable spin direction of RHIC, thus beam energy equal to 24.2 GeV is referred to as"magic energy".

is deflected both vertically and horizontally such that its axis lays in a plane of reflection symmetry. At the end of the section a second switching magnet, ring selector splits the beams into two branches, one leading to the RHIC ring in which the particles rotate clockwise and the other to the counter-clockwise ring.

3.1.3 RHIC rings

The RHIC accelerator-storage rings are composed of two identical, quasi-circular intersecting rings of superconducting magnets with a circumference of 3.8 km. They have the unique capability of colliding protons with both transverse and longitudinal polarization [73]. The two rings, known as the “Blue ring” and the “Yellow ring”, are separated horizontally by 90 cm and cause beams (”Blue beam” and ”Yellow beam”) to orbit clockwise and counter-clockwise respectively. The beams are collided head-on in the centers of six interaction regions (IRs) at six locations of the collider. Each IR is spaced equidistant around the circumference, separated by six arc sections as shown in Fig. 3.1. Superconducting magnets with very high magnetic fields are used exclusively for both storage rings at RHIC in order to attain high energies[1]. RHIC has altogether 1740 superconducting magnets. At present it can accelerate, store, and collide particle species from mass number A =1(protons) to A$\sim$200 (gold). RHIC has 360 RF buckets for each ring. In order keep space between bunches only one of every three buckets is filled, therefore, a ring can store 120 bunches in total. However, experimentally only 111 of them are filled while 9 of them are left for the so-called abort gaps[2]. Once the beam is injected filled bunches at a given time in a ring are called a “fill”. A typical fill of proton-proton collision usually lasts for about 10 hours at the full energy before dumping, when the instantaneous luminosity reaches a minimum required level.

[1] The top energy RHIC can operate for heavy ion beams (e.g., for gold ions) is 100 GeV/u and for proton beam is 250 GeV.

[2] Abort gaps are used in order to dump the beams safely.

Maintaining the polarization of beams with increasing energy in hadron colliders is extremely challenging due to the increased density and strength of the spin resonances. To preserve beam polarization the use of Siberian snakes have been implemented at RHIC. The RHIC rings have four such snakes to maintain stable polarization. The rings also contain four spin rotators installed on both sides of the collision points at the STAR and the PHENIX, in order to precess the spin from transverse (the stable spin direction in the ring) to longitudinal at the interaction region. After exiting the IR the beam spins are precessed back to the transverse direction. In addition, RHIC also have polarimeters to measure the polarization of the beams. More details about Siberian snakes, spin rotators, and polarization measurements can be find in the following sections.

3.1.4 Maintaining Polarization, Siberian Snakes and Spin Rotators

Controlling both the orbital motion and the spin motion are essential aspects of accelerating polarized beams [84]. Although the effect of the spin on the orbit is negligible, the effect of the orbit on the spin is usually very strong which results in complications in preserving the beam polarization as it accelerates to higher energies. Therefore, understanding the evolution of spin during acceleration is crucial in order maintain it. The evolution of the spin direction of a beam of polarized protons in external magnetic fields, such as those in a circular accelerator, is governed by the Thomas-BMT equation [73, 85],

$$\frac{d\vec{S}}{dT} = -\frac{e}{\gamma m}[G\gamma\vec{B}_{\perp} + (1+G)\vec{B}_{\parallel}] \times \vec{S} \tag{3.1}$$

where the spin vector $\vec{S}$ is expressed in the rest frame of the particle, G is the anomalous magnetic moment (G=1.7928 for the proton and $\gamma = E/m$), and $\vec{B}_{\perp}$ and $\vec{B}_{\parallel}$ are the magnetic field components transverse and parallel to the beam direction. This simple precession equation is very similar to the Lorentz force equation which governs the evolution of the orbital motion of a charged particle with velocity v, in an external magnetic field perpendicular to the particle as,

$$\frac{d\vec{v}}{dt} = -\frac{e}{\gamma m}[\vec{B}_{\perp}] \times \vec{v}. \tag{3.2}$$

By comparing equations 3.1 and 3.2, one finds that in the ideal case of a circular synchrotron where the horizontal magnetic field disappears and only a vertical guiding magnetic field perpendicular to the particle's motion exists, the two equation only differ by a factor $G\gamma$. This implies that in the ideal case the spin vector rotates $G\gamma$ faster than the orbital motion. The quantity known as the spin tune, ν_{sp}, is used to characterize the depolarizing effect in a collider. The ν_{sp} is defined as the number of full spin precessions a particle makes in a synchrotron in each orbital revolution[1]. In an ideal case, with no depolarization effects, $\nu_{sp} \equiv G\gamma$.

In a real synchrotron accelerating beams encounter horizontal magnetic fields which induce numerous depolarizing resonances causing loss of polarization of the particles [73]. These horizontal fields produce small perturbations of the spin vector from the vertical direction. These perturbations tend to average out as long as the perturbation frequency does not match the spin precession frequency. However, if the two frequencies are equal the perturbing effects add coherently and a depolarizing resonance occurs. There are two main types of depolarizing resonances that correspond to such spin-perturbed fields: imperfection resonances and intrinsic resonances. The imperfection resonances occur due to magnet error or mis-alignments. The intrinsic resonances can occur whenever the spin tune matches the vertical betatron tune[2][73]. This happens when there are deflection in the vertical betatron oscillation[3] which is caused by the quadrupole focusing fields. The strength of both types of these resonances increases with the beam energy.

[1] For example, at the highest RHIC energy (250 GeV), this number reaches 478.

[2] Total number of betatron oscillations over one full turn of the machine.

[3] The envelope around all the trajectories of the particles circulating in the FODO (quadrupole focusing and de-focusing) lattice is characterized by a periodic function known as the β function. The oscillation of particles are called betatron oscillation.

The resonance condition for depolarizing resonances caused by field imperfections occur at integer values of $G\gamma$, as in $\nu_{sp} = G\gamma = n$, where n is an integer. If n is large these resonances can be quite strong and could flip the direction of the polarization as the energy is ramped. The condition for intrinsic resonances is $\nu_{sp} = G\gamma = kP \pm \nu_y$, where k is an integer, ν_y is the vertical betatron tune, and P is the super periodicity[1]. Traditionally these resonances can be overcome by applying harmonic corrections to the vertical orbit for imperfection resonances and by using a betatron tune jump for the intrinsic resonances. However, at RHIC "siberian snakes" are used in order to reduce the effect of the these depolarizing resonances.

Siberian snakes generate a 180^0 rotation of the spin vector about a horizontal axis each time the beam passes through it without generating a net orbit distortion. There are two snakes on opposite sides of both RHIC rings, which produce rotations around two perpendicular horizontal axes (say x, z). The 180^0 rotations of the spin vector about two perpendicular horizontal axises from the two snakes is equivalent to a 180^0 rotation of its precession around the vertical axis (y). Figure 3.3 illustrates the precession of the spin vector for a transversely polarized beam as it traverses through a full siberian snake along the beam direction. As the snake combination rotate the spin precession by 180^0 in opposite directions between two passes, the depolarizing resonances effectively cancel out as long as the spin rotation from siberian snakes is much larger than the spin rotation due to the resonance driving fields. Therefore, a stable vertical polarizing vector can be maintained.

Each of the siberian snake consists of a set of four superconducting helical dipole magnets which are capable of producing a central field of up to 4 T which spirals through 360^0 over a length of approximately 2.4 m. These magnets, powered in pairs, can generate the required 180^0 spin rotation from vertically up to vertically down without affecting the particle trajectory.

[1] Number of identical sections of a accelerator. For example, 12 for AGS and 3 for RHIC.

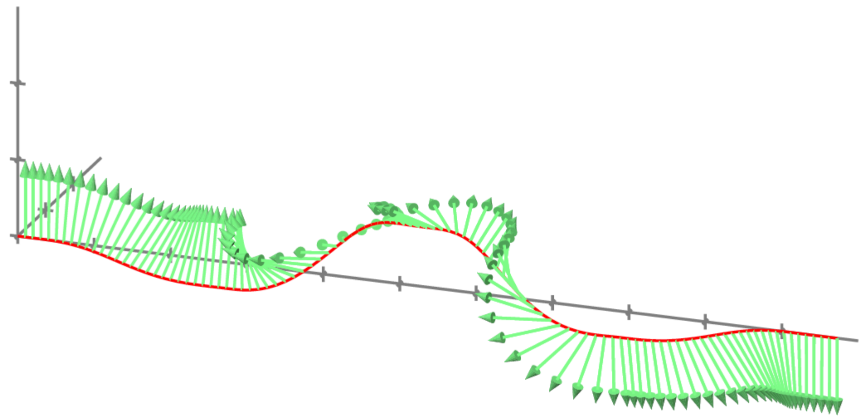

Figure 3.3.: Trajectory and spin through a RHIC Siberian Snake.

There are four spin rotators around the STAR and PHENIX interaction regions at RHIC [73, 85]. There are two rotators for each beam which consist of 4 helical dipoles in succession, each with dipole fields that begin vertically and end horizontally as shown in Figure 3.4. The handedness of the rotators are alternated as “right-left-right-left” when moving clockwise around both rings. For each beam one magnet rotates the spin vector 90^0 from transverse to longitudinal polarization before it enters the interaction region, and the second magnet rotates the spin vector back to transverse polarization after leaving the interaction region. The D0 and DX magnets precess the spin vector in the horizontal plane aiding spin rotators to switch transverse polarization to pure longitudinal polarization and back to the transverse polarization when exiting the IR region. The efficiency of the rotators assure the purity of the longitudinal polarization at the IR. Since the performance of rotators could affected due to various technical issues subsequently affecting purity of the longitudinal polarization, local polarimeters are used at each IR to track the longitudinal polarization, in addition to RHIC polarimeters. Since both the STAR and PHENIX interaction regions have spin rotators the two experiments can independently choose to have either longitudinally or transversely polarized collisions.

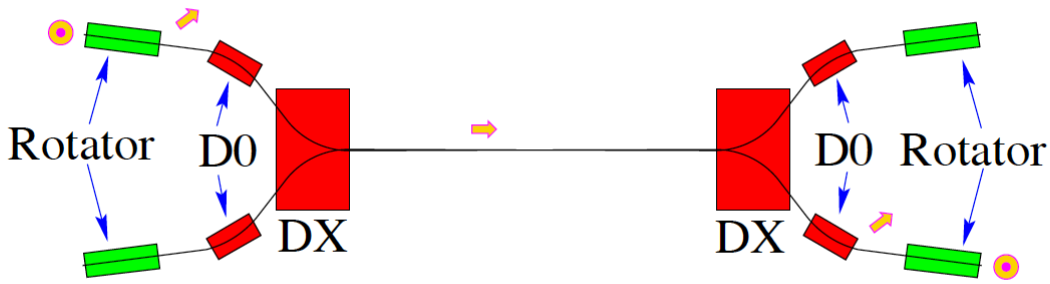

Figure 3.4.: RHIC spin rotators in a interaction point. Between the rotators and experiment are four dipoles (D0 and DX) to steer the beams into head-on collisions.

3.1.5 RHIC Polarimtery

The measurement of the beam polarization is a critical component of the successful commissioning of acceleration and storage of polarized beams at RHIC. Precise and absolute beam polarization measurements are crucial for the RHIC spin physics program because all spin-dependent results are normalized by the beam polarization P_B. Therefore, normalization uncertainty contributes directly to systematic uncertainties of final physics results. The RHIC polarimetry is based on the asymmetry in small angle elastic scattering of hadrons in the Coulomb-Nuclear Interference(CNI) region. In the CNI region the predicted asymmetry is significant and largely independent of energy for energies above a few GeV[1]. There are two proton-carbon (p-C) polarimeters[86], one for each ring, which are used for relative polarization measurements and one hydrogen gas jet (H-jet) polarimeter, at one collision point, which is used for absolute polarization measurements [87]. Both polarization measurements together are capable of providing a single polarization value for each beam for a given RHIC fill[73].

The relative polarization measurement uses a spin-sensitive process with

[1] This is due to the small hadronic spin flip expected at large energies.

higher rates. In principle, vertical beam polarization can be measured by determining the asymmetry in the yields for left and right scattering of the particle production, using a reaction with a known analyzing power A_N. Therefore, one can write the beam polarization in terms of the analyzing power for proton-carbon scattering, A^pC_N as shown in Equation 3.3,

$$P_B = \frac{1}{A_N^{pC}} \frac{N_L - N_R}{N_L + N_R} = \frac{\epsilon_N}{A_N^{pC}} \tag{3.3}$$

where $N_{L(R)}$ is the number of recoil carbons to the left (right) of the beam polarization direction and ϵ_N is the raw left-right asymmetry. Since absolute A_N^{pC} is not known very well at RHIC energies, p-C polarimeters are not used to provide an absolute polarization measurement. However, the elastic scattering in the small angle CNI region is predicted to have a calculable analyzing power of about 3-5% as well as a large cross section over the whole RHIC energy range. This large cross section allows for several high statistic measurements of the asymmetry in a short time period ($<$ 1 minute) during each RHIC fill.

The carbon targets are moved across the beams to measure a left-right asymmetry (with respect to the polarization vector) of the elastically scattered protons in the beam from the carbon nuclei. In the CNI region scatterings protons are scattered at very forward angles causing carbon nuclei to recoil approximately perpendicular to the beam line. As shown in Figure 3.5, six individual Silicon Strip Detectors (SSD) are located inside the beam pipe to detect the recoil carbons. The SSDs are mounted in a vacuum chamber at 45, 90, and 135 degrees azimuthally in both left and right sides with respect to the beam.

Despite not providing absolute polarization measurements, pC polarimeters are quite useful in obtaining critical relative polarization measurements among different fills. Since several measurements can be made within a given fill for each beam, p-C measurements are used to track stability of the polarization over the course of a given fill and between fills. Moreover, pC polarimeters also provide a measurement of the polarization profile, which is the polarization change across the beam's transverse dimension. This is done by scanning the carbon targets

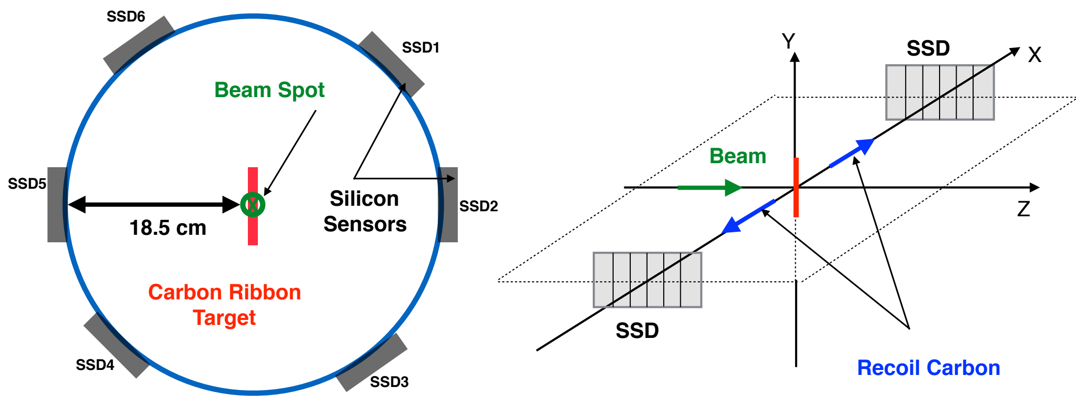

Figure 3.5.: A top view of the p-C polarimeter with six silicon detectors inside the beam pipe (left), a cross section view indicating the beam direction and the recoil carbon direction

across the beam to measure the polarization at different points in the beam's transverse profile.

The other polarimeter at the RHIC, the polarized atomic hydrogen jet target polarimeter (H-Jet), serves as an absolute calibration for the RHIC fast PC polarimeters [87]. Similar to the pC polarimeters, H-Jet polarimeters are based on elastic proton-proton scattering in the CNI region between polarized H target protons and the beam protons. Since the p-p elastic scattering process is a 2-body exclusive scattering of identical particles, the analyzing power, A_N^{pp}, is the same for both the target and beam protons, and thus expressed as,

$$A_N^{pp} = \frac{\epsilon_N^{beam}}{P_{beam}} = \frac{\epsilon_N^{target}}{P_{target}} \tag{3.4}$$

The absolute beam polarization, P_{beam}, can be expressed in terms of the target polarization, P_{target}, and the raw asymmetries (left-right) measured for both the target, ϵ_N^{target}, and the beam, ϵ_N^{beam} as shown in Equation 3.5. Due to the particle identity between the target and the beam in H-jet polarimetry, in contrast to the pC polarimetry, common factors of the systematic uncertainty of ϵ_N^{target} and

ϵ_N^{beam} are canceled. Therefore, by accumulating enough statistics $\Delta P_{beam}/P_{beam} \sim \Delta P_{beam}/P_{target}$ can be achived. The target spin states are varied in time so that the raw target asymmetry, ϵ_N^{target}, can be measured by averaging over the spin states of the beam. Similarly, the beam asymmetry, ϵ_N^{beam}, is measured by averaging over the spin states of the target.

$$P_{beam} = \frac{\epsilon_N^{beam}}{\epsilon_N^{target}} \times P_{target} \tag{3.5}$$

In order to measure the polarization of the H-Jet target, P_{target}, another polarimeter, the Breit-Rabi polarimeter, is used [87]

The H-jet polarimeter consists of three main parts: a Polarized Atomic

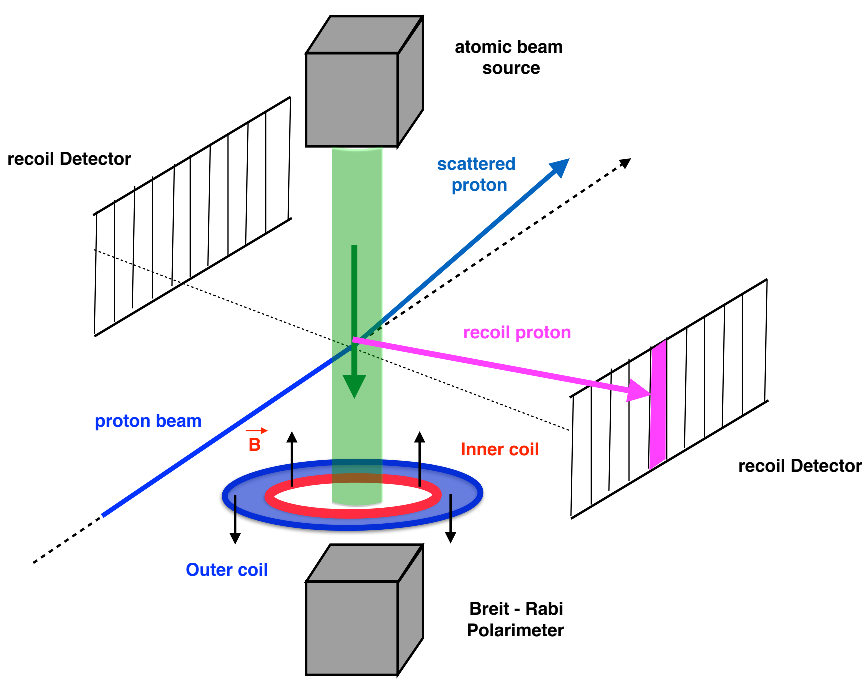

Figure 3.6.: A schematic diagram of H-Jet polarimeter.

Beam Source (ABS), a Scattering chamber which includes left-right pairs of silicon strip detectors, and a Breit-Rabi polarimeter (BRP) as shown in the schematic diagram in Figure 3.6. The ABS serves as the target for the polarimeter, which crosses the RHIC beam in the vertical direction and contains about 10^{12} atoms/cm^2. The polarimeter axis is vertical and the recoil protons are detected in the horizontal plane. The CNI elastic proton-proton collision asymmetry peaks at a momentum transfer of ~0.001 - 0.02 GeV / c^2, which corresponds to the recoil proton scattering angles of $85^0 - 89^0$ for the RHIC beam energies of 25-250 GeV. Therefore, silicon strip recoil detectors are situated 80 cm from the jet-target.

In contrast to the cross section of elastic proton-carbon scattering in the CNI region, the cross section of the proton-proton elastic scattering in the same region is rather small. Therefore H-Jet polarimeter measurements are integrated over much longer time intervals than the PC polarimeter measurements.

3.2 Solenoidal Tracker at RHIC (STAR)

The STAR [88] is a multipurpose detector located at the 6 o' clock interaction position at RHIC. As RHIC was initially designed for heavy ion collisions, STAR was originally constructed with the physics goal of investigating the behavior of strongly interacting matter at high energy densities and searching for signatures of the formation of quark-gluon plasma (QGP) through heavy ion collisions. However, once the polarized protons program started at RHIC, STAR was subsequently optimized and upgraded with various detector elements in order to fulfill physics goals related to polarized proton collisions such as the spin physics program at the RHIC. The STAR detector was designed primarily for measurements of hadron production over a large solid angle, therefore it has a large acceptance coverage. It is capable of providing high precision tracking and energy measurements of charged particles required for the determination of contributions of quark-antiquark polarization and gluon polarization to the spin of the nucleon which are the two major physics goals of the RHIC spin physics program. The former is the subject of this thesis work.

Quite different but complementary, the PHENIX [89] detector at RHIC was primarily designed for measurements of leptons and photons over a more limited range of solid angles. Despite having different detector capabilities and acceptance coverages, PHENIX also provides measurements required to study the spin structure of the nucleon. The PHENIX experiment was closed in 2016 temporality for upgrades, leaving STAR the only experiment currently being operated at RHIC. The measurement and analysis described in this thesis are performed using the STAR detector.

As the name suggests, the STAR detector has a solenoidal geometry. Figure 3.7 shows a schematic view and Fig. 3.8 shows a transverse and longitudinal plane view of the STAR detector. It consists of several subsystems which per-

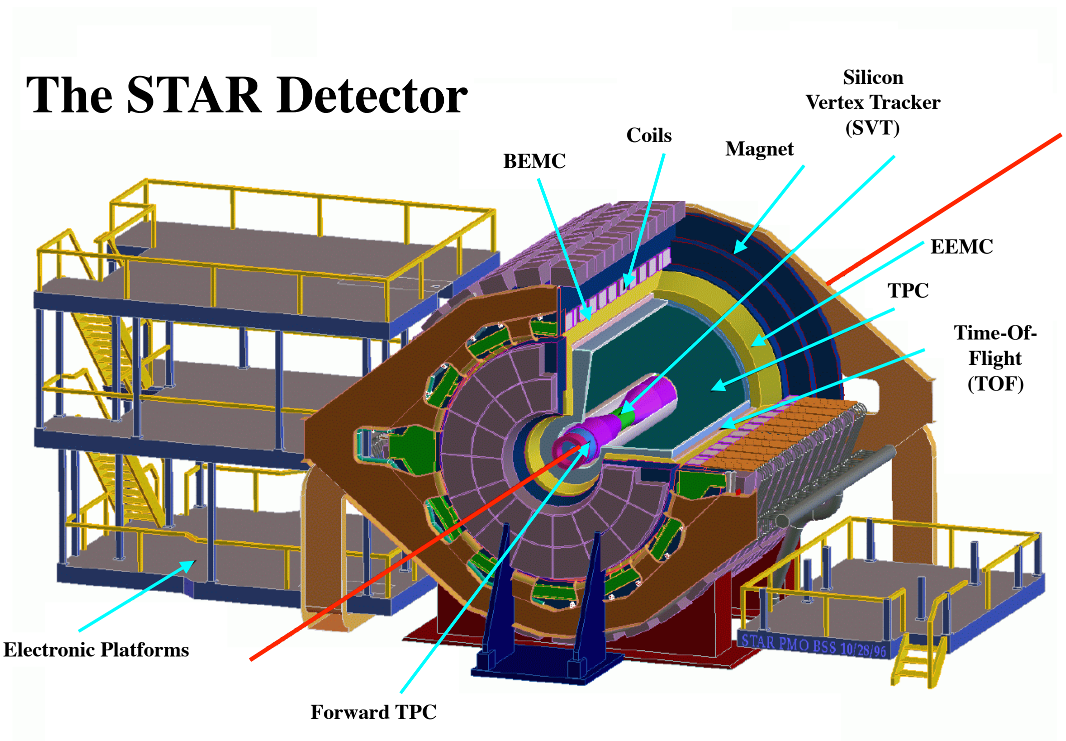

Figure 3.7.: The STAR detector overview.

form various measurements. Two main subsystems that are extensively used in this analysis, the Time Projection Chamber (TPC) and the Barrel and Endcap

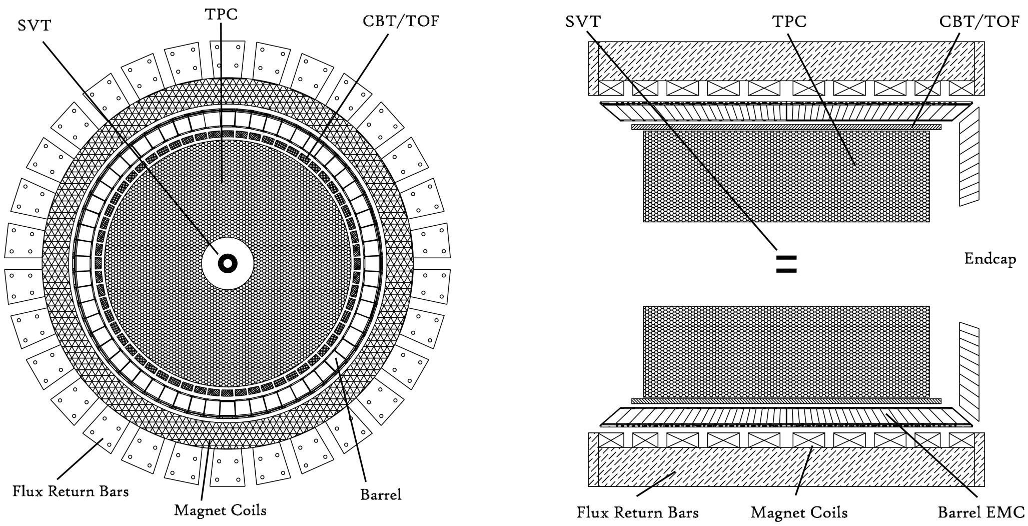

Figure 3.8.: The transverse and longitudinal plane view of the STAR detector.

Electromagnetic Calorimeters (BEMC and EEMC) are discussed in Sec. 3.2.1, 3.2.2, and 3.2.3 respectively.

3.2.1 Time Projection Chamber (TPC)

The TPC is the main subsystem that is used to reconstruct charged particle tracks at STAR [90]. It can record charged particle tracks, measure their momenta over a range of 100 MeV/c to 30 GeV/c, and identify the particles by measuring their ionization energy loss (dE/dX) over a limited momentum range (< 1 GeV). The TPC is a large cylindrical detector that consists of a 4.2 m long drift volume with an inner radius of 50 cm and an outer radius of 200 cm. This geometry makes it the largest TPC in the world and it covers the full azimuthal angle around the beam line and the pseudorapidity range $|\eta| \leq 1.8$. Figure 3.9 shows the schematic view of the STAR TPC. The TPC is situated inside a large solenoidal magnet [91] which can be operated at a uniform magnetic field with a maximum value 0.5 T produced by normal-conductor coils. The drift volume

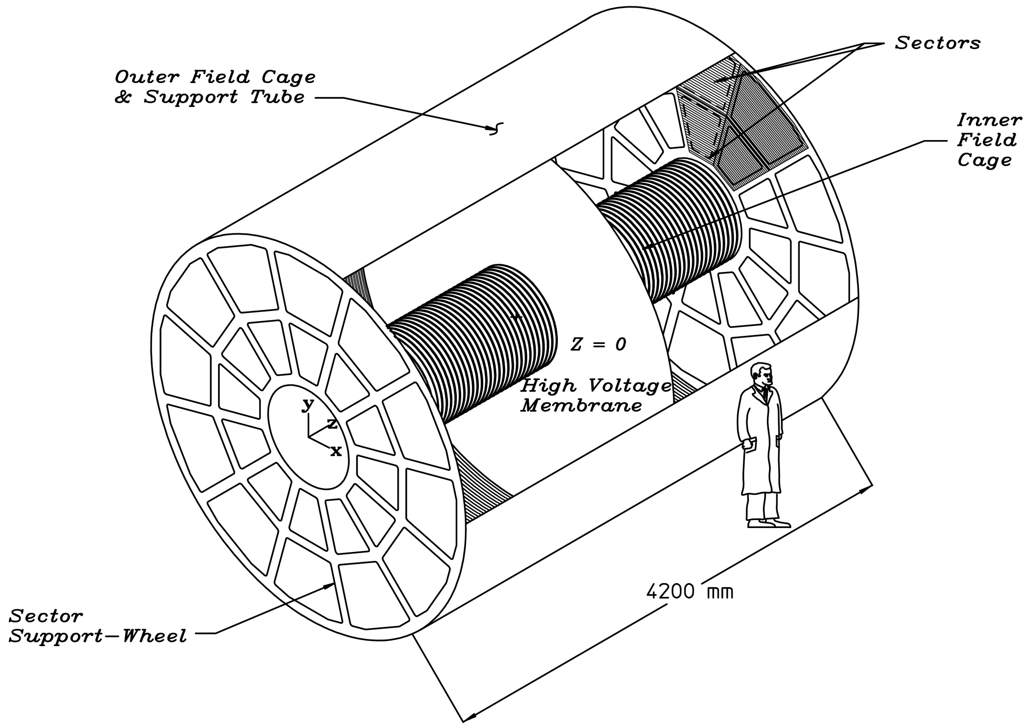

Figure 3.9.: Schematic view of the STAR TPC

of the TPC is filled with P10 gas [92] (10% methane, 90% argon) regulated at 2 mbar above atmospheric pressure which ensures that the drift velocity of secondary ions plateaus at a relatively low electric field, thus simplifying the field cage design. In addition, by circulating the gas continuously, the purity [1] inside the drift volume is maintained. The main components of the TPC are the thin conductive central membrane (cathode), readout end caps at both sides (anode), and the inner field cage which creates a uniform geometrical gradient between the cathode and the anode as required to define a uniform electric field. A uniform electric field of 135 V/cm is defined along the beam direction by holding the anode at ground potential and the cathode at the center of the TPC at +28 kV. The readout system [93] is based on Multi-Wire Proportional Cham-

[1] Purity is maintained by reducing electro-negative impurities such as oxygen and water, which capture drifting electrons.

bers (MWPC) with readout pads providing precise x,y positions of the charged particles tracks.

The TPC can reconstruct the full three-dimension trajectory of the charged particle tracks. This is achieved as follows. The projections of a track on the anode at the end sectors provide the $x - y$ coordinates of the track. The z coordinate is obtained by combining the drift time of ionization electrons with their drift velocity that is measured by a dedicated laser system [94]. In addition to precisely measuring the drift velocity of the charged particles, the laser system is also used to calibrate the TPC[1]. Having measured both the position in $x - y$ space at the end-caps and z position along the beam line the three dimensional trajectories of all charged particles can be reconstructed.

When charged particles travel through the uniform magnetic field they bend into helical trajectories, with a radius proportional to the particle's transverse momentum, p_T. By precisely measuring the transverse position of ionization electrons in the end-cap anode (and thus the radius of curvature of the track) the transverse momentum of charged particles can be measured. The total momentum can then be obtained by measuring the angle the track makes with respect to the z axis. For the majority of tracks, the momentum resolution of the TPC reach a value of $\delta p/p = 0.02$. However, such a resolution cannot be obtained for high-p_T charged particle tracks, such as the ones that are interested in this thesis work, the tracks that belong to $e^{\pm}$ decayed from W bosons. These electron and positron tracks have p_T which peak at $\sim$ 40 GeV/c. Therefore, they will bend with a larger radius of curvature in the magnetic field, making the momentum resolution less precise than that of the low momentum tracks. Thus, selection of W events in this analysis are primarily based on the calorimeter energy information, while the TPC momentum is used to identify QCD type background

[1] The aluminum stripes that are attached to the cathode eject photo electrons when laser photons hit the strips. Since the position of the stripes are precisely measured, these ejected electrons can be used for spatial calibration of the TPC.

events. Despite, the spatial resolution of high-p_T tracks in the TPC is accurate to $\sim 1-2$ mm (displacement in the y axis caused by the bending). Therefore, a clean separation of positive and negatively charged particle tracks that bend in opposite directions in the magnetic field is possible, resulting a clear separation of W^+ from W^- for this analysis.

Finally, the TPC can determind charged particles type known as particle identification (PID) [95] based on the ionization energy loss, dE/dX, by the particles as they traverse the TPC gas. Different particles undergo different ionization energy losses as a function of momentum. However, as the momentum increases, measurement of dE/dX becomes inefficient[1], thus PID is used only for particles with $p_T \leq 1$ GeV at STAR.

3.2.2 Barrel Electromagnetic Calorimeter (BEMC)

The BEMC is a part of the full calorimeter system at the STAR which provides calorimetry in the mid-rapidity region [96]. It is designed to measure the energy of electrons and photons over the pseudorapidity range $|\eta| < 1$, over the full 2ϕ in azimuth. As shown in Figure 3.7, the BEMC is located in the space between the TPC and the magnet coil, with inner radius of ~ 220 cm from the beam axis. The BEMC is a sampling calorimeter [97] which the calorimeter material is segmented into altering layers of lead and scintillator. The lead layers serve as the absorption medium while the scintillator provides the active medium for the calorimetry.

The BEMC is segmented into modules both in η and ϕ direction and the calorimeter stack of each module contains 21 layers of scintillator tiles alternately placed in-between 20 layers of 5 mm thick lead. Starting from the outer edge of the BEMC (outside of the TPC) the first 19 layers of scintillator are 5 mm thick and the last 2, which face the TPC, are 6 mm thick. The latter two

[1] When momentum increases particles need to travel further and further in order to lose their energy, therefore beyond the geometry of the TPC.

scintillator layers are used in the pre-shower[1] portion of the BEMC [96]. The total thickness of the BEMC is $\sim 20X_0$ [2] (radiation length) at $\eta = 0$, which satisfies the requirement to contain the full electromagnetic shower induced by a particle with transverse energy, $E_T = 60$ GeV. The requirements of the W program is well satisfied by this thickness setting of the BEMC as the transverse energy of decay $e^{\pm}$ from W boson is distributed about a peak around ~ 40 GeV with a sharp drop towards E_T larger than 60 GeV.

The BEMC consist of 120 modules. Each side of the STAR from $\eta = 0$ (y=0), 60 modules are mounted in ϕ. Each module is further segmented into 40 towers, 2 in ϕ and 20 in η with each tower being 0.05 in $\Delta\phi$ by 0.05 in $\Delta\eta$, thus segmenting the full calorimeter into 4800 towers. The configuration and segmentation of a single module is schematically illustrated in Fig. 3.10. The light produced in the 21 active layers of scintillator, due to the energy deposition by charged particles in each tower is collected in wavelength shifting fibers (WSF). For each tower, the 21 WSFs transport the light to a single photomultiplier tube (PMT) which measure the energy in the form of an ADC signal. At $X_0 \sim 5.6$ there exists a shower maximum detector (SMD). Roughly at the position of the maximum electromagnetic shower profile, the SMD provides fine spatial resolution based on shower position, shape, and amplitude. However, SMD was not used in the analysis discussed in this thesis.

In contrast to the momentum resolution of gas detectors (such as TPC), typically the energy resolution in calorimeters improves with energy as $1/\sqrt{E}$, where E is the energy of the incident particle. In particular for the BEMC [96] the tower energy resolution was found to be $\delta E/E = 14\%/\sqrt{E}$ GeV $\oplus$ 1.5 %. As the

[1] This part is used to measure longitudinal shower development at relatively smaller radiation lengths in comparison to the main detector, to facilitate discrimination of incident electrons or positrons from incident photons.

[2] Is a parameter which depends on the characteristics of the material and is defined as the, average distance x that an electron needs to travel in a material to reduce its energy to $1/e$ of its original energy.

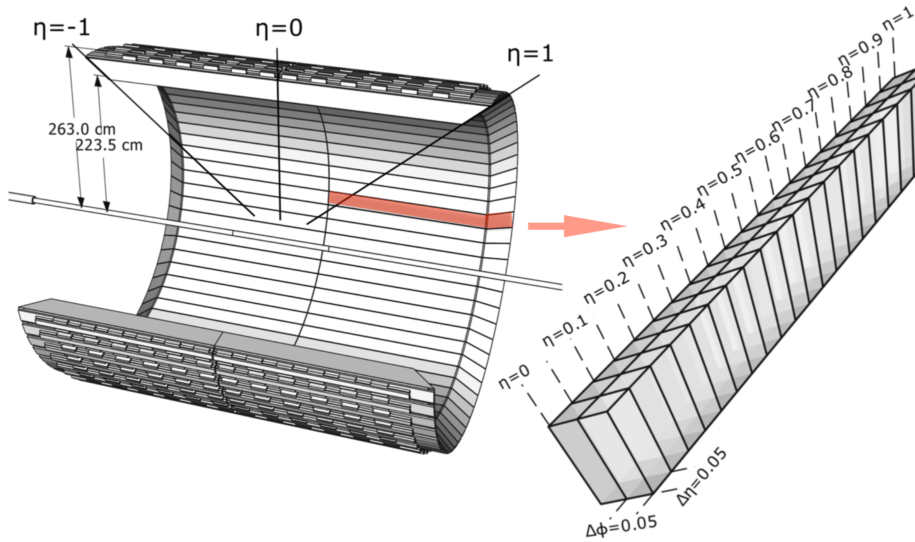

Figure 3.10.: Schematic view of the BEMC which consist of 120 modules in $\eta - \phi$ space and segmentation of 80 towers in a single module.

$e^{\pm}$ from the W decay are highly energetic, the BEMC provides the most precise energy measurements for this analysis and, thus, was used extensively to identify them.

3.2.3 Endcap Electromagnetic Calorimeter (EEMC)

The remaining part of the calorimeter system at the STAR is the EEMC [98], which performs calorimetry in the forward pseudorapidity region. The EEMC is located at the west side of the STAR, covering the pseudorapidity range 1.086 $\leq \eta \leq$ 2.00 over the full azimuthal angle. Similar to the BEMC, the EEMC is a type of sampling calorimeter composed of longitudinally alternating layers of lead and scintillator. It is transversely segmented into 720 towers with particle showers progressing in each tower longitudinally. Each of the towers in the EEMC covers slightly a larger area in $\eta - \phi$ space with $\Delta\phi = 0.1$ radians in azimuth and $\Delta\eta$ ranging from 0.057 to 0.099. Due to the larger transverse energy of charged particles that travel in the forward direction, the amount of X_0 needed to contain a full shower profile is increased. Therefore, the EEMC is designed with ~ 22 X_0 near $\eta = 2$ and increased up to ~ 28 X_0 at $\eta = 1$. In this analysis the EEMC was only used for QCD backgrounds reduction as discussed in Chapter 8.

CHAPTER 4
ANALYSIS PREREQUISITES

This chapter describe several aspects that are needed to understand the technicality of the analysis. The first section provide a brief overview of the relativistic kinematics of high energy particle collisions. Section 4.2 describe the STAR coordinate system. Section 4.3, and 4.4 provide a brief summary of the STAR TPC charged particle's vertex reconstruction and the charge sign separation mechanism respectively.

4.1 Relativistic High Energy Collision Kinematics Overview

In particle physics, high energy collisions of particles are treated relativistically. Therefore, particle kinematics are described based on the principle of the special theory of relativity. In relativistic kinematics, the energy E and the three momentum $\vec{p}$ of a particle of mass m is describe using a four vector (energy-momentum four vector) p^μ,

$$p^\mu = \left(\frac{E}{c}, p_x, p_y, p_z\right) \tag{4.1}$$

which transform like a time and space coordinate under the Lorentz transformations[1]. However, the square value of this quantity is invariant under the Lorentz transformation. Therefore, it is known as the invariant mass, m_{inv} of the particle which can be expressed in terms of natural units[2] as:

$$m_{inv}^2 = p^\mu \cdot p^\mu = E^2 - \vec{p} \cdot \vec{p}. \tag{4.2}$$

[1] Coordinate transformations between two frames of reference that are moving at constant velocity relative to each other.

[2] System of units in which the velocity of light, $c = 1$ and the plank constant $\hbar = 1$.

Natural units are being used to describe all the kinematics variables throughout this thesis. Let's consider a two particles (hadrons) collision system similar to the RHIC as shown in Figure 4.1. The masses and four-momentum of two incoming hadrons are m_1, m_2 and p_1^μ, p_2^μ respectively. Let's consider the interaction between two partons with four-momentums $\hat{p}_1^\mu$, $\hat{p}_2^\mu$, which takes fractions of momentum x_1, x_2 from the respective hadron. The four-momentum of outgoing scattered partons (or parton fragments) are denoted as $\hat{p}_3^\mu$ and $\hat{p}_4^\mu$. According to

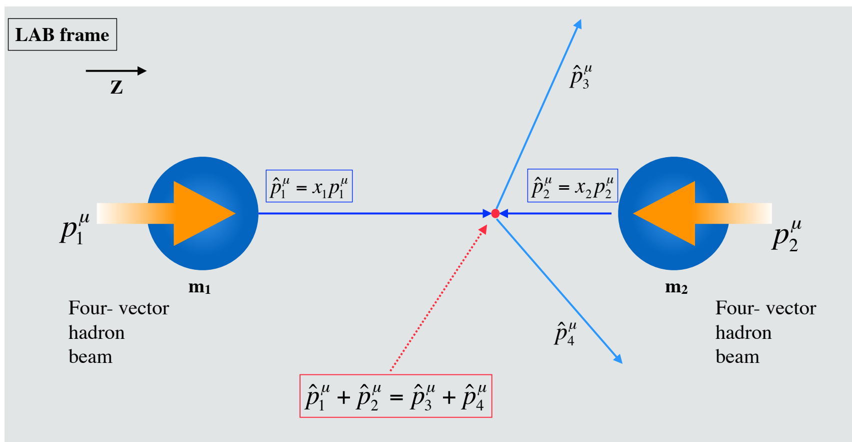

Figure 4.1.: Two particles collision systems viewed in the LAB frame.

Equation 4.2, the total invariant mass, M, of the system can be written in terms of four momentum vectors of the incoming or outgoing partons as,

$$M^2 = (\hat{p}_1^\mu + \hat{p}_2^\mu)^2 = (\hat{p}_3^\mu + \hat{p}_4^\mu)^2. \tag{4.3}$$

Now, in terms of partonic momentum fraction x_1, x_2,

$$M^2 = (x_1 p_1^\mu + x_2 p_2^\mu)^2 \simeq 2x_1 x_2 p_1 \cdot p_2. \tag{4.4}$$

Mandelstam variable[1], s, of this collision can be written as follows:

$$s = (p_1^\mu + p_2^\mu)^2 = 2p_1 \cdot p_2, \tag{4.5}$$

[1] Quantities which often use to describe the kinematics in relativistic scattering processes.

which leads to the relation between M^2 vs partonic momentum fractions as

$$M = \sqrt{x_1 x_2}\sqrt{s}. \tag{4.6}$$

In the center of momentum[1] (CM) frame, under Lorentz transformations along the axis of incoming hadrons, M is equal to the center of mass energy, E_{CM}. It can be also shown that the $\sqrt{s}$ in the CM frame is equal to the E_{CM}. Thus $\sqrt{s}$ used to represent the CM energies in relativistic collisions. According to Equation 4.6, it can be shown that $\sqrt{s}$ required to produce a W boson from the interaction of two partons in the $p + p$ collision should be roughly equal to 500 GeV as follows. As gluons are carrying roughly 50% of the proton momentum and by assuming that the remaining 50% is equally distributed among the three valance quarks one finds a quark with the momentum fraction $x_1 = x_2 = 1/6$. Now the mass of the W boson is known well and measured to be 80.385$\pm$ 0.015 GeV/c^2. Therefore, according to Equation 4.6, $\sqrt{s} \approx 80/\sqrt{(1/6) \times (1/6)} = 480$ GeV. In addition one can also showed that in the mid-rapidity (see below) region, where $x_1 \sim x_2 = x$, the RHIC kinematic coverage is ~ 0.16.

4.2 STAR Coordinate System

The coordinate system used in this analysis at the STAR interaction point is a spherical system as shown in Figure 4.2, where θ is the scattering angle and ϕ is the azimuthal angle. The z axis is parallel to the beam axis where the direction of the blue beam (south to north) is considered as the positive z direction. The y axis is pointed upward while the positive direction of the x axis is pointing to the west. In this coordinate system, the transverse momentum p_T is defined as,

$$p_T = |\vec{p}| \sin\theta = \sqrt{p_x^2 + p_y^2} \tag{4.7}$$

which is an invariant quantity under Lorentz transformations. Therefore, often (also in this analysis) the p_T of final state particles are used to extract the kine-

[1] An inertial frame in which the total momentum of the system vanishes.

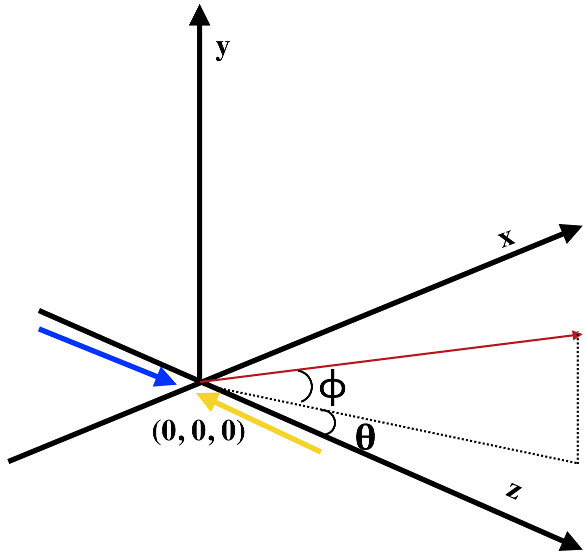

Figure 4.2.: Coordinate system at STAR interaction point

matic information of collisions. The longitudinal momentum, $p_L = |\vec{p}| \cos\theta = p_z$, along the z direction is not invariant. The quantity known as rapidity[1] of a relativistic particle can be written as,

$$y = \frac{1}{2} ln\Big(\frac{1+\beta}{1-\beta}\Big) = \frac{1}{2} ln\Big(\frac{E+p_L}{E-p_L}\Big) \tag{4.8}$$

where, β is the ratio of the velocity of a particle to that of light in the standard definition and p_L is the longitudinal momentum. The rapidity is an important quantity that used to formulate partonic momentum fractions (x_1, x_2) mentioned above by the following relationships.

$$x_1 = \Big(\frac{Mc^2}{\sqrt{s}}\Big) e^y, \tag{4.9}$$

[1] Represent the rotation in space time through a hyperbolic angle. If a particle scattered in a XY plane from a collisions of beams traveling along the Z axis, the rapidity relates the angle between the XY plane and the scattered direction. If a particle scattered close to transverse to the beam axis, the rapidity will be zero. But if when a particle is moving close to the beam axis in either direction the rapidity tend to $\pm\infty$.

$$x_2 = \left(\frac{Mc^2}{\sqrt{s}}\right)e^{-y}. \tag{4.10}$$

The mid-rapidity region mentioned in this text is referred to the region where $y = 0$. At $y = 0$, symmetric collisions occur for $x_1 = x_2 = x$. When $y < 0$, backward scattering occur for $x_1 < x_2$ and when $y > 0$, forward scattering occur for $x_1 > x_2$. However, y is not an invariant quantity. Therefore, y is not often used to represent experimental observable. The quantity we use in this analysis is called, pseudorapidity, η. The pseudorapidity is referred to as a special situation of rapidity for the case which the rest mass of the particle is negligible ($E \gg m_0$), and can be written as:

$$\eta = -\ln\tan\left(\frac{\theta}{2}\right). \tag{4.11}$$

The pseudorapidity only depend on the scattering angle (θ), which is an easily measurable quantity in an experiment. Due to the large energy involved with high energy particle collisions particles can be often treated as massless. Therefore, η is used to related the partonic kinematics with final state observable instead of y. Therefore, in order to provide a perspective of kinematic capabilities, coordinates of all the subsystems at STAR, the reconstructed track coordinates at TPC, and the calorimeter tower coordinates, etc., are described by η and ϕ instead of θ and ϕ. The leptonic asymmetry results in this thesis as well represented as a function of η.

4.3 Primary Vertices Reconstruction in TPC

The primary vertex of a collision at TPC is refers to the vertex location of a given event which corresponds to the collision(s) that fired the trigger(s) associated with that event. At STAR a given TPC event contains several collisions. However, a event could be mostly triggered by a single or two collisions. The findings of vertices belong to triggered collisions are done during the primary vertex reconstruction process by the STAR software group. A brief summary of this process is given here.

The “Pile-up Proof Vertex (PPV) Finder [99] at STAR is a dedicated vertex reconstruction package which is designed to determine the primary vertex location along the beam axis for low multiplicity events (such as $W \rightarrow e^{\pm}$ event) which are embedded in pile-up events that are roughly about two orders of magnitude larger. The pile-up refers to the events that are not associated with a triggered collision. The primary vertices of this analysis were reconstructed using the PPV finder.

The PPV finds the z position of a vertex as follows. First, charged particles tracks belong to each TPC event are selected with some requirements. For example, selected tracks are supposed to extrapolate within 3 cm of the beam line. The extrapolated point closest to the beam-line (distance of closest approach (DCA)) is supposed to have the vertex z position, such that $|z| <$200 cm. Tracks that pass these quality requirements are then given weights based on the probability of those being corresponds to the triggered collision. The weights are increased if a track can be extrapolate to a point in a calorimeter tower with a deposited energy or cross the TPC central membrane. As the calorimeters are fast detectors[1], energy deposition by a TPC track in the calorimeter implies that the track is likely to be associated with the triggered collision[2]. Next a likelihood of a given vertex to be a primary vertex is defined based on the weights discussed above. Then the vertices are classified by what is known as the “rank”, which is loosely correlated with this likelihood. Ranks are assigned to the vertex candidates based on their likelihood and number of matched tracks. Vertices with two or more matched tracks and vertices with a single matched track are given a positive rank which considered as primary vertices, and vertices with no matched tracks are given a negative rank which are considered, not.

[1] In contrast to slow detector like the TPC fast detectors have a response time which is less than the time between bunch crossings.

[2] Although the probability of these tracks belonging to a pile-up track arising from a previous or later bunch crossings is decreased, the energy requirement does not eliminate the possibility of them belonging to a pile-up tracks arising from the same bunch crossing.

4.4 Charge sign Reconstruction in TPC

As mentioned in Sec. 3.2.1 the charge of the particles that are scattered in the TPC are determined using the information of the bending of their track curvatures. As the TPC at STAR is situated in a 0.5 T magnet, all charged particles tracks curvatures are bended either left or right in the magnetic field depending on their charge sign. However, since the radius of track curvature is proportional to the the transverse momentum (p_T), the displacement (in the transverse plane) caused by the bending is proportional to the inverse of p_T. Figure 4.3 shows the resulted displacement of 15 cm by charged particles with a p_T of 5 GeV/c which are bended left and right in the magnetic field. The decay

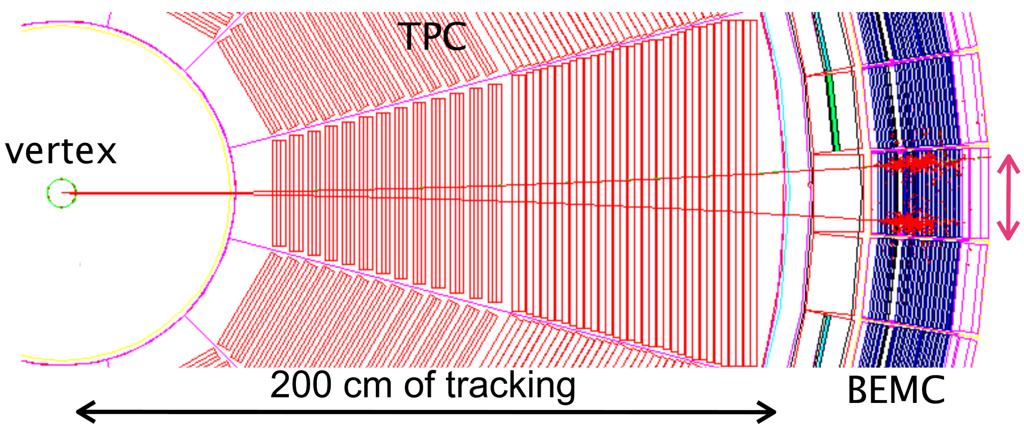

Figure 4.3.: A MC simulation of distance of the separation between an electron and a positron with p_T = 5 GeV/c bending in the 0.5 T magnetic field at STAR

electrons and positrons from W boson have much higher p_T of 25-50 GeV/c. Therefore, the displacement is much smaller (on the order of 1-2 cm), making it more challenging to distinguish the two charge signs. In addition, the large amount of pile-up in high-luminosity environment arising from non-triggered collisions makes it even harder to separate the charge sign of high p_T particles. Therefore, during the calibration of the TPC the distortion to the space charge that are occurring from pile-up are corrected in order to provide a clear separation between the two charge signs.

CHAPTER 5
CALIBRATION OF THE BEMC

This chapter reviews the calibration details of the BEMC, one of the subsystem that was primarily used for this analysis. This calibration was carried out as a part of this dissertation work.

5.1 Introduction

In general, calibration of calorimeters can be divided into several categories based on the purpose(s) and, thus the tool(s) employed [97]. Several purposes of calorimeter calibrations are listed below.

- To set the absolute energy scale for charged particles under experimental conditions.
- To monitor variation in the detector responses with time.
- To monitor relative response of calorimeter unit cells.[1]
- To equalize the cell-to-cell output signal in order to obtain a response as uniform as possible.

Not all of the purposes listed above, can be achieved using a single calibration. Therefore, usually several methods are combined together. There are three main types of calibration methods: hardware calibration[2], test beam calibration[3], and

[1] The smallest segmented volume of a calorimeter material (a tower).

[2] A calibration method used to equalize and monitor the cell-to-cell response of a calorimeter and of the associated electronics.

[3] A type of calibration that is performed on a calorimeter using test beams before being used in a actual experiment.

in-situ calibration. The latter is the type of the calibration that was performed on the BEMC and, thus is relevant for this discussion. An *in-situ* calibration is a calibration performed using physics samples that are collected during an experiment, allowing one to perform under the conditions that are unique to the experiment.

The purpose of the calibration that was performed in this analysis was to set the final absolute energy scale of the STAR BEMC for the data collected in 2013. Therefore, an *in-situ* calibration was performed in two steps. First, a relative, tower by tower calibration was performed using the minimum ionizing particles (MIPs) and is discussed in Sec. 5.2. The characteristic MIP peak position in the MIP ADC[1] spectrum was used to extract the relative calibration gain constants. Then, an absolute gain calibration was performed using the E/p method for electrons and positrons, $e^{\pm}$. Section 5.3 describes the details of this. Finally, tower-by-tower absolute energy scales were obtained by combining these two steps.

The final goal of this thesis work is to determine the single spin asymmetry for W boson production. The identification and reconstruction processes of the $W^{\pm}$ bosons are heavily dependent on the energy response in the calorimeter. In contrast to many other analyses which uses TPC Particle Identification (PID)[2] techniques to identify scattered charged particles in a collision, the scattered $e^{\pm}$ from decay of W bosons are identified by reconstructing the corresponding transverse energy in the calorimeter towers. The W decay $e^{\pm}$ belong to charged particle tracks with large transverse momentum in the TPC making such PID cuts no longer applicable. Therefore a proper energy scale calibration of calorimeter towers is essential for this analysis. The most recent energy calibration of the BEMC that was available when the analysis of this thesis begin (STAR 2013 data at $\sqrt{s} = 510$ GeV), has performed during 2009 using data collected at $\sqrt{s} = 200$

[1] Analog-to-digital converter: the calorimeter signal output is recoded as ADC signals.

[2] PID technique is based on energy loss per unit distance (dE/dx) due to ionization by charge particles.

GeV. The most recent prior W asymmetry analysis (STAR 2011 + 2012 data at $\sqrt{s}$ = 500 and 510 GeV [100]) at STAR as well was based on the 2009 BEMC calibration. However, during the analysis of the STAR 2013 data, it was found that some kinematic variables that were measured using the calorimeter (listed below) deviated from expected results or simulation results, indicating a necessity of a new BEMC calibration. Moreover, several other features had also motivated this, which altogether are listed below.

- A shift ($\sim$ 2 - 3 %) in the invariant mass peak of the reconstructed Z boson as shown in Figure 5.1 (a) was observed, in comparison to the simulated Monte Carlo (MC)[1] of $Z \to e^+ + e^-$. Unlike $W \to e^\pm + \nu$, $Z \to e^+ + e^-$ is a physics process which full kinematics of the final state particles can be reconstructed at the STAR. Therefore, the respective shift indicated a possible inadequacy of the absolute energy scale.

- A shift in the "Jacobian peak"[2] in the transverse energy distribution of reconstructed $e^\pm$ which decayed from W bosons as shown in Figure 5.1 (b) was observed, in comparison to simulated MC of $W^\pm \to e^\pm + \nu$. The respective shift had indicated possible inadequacy of the absolute energy scale.

- All prior BEMC calibrations that were performed at the STAR were for CM energy, $\sqrt{s}$ = 200 GeV $p+p$ collision data only. No calibrations were ever performed for $\sqrt{s}$ = 500 (510) GeV $p+p$ collision data since the commissioning of such runnings in 2009 (2012).

- The RHIC luminosity had increased tremendously (see sec 6.1) since 2009. The calorimeter responses can be changed due to the increased radiation

[1] MC simulation is a computerized mathematical technique widely used in high energy particle physics.

[2] A characteristic energy peak of W decay $e^\pm$; see sec 2.5.1 for more details.

caused by the high luminosity environment subsequently affecting the absolute energy scale.

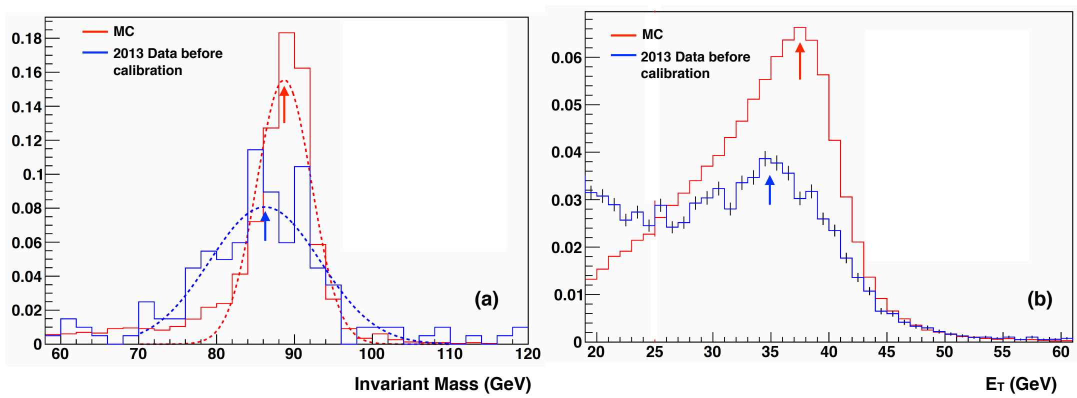

Figure 5.1.: The reconstructed invariant mass distribution of Z bosons before the BEMC calibration in comparison to $Z \rightarrow e^+ + e^-$ MC (a) and E_T distribution of reconstructed $e^\pm$ from W decay before the BEMC calibration in comparison to $W^\pm \rightarrow e^\pm + \nu$ MC (b)

For the same reason mentioned in Sec. 6.1 two set of calibrations were performed using STAR 2013 data from the period I and the period II separately. Subsequently two sets of gain constants were obtained. The rest of this chapter describes the method used in the calibration, followed by a comparison of the results to prior calibrations and a complete study of systematic uncertainties.

5.2 Relative Calibration Using MIPs

MIPs are high energy charged particles such as pions, muons, kaons and protons. Majority of these particles are hadrons along with a small admixture of muons and electrons. They are produced abundantly in every collisions at RHIC. However, MIPs do not initiate an electromagnetic shower cascade like electrons or photons, and therefore deposit very little energy ($\sim$ 20-30 MeV) in the calorimeter material while passing through it. The resulting pedestal-corrected ADC spectrum of the calorimeter tower consist of a characteristic peak called, the "MIP-peak". In highly relativistic environments, as in RHIC, the position of the MIP-peak is nearly independent of momentum and particle species. Therefore, by investigating the MIP peaks in each tower of the calorimeter a relative calibration of towers can be achieved.

5.2.1 Data Sample and Method

The same list of runs used in the asymmetry analysis, but events corresponds to different trigger settings were used for the calibration. For the relative calibration, events triggered by the STAR minimum bias[1] requirement [101] were used. An abundance of MIPs responses tower-by-tower were observed in the data set. The MIP energy deposition has a functional form as shown in Equation 5.1, which was determined via test beam data and simulation fits to spectra [102].

$$MIP = (264 \pm 4_{stat} \pm 13_{sys} MeV) \cdot \frac{1 + 0.056\eta^2}{\sin(\theta)} \tag{5.1}$$

Here, η is the pseudo-rapidity of the tower and θ is the scattering angle. From this relation one expects to see a peak approximately at 20 ADC channels above pedestal[2], as shown in Figure 5.2. Of the events considered, TPC tracks with momentum, $p > 1$ GeV, which entered and exited the same calorimeter tower were used. A single track per tower was considered in order to reduce the background energy deposition. Corresponding MIP ADC distributions of towers were obtained and each distribution was fitted with a gaussian$\times$landau function which best described the signal and the background regions of the spectrum as shown in Figure 5.2. The MIP ADC value above 6 was considered for the fitting. The fitted mean value was taken as the mean MIP ADC value for the given tower. Next, a quality analysis (QA) check was performed for every single tower in or-

[1] Events that are triggered with minimum detector requirements.

[2] Base response of towers coming from electronics and background noise: when taking actual measurement pedestal must be subtracted.

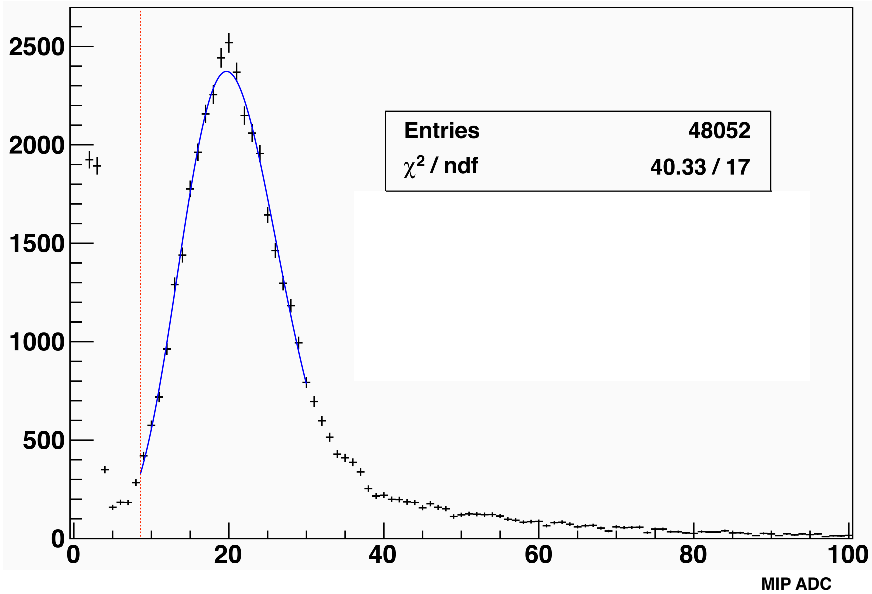

Figure 5.2.: A typical MIP ADC distribution (black points) and gaussian $\times$landau fit (in blue) for a single calorimeter tower.

der to ensure the quality of the MIP peak extraction. Relative gain constants were calculated for those towers which passed the QA according to the following formula,

$$C_{relative} = \frac{0.264(1 + 0.056 \cdot \eta^2)}{ADC_{mip} \cdot \sin(\theta)}. \tag{5.2}$$

5.2.2 Results of the relative calibration

In period I, 4.7% of the 4800 towers were identified as "bad"[1] towers from the QA while 6.1% of towers were identified as "bad" in period II. The increase in "bad" towers for period II was found to be caused by a missing module in the calorimeter. Figure 5.3 shows $\eta - \phi$ distributions of calculated relative gain constants of all towers which passed the QA during period I and II calibrations

[1] Towers with two or more peaks, peaks with significantly larger or smaller peak position than expected, and towers with no MIP peaks found labeled as "bad".

where each tower is represented by a single bin. Towers which failed the QA are represented by white color bins which are masked out in the database. A uniform distribution of relative gain constants can be seen. The time dependance of MIP peak values during data taking were also studied and found to vary (decreased) by approximately 2% during period I, and were fairly stable during period II.

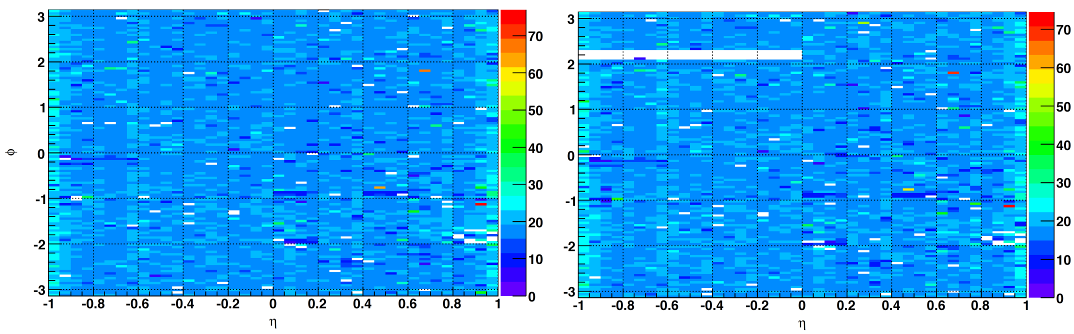

Figure 5.3.: Relative gain constants of the calorimeter towers of run 13 periods I (left) and II (right).

5.3 Absolute Calibration Using Electrons

In high energy collider experiments, scattered electrons can be treated as massless, when the momentum of those particles are on the order of GeV/c which is a reasonable assumption to make. Thus, the E / p of electrons and positrons is nearly equal to one. The E / p method is an well known method, used in absolute calibration of calorimeters in high energy collider experiments. As discussed in Sec. 3.2.1, the STAR tracking detector, TPC has a good resolution for low momentum (< 20 GeV) charge particle tracks. Since electrons deposit all of their energy in the calorimeter towers, by measuring E/p of isolated $e^{\pm}$, the calorimeter energy scale can be adjusted.

5.3.1 Data Sample and $e^{\pm}$ Selection Method

The same list of runs used in the relative calibration, is used for the absolute calibration, but only the events triggered by the STAR Barrel High Tower Trigger 3 (BHT3) [101] and the STAR Jet Patch Trigger 2 (JP2) [101][1] were considered. A strong momentum dependance of E/p of isolated electrons were seen in BHT3 triggered events around and above the energy threshold ($\sim$ 4 GeV) as shown in Figure 5.4 (a). Hence, a rather low momentum region was considered for BHT3 triggered events (1.5 - 3.0 GeV)[2] in order to avoid possible trigger bias effects. As for the electrons triggered by JP2, E/p was found to be fairly stable with momentum as shown in Figure 5.4 (b). Therefore, the momentum range of 1.5 - 10 GeV was considered for JP2 triggered events. In addition, events triggered by the BHT3 trigger exhibited a systematically lower $< E/p >$ in comparison to the events triggered by the JP2 trigger. This difference was added to the systematic uncertainty.

Once the decision on the trigger selection was made, a single TPC track was matched to a single calorimeter tower requiring the track to enter and exit the same tower. Next a 3×3 tower cluster was formed around the tower ("center tower") which the candidate track is being matched, requiring that no tracks are matched to neighboring towers in the cluster as shown in Figure 5.5. Furthermore, the energy in the highest neighbor was required to be less than 50% of the energy in the center tower. Next, PID cuts [95], such as dE/dx, "nSigma-Electron" ($n\sigma_e$)[3] and "nSigmaPion" ($n\sigma_\pi$)[4] were used to identify electron tracks in the TPC. Respective distributions of dE/dx, $n\sigma_e$, and $n\sigma_\pi$ can be seen in

[1] These two triggers are primarily used in W and Jet analysis respectively at STAR.

[2] BHT (Barrel High Tower) triggers are setup so that trigger would fire as long as a single tower energy corresponds to a single track passes the threshold energy. Therefore, there are exist tracks from the same event which deposit less energy in towers than the triggered tower. In this analysis towers belongs to these tracks as well were considered.

[3] Width (RMS) of normalized dE/dx of electrons.

[4] Width (RMS) of normalized dE/dx of pions.

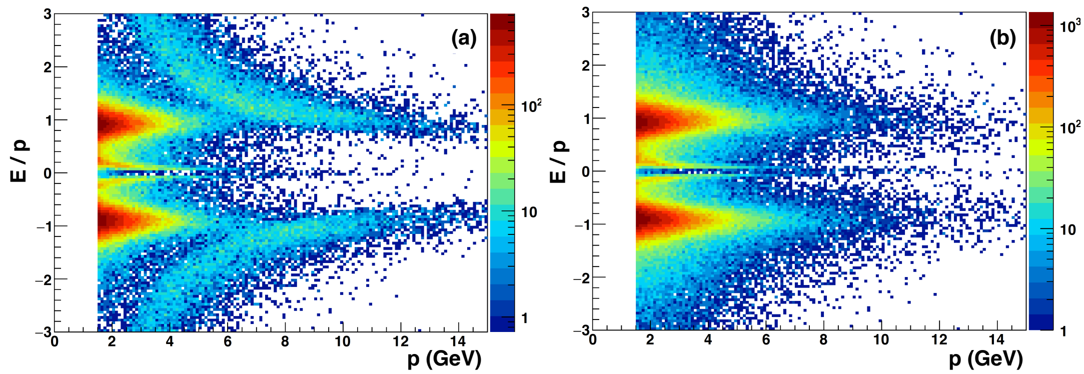

Figure 5.4.: E/p as a function of momentum of isolated electrons triggered by : BHT3 trigger (a) and JP2 trigger (b).

Figure 5.6 (a), (b), and (c) and the data selection regions are marked by the arrows. First, cuts were applied on the dE/dx distribution to select the region where $e^{\pm}$ belong to. Next, $n\sigma_e$ distribution was obtained for the selected region in the dE/dx distribution and cuts were again placed to select the corresponding region of $e^{\pm}$. Similarly, the cuts were placed for the other distributions as well. After placing various PID cuts a clear reduction of background events can be seen.

Following these requirements, the deposited energy in the center tower was measured, and it was taken as the Energy, E, of the candidate $e^{\pm}$ track. Then, measured E was corrected based on correction factors that were obtained from simulation in order to account for the energy loss in material between the TPC and the BEMC tile and for the η dependences. These corrections factors were calculated using the GEANT [103] simulation for a given pseudo rapidity bin by throwing electrons at several different energies, and calculating the amount of their energy deposited in the tower they struck as a function of $R = \sqrt{\Delta\phi^2 + \Delta\eta^2}$ (TDR) from the center of the "center tower" (also illustrated in Figure 5.5). However, the corrections were found to be ineffective at larger TDR values and therefore a relatively tight requirement was placed on TDR which can be seen

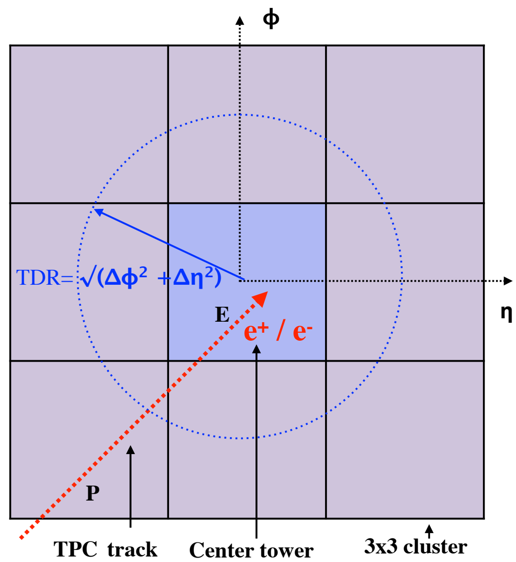

Figure 5.5.: Illustration of the TPC track matching to the calorimeter tower

in the TDR distribution of the data in the Figure 5.6 (d). In addition, possible transverse energy leakages in towers were also accounted for in the corrections. Finally, the momentum, p of the $e^{\pm}$ tracks were measured in the TPC.

Unlike MIPs however, abundant electrons are hard to find tower by tower at STAR. Therefore e^{+}, e^{-} that strike towers at a given pseudo-rapidity bin called as "η-ring" were added together (40 η-ring were constructed with 120 towers in each ring). Then the E/p spectrum for each η-ring was obtained by considering all the isolated electrons and positrons from all the towers. An average E/p value was obtained for each η-ring by fitting the E/p spectrum using a gaussian function for the signal region and an exponential function for the background region, as shown in Figure 5.7 (for η-ring of $\eta \sim 0.75$). The background contamination was properly modeled by the combination of the two curves. Next, the gaussian mean of the fitted function was extracted as the average E/p and was then used to calculate the absolute calibration constant defined as,

$$C_{absolute} = \frac{C_{relative}}{\langle E/p \rangle} \tag{5.3}$$

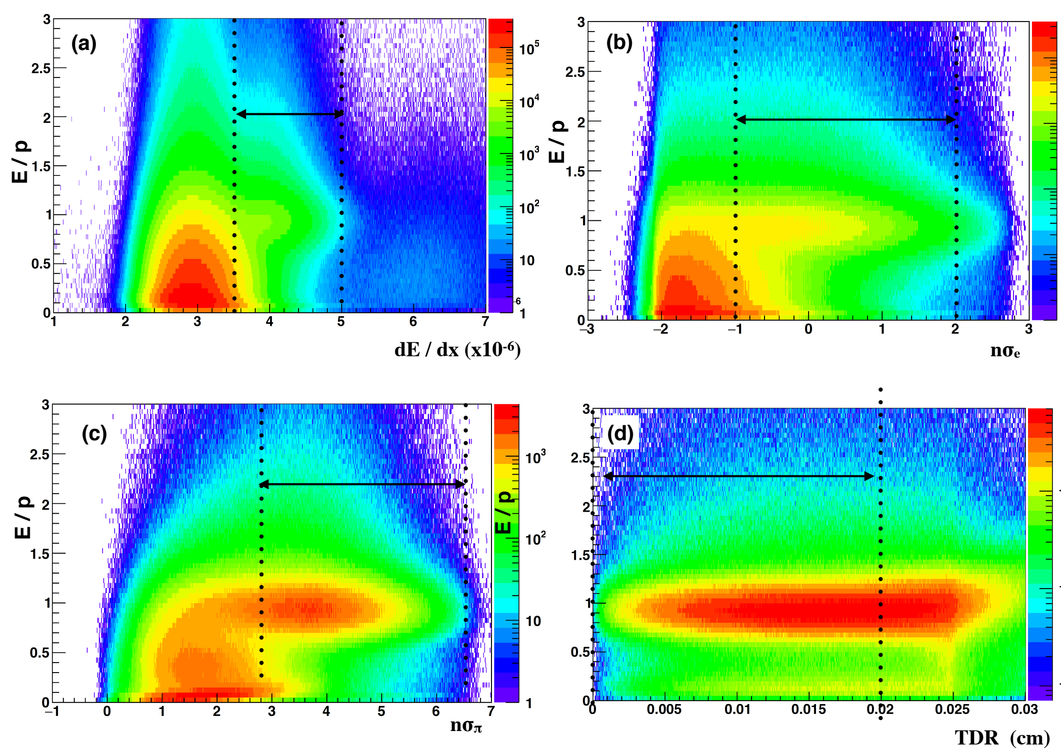

Figure 5.6.: PID cuts distributions : E/p vs dE/dx (a), E/p vs $n\sigma_e$ (b), E/p vs $n\sigma_\pi$ (c), E/p vs TDR (d).

where $C_{relative}$ is defined in Equation 5.2.

Figure 5.8 shows the distribution of the average E/p values of all 40 η-rings in the BEMC. Each ring covers a window of $\Delta\eta$ of 0.05. Rings 1 and 40 cover η ranges between [-1, -0.975] and [0.975, 1], while rings 20 and 21 cover the η ranges between [-0.025, 0] and [0, 0.025], respectively. These E/p values were then used to calculate absolute gain values for each tower according to the formula shown in Equation 5.3. The $\langle E/p \rangle$ was relatively constant at mid-rapidity corresponding to the inner η rings (rings 3 to 38) and found to be vary within 5%. However, at larger rapidities (rings 1, 2, 39, and 40) $\langle E/p \rangle$ was found to be decreased by $\sim$ 20% in comparison to inner η-rings. This large variation at large rapidities

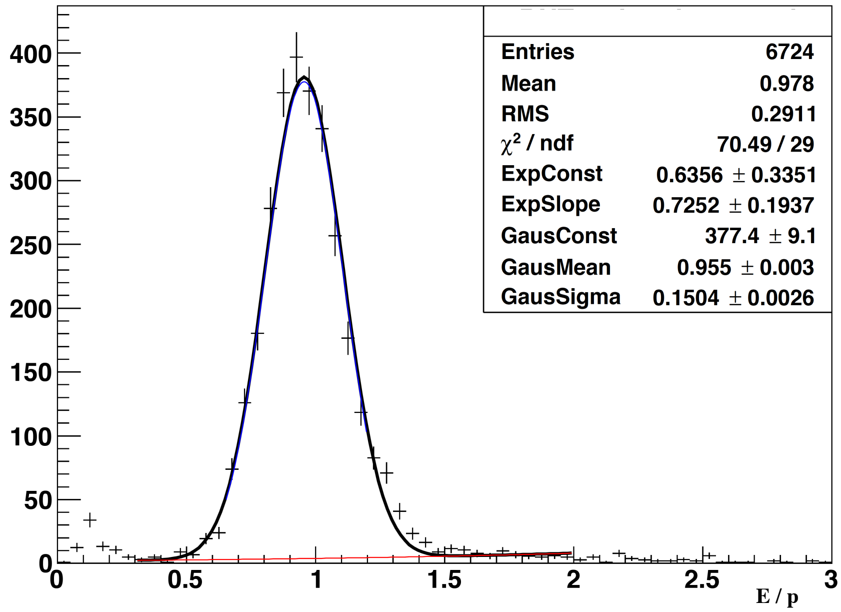

Figure 5.7.: Electron E/p spectrum of a given η-ring (black points), gaussian fit to the signal region (blue curve), exponential fit to the background region (red curve), and the sum of the two fits (black curve).

was attributed to the increase in dead materials[1] between the TPC and the front of the calorimeter tiles, which causes showers to begin earlier and allows more energy to escape the tower. However, during the W asymmetry analysis very few W candidates were found from these outer η-ring regions. Therefore, a systematic bias due to this effect was not assigned.

5.3.2 Results

A comparison of average gain constants between period I, period II, and prior year's BEMC calibrations at STAR was made. Average gain in each calibration was compared to the period I calibration. The period I average gain was found to be $\sim 3.5\%$ larger than that of 2009 $p+p$ 200 GeV calibration and approximately

[1] Various hardware materials such as detector component or supporting structures.

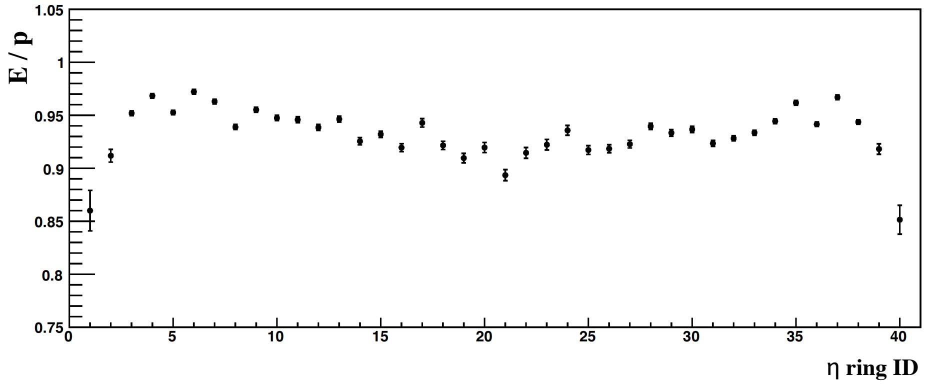

Figure 5.8.: Mean electron E/P values for all 40 η rings in the BEMC.

5% larger than that of 2012 $p+p$ 200 GeV calibration. Furthermore, the period II average gain was found to be 2.5% larger than that of period I. In general, changes in calorimeter gains in time and in different running conditions are expected. For example, in this calibration, the difference of 2.5% between period I and period II average gains was partially attributed to the increase in luminosity by $\sim$ 20% in period II. However, the changes were also caused by various systematic effects as discussed in Sec. 8.4. The 5% change in average gain constants between period I and 2012 calibrations was partially attributed by systematic effects caused by the use of different trigger options in the calibration method.

The invariant mass of Z boson and the Jacobian peak of W boson in mid-rapidity region were reconstructed again after the calibration. In contrast to Figure 5.1 consistency between data and MC was found in both situations as shown in Figure 5.9. This implied that the gain constants which were calculated at a relatively low energy scale (0 -15 GeV) are consistent at relatively high energy scale (20 - 40 GeV) with in the calculated systematic uncertainty as discussed below.

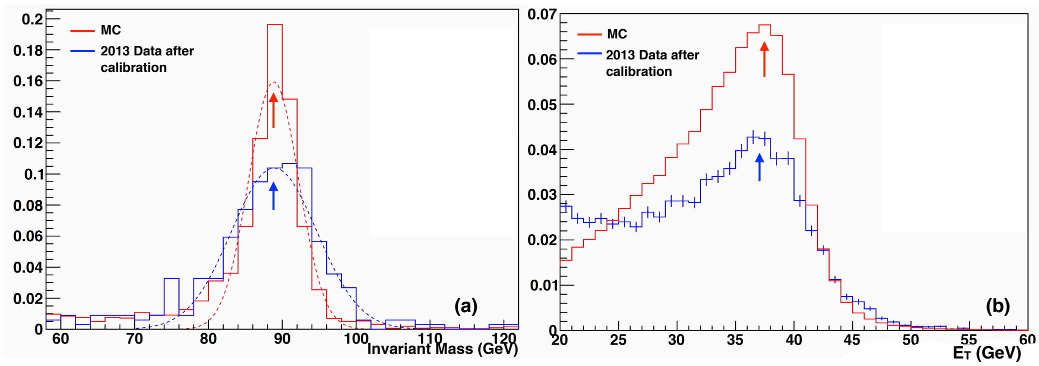

Figure 5.9.: The reconstructed invariant mass distribution of Z boson after the BEMC calibration in comparison to $Z \rightarrow e^{+} + e^{-}$ MC (a) and E_T distribution of reconstructed W boson after the BEMC calibration in comparison to $W^{\pm} \rightarrow e^{\pm}$ MC (b)

5.3.3 Systematic Uncertainty

To characterize the systematic uncertainty the effect of a wide range of parameters were examined. The impact on E/p by these parameters was investigated, calculated and subsequently assigned as the systematic uncertainty due to the calibration. The most significant contribution was introduced by the lower momentum cut that was placed during the selection of $e^{\pm}$. The momentum range that was available for the study was from 1.5 GeV to 10 GeV. A significant variation in the constructed $\langle E/p \rangle$ of $e^{\pm}$ was found for momenta below 3.0 GeV while a fairly stable behavior was seen for momenta above 3.0 GeV. In the low momentum range, a steadily increasing behavior of $\langle E/p \rangle$ was found. This behavior was caused by the increased in background in the low momentum region. The systematic uncertainty due to this momentum dependance was calculated by taking the absolute difference of $\langle E/p \rangle$ within the respective momentum range as shown in Figure 5.10 which resulted in an uncertainty of 2.2% for period I and 1.1% for period II.

The second most significant contribution to the uncertainty was found to

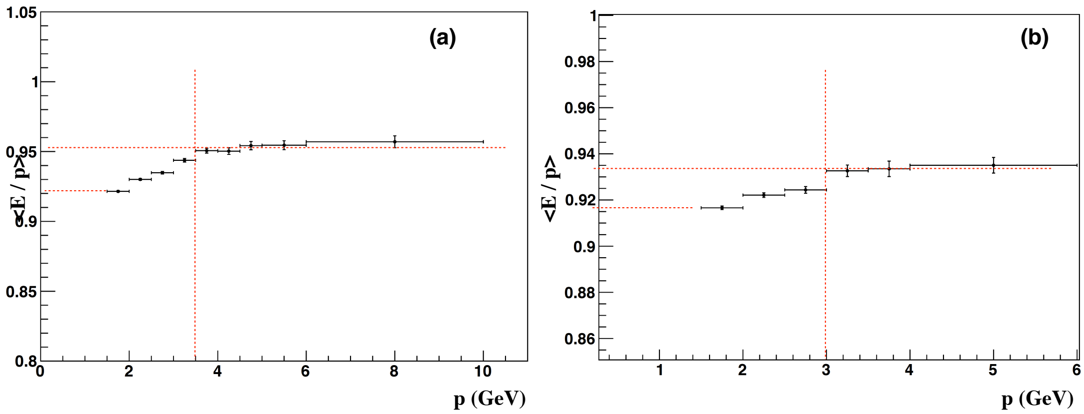

Figure 5.10.: The $< E/p >$ of sampled $e^{\pm}$ as a function of momentum for period I (a), and for period II (b).

be caused by differences between BHT3 and JP2 triggered $e^{\pm}$ events. In order to calculate the uncertainty due to this trigger bias, $\langle E/p \rangle$ was constructed using three $e^{\pm}$ samples which were triggered by either BHT3 only or JP2 only or by the combination of both BHT3 and (or) JP2. In the actual calibration, the latter trigger option was used. The calculated $\langle E/p \rangle$ of the respective trigger option preferred to R_1, R_2, and $R_{measured}$ are shown in Figure 5.11. The largest deviation to ($R_{measured}$) from either R_1 or R_2 was considered as the systematic uncertainty due to the trigger bias which resulted an uncertainty of 1.4 % in period I and 1.3 % in period II.

The dependance of the TDR cut on E/p was analyzed. The systematic uncertainty due to the TDR cut was calculated separately for inner η-rings, outer η-rings and for the entire detector. However, relatively small (< 0.5 %) statistical variation was found for both the inner and the outer rings. Therefore a systematic uncertainty due to TDR cut was not assigned.

The time dependance of E/p was estimated by calculating $\langle E/p \rangle$ of sampled

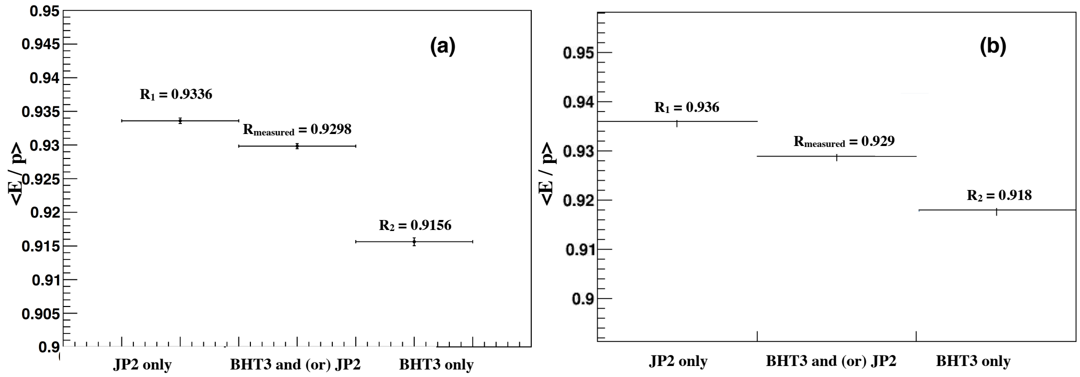

Figure 5.11.: The $\langle E/p \rangle$ of sampled $e^{\pm}$ triggered by BHT3 only (R_1), by JP2 only (R_2), and JP2 and (or) BHT3 ($R_{measured}$) for period I (a), and for period II (b).

$e^{\pm}$ by day[1] over the entire 2013 data collection period as shown in Figure 5.12. The spreads of $\langle E/p \rangle$ were assigned as the systematic uncertainty which resulted in an uncertainty of 0.8% for period I. However, no significant statistical bias was found for period II, and therefore, no uncertainty was assigned.

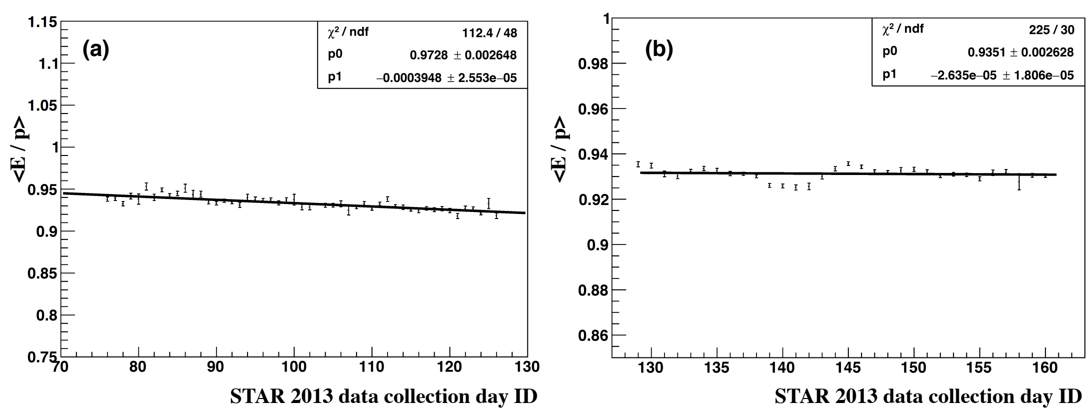

Figure 5.12.: The $\langle E/p \rangle$ of sampled $e^{\pm}$ as a function of time (per day) for period I (a), and for period II (b).

[1] Each physics day of the STAR data collection period is numbered.

The luminosity dependance of E/p was estimated by calculating the $\langle E/p \rangle$ of sampled $e^{\pm}$ by dividing the data set into several ZDC[1] ranges as shown in Figure 5.13. However, the impact on $\langle E/p \rangle$ due to the change in luminosity was found to be relatively small (< 0.5 %), and therefore no systematic uncertainties were assigned.

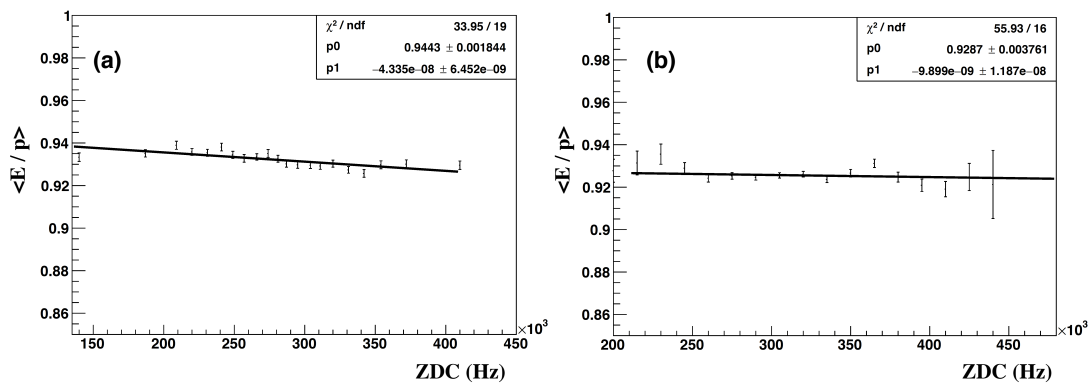

Figure 5.13.: The $\langle E/p \rangle$ of sampled $e^{\pm}$ as a function of ZDC rate for period I (a), and for period II (b).

The BEMC calorimeter consists of 30 modular crates[2]. Timing effects[3] of crates can potentially impact the calorimeter system such as the trigger system. This effect was investigated by calculating the $\langle E/p \rangle$ for sampled $e^{\pm}$ per crate. However, no significant deviation from statistical variation was found as shown in Figure 5.14 for both period I and period II. The RMS of $\langle E/p \rangle$ between the crates was assigned as the systematic uncertainty. Thus, crate to crate dependance introduced an uncertainty of 1.2% for both period I and II.

The total uncertainty of period I, by adding each contribution in quadrature was found to be 3.0%. Similarly, for period II, the total uncertainty of 2.0%

[1] ZDC rate represent the instantaneous luminosity during each collision.

[2] Type of electronics and support infrastructure commonly used for trigger electronics and data acquisition in particle detectors.

[3] Time phase shifts of crates which correlated with crate power cycles.

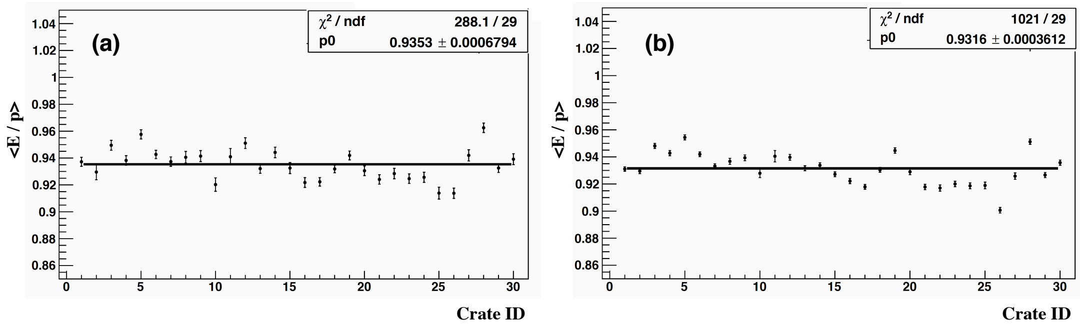

Figure 5.14.: The $\langle E/p \rangle$ per crate for period I (a), and for period II (b).

was obtained. A summary of uncertainties from each contribution is listed in Table 5.1.

	Systematic Error Period I [%]	**Systematic Error Period II** [%]
Trigger bias	1.4	1.2
Low momentum cut	2.2	1.1
TDR cut	0	0
Time Dependance	0.8	0
Luminosity (ZDC rate) dependance	0	0
Crate Dependance	1.2	1.2
Total (Added in quadrature)	3.0	2.0

Table 5.1.: Contributions to total systematic uncertainty.

5.3.4 Conclusion

The BEMC has been successfully calibrated in-situ using MIPs and electrons and positrons separately for the data collected during period I and period II of RHIC 2013 $p + p$ running at $\sqrt{s} = 510$ GeV. The calibration uncertainty, quoted as a systematic bias, was found to be in the order of 3% for both periods, which is similar to the systematic bias found during RHIC 2012 $p + p$ running at $\sqrt{s} = 200$ GeV calibration. This uncertainty represents that maximum bias of the BEMC calibration. Therefore, the systematic uncertainty on single-spin asymmetries measured in this thesis, due to the calibration bias was calculated by shifting tower energies by 3.0% before the tower cluster reconstruction.

CHAPTER 6
DATA AND SIMULATION SAMPLES

In this chapter, the process of selecting data and simulation samples is discussed.

6.1 Data sample

The data analyzed in this thesis were collected by the STAR experiment at RHIC in 2013, during longitudinally polarized $p+p$ collisions at a center of mass energy of $\sqrt{s} = 510$ GeV. In 2009, the RHIC collider was successfully operated for the first time at $\sqrt{s} = 500$ GeV of $p + p$ running in comparison to prior year's $p + p$ running at $\sqrt{s} = 200$ GeV. The first measurements of parity violating $W^{\pm}$ single spin asymmetries [104] and W production cross section [105] were performed using data collected by the STAR experiment in the same year. In 2011 (2012), RHIC ran in longitudinally polarized mode at $\sqrt{s} = 500$ (510) GeV. During these two years, STAR collected a relatively large set of data which subsequently provided the opportunity to measure for the first time, the lepton pseudo-rapidity dependance of the single spin asymmetries.

Over the years, the capability at RHIC of delivering large luminosity at high energy polarized proton collisions has improved tremendously while also maintaining a stable polarization. In 2013, RHIC delivered its highest luminosity for a polarized $p + p$ run at $\sqrt{s} = 510$ GeV so far [106]. A summary of RHIC delivered luminosity of polarized $p+p$ runs since it's commissioning can be seen in Figure 6.1. Due to the high delivered luminosity in 2013 by RHIC, STAR was able to collect a significantly large data sample, which was more than three times larger than the dataset collected in prior years with an average beam polarization

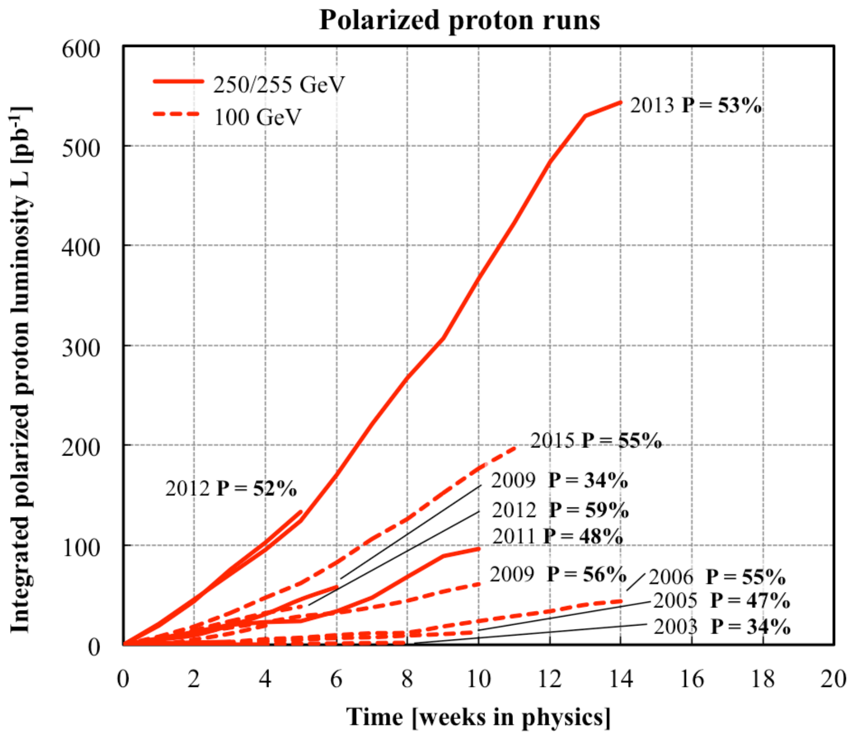

Figure 6.1.: RHIC delivered luminosity during polarized $p + p$ runnings [106]

of 54%[1].

The actual physics data taking period commenced after several weeks of test running, on the day 74 and ended on day 161. Typically, the continuous data taking is subdivided into so-called "runs". During each run, all the data taking parameters such as detector performances, trigger performances, and beam specific parameters such as spin patterns and bunch crossings details are monitored by the shift crews. If any imperfection is identified, the data taking can be interrupted by stopping the run and resumed starting a new run after addressing the particular issue(s). Therefore for a given run, the range of data taking duration can be vary from a few minutes to as long as an hour. Each run is assigned a

[1] $\sim$ 50% is relatively good beam polarization RHIC can achieve with respect to the 85 % of the source polarization, where polarization losses occur at every stage in the collider chain due to numerous depolarizing effect discussed in Chapter 4.

unique number for reference and various information such as the trigger, event size, subsystems used, beam specific parameters, and the status[1] are recorded in a run specific data base for offline usage. The data taking period in 2013 was interrupted between day 127 and 128 due to the installation of the STAR Heavy Flavor Tracker [HFT] detector system. Since the geometrical properties of the STAR was changed due to the new detector installation, the data were analyzed separately for the two periods, period I and period II referring to before and after the HFT insertion. In addition, the calibration of the BEMC discussed in Chapter 5 (also the calibration of the TPC, not discussed in this thesis) as well performed separately for the two periods. However, the final asymmetry results are presented combining the analysis of these two periods.

After careful quality assurance checks (QA) in terms of various aspects a list of 937 run numbers in period I and 710 run numbers in period II were utilized in this work and are given in Appendix A. Sections 6.1.1, 6.1.2, 6.1.3, and 6.1.4 describe the collected data sample in terms of the trigger requirement, spin patterns, data quality QA, and the measurement of integrated luminosity respectively. The rest of the chapter details the production of Monte Carlo (MC) simulation samples. The MC simulation samples were used to estimate the portion of electroweak background contribution to the W signal as discussed in Chapter 8 and to compare the W selection procedure with data.

6.1.1 Trigger Selection

The data selection for the analysis begins at the trigger level. The STAR trigger system is designed to select and begin the Amplification-Digitization-Acquisition (ADA) cycle for the slower detectors which are operated at ∼500 Hz frequency, based on the information from the fast trigger detectors which are operated at RHIC bunch crossing rate of ∼10 MHz [101]. Since the ADA cycle

[1] Status can be either "good", "bad" or "questionable" based on the conditions during the data taking.

can only perform at a rate almost five orders of magnitude slower than the bunch crossing rate, four successive trigger levels have been implemented in order to select collision events[1] at STAR. First three trigger levels 0, 1 and 2 are based on the fast detector information and described in detail in Ref. [101]. The final trigger decision is made at level 3, which is based on the tracking information in slow detectors where our actual physics analysis are carried out. For the purpose of different physical goals, different trigger configurations are designed. For the W analysis in general, two triggers, BHT3*L2BW and EHT3*L2EW are designed based on detector responses of the BEMC and EEMC respectively. The work in this thesis is based only on the data triggered by the BHT3*L2BW in the mid-rapidity region ($|\eta| < 1$).

As mentioned in Sec. 2.5.1 $W^{\pm} \rightarrow e^{\pm}\nu$ can be characterized by the Jacobian peak, which appears at large transverse energies, E_T (of the order of half of the W boson mass) of decay $e^{\pm}$ in the mid-rapidity region. This feature has been implemented when designing the W trigger at STAR which searches for large E_T responses in the calorimeter. It involves a two staged localized energy requirement in the BEMC towers. The first stage (at level 0) requires that at least a single BEMC tower to contain the deposited energy above the threshold value of $E_T = 7.3$ GeV corresponds to the event which was considered. This trigger decision is known as the high-tower 3 (BHT3) trigger in the level-0 STAR trigger system. The second stage is a level-2 software algorithm which looks for a seed tower with E_T above 5 GeV and requires the E_T sum of a 2×2 cluster of towers which contain the seed tower to exceed threshold of 12 GeV. The events satisfying the BHT3*L2BW trigger condition explained above are written to a separate stream of data known as the "St_W", which is then subjected to further offline QA before being used to reconstruct W candidate events.

[1] Event is a single interaction where rate can approach the RHIC crossing rates for the highest luminosity beams.

6.1.2 Spin Patterns

The spin QA is one of the earliest QA that performed on the data before the offline production[1]. This investigation checks whether the intended collisions of four helicity combinations, $++$, $+-$, $-+$, and $--$ have collided at the STAR interaction point as assigned by the RHIC Collider-Accelerator Department (CAD). During this QA spin patterns of each RHIC fill assigned by the CAD were checked and ensured that those matched with corresponding spin patterns recorded by the STAR database. In addition, the stability of spin patterns was checked by ensuring that assigned the spin pattern of a given RHIC fill was continued during the entire fill. The spin patterns are assigned by switching the helicity of bunches from positive to negative and vice versa. According to the pattern this could be either between consecutive bunches or every other bunches or in between more than two bunches. In prior RHIC pp running, spin patterns were repeated after every four bunches. However, in 2013 those were repeated after every 8 bunches.

In order to ensure that all four helicity combinations are all colliding in a given fill, two different spin patterns are assigned for the two beams in a given fill. In addition, several such spin patterns were used between consecutive fills in order to reduce any potential systematic effects. The table 6.1 shows the spin patterns used in 2013 for blue and yellow beams and the assigned collision arrays between the patterns. One can see that four spin patterns in each beam allow eight (P21 to P28) collision arrays which provide intended four helicity combinations. The spin patterns were arranged so that the colliding helicity combination alters between every other collision. For example, one can see this from the P23 collision array which is illustrated in Fig. 6.2. Once the colliding spin pattern of each fill from CAD was identified and the stability of the pattern was confirmed, one must then check the colliding patterns at the STAR interaction point. As

[1] Process refers to the reconstruction of tracks and interaction vertices of particles using software algorithm from the information recorded during the data collection

Spin Pattern		Collisison Arrays
Blue Beam	Yellow Beam	
B1: ++−−++−−	Y4: ++−−−−++	B1×Y3 (P21), B1×Y4 (P22)
B2: −−++−−++	Y3: −−++++−−	B2×Y3 (P23), B2×Y4 (P24)
B3: −−++++−−	Y2: −−++−−++	B3×Y1 (P25), B3×Y2 (P26)
B4: ++−−−−++	Y1: ++−−++−−	B4×Y1 (P27), B4×Y2 (P28)

Table 6.1.: The spin patterns of the two beams and collision arrays in RHIC 2013 running

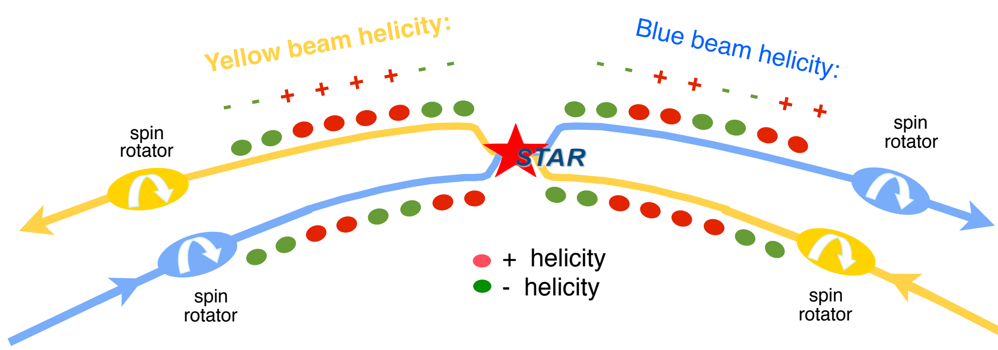

Figure 6.2.: A single spin pattern (P23) for the blue and yellow beams colliding at the STAR interaction region.

mentioned in Chapter 3 each RHIC beam contain 120 bunches including a abort gap provided by 9 empty bunches. In both beams last 9 bunches are kept empty. If bunches of blue beams collided with bunches of yellow beam starting bunch ID's 0 of both beams the same helicity assignment for the bunches from the CAD is valid at the STAR interaction point. However, at the STAR, there is a offset between the beams, meaning the beams are cogged[1] at the STAR. At STAR blue beam bunch ID 0 collides with yellow beam bunch ID 80, thus one cannot directly assign the helicity configuration used by CAD at the STAR interaction region. But this can be determined using the information from abort gaps of the two beam in a bunch crossing spectrum obtained at the STAR. This was done after the offline data production and the spin state of each of the triggered collision at the STAR interaction region was determined and reordered in the STAR offline database. During this process, any runs that corresponds to bunch crossings with additional offsets than the fixed offset and fills with unintended missing bunches were identified and those were masked in the STAR data base. Finally, all these spin information was used to sort events based on the helicity combination during analyses. A list of run that was identified as having stable spin patterns were then subjected to a run QA which discussed in the next section.

6.1.3 Data QA

Similar to the spin pattern QA, the run QA as well was performed in two steps before and after the offline data production. Before the production, this was performed via checking STAR run logs[2], fast online plots[3] and STAR electronic shift logs[4]. Any runs with issues that were unsatisfactory for the analysis were removed. Next, the more detailed QA was performed after the offline data production by checking distribution of basic kinematic variables from the main detectors used in this analysis. In TPC mean values of the parameters such as

[1] RHIC bunches are cogged meaning beams are set such that the first bunches collide only at specific points. At STAR interaction point, fixed offset of 80 bunches between the two beams are set.

[2] Online data base which contain run information.

[3] These plots are obtained during the data taking which tracks the performances of various element such as detectors, scalers, triggers, and bunch crossings.

[4] Online log books which contains notes from the shift crews during the data taking.

η, ϕ, p_T, dE/dX (energy loss by the charged particles due to ionization), DCA[1] and χ^2 of reconstructed charge particle tracks were examined. The respective η, ϕ distributions and E_T deposition in BEMC and EEMC towers were also examined. An average value was obtained for each parameter per run. Runs with average values beyond acceptable variance were removed. The distributions of two quantities that were inspected during the QA, (TPC track η and BEMC tower E_T) can be seen in Figure 6.3 as a function of run index for period I, where outlier runs have been thoroughly investigated before removing from the analysis. Any runs which failed the above conditions were removed from the final run list used for the asymmetry analysis.

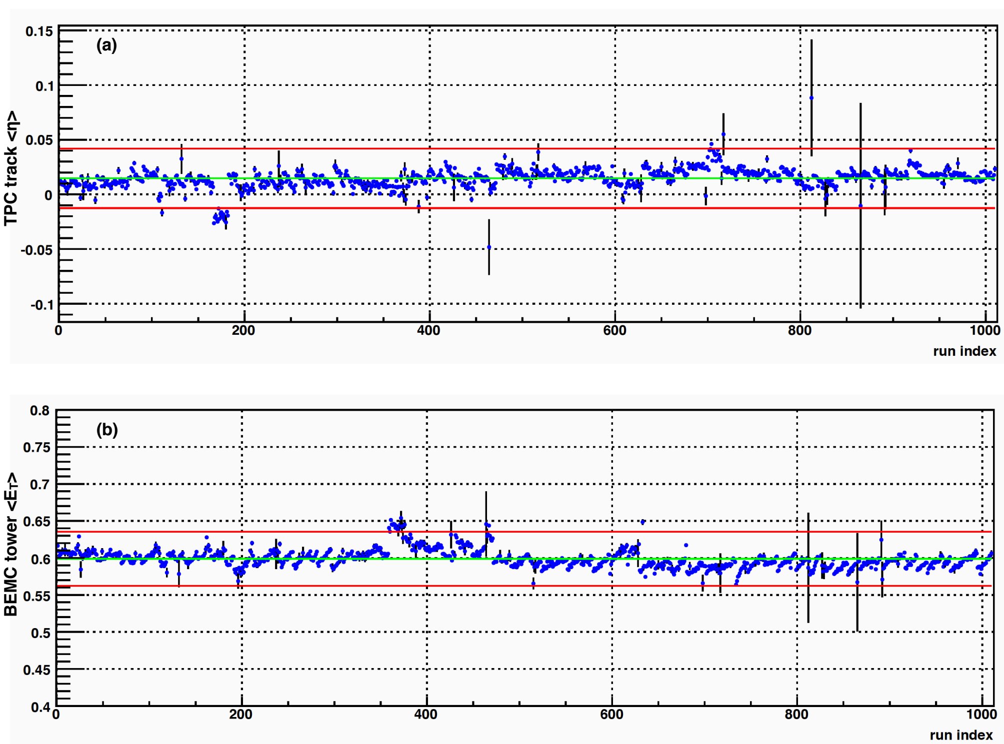

Figure 6.3.: TPC track $\langle\eta\rangle$ (a) and BEMC tower $\langle E_T\rangle$ (b) distribution of the data used during QA

[1] Minimum distance from reconstructed track to the beam line.

6.1.4 Integrated Luminosity

In particle physics experiments, luminosity can be described as the quantity that measures the ability of a particle accelerator to produce the required number of interactions. When two beams collide, the instantaneous luminosity, can be defined as the overlap integral of the particle density of each beam. Under the assumption that the beams have Gaussian transverse profiles, the luminosity $\mathcal{L}$ for bunched beams can be written as,

$$\mathcal{L} = \frac{f_{rev} K}{2\pi\sigma_x\sigma_y} \tag{6.1}$$

where f_{rev} is the revolution frequency of RHIC beams, $K = \Sigma_i N_i^a N_i^b$ is the product of the bunch intensities (N_i) of the two beams (a, b) summed over all bunches, and σ_x, σ_y are the transverse widths of the beam overlap region. At RHIC, the intensity of each bunch is determined during a scan by the Wall Current Monitors[1] [107]. The transverse widths of the beam overlap region which subsequently used to calculate the effective cross section values, are measured using the vernier scan technique[2] [108][109]. During the data taking at STAR dedicated vernier scan runs with controlled beam position displacements were obtained for this purpose. In RHIC 2009 running, STAR had implemented a dedicated W trigger for the vernier scan based on the BHT3 [110] which had been used to measure the absolute luminosity for the W cross section analysis. However, for the asymmetry analyses, absolute luminosity values are not needed. Therefore, for this analysis, the vernier scan results are obtained based on the information of the coincidence trigger of the STAR Zero Degree Calorimeter (ZDC). The total integrated luminosity $L = \int \mathcal{L} dt$ of the data sample of 937 runs of L2BW trigger of period I and 710 runs of the same trigger in period II used for this analysis was calculated to be 125.6 pb^{-1} and 121 pb^{-1} respectively.

[1] A device which can measure the instantaneous value of the beam current.

[2] One beam is swept stepwise across the other, while measuring the collision rate as a function of beam displacement.

6.2 Simulation Sample

Simulation samples were used for two purposes: to estimate background contributions from electroweak processes and to compare various predicted quantities to data. In general, the production of simulation sample at STAR involves several steps. First, a Monte-Carlo (MC) technique based on PYTHIA [111] is used to generate high energy physics events of interest. Next, these generated events are sent through the GEANT [103] model of the STAR detector in order to obtain detector responses for the simulated events. Finally, events are embedded in to STAR "Zero bias" events [1] in order to account for pile-up effects in the detector. These steps are described briefly in the following sections.

6.2.1 PYTHIA based MC simulation

MC simulation samples of $W^{\pm} \to e\nu$ and $W^{\pm} \to \tau\nu$ decay channels in $pp \to W^{\pm} + X$ process and $pp \to Z/\gamma^{*} \to e^{+}e^{-}$ decay channel were generated using PYTHIA 6.4.4 [111] event generator (with Perugia 0 tune [112]). However, τ from W decay in PYTHIA is treated as unpolarized and does not decay. Therefore, an additional package of TAUOLA [113] was used when generating $W^{\pm} \to \tau\nu$ decay channels. In order to generate a PYTHIA event, one must specify the coordinates of the vertex (interaction point). This was done by assuming Gaussian distributions for x_{vertex}, y_{vertex}, and z_{vertex} with widths determined based on the width of vertex distributions of the real data. Since collisions occur along the beam line, x_{vertex} and y_{vertex} widths are relatively small. For the z_{vertex}, a width of 42.0 cm was assigned during this production based on the RMS of the z_{vertex} distribution of the data. A comparison of reconstructed z_{vertex} distribution between data vs embedded simulation of $W^{\pm} \to e\nu$ is shown in Figure 6.4. A good consistency between the two distributions of data and simulation can be

[1] Events which are triggered only by the coincidence of east and west ZDC responses. No other detector requirement are imposed.

seen. The statistics of embedding events of each decay channel were predeter-

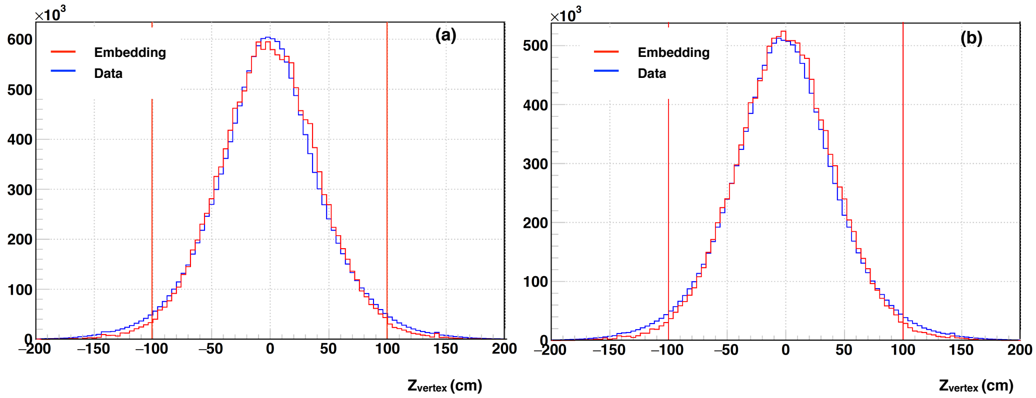

Figure 6.4.: Z_{vertex} distribution of data and embedding for Period I (a) and Period II (b).

mined to be larger than ($\sim$ one order of magnitude) the integral luminosity of data, in order to reduce the statistical uncertainty of each sample. Table 6.2 lists the statistics of embedded MC events. Once the MC events are generated using

Event Channel	PYTHIA cross-section (pb)	events size (Period I)	events size (Period II)
$W^+ \to e^+\nu$	98.5	135.9 K	141.6 K
$W^- \to e^-\nu$	31.3	43.6 K	45.7 K
$Z/\gamma^* \to e^+e^-$	23.9	31.2 K	32.9 K

Table 6.2.: Statistics of embedded MC samples.

PYTHIA, the events are sent through the GEANT version of the STAR detector in order to obtain the detector response. At this stage the process of embedding is also performed as explained in 6.2.2. Next, the tracks / vertex reconstruction and W / Z reconstruction are performed the same way using the same algorithm as the data that discussed in Chapter 7.

6.2.2 Embedding procedure of MC simulation samples

Due to the high rate of bunch crossing on the order of several hundred kHz many pile-up tracks exists in the TPC at any given time. Pile-up tracks refer to those tracks which are not associated with the triggered collision. The pile-up effect arises due to the time difference between the bunch crossing period at RHIC and the TPC drift time of ionization electrons. The period of bunch crossing at RHIC is about 107 ns. However, after each triggered collision at STAR, ionized electrons take ∼38 μs to drift through the TPC volume. Therefore pile-up tracks are produced from non-triggered collisions from the same bunch crossing as the triggered collision or a collision that occurred in an earlier or later bunch crossing. The MC simulation samples do not exhibit this pile-up environment. However, for a proper and accurate comparison between data and simulation, the pile-up environment needs to be present in the simulation as well. In order to accomplish this, the full GEANT detector response of simulated events were embedded into the STAR zero-bias triggered event prior to the track reconstruction.

The STAR zero-bias triggered events are recorded simultaneously with the physics trigger events with no detector requirements, and thus best represent the pile-up environment in the TPC for any triggered collision. The density of the pile-up tracks in the TPC are approximately proportional to the instantaneous luminosity. Therefore, zero-bias events which were taken during each run in the data sample were considered in order to ensure that the same instantaneous luminosity (and therefore the luminosity of pile-up events) as the real data was represented while reproducing pile-up effects in the embedding sample. The amount of required zero-bias events for each run were calculated based on the formula in the Equation 6.2.

$$N_i^{ZB} = \frac{L_i}{L_{total}} \times N_{total} \tag{6.2}$$

where N_i^{ZB} and L_i are the number of zero-bias events considered and the integral luminosity of the i^{th} run respectively, N_{total} is the total number of MC events listed for each decay channel in Table 6.2 and L_{total} is the total integrated luminosity of the data sample as noted in Section 6.1.4. The instantaneous luminosity of a collision can be characterized by the coincidence rates of the ZDC detector at the time of the collision. Therefore, by comparing the ZDC rate distributions between data and embedding, efficiency of embedding process can be checked. Figure 6.5 shows the ZDC rate distributions of the total integrated luminosity of data and embedded MC where. As the two distributions are consistent, one can say that the luminosity weights in data have been fairly well described by the sampled zero-bias events which were used for the embedding. This implies that the pile-up effects are well accounted for the simulation production.

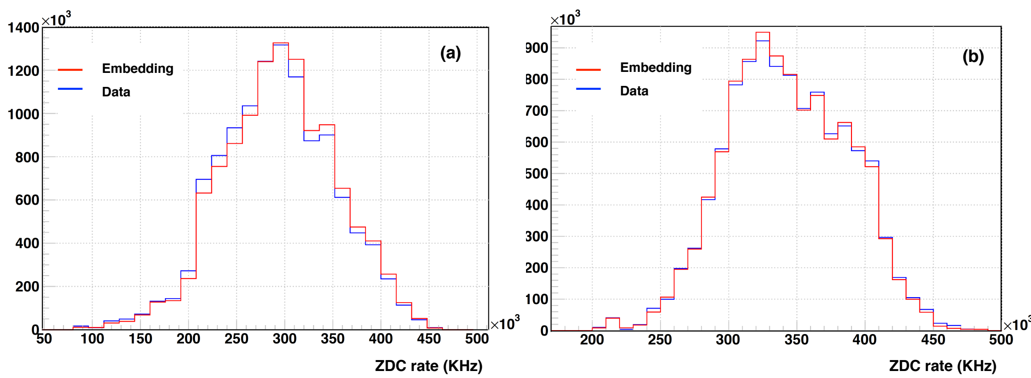

Figure 6.5.: The ZDC rate distribution of data and embedding for Period I (a) and Period II (b).

CHAPTER 7
DATA ANALYSIS

This chapter details the analysis of the selected data and embedded MC samples. Both the data and the MC samples were analyzed using the same algorithm and each analysis step of the data were compared with the MC. The data of period I and II were analyzed separately. However, the various distributions shown in this chapter were obtained after combining the individually analyzed data samples of the two periods. The first section describes the basis of the analysis algorithm and the rest of the chapter is focused on the analysis itself.

7.1 Basis of the W / Z reconstruction algorithm

As explained in Sec. 4.1, almost all the CM energy available is required to create a W / Z boson at RHIC. Thus, the production of W / Z boson at STAR experiment leaves little or no transverse energy in the system while emitting the remaining beam fragments in the very forward / backward direction, mostly out of the STAR TPC acceptance. Therefore, the decay electrons and positrons from W and Z bosons can be characterized by the isolated tracks in the TPC with high transverse momentum, p_T, and large transverse energy deposition, E_T, in the calorimeter. In addition to this, $e^{\pm}$ which decayed from a W boson have the unique feature of large imbalance in the reconstructed sum of the p_T vector ("vector p_T sum"), due to the undetected neutrino in the final state. Taking these features into account, an analysis algorithm is designed for STAR in order to identify and reconstruct high p_T electrons and positrons which decayed from W and Z bosons by reducing QCD type background. The main type of QCD background are the "di-jet" type background events which correspond to back-to-back jets in the STAR detector system which originated from parton fragmentations.

The analysis algorithm has several levels as listed below.

1. Trigger level
2. Event level
   (a) Primary vertex / primary track selection
3. High-p_T / high E_T candidate $e^{\pm}$ level
   (a) High-p_T candidate $e^{\pm}$ track selection
   (b) High-p_T / high E_T candidate $e^{\pm}$ track and EMC cluster matching
   (c) High-p_T / high E_T $e^{\pm}$ candidate EMC cluster isolation
4. W / Z candidate level

The algorithm starts at the trigger level where certain trigger requirements are implemented during the data taking itself as discussed in Sec. 6.1.1. At the trigger level, loosely placed energy requirements in the calorimeter, select collision events which have a certain probability to be a W or Z decay event. Next, at the event level, cuts are designed to identify low multiplicity events such as from W or Z decays. These low multiplicity events are embedded in the high pile-up TPC environment and are identified by reconstructing the primary vertices which belong to the triggered events as discussed in Sec. 4.3. During the selection of high-p_T / E_T $e^{\pm}$ events, various cuts are applied to select high p_T TPC primary tracks, which are associated with primary vertices. These tracks are then extrapolated to the calorimeter towers and various tower and cluster requirements are imposed based on the calorimeter energy response in order to isolate high-E_T EMC tower clusters. Finally, W and Z bosons candidates are identified while reducing the QCD jet type background events based on the topological and kinematic differences between them.

Simulated events of a W boson decay into an electron and a neutrino ($W \to e\nu$), a QCD type di-jet ($pp \to jets$), and a Z boson decay into a pair of electron and a positron ($Z \to e^+ + e^-$) from $p+p$ collision at $\sqrt{s} = 500$ GeV in the STAR detector are shown in Figure 7.1 (a), (b), and (c) respectively. The $W \to e + \nu$

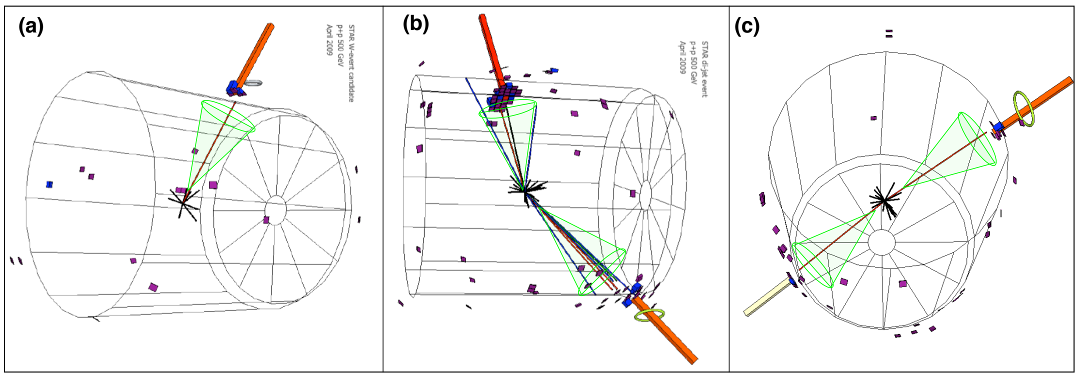

Figure 7.1.: Simulated events of a $W^\pm \to e^\pm\nu$ event (a), QCD type di-jet event (b), and $Z \to e^+ + e^-$ event (c)

event corresponds to a single isolated high-p_T TPC track which is being matched to an isolated calorimeter tower cluster with large energy deposition but with little or no coincident energy opposite in ϕ. The $Z \to e^+ + e^-$ event corresponds to a pair of back-to-back isolated high-p_T TPC tracks which are being matched to isolated calorimeter tower clusters. In contrast, the QCD type di-jet event correspond to several TPC tracks which are being matched to several calorimeter clusters.

7.2 Event Selection

Of the TPC events triggered by W triggers, only the events which contain primary vertices were considered. Primary vertices were reconstructed based on the PPV method as discussed in Sec. 4.3. Two requirements were used to select events with primary vertices:

- Vertices were required to have a positive “rank”[1]

- $|Z_{vertex}| < 100$ cm

The distribution of rank of the reconstructed vertices by the PPV of triggered events and $|Z_{vertex}|$ distribution of the respective positive rank events are shown in Figure 7.2 (a), (b) respectively. Events in the middle peak (single track vertices)

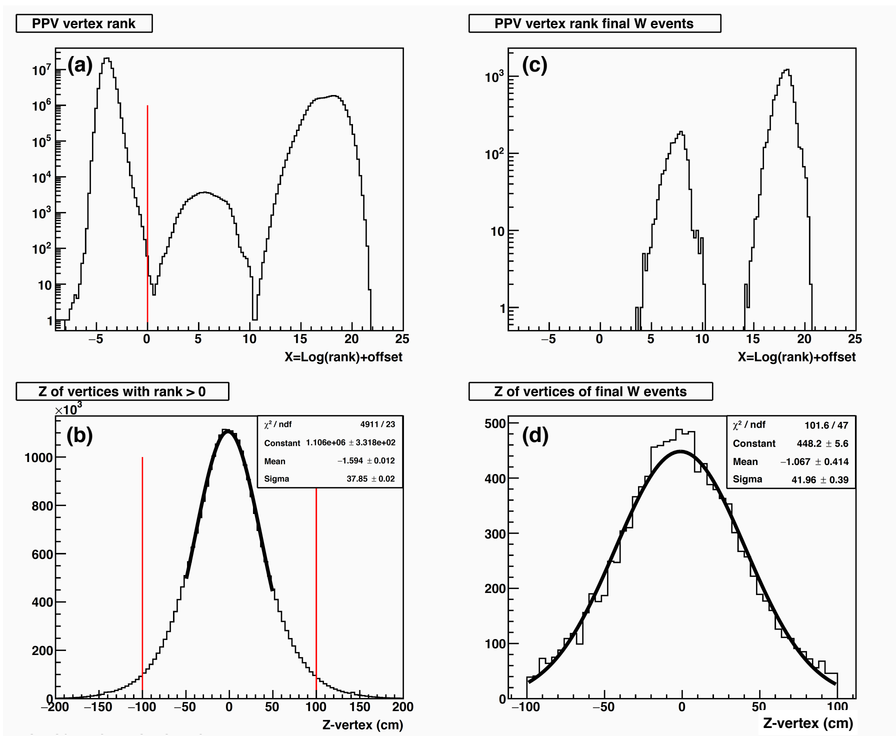

Figure 7.2.: Vertices reconstructed by PPV: rank of all vertices (a), Z_{vertex} distribution for vertices with rank >0 (b), rank of vertices for reconstructed W candidates (c), Z_{vertex} distribution for reconstructed W candidates (d).

and the right side peak (two or more track vertices) are corresponds to a positive rank. Out of those, events with $|Z_{vertex}| < 100$ cm were used for the analysis. The distributions (c), (d) in Figure 7.2 shows the respective vertices rank and Z_{vertex} distributions of final W candidates obtained towards the end of this chapter, in

[1] see Sec. 4.3

the energy range between 25< E_T <50 GeV. The distribution of the Z_{vertex} was approximately Gaussian with the RMS equal to 41 cm. The sample of events which satisfy these event selection requirements were subjected to the high-E_T $e^{\pm}$ selection requirements.

7.3 High E_T Candidate $e^{\pm}$ Track Selection

After selecting low multiplicity events based on PPV, the process of selecting high E_T $e^{\pm}$ candidate events starts from the track level.

7.3.1 Track Requirements

The TPC charged particle tracks which belong to primary vertices from the previous section are referred to as primary tracks. The following quality requirements were imposed on primary tracks in order to select the tracks which are highly likely to be high p_T $e^{\pm}$ candidate tracks in the TPC. In addition, these cuts were also designed to eliminate any pile-up tracks that were incorrectly (accidentally) tagged as primary tracks.

- A minimum of 15 TPC points must have been used during the track reconstruction.

- Maximum number of TPC points which have been used in the reconstruction, w.r.t the maximum TPC points possible (for fitting), must exceed 51%.

- The radius of the first TPC point that was used during the reconstruction nearest to the beam line must be < 90 cm.

- The radius of the last TPC point that was used during the reconstruction, farthest to the beam line must be > 160 cm.

- $p_T > 10$ GeV

The momentum cut, $p_T > 10$ GeV, was rather loosely placed despite W and Z decay $e^{\pm}$ tracks belong to tracks with even higher p_T ($\sim> 25$ GeV). Such a low cut was motivated due to the deterioration of the tracking resolution of the TPC with increasing momentum and therefore to select as many tracks as possible at TPC level. As the quality of these tracks are further expected to defined based on the calorimeter E_T information (which has better resolution at larger energies) during the next levels in the algorithm a rather low p_T cut was understood as a proper motive. Figure 7.3 shows the distributions of each the parameters listed above and the threshold values of the cuts are indicated by red lines. Next, these tracks were matched to the calorimeter towers as discussed in

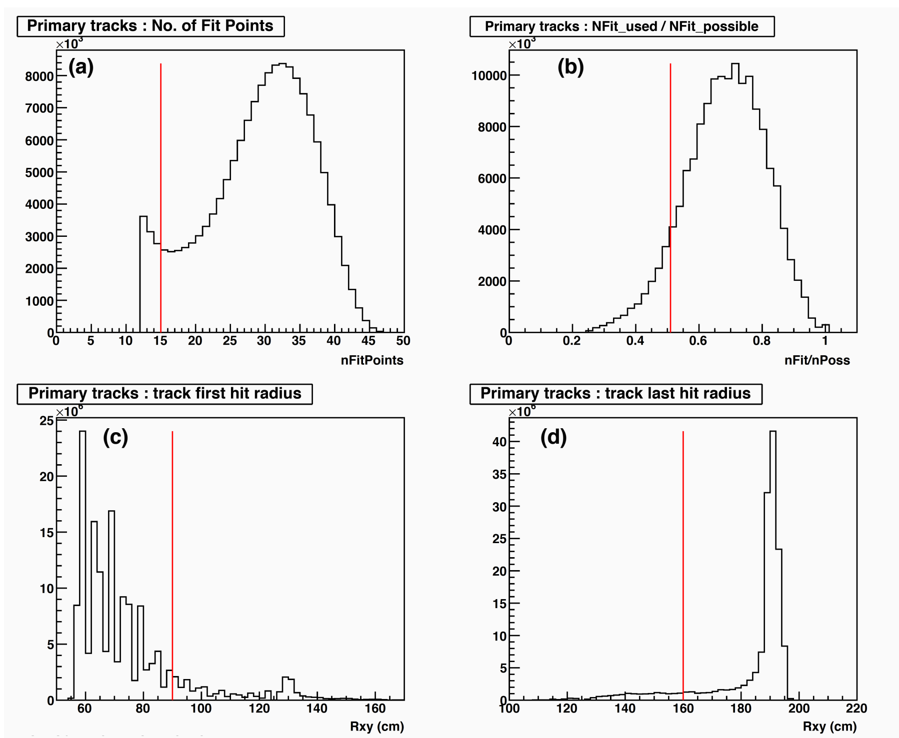

Figure 7.3.: Track quality cuts placed on reconstructed primary tracks: number of TPC hits used (a), Fraction of number of TPC hits used to allowed (b), radius of the track hit nearest to the beam line (c), radius of the track hit nearest to the beam line (d).

the following section.

7.3.2 Track - Cluster Matching Requirements

The $e^{\pm}$ candidate tracks which satisfy the quality track requirements from the previous section were extrapolated to the BEMC, as illustrated in Figure 7.4. The BEMC tower where a track was extrapolated and being matched is denoted

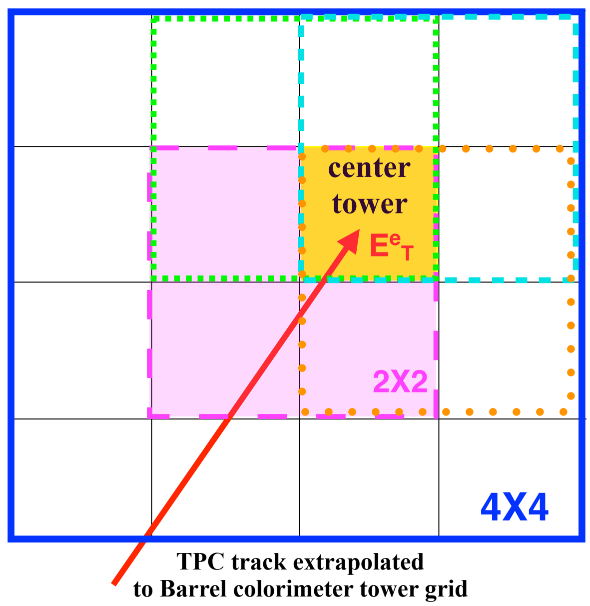

Figure 7.4.: Illustration of the extrapolation of the TPC candidate track to the BEMC tower, center-tower (yellow) and the reconstruction of the largest 2×2 summed E_T tower cluster, candidate cluster (pink) which contain the center-tower and the reconstruction of the 4×4 tower cluster (blue) around the candidate cluster which used in isolation requirements which is discussed in Sec.7.3.3

as the "center tower" (yellow). Four possible 2×2 tower clusters which contain the center tower were constructed (dashed boxes). The transverse energy sum of those 2×2 clusters, $E_{T(2\times2)}$ were computed and the cluster with the largest summed $E_{T(2\times2)}$ (pink) was assigned as the cluster which belongs to the candidate $e^{\pm}$ track and the $E_{T(2\times2)}$ of that cluster was considered as the candidate's transverse energy, denoted as E_T^e. Two requirements were demanded during this track-cluster matching process. First, the E_T^e was required to be larger than 14 GeV which ensure that the measured E_T^e was above the trigger threshold used for the W trigger. Next, a log-weighted position was determined for the candidate tower cluster by weighting its $\eta-\phi$ co-ordinate position based on the log of the E_T^e, requiring that the magnitude of the three-dimensional distance between this log weighted cluster position and the position where the candidate track is being extrapolated and matched, $|\Delta\vec{r}|$, to be less than 7 cm. This position matching requirement was placed in order to reject any candidate track where the corresponding energy deposition in the cluster may not have been originated from the particle which produced the TPC track, rather from neutral particles such as π^0, who leaves no tracks in the TPC. The distributions of track-cluster matching requirements can be seen in Figure 7.5 of the data in comparison to embedded MC which shows the distribution of 2×2 cluster E_T, distance between extrapolated track and centroid of the tower cluster and 2D distributions between one another after placing the E_T^e cut of 14 GeV. The magenta lines represent the threshold values of the cuts.

7.3.3 Energy Isolation Requirements

As mentioned before, $e^{\pm}$ from W decay are well isolated from other particles in $\eta-\phi$ space due to the large energy deposition in a isolated EMC cluster associated with the respective high-p_T track but with little or no coincident energy opposite in ϕ, in comparison to QCD di-jet type backgrounds. Two isolation requirements were imposed by taking these features into account. First, a 4×4 cluster was constructed around the candidate 2×2 cluster as shown in Figure 7.4 and the ratio of E_T^e of 2×2 to E_T sum of the 4×4, $E_T^e/E_{T(4\times4)}$ was required to be grater than

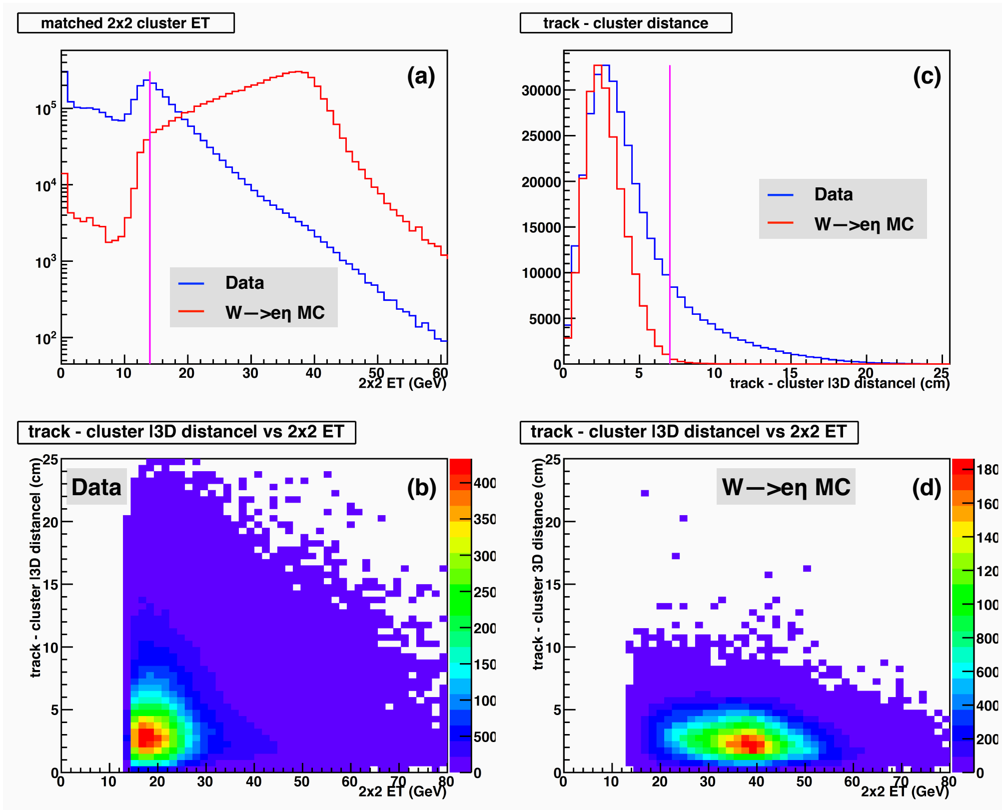

Figure 7.5.: Distributions of track-cluster matching requirements: 2×2 cluster E_T (a), distance between extrapolated track and centroid of tower cluster (b), distance between extrapolated track and centroid of tower cluster vs E_T^e for data (c) and for MC (d).

95%. This isolation requirement will be referred as "cluster isolation" through out this chapter. The distribution of cluster isolation ratio of data in comparison to MC is shown in Figure. 7.6 (a). Since the $e^{\pm}$ from W decay are expected to deposit essentially all their energy in the candidate 2×2 cluster, a significant amount of background was removed from this isolation requirement. The next isolation requirement was imposed by taking the ratio of E_T^e to summed E_T of a large area which belongs to a reconstructed cone around the candidate track. This particular cone is reconstructed with a radius of $\Delta R \equiv \sqrt{\Delta\eta^2 + \Delta\phi^2} = 0.7$ around the candidate track as shown in the illustration in Figure 7.7 and is

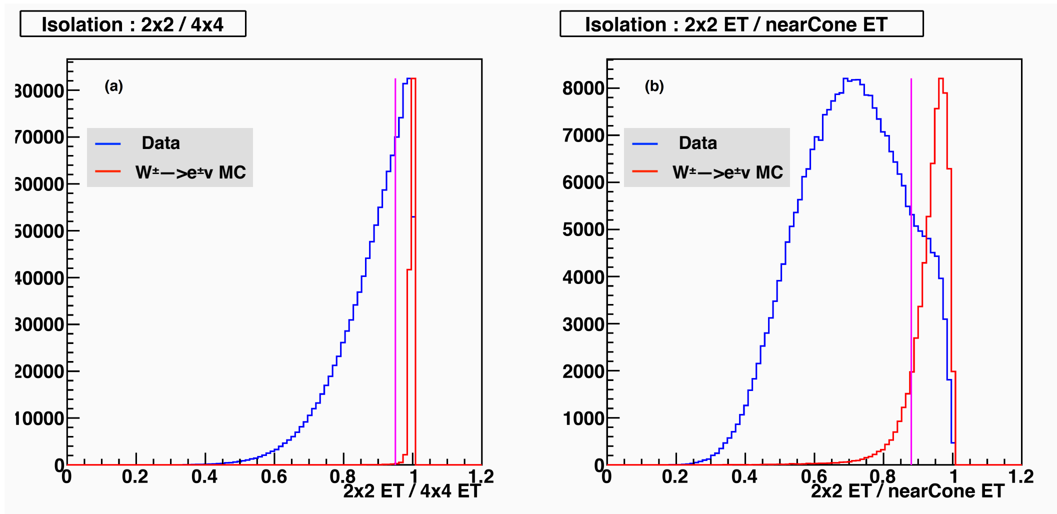

Figure 7.6.: $e^{\pm}$ isolation ratio distributions in comparison to $W^{\pm} \to e^{\pm}\nu$: cluster isolation, $E_T^e/E_{T(4\times4)}$ (a), near-cone isolation, $E_T^{\Delta R<0.7}$ / E_T^e (b)

denoted as the near-side cone.[1] Then the E_T sum of the near-side cone, $E_T^{\Delta R<0.7}$ is constructed by adding all the BEMC and EEMC tower E_T and TPC p_T of all the tracks that fall within the cone. However, the candidate track is excluded when summing the TPC track p_T within the cone in order to avoid double counting the p_T of the candidate track. Then the ratio, E_T^e / $E_T^{\Delta R<0.7}$ was computed and it was required to be greater than 88%. This isolation method is referred to as the "near-cone isolation" and the distribution of the ratio in the data is shown in Figure. 7.6 (b) in comparison to the respective MC distribution. Since the area considered in the near-cone isolation was significantly larger than the area considered in the cluster isolation, a rather loose threshold was used in order to make the cut more effective. Significantly large fraction of jet-like background events were eliminated at this step.

The next section describes the process of balancing the transverse momentum

[1] The base surface area of this cone with radius ΔR=0.7 contains roughly 550 EMC towers which are of 0.05×0.05 units size in $\eta - \phi$ space.

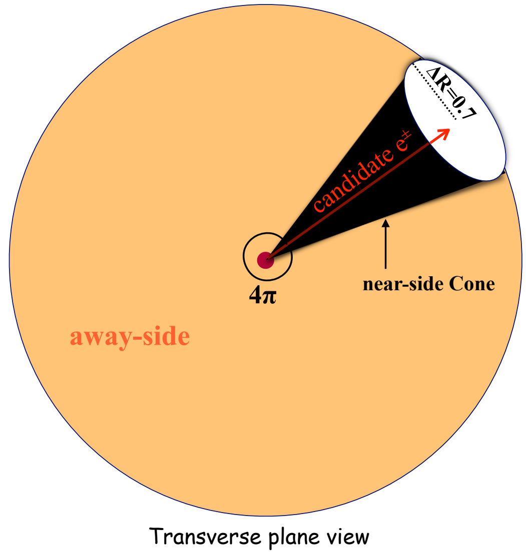

Figure 7.7.: Illustration of the near-side cone with radius $\Delta R \equiv 0.7$ around the $e^{\pm}$ candidate track (Red) in the transverse plane. The use of away-side region (orange) in order to construct the p_T-balance vector is discussed in Sec. 7.4.1

of candidate tracks within the 4π solid angle in order to select candidate $e^{\pm}$ which were decayed explicitly from W bosons.

7.4 $W^{\pm} \rightarrow e^{\pm}\nu$ Candidate Event Selection

The isolated $e^{\pm}$ sample from the previous section is primarily dominated by $W^{\pm} \rightarrow e^{\pm}\nu$ events, $Z \rightarrow e^{+} + e^{-}$ events, and QCD jet-type background events which passes all the prior $e^{\pm}$ selection requirements. In order to select $e^{\pm}$ which were explicitly decayed from W bosons, differences in the event topology between these processes were used. As explained in Sec 7.1, $W^{\pm} \rightarrow e^{\pm}\nu$ corresponds to a nearly isolated $e^{\pm}$ in the calorimeter and a neutrino close to opposite in azimuth which carries large E_T similar in magnitude to that of the $e^{\pm}$, but left undetected. Thus, a large missing transverse energy opposite in azimuth to the $e^{\pm}$ is associated with a W decay event. This resulted in a large imbalance in the vector p_T sum of all reconstructed final-state objects of a W decay event, in contrast to a $Z \rightarrow e^{+}+e^{-}$ decay event or a QCD jet-type background event which are characterized by a small magnitude of this vector p_T sum. The following two sections describe the use of this feature in order to select W events.

7.4.1 Signed p_T Balance Requirement

In order to reconstruct the vector p_T sum of all reconstructed final-state objects referred to as $\vec{p}_T^{\,balance}$, the p_T of the candidate track and p_T of all the jets whose thrust axes[1] are in the away-side of the near-side cone as shown in orange color region in Figure 7.7 were considered. These jets were reconstructed using a standard algorithm known as the anti-k_T[114] algorithm[2] which is widely used in the reconstruction of particle jets in high energy particle collision experiments. The parameters used for the jet reconstruction at the STAR experiment cited above are listed in the Appendix **??**. Next, the $\vec{p}_T^{\,balance}$ is defined as the vector sum of the $e^{\pm}$ candidate's p_T vector, $\vec{p}_T^{\,e}$ and the p_T vectors of all reconstructed jets mentioned above, $\vec{p}_T^{\,jets}$ as shown in Equation[3] 7.1.

$$\vec{p}_T^{\,balance} = \vec{p}_T^{\,e} + \sum_{\Delta R > 0.7} \vec{p}_T^{\,jets} \tag{7.1}$$

The magnitude of the $\vec{p}_T^{\,e}$ is equal to the candidate transverse energy, E_T^e while the vector direction is defined by the momentum direction of the candidate TPC track. The scaler quantity, signed p_T balance in Equation 7.2 is then defined as the magnitude of the $\vec{p}_T^{\,balance}$, with the sign given by the dot product of the p_T balance vector and the p_T of $e^{\pm}$ candidate vector,

$$signed\, p_T\, balance = sign(\vec{p}_T^{\,e} \, . \, \vec{p}_T^{\,balance}) \; |\vec{p}_T^{\,balance}|. \tag{7.2}$$

[1] The thrust variable characterizes the event shape. For example, the region where energy deposit is maximized in a di-jet event, one can find the direction that maximize the scale sum of the projection of momenta along it, which is defined as the thrust axis.

[2] The STAR experiment use anti-k_T algorithm to construct hadron jets as discussed in following measurements [115].

[3] $\Delta R > 0.7$ indicates the away-side region.

The distributions of signed p_T balance as a function of E_T^e is shown in Figure 7.8 (a) in comparison to the MC in Figure 7.8 (b). For $e^{\pm}$ events decayed from W bosons, signed p_T balance is highly correlated with E_T^e of $e^{\pm}$. This can be seen clearly in the $W^{\pm} \rightarrow e^{\pm}\nu$ MC distribution where no backgrounds are present. In contrast, Z decay or jet-type backgrounds events corresponds to smaller signed p_T balance for all energies since the candidate tracks p_T is being balanced by the p_T of all reconstructed objects in the away-side region. Therefore, a cut is imposed at 14 GeV on signed p_T balance in order to remove events with smaller signed p_T balance as shown by the magenta lines. A significant por-

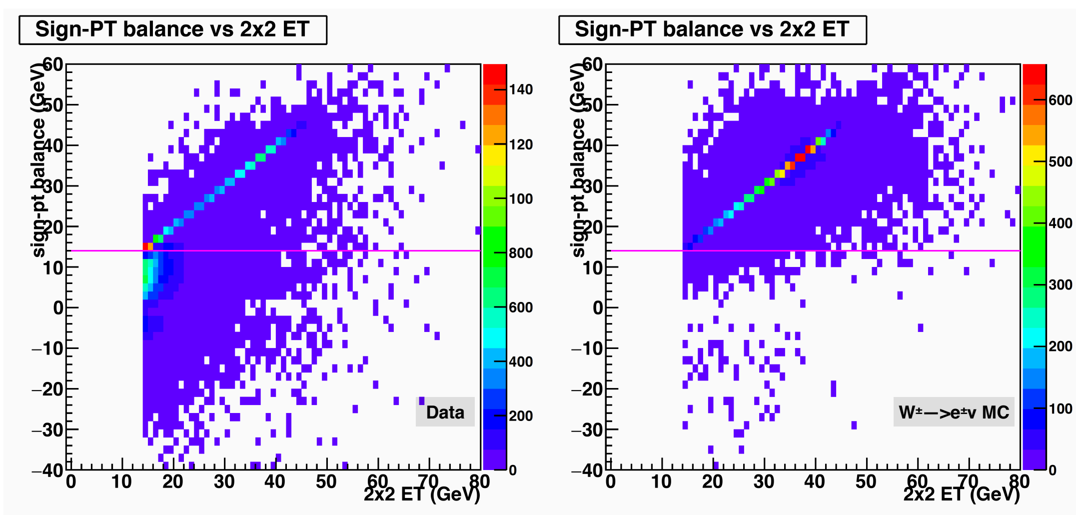

Figure 7.8.: Signed p_T balance vs E_T^e for data (a) and for $W^{\pm} \rightarrow e^{\pm}\nu$ MC (b)

tion of the background was removed due to this cut. In addition, to further increase the effectiveness of the use of p_T imbalance feature, an additional cut was imposed based on the reconstructed away-side energy.

7.4.2 Away-side E_T Requirement

Away-side energy E_T^{away}, quantify the large "missing" transverse energy of final state objects of W decay event opposite in azimuth to the $e^{\pm}$. The E_T^{away} was constructed by adding all the BEMC and EEMC tower E_T and TPC track p_T of all the tracks in the away-side region of the isolated $e^{\pm}$ from Sec 7.3.3. The same "missing" transverse energy was quantified when reconstructing the p_T balance vector in the Sec. 7.4.1. However only the reconstructed "jets" in the away-side region were considered. Here, E_T^{away} was determined considering all the tracks in the away-side, not only the ones which belong to a reconstructed jet. By doing so, a track(s) which belong to a particular jet but was not included during the jets-reconstruction process due to possible inefficiencies in the jet algorithm, were considered. For W decay events, E_T^{away} should be significantly smaller in comparison to jet-type background events. A cut was imposed on the reconstructed E_T^{away}, and the threshold value was determined based on the mean of the E_T^{away} of the respective MC distribution. Figure 7.9 (a) shows the E_T^{away} distribution of data and MC with magenta line showing the cut, which required E_T^{away} to be less than 11 GeV. Figure 7.9 (b) and (c) shows the same distributions of signed p_T balance vs E_T^e as in Figure 7.8 but only for the events which passes both signed p_T balance cut and E_T^{away} cut of the data and the MC respectively. By comparing distributions in Figure 7.9 and 7.8 one can see that a certain amount of background was removed and the correlation of signed p_T balance vs E_T^e was more refined. These events were taken as the final raw W yields which passes all the selection cuts that were imposed by the W reconstruction algorithm.

The Figure 7.10 shows the progression of selection cuts as a function of E_T^e. Since this progression is shown as a function of E_T^e one can clearly see the emergence of the characteristic Jacobian peak which peaks around roughly half of the W mass. Here, the histogram represented by the black line corresponds to the sample of $e^{\pm}$ events which passed vertex and track selection requirements

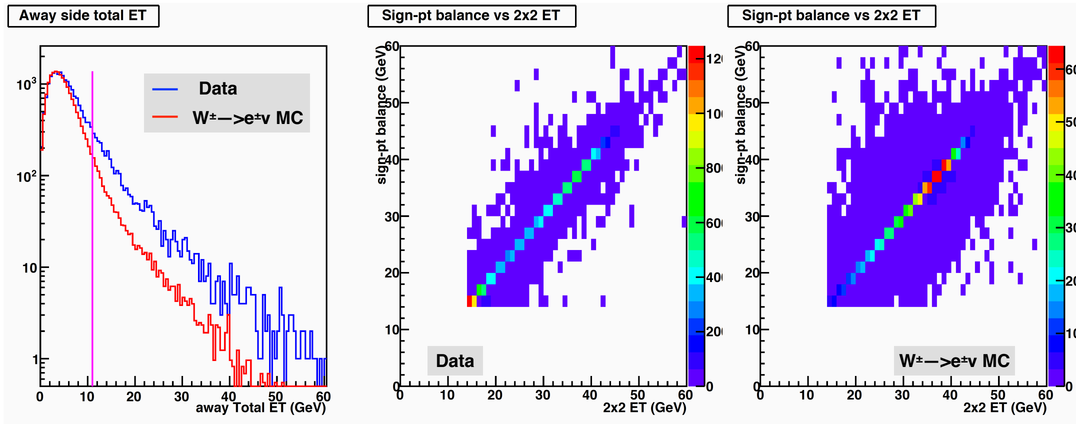

Figure 7.9.: E_T^{away} distributions of data in comparison to $W^{\pm} \to e^{\pm}\nu$ MC (a), signed p_T balance vs E_T^e for data (a) and for $W^{\pm} \to e^{\pm}\nu$ MC (b) of final W yields after the away E_T cut.

discussed in Sec. 7.2 and 7.3.1 respectively and then being extrapolated to a BEMC tower. The blue filled histogram corresponds to the sample of candidate $e^{\pm}$ events which passed the track-cluster matching requirements discussed in Sec. 7.3.2 and the cluster isolation requirement explained in Sec. 7.3.3. The sample of $e^{\pm}$ events which passed the near-cone isolation requirement discussed in the latter section are represented by the green filled histogram and finally the final raw W yields as discussed in Sec. 7.4.2 which passes all the W selection cuts imposed by the algorithm are indicated by the red histogram. The total number of events that were triggered by the W trigger and was used as input events to the algorithm chain were on the order of $\sim 10^7$ (22385868). The statistics of the total out put events (final raw W yields) are on the order of $\sim 10^4$ (17509). Among this, yields in the region of E_T^e below 25 GeV mostly belong to QCD type background events that are needed to be removed. Thus, only the statistics between $(25 < E_T^e < 50)$ GeV called, "golden Ws", were considered for the asymmetry analysis. The number of golden Ws can be roughly considered as the total number of W boson produced in the $p+p$ collision at the RHIC. Therfore, from this analysis, one can conclude that in 2013 RHIC has produced roughly about 10000 W bosons. Figure 7.11 gives a view of the progression of cuts used to select W events in terms of the reduction of the statistics of the data sample in each step due to the reduction of backgrounds. The next section discuss the process of separating the final W yields based on their charge sign.

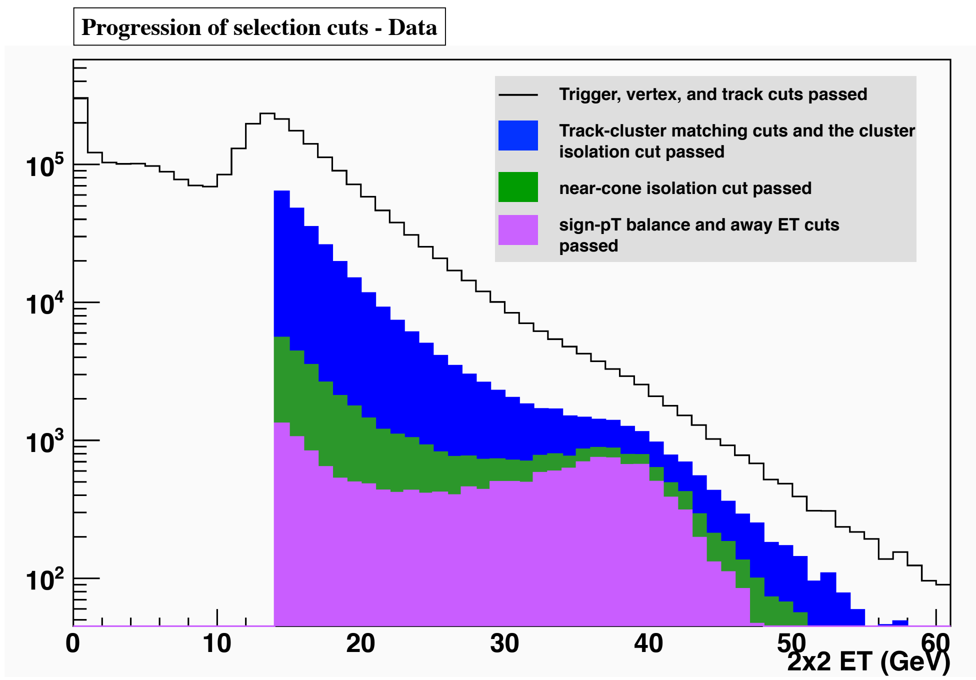

Figure 7.10.: Progression of cuts in W reconstruction algorithm as a function of E_T^e

7.5 Charge Sign Reconstruction Requirements

In order to discriminate W^+ boson production from W^- boson production, electrons and positrons from W decay must be separated. At STAR this is achieved by taking advantage of the bending of charged particle tracks in the magnetic field as discussed in Sec. 4.4. A proper charge sign separation of elec-

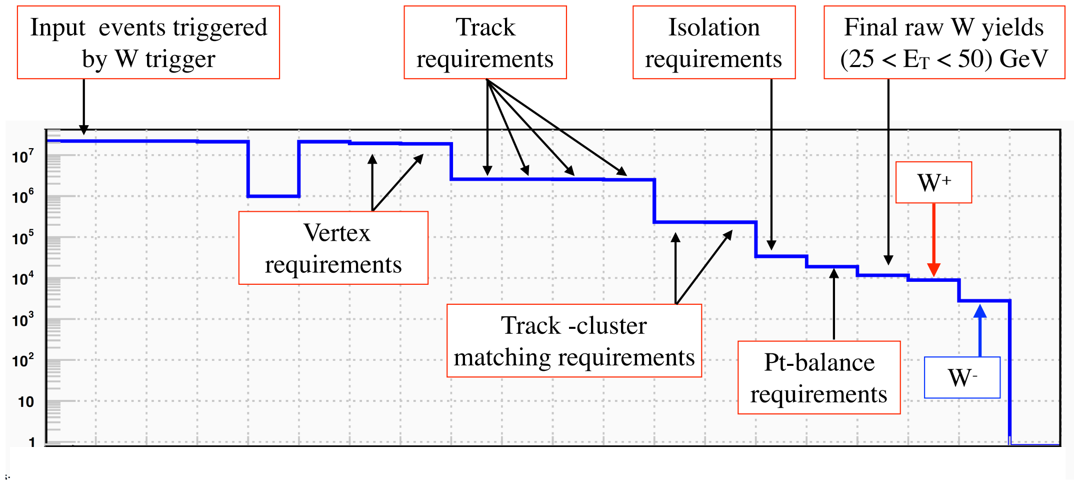

Figure 7.11.: Reduction of statistics in each step of W reconstruction algorithm

trons and positrons is a critical aspect in this analysis. Any contamination of the wrong charge sign due to the mis-identification can directly affect the final asymmetry results of W^+ and W^-, since they have opposite signs. The resulting charge separation of the final raw W yields is shown in Figure 7.12 (b) along with the respective charge sign separation of associated global tracks in Figure 7.12 (a). The reconstructed charge, Q (either + or $-$) was multiplied by $1/p_T$ in order to effectively represent the charge sign and was plotted as a function of E_T^e. The primary tracks have a reconstructed vertex associated with them, where as global tracks do not. One can see from the charge sign distribution of global tracks that the inclusion of the vertex position in the primary track reconstruction to has a significant impact on the $1/p_T$ resolution.

In order to avoid any contamination from the wrong charge sign, in particular at overlapping region between separated yields around 0 of $1/p_T$, a cut was placed at $|Q \times E_T^e/p_T| = 0.04$ which excluded all the events in between the charges as shown in Figure 7.13 (a). Since the ratio of E_T^e to p_T of $W^{-(+)}$ decayed electrons (positrons) are approximately equal to one, a clear Gaussian distribution centered around 1 (-1) of $|Q \times E_T^e/p_T|$, can be seen. Another cut was placed at $|Q \times E_T^e/p_T| = 0.08$ by excluding tails in the fitted distribution which can clearly seen from the 1-D distribution of $|Q \times E_T^e/p_T|$ of golden Ws in Figure 7.13 (b). Here, the data are fitted with a double Gaussian shape indicted by the solid red line and the excluded regions are marked by the grey hashed bands. A clear valley between candidate events with opposite charge sign can be seen, thus systematics uncertainties due to any charge sign misidentification were not assigned during the systematic calculation of the asymmetry, which is discussed in Chapter 9.

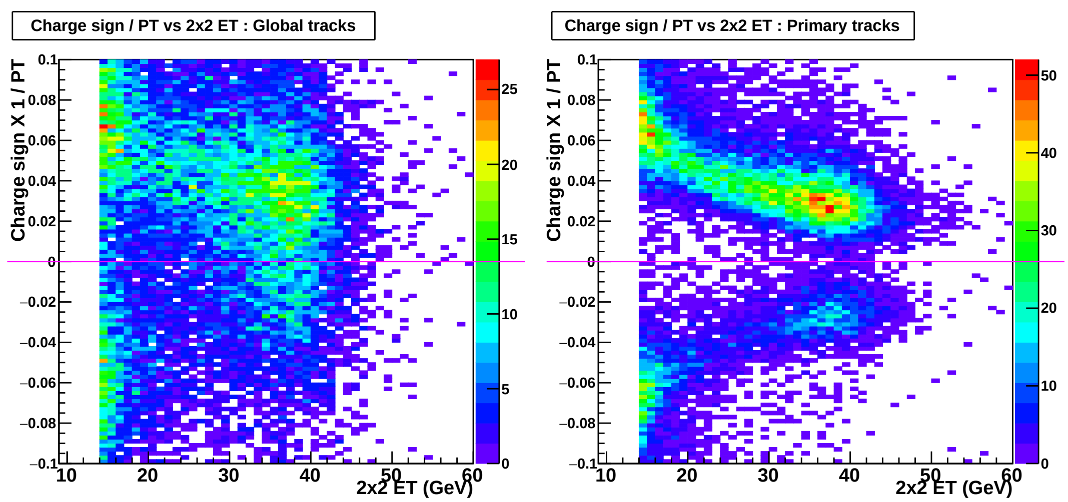

Figure 7.12.: The product of the reconstructed charge sign, Q and $1/p_T$ of final raw W yields as a function of E_T^e for associate global tracks (a), and for primary tracks (b)

7.6 Final charge separated raw W yields

The final charge separated raw W yields, which satisfied all the selection requirements discussed in the previous sections, are shown as a function of E_T^e in Figure 7.14. The characteristic Jacobean peak for the decay $W^{\pm} \to e^{\pm}\nu$ is clearly seen above the remaining backgrounds at $E_T^e \sim M_W/2$. These raw

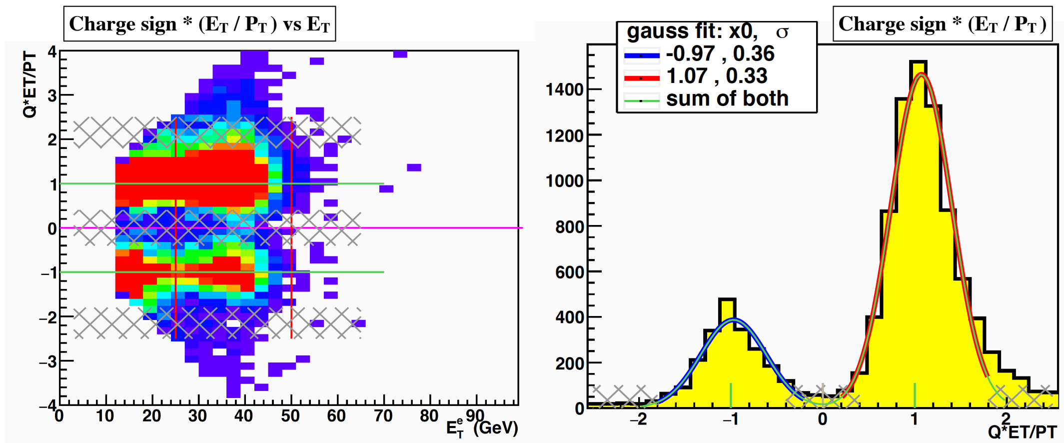

Figure 7.13.: The product of the reconstructed charge sign, Q and E_T/p_T of golden Ws as a function of E_T^e

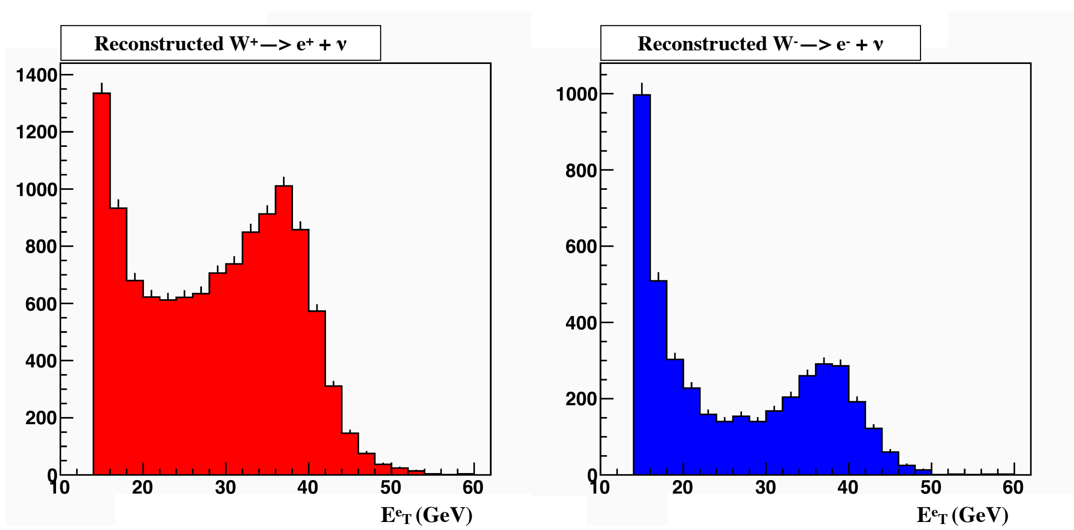

Figure 7.14.: Final charge separated raw W candidate yields as a function of E_T^e which pass all selection cuts: for $W^+ \to e^+ + \nu$ (a) and for $W^- \to e^- + \bar{\nu}$ (b).

yields still contain some residual QCD background events and some electroweak background events. The estimation of those background events is the subject of the next chapter.

7.7 $Z \to e^+ + e^-$ Candidate Event Selection

The reconstruction of the Z boson from its decay products of electrons and positrons follows the same procedure as the W boson discussed above. The trigger selection (Sec. 6.1.1), event selection (Sec. 7.2), and high E_T $e^\pm$ selection (Sec. 7.3) requirements were imposed same as the W reconstruction, thus the Z candidate event selection (separation) begins with the same isolated $e^\pm$ sample from Section 7.3. As shown in Figure 7.1 event topology of a Z candidate event in the calorimeter can be represent by a pair of isolated back-to-back $e^\pm$ candidates tracks, with opposite charge sign.

7.7.1 Z event selection requirements

Since, e^+ and e^- decayed from a Z boson should corresponds to two isolated tracks in the TPC which originated from the same vertex, only the events with two or more tracks originated from the same vertex were considered. Any events in the isolated sample from section 7.3, with primary vertices which associate with single tracks were excluded. The decay e^+ and e^- from Z events nearly travel in opposite direction in azimuth. Therefore, for each matched isolated EMC cluster, a corresponding matched second isolated EMC cluster must exist in the opposite direction in azimuth. Thus, any event which does not satisfy this requirement was removed. In addition, several other cuts such as a cut which demanded a minimum requirement for the separation between two tracks in ϕ space in order to ensure that the corresponding e^+ and the e^- fired back-to-back as required by the momentum conservation were imposed. Finally, the charge sign of each of the pair of isolated tracks was determined and only the events with opposite charge signs for the two tracks were considered. During this process remaining QCD backgrounds in the isolated $e^{\pm}$ sample from section 7.3 were removed. Figure 7.15 shows the progression of the cuts in terms of the reduction of statistics similar to the case of W event selection which was shown in Figure 7.11. By considering the final output events, in 2013 RHIC running, approximately 300 Z bosons were produced.

The invariant mass distribution of the Z candidates was reconstructed and is shown in Figure 7.16 in comparison to the reconstructed invariant mass distribution of simulated $Z/\gamma \rightarrow e^{+} + e^{-}$ MC events. A clear signal peak at

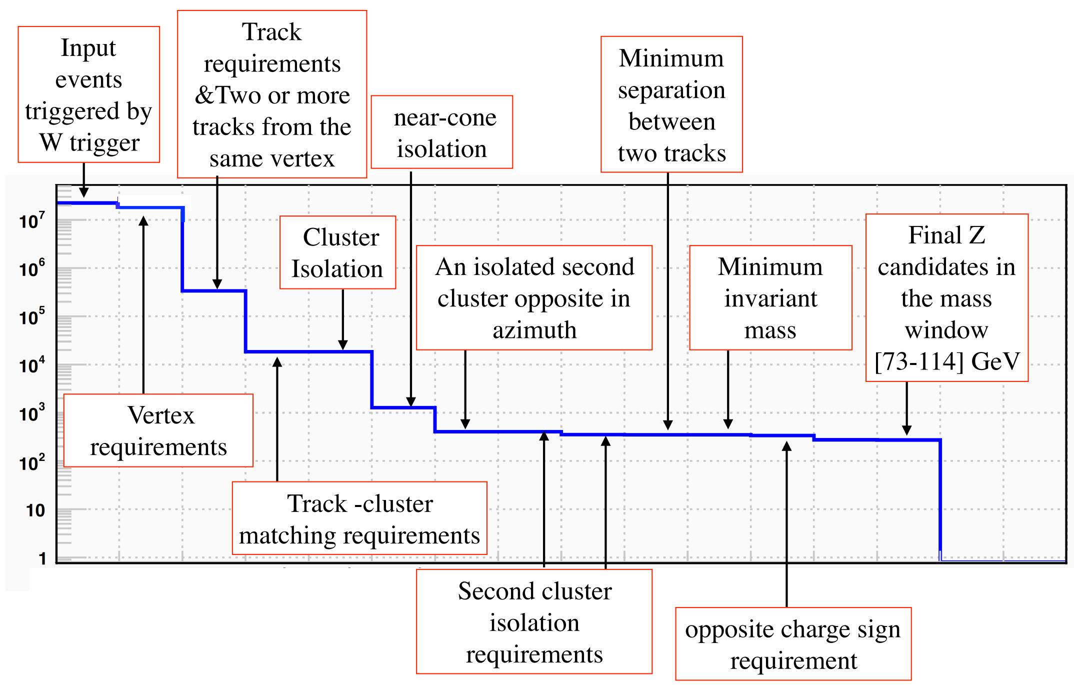

Figure 7.15.: Reduction of statistics in each step of Z event reconstruction

$m_{e^+e^-} \sim M_Z$ can be observed, which is consistent with the MC. In addition,

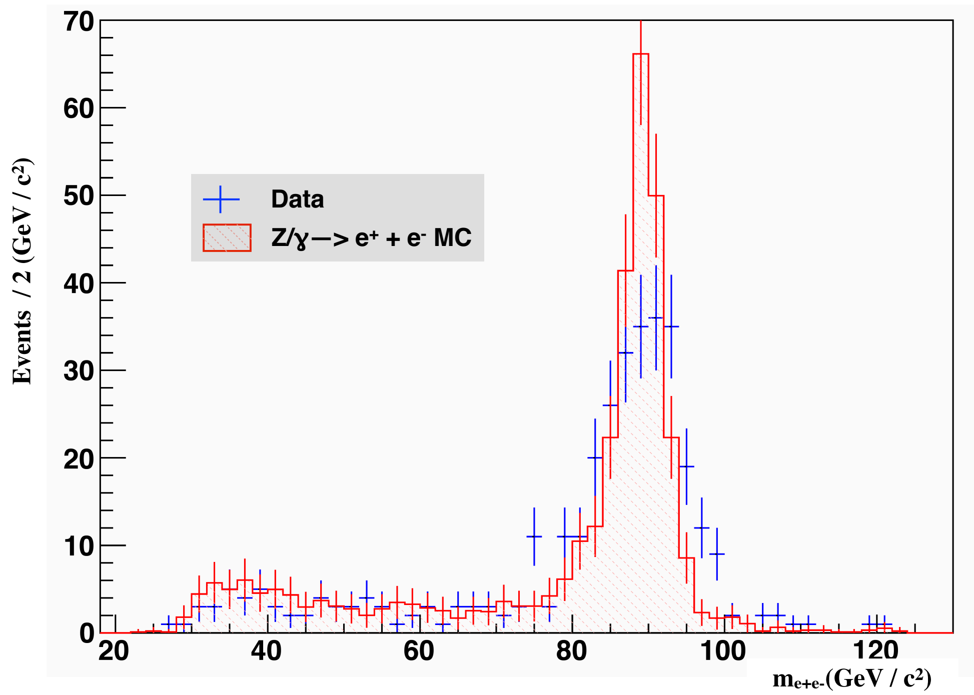

Figure 7.16.: Invariant mass distribution of the final Z candidate events in comparison to $Z/\gamma \rightarrow e^+ + e^-$ MC events

there is a indication of a small signal at lower invariant mass which is likely a result of lower mass Drell-Yan pairs [1].

[1] Similar to the Z boson production which occur due to the annihilation of a quark and a antiquark from the two protons a virtual photon also can be produced which decay into a e^+ and e^- same as the Z boson. But the reconstructed invariant mass of such process is evidently smaller than the invariant mass of the process of a Z boson production.

CHAPTER 8
BACKGROUND STUDY

This chapter describe the details of the estimation of any remaining background events from the final raw W yields that were obtained in Sec. 7.6 in the previous chapter. The W selection algorithm was well designed to select W candidate events while eliminating high multiplicity QCD di-jet / multi-jet type background events and $Z/\gamma \rightarrow e^{+} + e^{-}$ background events. However, due to the non-hermetic nature of the STAR detector, certain fraction of QCD jet type background and Z[1] background events pass the cuts that were used in the W selection algorithm. Two procedures, known as "Second EEMC" and "Data-driven QCD", were used to estimate the QCD jet type background contribution. These are discussed in Sec. 8.2.1 and Sec.8.2.2 respectively.

A certain amount of Z background events and events that correspond to the tau decay mode of W bosons, $W^{\pm} \rightarrow \tau\nu$, are indistinguishable in the final raw W yields. Therefore, these background components were estimated using embedded MC samples of $Z/\gamma \rightarrow e^{+} + e^{-}$ and $W^{\pm} \rightarrow \tau\nu$ respectively that are described in Sec. 6.2.1. The details of the estimation of these background events are discussed in Sec. 8.1. In Sec. 8.3, a comparison between the data and MC simulation is discussed. Finally, the calculation of the systematic uncertainty of the background estimation procedure is discussed in Sec. 8.4.

The final result of this dissertation, the W single-spin asymmetry, is calculated separately for W^{+} and W^{-} as a function of the electron pseudorapidity, η_e, in 4 STAR pseudorapidity bins. Therefore, the residual background contributions are well estimated separately for W^{+} and W^{-} in each STAR-η bin as illustrated

[1] Z background always refers to the $Z/\gamma \rightarrow e^{+} + e^{-}$ background events

in Figure 8.1. The η bins are indexed from 1 to 4 starting from η = -1.1 to η = +1.1, each with bin width of 0.5. The distributions of various background

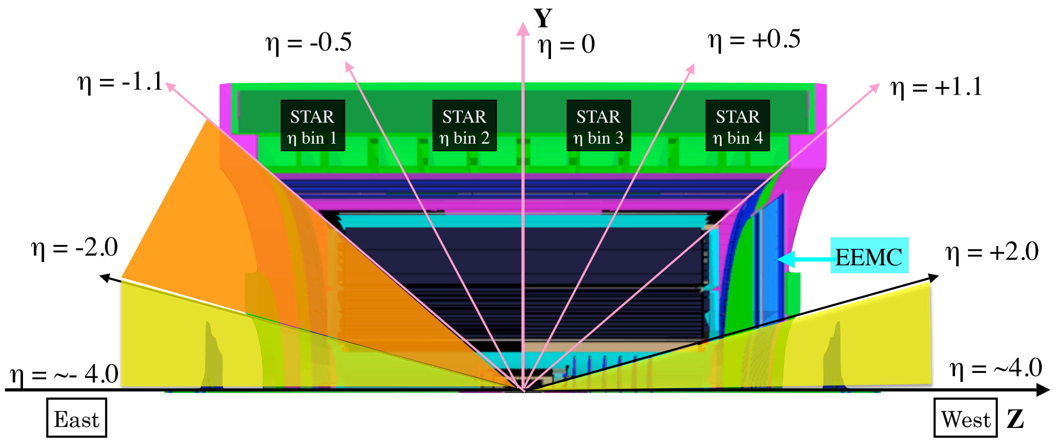

Figure 8.1.: η ranges of four STAR η bins and η ranges where no calorimeter coverage exists: -2< η <-1.1 (orange), $|\eta| > 2$ (yellow)

components that are estimated in this chapter are shown separately for the two analysis periods, I and II. However, combined distributions of the two periods are shown towards the end of the chapter.

8.1 Estimation of Electroweak Background Component

Electroweak background refers to the processes that follows the weak interaction similar to that of W boson production. This includes Z boson production and other decay modes of W other than $e^{\pm}$. In this analysis, two types of electroweak background components, $W^{\pm} \rightarrow \tau^{\pm}\nu$ and $Z \rightarrow e^{+} + e^{-}$ were estimated.

8.1.1 $W^{\pm} \rightarrow \tau^{\pm}\nu$ background

The main decay modes of the W^+ boson[1] are shown in table 8.1. The W signal that we are interested in is the decay mode of the W boson to an $e^{+,(-)}$ and an electron neutrino (anti-electron neutrino) $\nu_e(\bar{\nu_e})$ with a branching ratio of 10.75%. The W decay mode to hadrons is likely indistinguishable from the QCD jet type background stream and is excluded during the W selection process. The W decaying to a muon lepton (μ) and a muon neutrino (ν_μ) does not contribute to our data sample because muons penetrate through our calorimeters. However, the decay of the W to a tau lepton (τ) and a tau neutrino (ν_τ) with a branching ratio of 11.25 % can create a background. The τ can decay to an e^-, ν_e, and a ν_τ with a branching ratio of 17.39% [116] contributing as a background to the signal spectra. This secondary decay of W to e via tau lepton contains, an e, and three

Decay mode	**Branching Ratio**
$e^+ + \nu$	10.75 %
$\mu + \nu_\mu$	10.57 %
$\tau^+ + \nu_\tau$	11.25 %
hadrons	67.60 %
invisible	1.4 %

Table 8.1.: Some decay channels and branching fractions of the W boson

neutrons (ν_e, $\bar{\nu}_\tau$, and ν_τ) in the final state, where all neutrinos escape detection leaving only the electron to be detected. These type of secondary electrons from $W \rightarrow \tau\nu$ are subsequently reconstructed as isolated candidate electrons with a large missing energy in the calorimeter opposite in azimuth, making it effectively indistinguishable from a $W \rightarrow e + \nu$ signal. However, the isolated E_T of such a secondary $e^{\pm}$, is rather low on average in comparison to the isolated E_T of the

[1] The W^- have the same decay modes of charge conjugate with same branching ratios.

primary $e^{\pm}$ from the signal, because it shares the energy with three neutrinos in the final state. As a result, background contribution from W to τ decay is largest at low E_T^e and is rather small at the maximum of the Jacobian peak.

As mentioned before, these background events from $W \to \tau\nu$ were estimated using the $W \to \tau\nu$ MC sample. Secondary $e^{\pm}$ in the MC sample were reconstructed using the same W selection algorithm and were used as the $W \to \tau\nu$ background contribution to the W signal spectra. Figures 8.2 and 8.3 show the estimated $W \to \tau\nu$ background contribution to W^+ and W^- in 4 STAR-η bins for periods I and II respectively.

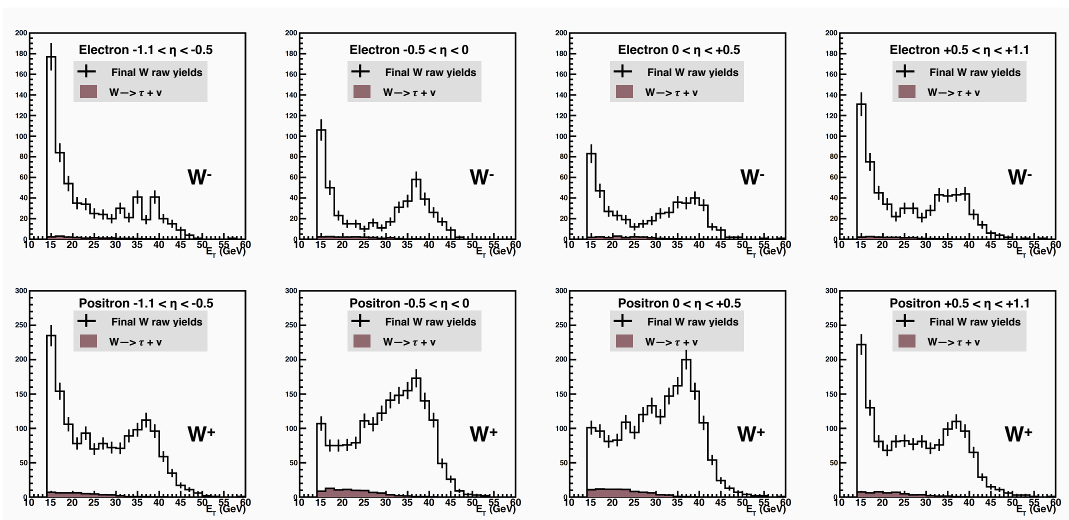

Figure 8.2.: Estimated $W \to \tau + \nu$ background contributions (brown) plotted along with final raw W candidate yields for W^+ and W^- in each STAR η bins for period I analysis.

8.1.2 $Z \to e^+ + e^-$ background

The decay electrons and positrons from Z bosons can be a background to the $W \to e\nu$ signal. The majority of these background events are removed dur-

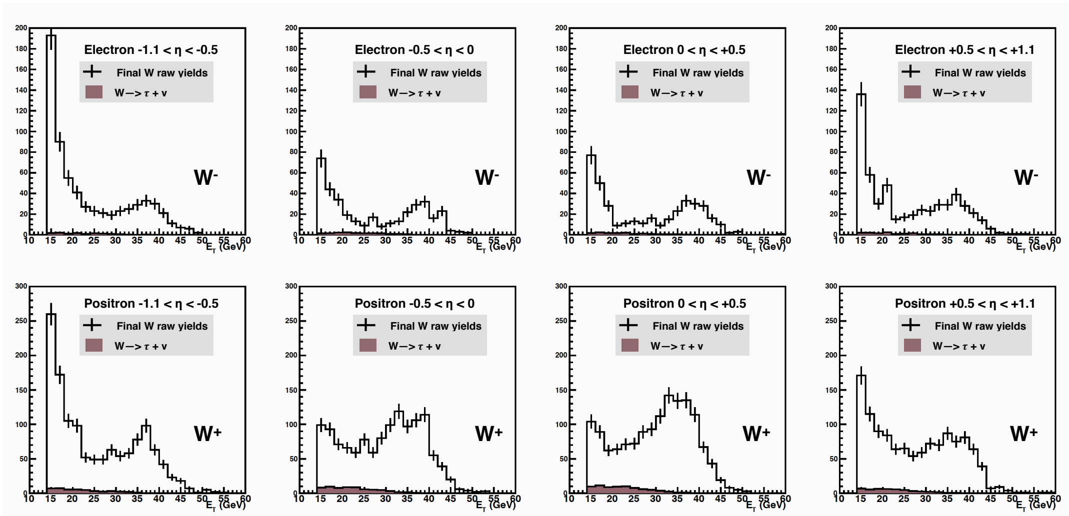

Figure 8.3.: Estimated $W \to \tau + \nu$ background contributions (brown) plotted along with final raw W candidate yields for W^+ and W^- in each STAR η bins for period II analysis.

ing the W selection algorithm as discussed in Sec. 7.4 due to the topological differences between the two types of processes. However, a number of Z decay events are inseparable from W signal events when either, decay $e^{+,-}$, is undetected while transversing through an non-acceptance region in the detector. In addition, certain amount of Z background events remain in the W signal either due to detector inefficiencies or inefficiencies in the cuts that were used to remove those events. In order to estimate the Z background contribution, an embedded MC sample of $Z \to e^+ + e^-$ was used. The $e^\pm$ from the Z decay events were reconstructed in the MC sample using the same W selection algorithm and were taken as the Z background contribution to the W signal. Figures 8.4 and 8.5 show the estimated Z background contribution to W^+ and W^- in 4 STAR-η bins for period I and period II respectively.

In comparison to other types of background contributions, the Z background contribution to the W signal is extremely small. This is partially caused by

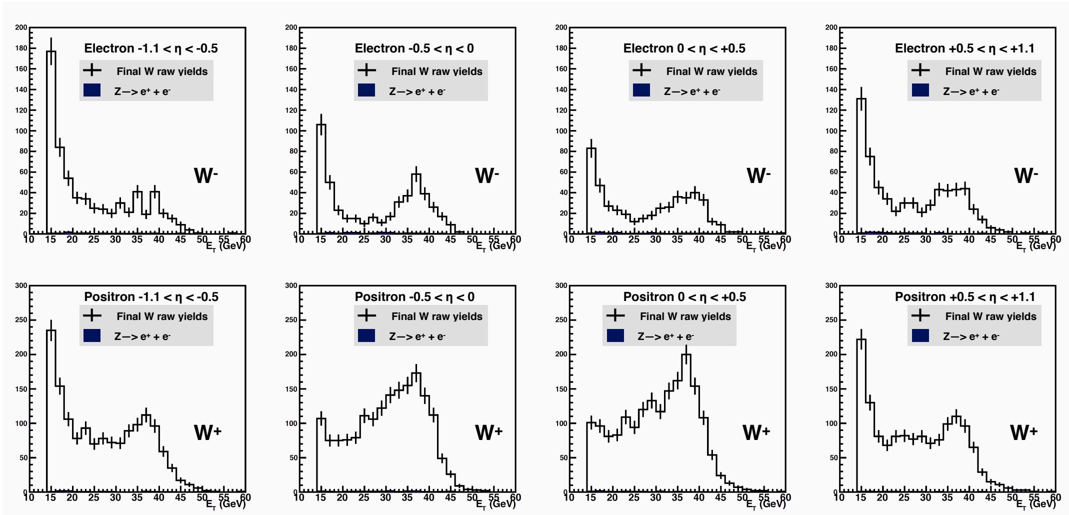

Figure 8.4.: Estimated $Z \rightarrow e^+ + e^-$ background contributions (dark blue) plotted along with final raw W candidate yields for W^+ and W^- in each STAR η bins of period I analysis.

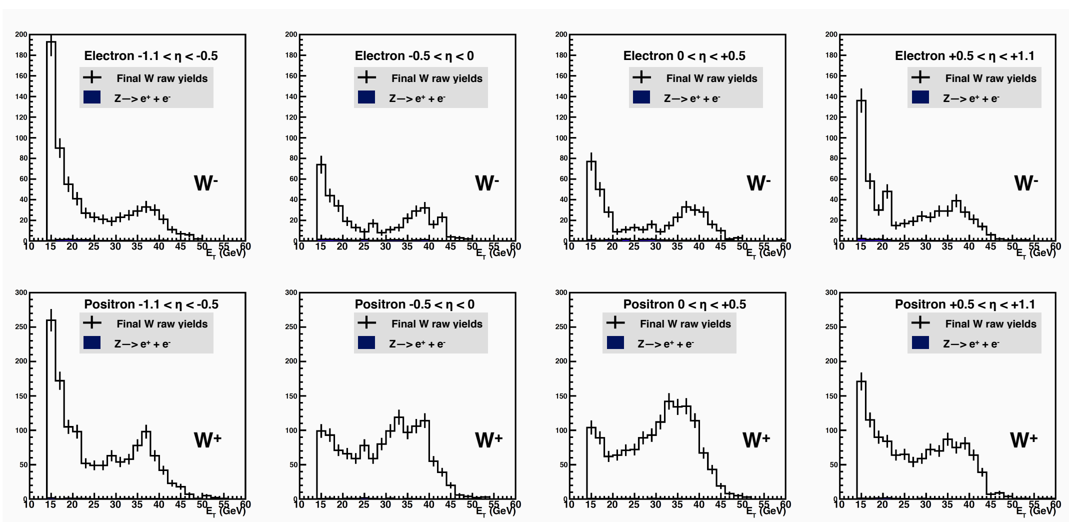

Figure 8.5.: Estimated $Z \rightarrow e^+ + e^-$ background contributions (dark blue) plotted along with final raw W candidate yields for W^+ and W^- in each STAR η bins of period II analysis.

the relatively small Z boson production cross section in the kinematic range available at RHIC [105]. However, it must also be noted that roughly about half of the total Z background events in the W signal were estimated here and the rest of the Z background events were estimated as a part of the second EEMC background estimation process which discussed in Sec. 8.2.1. Unlike the other background distributions, the Z background distribution is approximately constant as a function of E_T^e.

8.2 QCD type Background Estimation

The TPC of the STAR detector has no coverage in $|\eta| > 1.3$ and the calorimeter system has no coverage in $-2 < \eta < -1.1$ and $|\eta| > 2$. Thus, any di-jet type QCD background event (or Z decay event) where one jet / jet fragment (or either $e^{+,-}$) falls into the η region specified above is highly likely to pass the final W candidate selection cut, the sign-p_T balance. In order to remove these background events two procedures were implemented. The orange (yellow) shaded region in Fig. 8.1 represents the η range $-2 < \eta < -1.1$ ($|\eta| > 2$) of non-existence calorimeter coverage in STAR which subsequently give rise to the contamination of QCD background in the W signal and are thus being estimated using the second EEMC (Data-driven QCD) background procedure.

Both of these procedures were designed primarily to remove the QCD di-jet type background events that were accepted due to the existence of non-acceptance regions in the STAR detector. Alternatively, a single data-driven QCD method could have been used to estimate all the backgrounds. However, since the EEMC does exist on the west side (but not in the east side) of the STAR and had been used to reject backgrounds during the W selection process, the second EEMC method was designed to estimate background events that should have been rejected by a second fictitious EEMC in the east side of the STAR.

8.2.1 Second EEMC Background

The STAR EEMC provides full azimuthal coverage for the pseudorapidity region of $1.09 < \eta < 2.0$. In the W selection algorithm, EEMC was utilized to remove QCD di-jet type background events when the jet opposite in azimuthal (ϕ) space of a candidate $e^{\pm}$ that is from a di-jet event deposits a significant amount of energy in the EEMC towers. The use of EEMC during the near-cone isolation and sign-p_T balance reconstruction is discussed in sections 7.3.3 and 7.4.1. There is, however, no EEMC on the East side of the STAR detector. Thus, any background $e^{\pm}$ candidate event which belongs to a QCD di-jet type event which has an opposite side jet in the range $-2 < \eta < -1.09$ would satisfy the final $W \to e\nu$ requirement. This is due to the opposite-side jet escaping detection, leading to a large p_T-balance vector. In addition, this also affects the near-cone isolation since the EEMC towers are included in the cone used in near-cone isolation. If this cone overlaps with the missing east side EEMC acceptance, QCD background events may satisfy the W isolation requirement.

To elaborate on this let's consider an example of two types of di-jet background events in STAR η-bin 4 as shown in Figure 8.6 (b). The reconstruction of "jet A" in the STAR η-bin 4 indicates that its near-cone overlaps with the EEMC towers in the west side of STAR. Since the EEMC exist in the west side of STAR, the near cone isolation method works well and the corresponding $e^{\pm}$ candidate of the "jet A" will be removed during the near cone isolation. Now let's consider "jet B" where jets A and B can be reconstructed together as a forward-forward[1] di-jet event. During the p_T balance requirement the away-side jet p_T of the candidate $e^{\pm}$ of jet A is calculated. This di-jet background event will be removed as a result of the small p_T imbalance since jet B can be detected and reconstructed in the west EEMC. However, in the case of a back-to-back di-jet event in η-bin 4 the situation is different. Jet C and jet A can be considered as

[1] A di-jet event where both the jets are detected in the forward region.

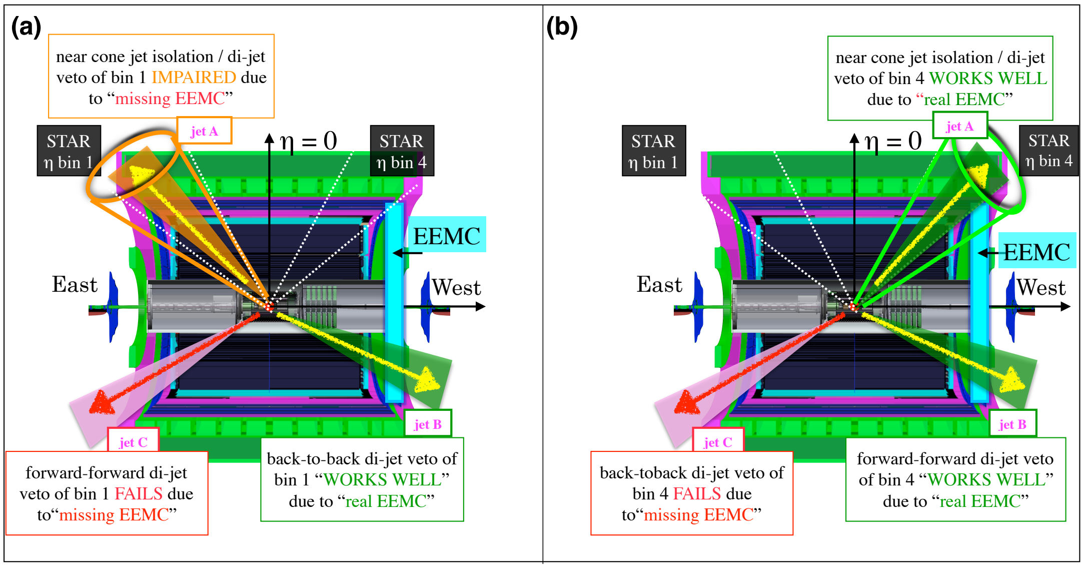

Figure 8.6.: Illustration of the estimation of second EEMC background: forward-forward (jet A - jet C) and back-to-back (jet A - jet B) di-jet events in STAR-η bin 1 (a), forward-forward (jet A - jet B) and back-to-back (jet A - jet C) di-jet events in STAR-η bin 4 (b).

two corresponding jets of a back-to-back QCD di-jet event. Since jet C cannot be reconstructed due to the missing EEMC in the east side of STAR this di-jet background event is highly likely to pass the final W selection requirement as a result of a large reconstructed p_T imbalance similar to a $W \to e\nu$ event. The corresponding two situations in the STAR η-bin 1, as shown in Figure 8.6 (a), are similar but mirror reflected. The forward-forward di-jet background event (Jet A-Jet C) in the STAR η-bin 1 will be accepted during the W selection while the back-to-back to di-jet background event (Jet A-Jet B) will be removed. In addition, the near-cone isolation of jet A in the STAR η-bin 1 is impaired since the cone partially overlaps with the non-existent EEMC in the east side.

As explained above, since the background acceptance and rejection behaviors between the STAR η-bin 1 and 4 can be considered as mirror reflections of each other, the background events that were rejected by the STAR η-bin 4 were estimated and used as the same amount of background events that should have been rejected by the STAR η-bin 1 (but was accepted due to the missing EEMC in the east side of the STAR) and vice versa. Similarly, the STAR η-bins 2 and 3 are considered as mirror reflected η-bins and therefore the same procedure was implemented when estimating the background events. However, this assumption can be considered as reasonable only if the detector acceptance conditions between the mirror η-bins in BEMC are either identical or nearly equal. In particular, during the period II data taking, asymmetric detector conditions were observed due to a missing module of the BEMC on the east side, thus between mirror η bins. In order to take these asymmetric detector conditions into effect the estimated background contributions were luminosity weighted based on the luminosity of an unbiased QCD yield sample of each η bin.

The amount of rejected background events from the real west EEMC in each STAR η-bins was estimated by repeating the W selection algorithm but with the EEMC towers excluded from the isolation ratio, $E_T^e\ /E_T^{\Delta R<0.7}$, and from the reconstruction of p_T jet sum, $\vec{p}_T^{\,jets}$ in the $\vec{p}_T^{\,balance}$. The difference between the final W yields as a function of E_T^e from these two passes, with and without EEMC, was a direct measurement of background events that were rejected by the real EEMC and therefore, the second EEMC background component. The estimated background events in each STAR η bin, denoted as "second EEMC", is shown in comparison to the final raw W yields for W^+ and W^- in Fig. 8.7 and Fig. 8.8 for period I and period II respectively.

As mentioned in Sec. 8.1.2, not only the QCD di-jet type background events, but also a number of Z decay background events, corresponding $e^{+,-}$ opposite in ϕ of a candidate $e^{+,-}$ track that falls in the second EEMC region, were also counted and estimated as second EEMC background during this process. However, the Z backgrounds were separately estimated using a $Z \rightarrow e^+ + e^-$ MC sample as explained in Sec. 8.1.2. In order to avoid double counting of the es-

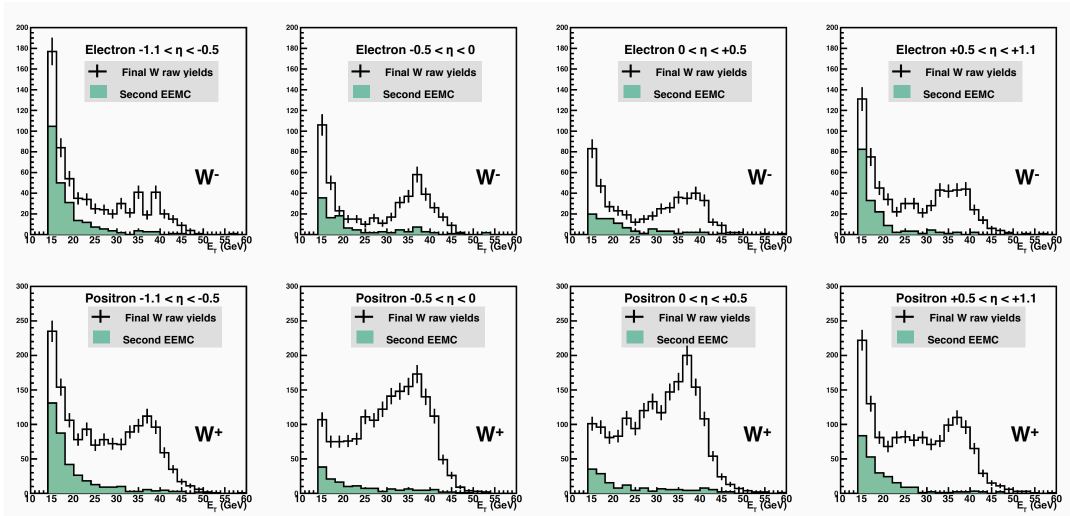

Figure 8.7.: Estimated second EEMC background contributions (green) plotted along with final raw W candidate yields for W^+ and W^- in each STAR η bins for period I analysis.

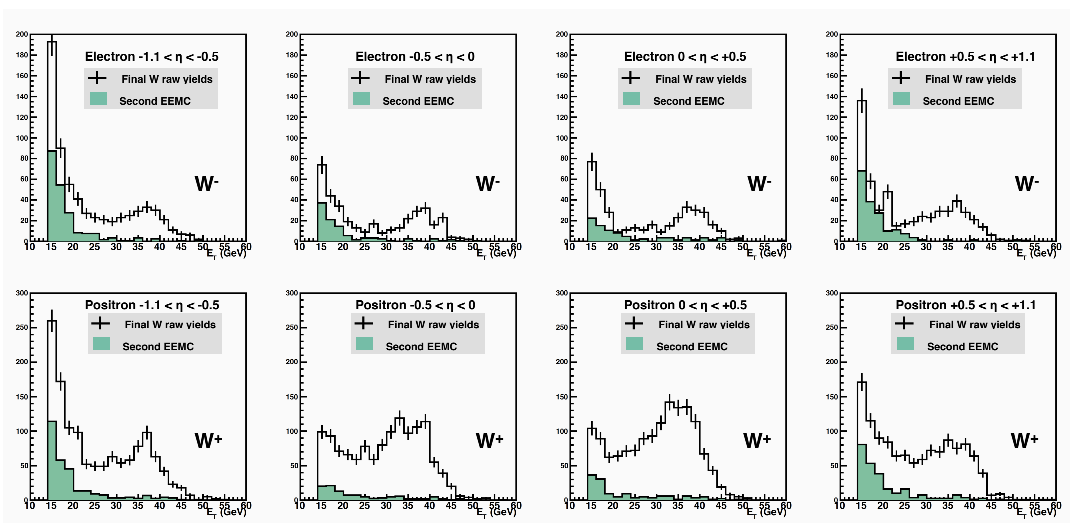

Figure 8.8.: Estimated second EEMC background contributions (green) plotted along with final raw W candidate yields for W^+ and W^- in each STAR η bins for period II analysis.

timation of Z background events which belong to the second EEMC region, the portion of Z background contribution in the total second EEMC background were estimated and subtracted during the Sec. 8.1.2.

8.2.2 Data-driven Background

This section describes the data-driven method that was used to estimate the QCD di-jet type background events that were accepted during the W selection algorithm when one of the jets or a jet fragment of di-jet events escape detection in the pseudorapidity range of $|\eta| > 2$. The contribution of these remaining background events were estimated by determining a data-driven QCD background distribution shape as a function of E_T^e. This was obtained by normalizing an E_T^e distribution of a QCD multi-jet sample to the E_T^e distribution of the final raw W yields.

A sample of events that passed all the W selection cuts imposed by the W selection algorithm, but failed the sign-p_T balance cut, described in Sec. 7.4 were considered for the QCD multi-jet sample. This sample is dominated by QCD multi-jet background events where one jet echos a candidate $e^{\pm}$ but the event was rejected due to the reconstructed jet opposite in the azimuth. However, this sample also contains a small contribution of $Z \rightarrow e^{+} + e^{-}$ decay events since those events also fail the sign-p_T balance cut. Since the purpose of the data-driven procedure is to estimate the QCD type background component (and the Z background component has been estimated) the respective Z contamination must be removed in order to have the sample largely consisting of only QCD type events. The process of excluding the Z decay events is described in Sec. 8.2.3. After removing the Z background events, the distribution (in E_T^e) of the QCD sample (lets's call this "QCD$_{sample}$" distribution) must be normalized to the final raw W yields in order to obtain the data-driven QCD background shape.

In order to accomplish this, the E_T^e distribution of the final raw W yields, after subtracting all other types of background discussed in Sec. 8.1 and 8.2.1, was considered. This sample primarily consists of W signal and the residual QCD background events in the data, where the QCD background events mostly dominate at low E_T^e while the W signal events dominate at high E_T^e (lets's call this "signal$_{Raw}$" distribution). Ideally, the normalization of the data-driven background shape would be performed in an E_T^e region where no W signal is present so that the background shape would be normalized to the pure background. However, even in the lowest possible E_T^e window of the signal$_{Raw}$ distribution a certain amount of W signal events can be presented. Therefore, in order to remove these W signal events a $W^{\pm} \to e^{\pm}$ MC sample was used (let's call this "signal$_{MC}$" distribution). The normalization was achieved as follows. First, the reconstructed W signal events of the signal$_{MC}$ distribution in the E_T^e window of 14 to 18 GeV, N$_{signalMC}$ were subtracted from the yields of the signal$_{Raw}$ distribution in the same E_T^e window, N$_{signalRaw}$. This step removes any remaining W signal events in the signal$_{Raw}$ distribution. Next, a normalization constant, "norm", was defined by dividing the magnitude of the yields of the resulting signal$_{Raw}$ distribution, by the magnitude of the yields of the QCD$_{sample}$ distribution, N$_{QCD}$, in the same E_T^e window. This is shown in the formula in Equation 8.1.

$$norm\ [14 < E_T^e < 18] = \frac{N_{signalRaw} - N_{signalMC}}{N_{QCD}} \tag{8.1}$$

Finally, the normalized data-driven QCD background shape was obtained by scaling the QCD$_{sample}$ distribution with the normalization constants calculated above. Figure 8.9 shows the three distributions of QCD$_{sample}$, signal$_{Raw}$, and signal$_{MC}$ which were used to obtain the data-driven background shape along with the resulting nominal data-driven background shape of W^+ in period I. The yellow shaded region represents the E_T^e range which was used for the nominal normalization window. The estimated data-driven background contribution in each STAR η bin, denoted as "Data-driven", is shown in comparison to the final raw W yields of W^+ and W^- in Figure 8.10 and Figure 8.11 for period I and period II respectively.

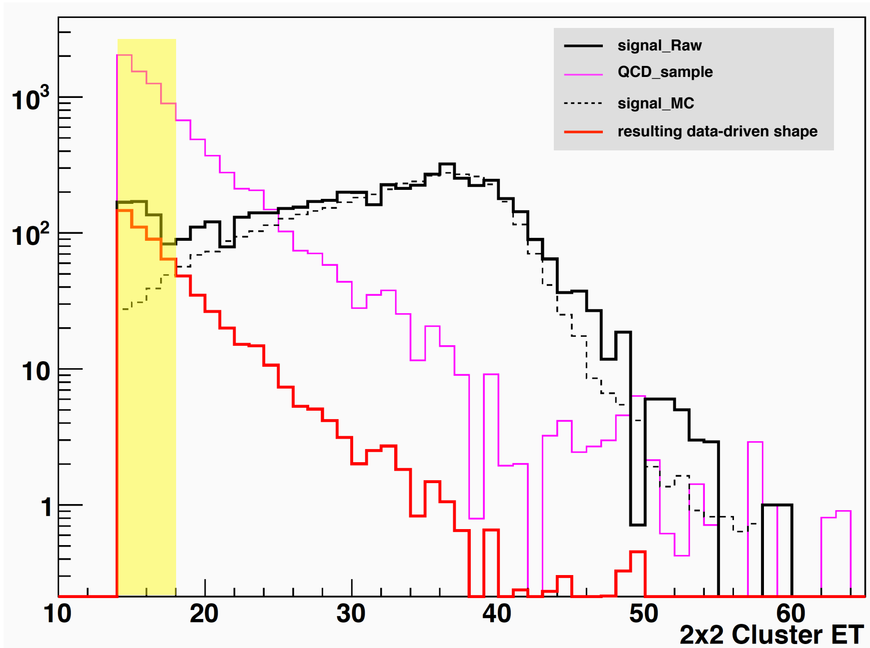

Figure 8.9.: Three distributions, signal$_{Raw}$, QCD$_{sample}$, and signal$_{MC}$ described in the text which used to obtain the data-driven shape and the resulting data-driven shape for W^+ in period I.

8.2.3 Removing $Z \to e^+ + e^-$ events from the QCD sample

The process of removing the $Z \to e^+ + e^-$ events in the QCD background sample was achieved by first identifying potential Z type events in the sample and then simply subtracting them off from it. In order to identify $Z \to e^+ + e^-$ events in the QCD background sample mentioned in Sec. 8.2.2 several additional requirements were imposed in addition to the cuts discussed in the W selection algorithm. This was achieved in two steps. First, events that have an isolated $e^\pm$ candidate and an additional isolated 2×2 cluster inside a matching reconstructed jet in the away-side were tagged. Among, only the events with the ratio of the energy of the isolated cluster inside the jet to the summed p_T of the jet, $E_T^{2\times2}/p_T^{jet}$, above 50 % were considered. Next from these events, events with an invariant mass in the range of 70 GeV/c^2 to 140 GeV/c^2 were tagged as potential Z decay

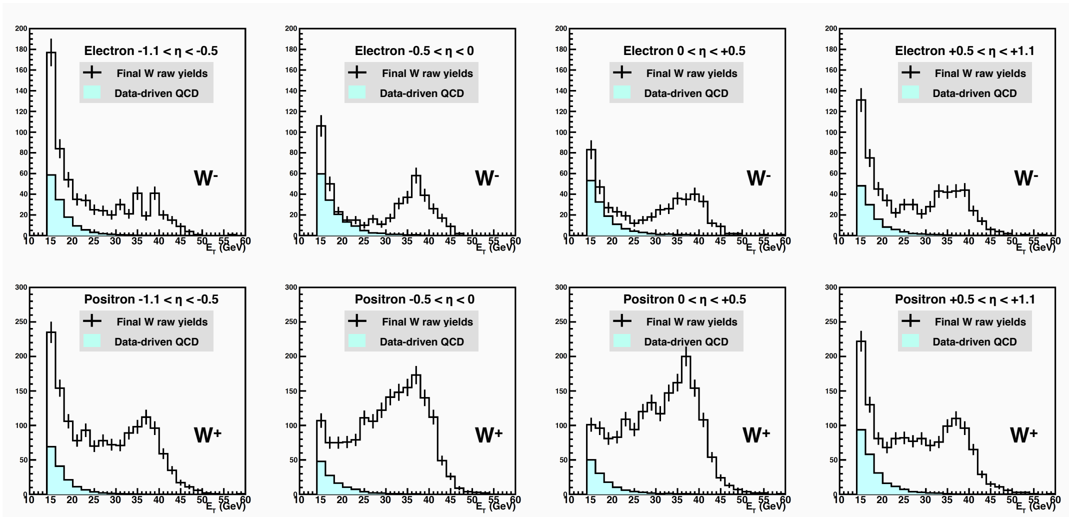

Figure 8.10.: Estimated data-driven background contributions (cyan) plotted along with final raw W candidate yields for W^+ and W^- in each STAR η bins of period I analysis.

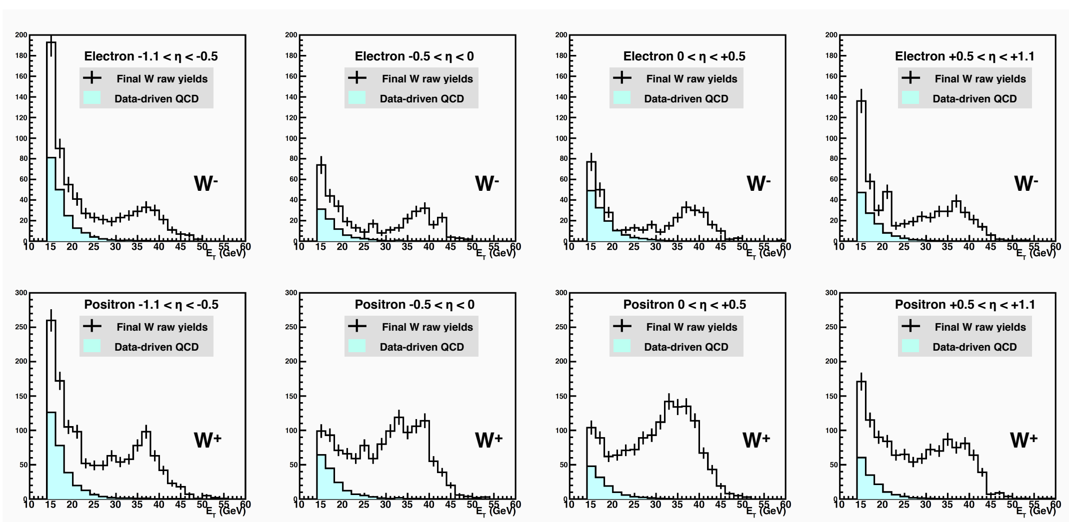

Figure 8.11.: Estimated data-driven background contributions (cyan) plotted along with final raw W candidate yields for W^+ and W^- in each STAR η bins of period II analysis.

events in the QCD sample. In contrast to the Z candidate event selection, where cuts were designed explicitly to select Z signal events, the requirements used to tag Z like events contaminated in this sample were rather loosely placed. Thus, many $Z \rightarrow e^+ + e^-$ like events were removed causing the sample to consist of mostly QCD type events. After removing the tagged Z like events, any remaining Z events in the QCD sample were further removed using the $Z \rightarrow e^+ + e^-$ MC sample by subtracting off the equivalent number of events which fail the sign-p_T balance cut in the Z MC sample.

8.3 Comparison between Data and MC

Figures 8.12 and 8.13 shows the final W signal yield distribution after both the electroweak and QCD background subtraction in comparison to the final raw W yield distribution before any background components are subtracted and the W yield distribution only after the electroweak background components are subtracted. It can clearly be seen that the majority of the subtracted background yields are QCD type, which largely dominate at the lower E_T^e region. Red lines indicate the E_T^e range that was used to calculate the asymmetry discussed in the next chapter.

The final W signal distribution, after subtracting all type of background components was compared to the $W \rightarrow e\nu$ MC signal in order ensure that a satisfactory agreement exists between the data and simulation. If the consistency between the data and simulation is reasonable, this implies that the methods used to estimate background components are efficient and suitable for the analysis. This comparison was done by first stacking the $W \rightarrow e\nu$ MC signal distribution on top of all of the extracted background components from the data, which were also stacked on top of each other. This was then compared to the final raw W yield distribution before substracting any background component that were discussed in the previous sections. Figure 8.14 and 8.15 shows these distributions

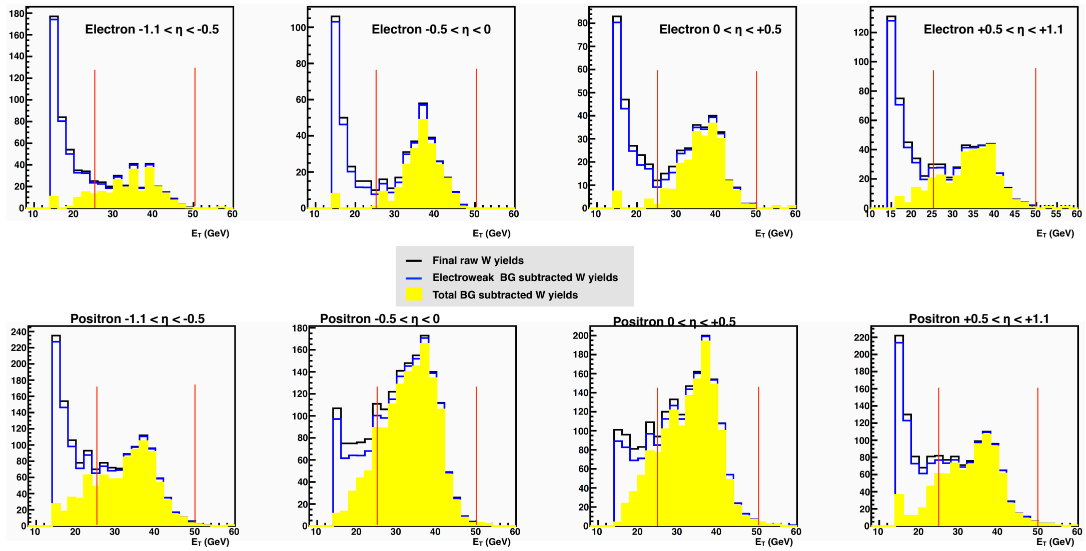

Figure 8.12.: Final W signal yield distribution after subtraction of all types of backgrounds (yellow), in comparison to final raw W yield distribution before subtracting any backgrounds (black), and the W yield distribution only after the Electroweak background subtraction (blue) for W^+ and W^- in each STAR η bins of period I analysis.

separately for W^+ and W^- in the 4 STAR-η bins for the period I and II analysis respectively. The black line represent the data while the red line represents the MC stacked on top of the background components as mentioned above. Respective background distributions are also plotted by stacking them on top of each other. A reasonable agreement was seen for period I, between the data and the simulated MC within the statistical uncertainty of the data. However, a certain discrepancy was observed for mid-rapidity bins (STAR-η bins 2 and 3) in the E_T^e range roughly between 30 to 40 GeV in the period II analysis. Since the agreement was satisfactory for the lower E_T^e range, where the background dominate the conclusion was made that this discrepancy was not caused by the inefficiency in the background estimation process but rather due to the observed relatively lower efficiency in the track reconstruction process. Relatively higher

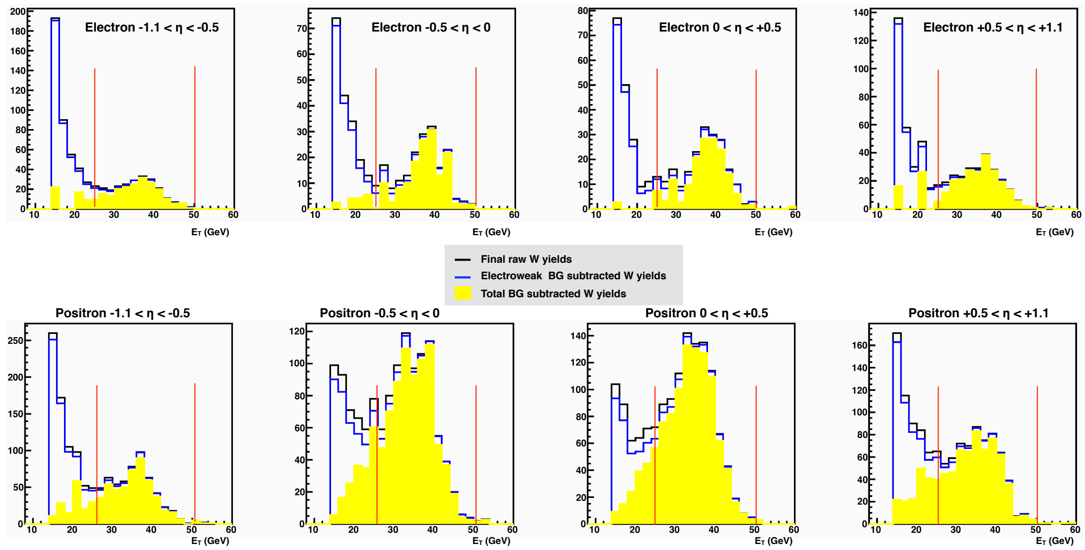

Figure 8.13.: Final W signal yield distribution after subtraction of all types of backgrounds (yellow), in comparison to final raw W yield distribution before subtracting any backgrounds (black), and the W yield distribution only after the Electroweak background subtraction (blue) for W^+ and W^- in each STAR η bins of period II analysis.

ZDC rates (see Fig. 6.5) during period II in comparison to period I, has caused lower track reconstruction efficiency in period II data. However, this does not affect the asymmetry analysis, thus systematics due to this effect were not considered. The background distribution combining period I and II data are shown in Figure 8.16 and Figure 8.17. In the latter, the mid-rapidity STAR-η bins (2, 3) and the forward-rapidity STAR-η bins (1, 2) are combined together.

8.4 Uncertainty of the Background Estimation Process

The systematic uncertainty of the background estimation procedure was quantified into a background dilution factor, β, which is defined as the ratio of signal to signal plus background. This quantity was used when calculating the spin

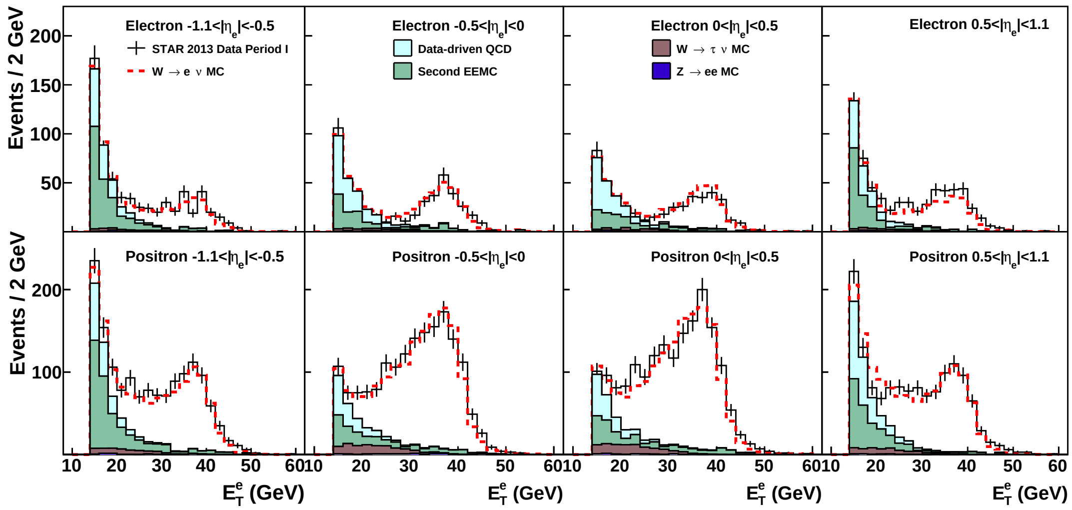

Figure 8.14.: E_T^e distribution of final raw W yields in comparison to $W \rightarrow e\nu$ MC (red) distribution. The various background contributions and $W \rightarrow e\nu$ signal are stacked on top of each other for comparison to the data of period I.

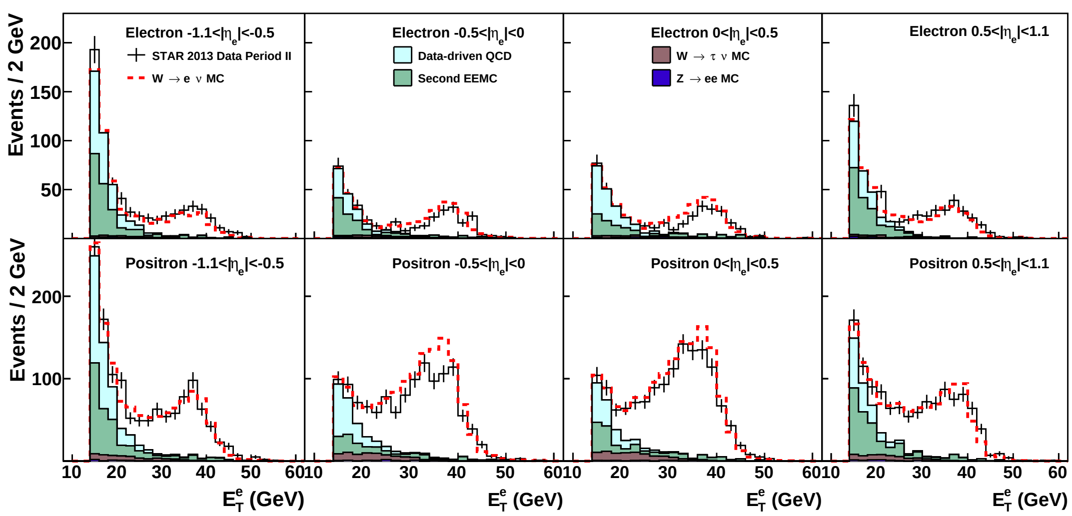

Figure 8.15.: E_T^e distribution of final raw W yields in comparison to $W \rightarrow e\nu$ MC (red) distribution. The various background contributions and $W \rightarrow e\nu$ signal are stacked on top of each other for comparison to the data of period II.

asymmetry and is discussed in detail in Sec. 9.4. The β can be calculated as

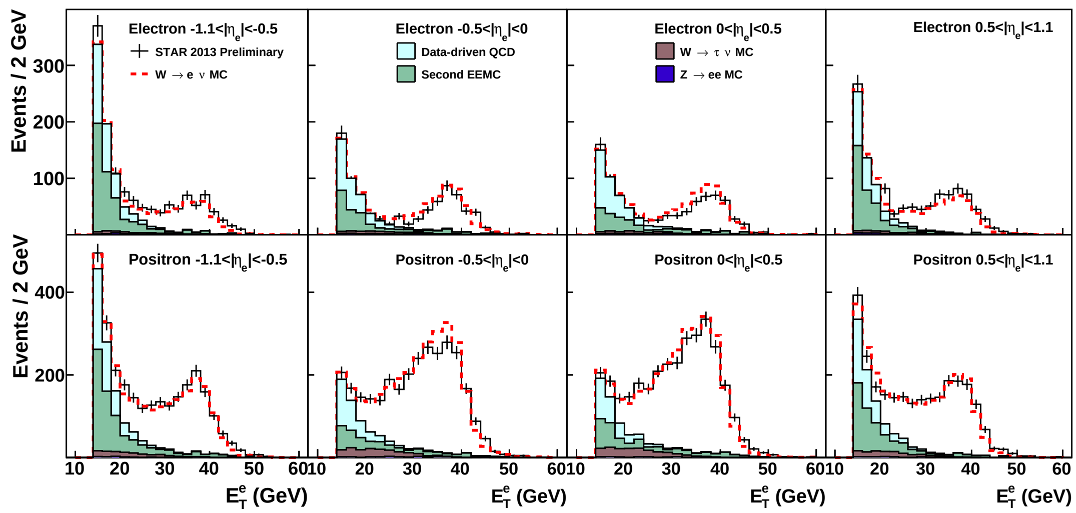

Figure 8.16.: E_T^e distribution of final raw W yields in comparison to $W \rightarrow e\nu$ MC (red) distribution. The various background contributions and $W \rightarrow e\nu$ signal are stacked on top of each other for comparison to the combined data of period I and period II.

shown in equation 8.2,

$$\beta = 1 - f_Z - f_{EEMC} - f_{QCD} \tag{8.2}$$

where f_Z, f_{EEMC}, and f_{QCD} are the fractions of the $Z \rightarrow e^+ + e^-$ background, second EEMC background, and the data-driven QCD background component contained in the final raw W candidate yields respectively. For the W single-spin asymmetry measurements, $W^{\pm} \rightarrow \tau^{\pm} + \nu$ channel is not considered as a background and thus was not included in the calculation of β as well. Each background fraction, f_i, was defined as follows:

$$f_i = \frac{N_i^{BG}}{N^{rawW}} \tag{8.3}$$

where, N_i^{BG} is the respective background yields and N^{rawW} is the final raw W yields in the E_T range of 25 to 50 GeV. The statistical uncertainty, f_i^{stat} of each

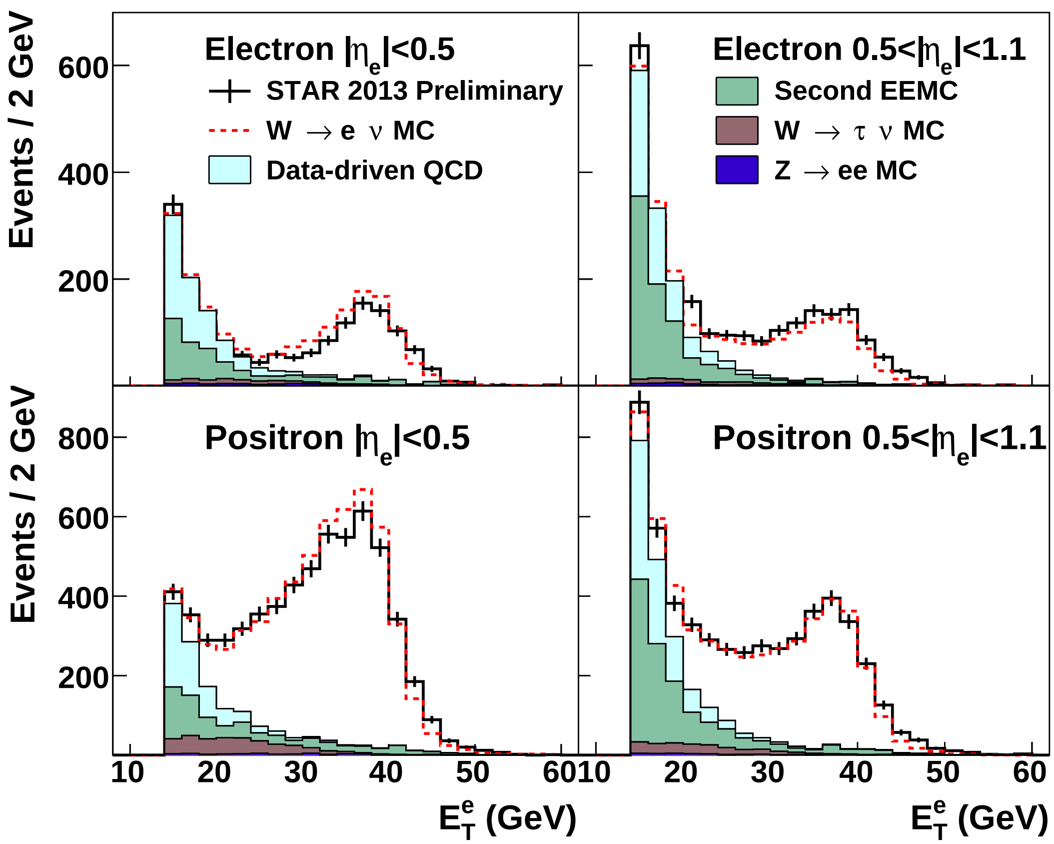

Figure 8.17.: E_T^e distribution of final raw W yields in comparison to $W \to e\nu$ MC (red) distribution. The various background contributions and $W \to e\nu$ signal are stacked on top of each other for comparison to the combined data of period I and period II. Mid-rapidity STAR-η bins (2, 3) and the forward-rapidity bins (1, 2) are combined together.

f_i was estimated using the method of propagation of uncertainty as shown in equation 8.4.

$$f_i^{stat} \approx |f_i| \sqrt{\left(\frac{\sigma_A}{A}\right)^2 + \left(\frac{\sigma_B}{B}\right)^2} \tag{8.4}$$

The total statistical uncertainty, f_{Total}^{stat}, was calculated as the quadrature sum of the each f_i^{stat} and was assigned as the statistical uncertainty of β. Table 8.2 shows the values of each f_i along with its statistical uncertainty f_i^{stat} in 4 STAR-η bins for W^+ and W^- for period I and period II analyses.

Next, the systematic uncertainty of β was calculated by obtaining a distri-

BG type / STAR-η bin	$f_Z \pm f_Z^{stat}$	$f_{EEMC} \pm f_{EEMC}^{stat}$	$f_{QCD} \pm f_{QCD}^{stat}$
Period I	W^-	W^-	W^-
1	0.0193±0.0029	0.0917±0.0194	0.0273±0.0025
2	0.0262±0.0034	0.1045±0.0206	0.0422±0.0039
3	0.022±0.0032	0.0892±0.0193	0.05±0.0045
4	0.0142±0.0022	0.0594±0.0139	0.0271±0.0023
Period I	W^+	W^+	W^+
1	0.0047 ±0.0008	0.0769±0.0103	0.0106±0.0008
2	0.0078±0.0008	0.0409±0.0058	0.0073±0.0006
3	0.0035±0.0005	0.0429±0.0059	0.0095±0.0007
4	0.0038 ±0.0007	0.0397±0.0072	0.0214±0.0015
Period II	W^-	W^-	W^-
1	0.0165±0.0027	0.0749±0.018	0.0422±0.004
2	0.0387±0.0051	0.0954±0.0234	0.0308±0.0035
3	0.0386±0.0049	0.1311±0.0269	0.0396 ±0.0044
4	0.0126±0.0022	0.0557±0.0151	0.021±0.002
Period II	W^+	W^+	W^+
1	0.0083±0.0012	0.0697±0.0113	0.0267 ±0.0021
2	0.006±0.0008	0.0412±0.0071	0.0145±0.0014
3	0.0052±0.0007	0.0414±0.0065	0.0076±0.0007
4	0.0052±0.0008	0.0665±0.0104	0.0101±0.0009

Table 8.2.: Estimated values of background fractions (f_i) and there statistical uncertainties (f_i^{stat}) of W^+ and W^- in the range of $25 < E_T^e < 50$ GeV from period I and period II analysis

bution for f_{QCD}. This process is explained in Sec. 8.4.1 and results in obtaining a range of f_{QCD} values, $f_{QCD}(i)$. Therefore, distributions was obtained for β for W^+ and W^- in each STAR-η bin by varying the f_{QCD} as shown in Eq. 8.2, and the mean value of each distribution was assigned as the nominal β value for the respective charge in each respective STAR-η.The RMS of the distribution was assigned as the systematic uncertainty, f^{syst}, of β and the total uncertainty of β, β_{sys}, was calculated as the quadrature sum of the statistical uncertainty, f^{stat}_{Total}, and the systematic uncertainty, f^{syst}. The distributions of β for W^+ and W^- in 4 STAR-η bins for the period I and period II analysis are shown in Figures 8.18 and 8.19 respectively. The values of each calculated β, along with total uncertainty,

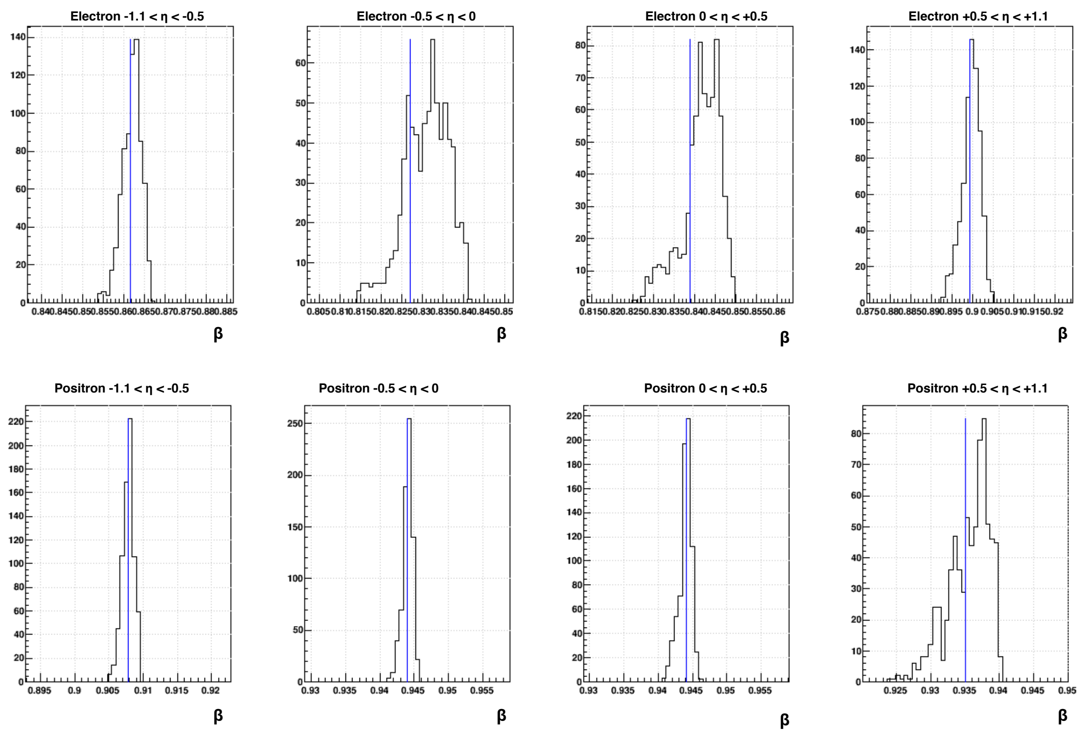

Figure 8.18.: β distribution of W^+ and W^- in period I.

is tabulated in table 8.3

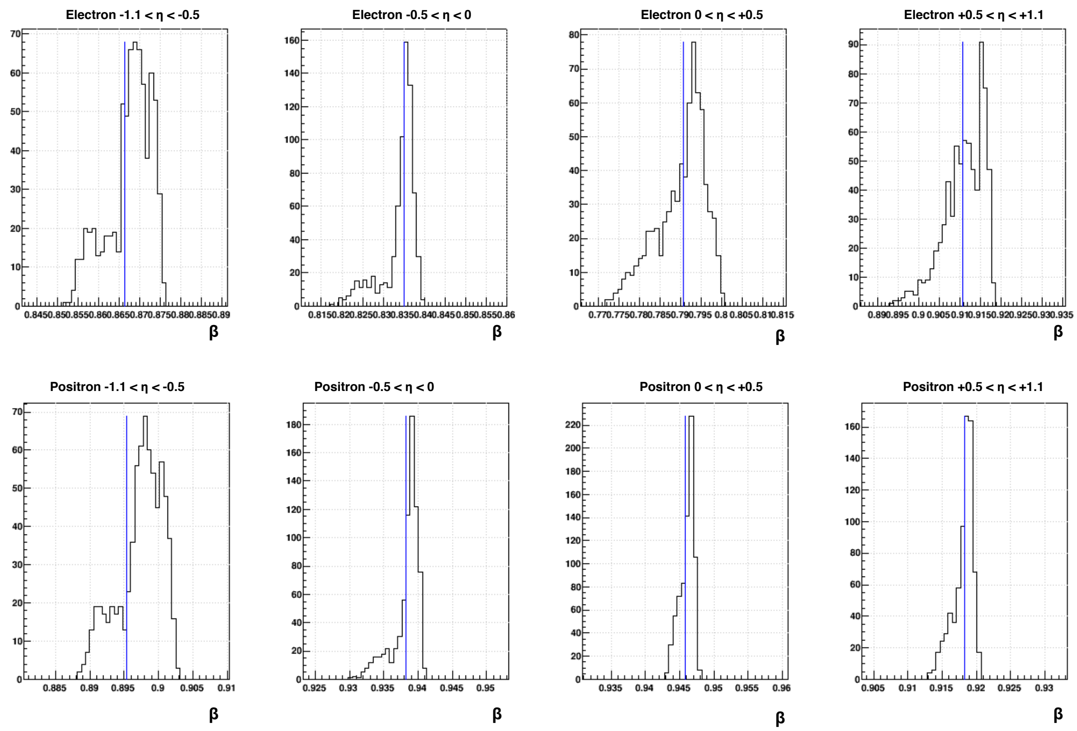

Figure 8.19.: β distribution of W^+ and W^- in period II.

STAR-η bin	Period I		Period II	
	W^-	W^+	W^-	W^+
	$\beta \pm \beta_{sys}$	$\beta \pm \beta_{sys}$	$\beta \pm \beta_{sys}$	$\beta \pm \beta_{sys}$
1	0.862±0.02	0.9078±0.0104	0.8675±0.0194	0.8974±0.012
2	0.831±0.0219	0.944±0.0059	0.8339±0.0245	0.9383±0.0076
3	0.8416±0.0206	0.944±0.006	0.7901±0.0283	0.9461±0.0067
4	0.8997±0.0144	0.9355±0.008	0.911±0.0162	0.9181±0.0106

Table 8.3.: β values and its total uncertainty, β_{sys} of W^+ and W^- in the range of $25 < E_T^e < 50$ GeV of period I and period II analysis.

8.4.1 Systematic Uncertainty of the data-driven QCD background procedure

The systematic uncertainty of the data-driven QCD background procedure was quantified and assigned as the systematic uncertainty of β. In order to accomplish this a set of data-driven QCD background shapes were obtained by varying several parameters that were used to obtain the shape. First, the threshold value of the sign-p_T balance cut, which was placed to select the QCD sample described in Sec. 8.2.2, was varied within a window of 5 to 25 GeV in steps of 0.25 GeV. This resulted in producing a set of 81 different QCD samples. Next, 10 normalization windows were introduced by varying the upper limit of the nominal normalization window, [14-16] GeV, which was used to obtain the nominal data-driven QCD background shape mentioned in Sec. 8.2.2, from 16 GeV to 20 GeV by steps of 0.5 GeV. Both these variations resulted in producing 729 sets of data-driven QCD background shapes as shown in Figure 8.20. It can be seen

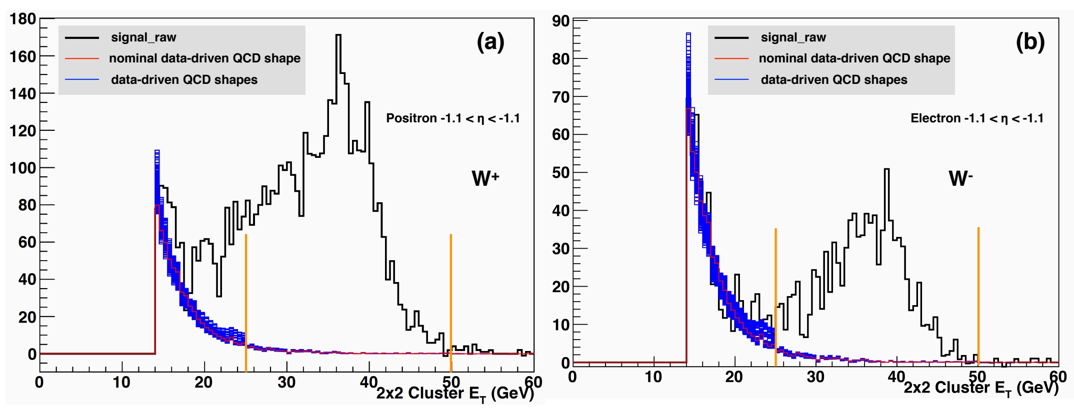

Figure 8.20.: 729 data-driven QCD background shapes (blue) used for the systematic studies discussed in the text : W^+ (a) and W^- (b)

that the deviation among the shapes are primarily visible in the low E_T^e region while the shapes overlap with one another in the high E_T^e range ($25 < E_T^e < 50$

GeV, indicated by the orange lines), where the asymmetry calculations are performed. The corresponding QCD background fractions, $f_{QCD}(i)$, from each of the 729 background shapes were calculated and used to obtain distributions for β as discussed in Sec. 8.4.

CHAPTER 9
RESULTS AND DISCUSSION

This chapter describes the details of the calculation of the single-spin asymmetry, $A_L^{W^\pm}$ from the reconstructed spin-dependent W yields. The final results are presented in comparison to several theoretical predictions. The full evaluation of systematic uncertainties of $A_L^{W^\pm}$ are also discussed. In addition, the results of the double-spin asymmetry, $A_{LL}^{W^\pm}$ are also presented.

As discussed in Sec. 2.5.1, single-spin asymmetry measurements only require one of the colliding beams to be polarized, thus bunches with alternating helicity in the polarized beam to be collided with bunches of an unpolarized beam. However, at RHIC both proton beams (blue and yellow) are polarized resulting in four possible helicity configurations between bunches that are colliding at the STAR interaction region. These four helicity configurations are labeled as $++$, $+-$, $-+$, $--$, which denote helicities of blue and the yellow beam respectively. Therefore, an originally written formula to extract the asymmetry based on a single polarized beam can be rewritten so that the actual spin asymmetry can be extracted due to the collisions between two polarized beams.

In the first section, the formulas that are required to calculate the asymmetry using spin dependent yields are extracted. Section 9.2 discuss the procedure of the relative luminosity correction of spin dependent yields. The resulting luminosity corrected W yields are tabulated in Sec. 9.3. The method of applying background corrections to the asymmetry is discussed in Sec. 9.4. The details of obtaining the average beam polarization values of the two beams are discussed in Sec. 9.5. In Sec. 9.6 the individual asymmetries per beam and per analysis period (I, II) are obtained. Finally, the results are presented in Sec. 9.7 which included an evaluation of full systematics uncertainties and discussion on comparison to several theoretical predictions.

9.1 Extraction of A_L from Spin Dependent Yields

The longitudinal single-spin asymmetry, A_L, for W boson production in collisions of longitudinally polarized beam with a unpolarized beam is shown in Eq. 2.17. As the scattering cross section is proportional to the ratio of measured yields to the luminosity, the A_L can be written in terms of measured yields N_+ and N_- when the helicity of the proton beam is positive and negative with respective luminosities, L_+ and L_- as,

$$A_L \propto \frac{N_+/L_+ - N_-/L_-}{N_+/L_+ + N_-/L_-} \tag{9.1}$$

As both beams are polarized at RHIC, A_L is measured for each beam independently while summing over the helicity of the other beam. These independent A_L values are combined to extract the final A_L using both beams. The asymmetry is calculated for each STAR-η bin separately, resulting in two corresponding A_L values for each bin from the two beams. The A_L values calculated per beam require use of the mirror reflected STAR-η bin as the two beams travel in opposite directions. To understand this better, let's consider the STAR-η bin configuration in figure 9.1. Here, 4 STAR-η bins that we have mentioned so far are denoted as η^{STAR} which are the physical η slices of the detector. These bins can be redefined as polarized beam η bins, 1, 2, 3 and 4 with respect to the polarized beam 1 (blue beam) which is headed in the positive Z direction. This beam give rise to corresponding asymmetry values $A_L(\eta)$ in each polarized blue beam η bin for measured yields at a given η^{STAR} slice. The polarized beam 2 (yellow beam) is identical to the beam 1 but it is headed in the negative Z direction. Now with respect to the yellow beam, 4 polarized beam bins can be defined as, $-\eta$ equal to -4, -3, -2, and -1. The minus sign and the reversal of the configuration of η bins are introduced by the change in both the momentum and the spin direction of

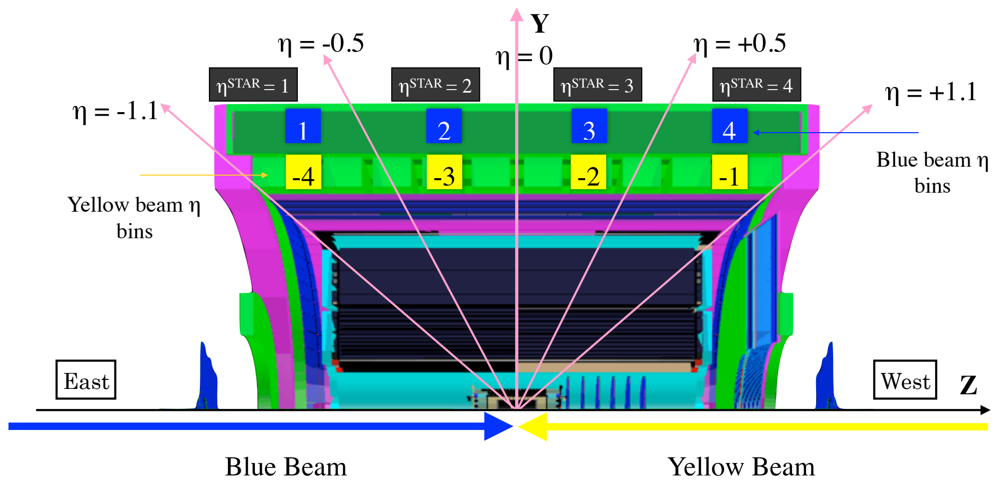

Figure 9.1.: The representation of corresponding polarized beam η bins for two beams in physical detector bins, η^{STAR}.

the polarized beam. Based on this, the yellow beam give rise to its corresponding asymmetry, $A_L(-\eta)$ in each polarized yellow beam $-\eta$ bin for measured yields at a η^{STAR} slice. As the two beams are identical, ideally the following relation should hold: $A_L(\eta = 1) = A_L(-\eta = -1)$ and so on for measured yields at a given η^{STAR} slice. The final asymmetry value is obtained by averaging the asymmetries measured using the two beams.

The luminosity corrected (see Sec. 9.2) spin-dependent yields, $M_i^{\eta^{STAR}}$ for a given helicity state i =++,+−,−+,−− at a given η^{STAR} slice can be written as a function of longitudinal asymmetries and beam polarization as followers [117]:

$$M_{++}^{\eta^{STAR}} = \sigma_0 L_{++}\varepsilon[1 + P_1 A_L(\eta) + P_2 A_L(-\eta) + A_{LL}(|\eta|)P_1 P_2] + bg_1 \tag{9.2}$$

$$M_{+-}^{\eta^{STAR}} = \sigma_0 L_{+-}\varepsilon[1 + P_1 A_L(\eta) - P_2 A_L(-\eta) - A_{LL}(|\eta|)P_1 P_2] + bg_2 \tag{9.3}$$

$$M_{-+}^{\eta^{STAR}} = \sigma_0 L_{-+}\varepsilon[1 - P_1 A_L(\eta) + P_2 A_L(-\eta) - A_{LL}(|\eta|)P_1 P_2] + bg_3 \tag{9.4}$$

$$M_{--}^{\eta^{STAR}} = \sigma_0 L_{--}\varepsilon[1 - P_1 A_L(\eta) - P_2 A_L(-\eta) + A_{LL}(|\eta|)P_1 P_2] + bg_4 \tag{9.5}$$

where σ_0 is the unpolarized cross section, L_i is the integrated luminosity of the i^{th} spin state, ε is the reconstruction efficiency, $P_{1(2)}$ is the polarization of the blue (yellow) beam, and $A_L(A_{LL})$ is the longitudinal single (double) spin asymmetry. As explained before $A_L(\eta)$ and $A_L(-\eta)$ are asymmetries measured by the blue and yellow beam respectively. Unlike the single-spin asymmetry, the double spin asymmetry is symmetric between negative η^{STAR} slices and positive η^{STAR} slices for both beams and thus, $A_{LL}(\eta) = A_{LL}(-\eta)$ for symmetric η^{STAR} slices (η^{STAR}=1, 4 and η^{STAR}=2, 3).

By using four spin-dependent yields from above equations 9.2, 9.3, 9.4 and 9.5, raw asymmetries, A_L^{raw} and A_{LL}^{raw} can be derived as:

$$A_L^{raw}(\eta) = \frac{1}{P_1}\frac{M_{++}^{\eta^{STAR}} + M_{+-}^{\eta^{STAR}} - M_{-+}^{\eta^{STAR}} - M_{--}^{\eta^{STAR}}}{\Sigma M_i^{\eta^{STAR}}} \tag{9.6}$$

$$A_L^{raw}(-\eta) = \frac{1}{P_2}\frac{M_{++}^{\eta^{STAR}} + M_{-+}^{\eta^{STAR}} - M_{+-}^{\eta^{STAR}} - M_{--}^{\eta^{STAR}}}{\Sigma M_i^{\eta^{STAR}}} \tag{9.7}$$

$$A_{LL}^{raw}(|\eta|) = \frac{1}{P_1 P_2}\frac{M_{++}^{\eta^{STAR}} + M_{--}^{\eta^{STAR}} - M_{+-}^{\eta^{STAR}} - M_{-+}^{\eta^{STAR}}}{\Sigma M_i^{\eta^{STAR}}} \tag{9.8}$$

where $\Sigma M_i^{\eta^{STAR}} \equiv M_{++}^{\eta^{STAR}} + M_{+-}^{\eta^{STAR}} + M_{-+}^{\eta^{STAR}} + M_{--}^{\eta^{STAR}}$ is the sum over all four helicity states. It must be noted that some background yields in background terms, "bg_i" in Equations (9.2) to (9.5) give rise to non vanishing single-spin asymmetries. Therefore, one should correct raw asymmetries for these backgrounds asymmetries in order to obtain the W signal asymmetries. The W signal asymmetries, $A_L^W(\eta)$ and $A_L^W(-\eta)$ for each beam are obtained by subtracting the portion of the asymmetry corresponds to those background yields from the raw asymmetries. This background correction procedure is discussed in Sec. 9.4. Then, the final result, A_L is calculated taking the weighted average of $A_L^W(\eta)$ and $A_L^W(-\eta)$ of the two beams.

9.2 Relative Luminosity Factors

During collisions at RHIC, each helicity state, i=++, +−, −+, −− is represented in every RHIC fill and alternated between two bunches continuously in a given fill. Therefore, ideally each spin state should integrate to the same delivered luminosity. However, in the case when missing bunches[1] are present are presented in a fill and when some bunches are more (or less) intense than others[2] slight differences between integrated luminosity of each spin state can occur. Therefore, in order to correct for these differences, spin sorted W yields, $N_i^{\eta^{STAR}}$ are normalized using a relative luminosity factor, R_i such that $M_i^{\eta^{STAR}} = N_i^{\eta^{STAR}}/R_i$. The R_i is defined as $R_i \equiv 4L_i/\Sigma_i L_i$ where L_i is the integral luminosity of the i^{th} spin state.

In order to calculate R_i, a statistically independent set of QCD background sample was considered. The QCD processes are parity conserved and therefore expected to exhibit no physical asymmetry ($A_L = 0$). Also QCD background events were available in large statistics and therefore the calculated relative luminosity factors should result in smaller uncertainties.

The QCD events were selected from the same sample that was triggered for W discussed in Sec 6.1.1 and high-p_T track requirements discussed in Sec 7.3.1. Next, two specific requirements: 2×2 cluster E_T to be below 20 GeV and 2×2 to 4×4 tower E_T to be below 0.95 (opposite of the W candidate cuts discussed in Sec. 7.3.3) were imposed in order to ensure that all possible W like candidate events were excluded and the sample only consist of QCD events. Then these QCD events were separated by 4 spin states to calculate R_i.

As R_i is only a ratio of luminosities, the absolute luminosity values of QCD events in each of the spin states was not needed. Instead, the magnitude of yields in each spin states were used to form the relative luminosity ratios as:

[1] Missing bunches are not planned and occur when there is some issue in a cycle of the injectors.

[2] In particular this is true towards a end of a RHIC fill.

$R_i = 4N_i^{QCD}/\Sigma_i N_i^{QCD}$. The calculated relative luminosity values along with their uncertainties are shown in Table 9.1.

Spin State	**Period I**		**Period II**	
	N_i^{QCD}	$R_i \pm$ error $(1/\sqrt{N})$	N_i^{QCD}	$R_i \pm$ error $(1/\sqrt{N})$
$++$	218065	0.9947±0.005	170602	1.0058 ± 0.006
$+-$	218610	0.9972±0.005	168747	0.9949 ± 0.006
$-+$	218959	0.9988±0.005	168709	0.9947 ± 0.006
$--$	221253	1.0093±0.005	170388	1.0046 ± 0.006

Table 9.1.: The calculated relative luminosity factors from QCD events.

The systematic uncertainty on asymmetry due to the relative luminosity corrections were estimated and are discussed in Sec. 9.7.2.

9.3 Spin Sorted Yields

Once normalized by the relative luminosity correction factors, the "golden W yields" discussed in the Sec. 7.6 in the E_T range 25 GeV to 50 GeV are separated by four spin states and used as the $M_i^{\eta^{STAR}}$ to calculate raw asymmetries, A_L^{raw} as shown in Equations (9.6) to (9.8). The magnitude of these spin sorted yields are shown in Table 9.2 and in Table 9.3 for period I and period II respectively.

These yields still contain some background yields discussed in Chapter 8 and instead of subtracting them off, it is more efficient to correct for any non zero asymmetries from background. This procedure of estimating A_L^{BG} and subtracting from A_L^{raw} to obtain A_L^W is discussed in the following section.

Spin State / η^{STAR} bin	$M_i(W^+)$ sum	++	+−	−+	−−	$M_i(W^-)$ sum	++	+−	−+	−−
1	781	113	230	167	270	257	98	53	65	42
2	1246	195	304	305	440	270	90	66	67	47
3	1282	196	292	345	447	259	74	60	66	58
4	775	114	171	224	265	314	103	89	75	48

Table 9.2.: Spin sorted yields in period I.

Spin State / η^{STAR} bin	$M_i(W^+)$ sum	++	+−	−+	−−	$M_i(W^-)$ sum	++	+−	−+	−−
1	579	82	172	106	220	236	74	60	65	37
2	835	117	212	202	304	185	70	44	39	32
3	998	163	225	264	345	198	61	44	56	37
4	653	103	139	175	236	245	68	66	65	46

Table 9.3.: Spin sorted yields in period II.

9.4 Background Correction

The observed raw asymmetry A_L^{raw} can be written in terms of contributions from true W signal events and background events as follows:

$$A_L^{raw} = f_W A_L^W + f_{W\to\tau} A_L^{W\to\tau} + f_Z A_L^Z + f_{EEMC} A_L^{EEMC} + f_{QCD} A_L^{QCD} \tag{9.9}$$

where A_L^Z, $A_L^{W\to\tau}$, A_L^{EEMC}, and A_L^{QCD} are the corresponding single-spin asymmetries for Z background, $W \to \tau$ background, the second EEMC background, and the data-driven QCD background yields contamination in the W yields respectively. The $f's$ are the fractions of these background components in the W yields that were given in Table. 8.2 in the previous chapter.

The $A_L^{W\to\tau}$ which corresponds to $W \to \tau$ background, can be replaced by the A_L^W, as both $W \to e\nu$ events and $W \to \tau\nu$ events yield similar single and double spin asymmetries despite $W \to \tau$ events being a type of background for the $W \to e\nu$ signal. The only difference between the two asymmetries can arise from any existing differences in the rapidity distributions of tau leptons from $W \to \tau$ relative to the electrons from $W \to e$, as the tau leptons are not measured directly but only the decay electrons and positrons from them, $\tau \to e\nu_e\nu_\tau$. As explained in Chapter 2, due to the same V-A type charge weak current interaction in both the W production vertex and the W to tau decay vertex, tau leptons are produced in the almost perfect spin correlation, causing $e^+(e^-)$ decayed from τ leptons to be emitted preferentially in $\tau^+(\tau^-)$ momentum direction in the lab frame. This results in similar rapidity distributions between tau and its decay electrons. This property has been studied in other experiments [118], and in particular for W A_L analysis at the STAR this has been tested in [119] using simulated events of $W \to \tau$ which satisfy the same high-p_T candidate selection criteria for $e^\pm$. A strong correlation was observed between the rapidity distributions of $W \to \tau$ and its decay electrons. Therefore, the $A_L^{W\to\tau}$ is treated as same as the asymmetry of the W signal. Thus the equation 9.10 is reduced to:

$$A_L^{raw} = (f_W + f_{W\to\tau})A_L^W + f_Z A_L^Z + f_{EEMC} A_L^{EEMC} + f_{QCD} A_L^{QCD}. \tag{9.10}$$

And finally, since all $f's$ are normalized to one, A_L^W can be obtained as,

$$A_L^W = \frac{A_L^{raw} - (f_Z A_L^Z + f_{EEMC} A_L^{EEMC} + f_{QCD} A_L^{QCD})}{1 - f_Z - f_{EEMC} - f_{QCD}} = \frac{A_L^{raw} - \alpha}{\beta}, \tag{9.11}$$

where $\alpha = f_Z A_L^Z + f_{EEMC} A_L^{EEMC} + f_{QCD} A_L^{QCD}$ is considered as the polarized background contribution to the A_L^W, and the unpolarized background correction, $\beta = 1 - f_Z - f_{EEMC} - f_{QCD}$ is the same background dilution factors that are given in Table 8.3.

The dominant contribution to α is expected to come from the Z background yields as the second EEMC and QCD background are dominated by QCD processes, which conserves the parity and thus corresponds to zero single-spin asymmetries. However, any contamination of the Z background yields in the second EEMC and in the data-driven QCD could give rise to a non-zero single spin asymmetries. Therefore, the fractions of Z contamination in these two types of background are required to be investigated and determined whether those were non negligible and thus would give rise to sizable asymmetries for the two cases. First let's discuss the contribution from the Z background yields.

The value of the A_L^Z was determined during the STAR 2009 W analysis [104] using a full next-to-leading order (NLO) framework [69] and was calculated to be $A_L^Z = -0.06$ while taking a conservative systematic uncertainty of 50%. For this analysis as well the same value was considered. By considering the largest f_Z value in the table 8.2, $f_Z = 0.036$, the contribution to the α from Z was calculated as -0.06×0.036 which resulted in $f_Z A_L^Z = -0.002 \pm 0.001$. This value however is an order of magnitude smaller than the expected statistical uncertainty of the actual asymmetry values which would then resulted in a negligible impact on the asymmetry. Any contamination of Zs in the secondEEMC was estimated to be either smaller or equal to the largest f_Z value mentioned above, and any contamination of Zs in the data-driven QCD background which was expected to arise due to the Z veto process discussed in Sec. 8.2.3 was found to be further small. As the Z background contribution to the α, $f_Z A_L^Z$ itself was negligible, any non-zero asymmetries due to the contamination of Zs in the secondEEMC and in the data-driven QCD background were further smaller and, thus ignored. Therefore, A_L^W for each beam was calculated by simply correcting only for the unpolarized background as,

$$A_L^W(\eta) = \frac{A_L^{raw}(\eta)}{\beta}. \tag{9.12}$$

$$A_L^W(-\eta) = \frac{A_L^{raw}(-\eta)}{\beta}. \tag{9.13}$$

The A_L for each period, i= I, II was calculated by averaging the asymmetry values from each beam as $A_{L(i)} = A_{L(i)}^W(\eta) \oplus A_{L(i)}^W(-\eta)$, where $\oplus$ indicated the weighted average. Then the final, A_L result was calculated by averaging the asymmetry values from the two periods as $A_L = A_{L(I)}^W \oplus A_{L(II)}^W$.

9.5 Average Beam Polarization

In order to calculate the A_L^{raw} as stated in equations 9.6 and 9.7, average polarization values of each beam are required. The beam polarizations are measured using the RHIC polarimeters, and fill by fill results are provided by the RHIC polarimetry group [120]. The information given by the RHIC polarimetry group contains fill by fill polarization values at $t = 0$, P_0[1], the rate of polarization loss, P' and the beam current weighted mean polarization values P_{avg} for each beam. As the data set used for this analysis, does not contain all the runs in a given fill[2], taking these P_{avg} values given by the polarimetry group was not appropriate. Instead, the polarization values of each beam j (j = blue, yellow) during each run i, P_i^j was obtained using the fill-by-fill information from the RHIC polarimetry group as follows:

$$P_i^j = P_0^j - t_i \times P'^j, \tag{9.14}$$

where t is the "time of the run" which calculated as the time "t" to the run i of the fill from the start time of the fill at $t = 0$. Then the average polarization values for each beam, P_{avg}^j for the data set was determined from the luminosity weighted average over the runs as,

$$P_{avg}^j = \frac{\Sigma_i P_i^j L_i}{\Sigma_i L_i} \tag{9.15}$$

[1] Polarization value at the beginning of the fill.

[2] During our data QA we removed runs which do not satisfy our selection criteria.

where L_i is the luminosity of the i^{th} run and ΣL_i is the total luminosity of the data set. Figure 9.2 shows the calculated luminosity weighted polarization values as a function of run index for both blue and yellow beams. One can observed the fill

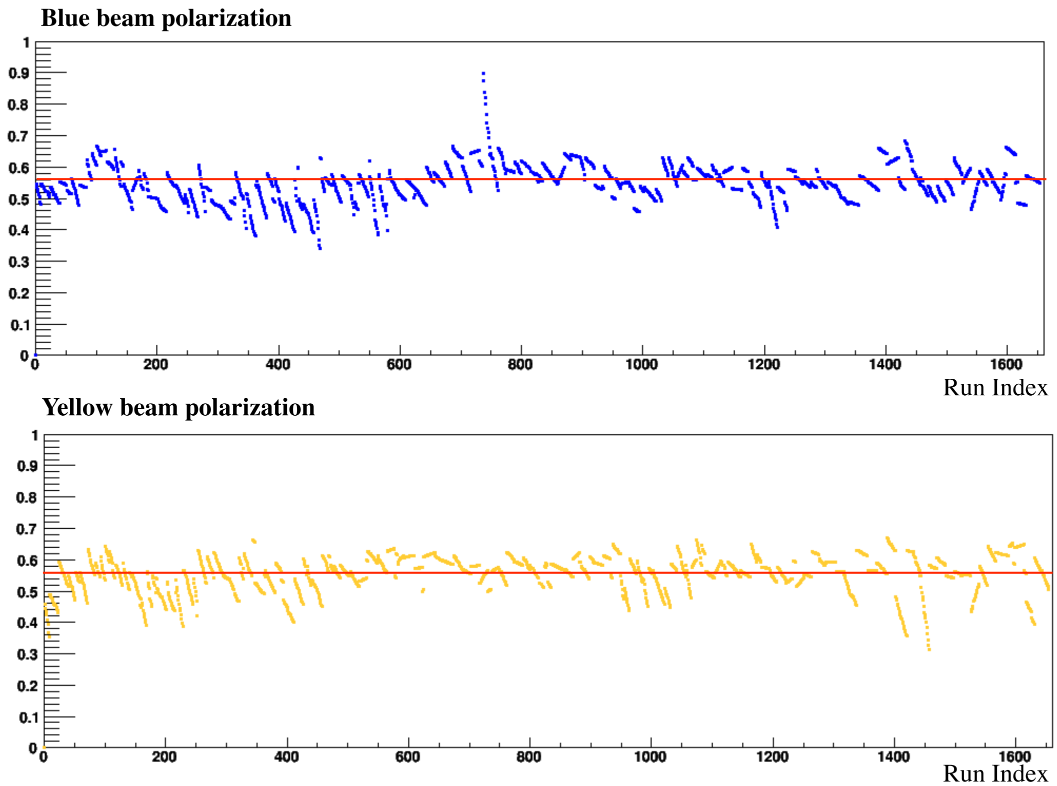

Figure 9.2.: Beam polarization for blue (a) and yellow (b) beam as a function run index. Lines indicate the luminosity weighted average values.

structure where polarization decreased with time and therefore with increasing run index in a given fill. The average polarization values were determined to be $P_1, P_2 = 56\%$ corresponding to both blue and the yellow beam which is indicated by the red lines.

9.6 Path to Final Results

Figures 9.3 and 9.4 shows the asymmetry values calculated for each polarized beam using the formulas given in equations 9.12 and 9.13 for period I and period II respectively. Points at STAR-η bin 8 represents the corresponding average values of data points in four STAR-η bins. As explained in Sec. 9.1, one should

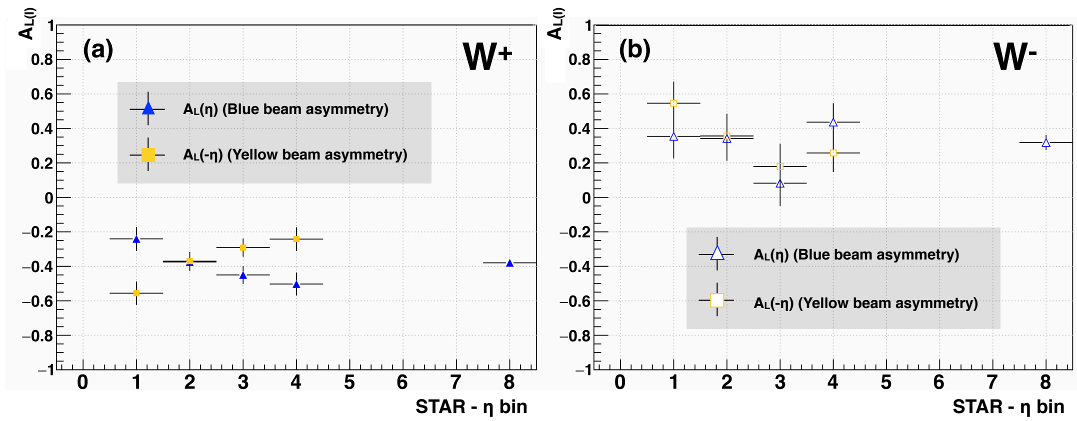

Figure 9.3.: The calculated asymmetry in period I, $A_{L(I)}$ per beam: $A_L(\eta)$ (blue) and $A_L(-\eta)$ (yellow) for W^+ (a) and W^- (b). The corresponding average value of the 4 bins is shown at STAR-η bin 8.

compare each blue point in each STAR-η bin with respective yellow points in the mirror STAR-η bin. For example, blue point in the STAR-η bin 4 should compare with the yellow point in the the STAR-η bin 1. The calculated asymmetry corresponding to each of the beam are consistent with each other within statistical uncertainties. Next, the asymmetry of each period, $A_{L(I)}$ and $A_{L(II)}$ which were obtained by taking the weighted average of asymmetry per beam are shown in Fig. 9.5 (a) and (b) respectively.

The vertical error bars of the calculated asymmetry in all figures shown in this chapter represent the statistical uncertainty of asymmetry which were

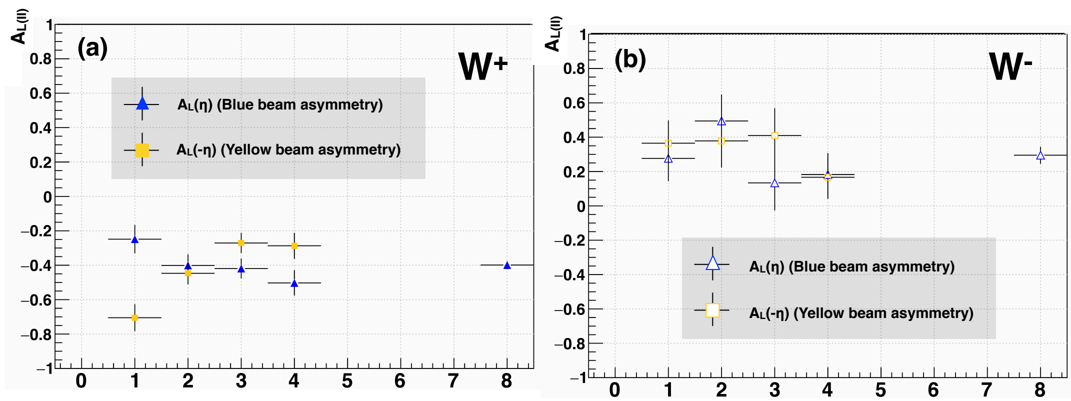

Figure 9.4.: The calculated asymmetry in period II, $A_{L(II)}$ per beam: $A_L(\eta)$ (blue) and $A_L(-\eta)$ (yellow) for W^+ (a) and W^- (b). The corresponding average value of the 4 bins is shown at STAR-η bin 8.

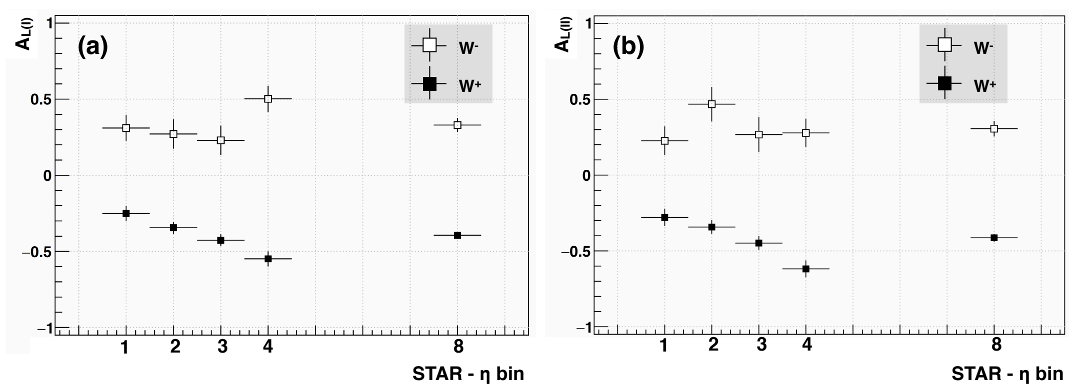

Figure 9.5.: The calculated asymmetry for period I data $A_{L(I)}$, (a) and for period II data $A_{L(II)}$, (b). The final A_L is obtained as the weighted average between asymmetry values of the two periods for W^+ and W^- separately. The corresponding average value of the 4 bins is shown at STAR-η bin 8.

calculated using the method of error propagation as shown in equation 9.16,

$$\delta A = \sqrt{\Sigma_i \left(\frac{\partial A}{\partial x_i}\right)^2 \delta x_i}. \tag{9.16}$$

According to the standard definitions, x_i are the variables used in calculating asymmetries and δx_i are their respective uncertainties. For example, when calculating $A_L^W(\eta)$ as shown in equations 9.12, $x_i = A^{raw}(\eta)$, β and corresponding $\delta A_L^{raw}(\eta)$[1] and $\delta\beta$ were calculated following the same error propagation method.

Horizontal error bars of each point do not indicate any physical meaning in the figures discussed so far. However the final results presented in the following section, widths of each horizontal bars are represented by the RMS of the η distribution of yields in the respective STAR-η bin. These η distributions of the spin sorted yields are shown in Fig. 9.6 and 9.7 for period I and II respectively. The separation of STAR-η bins are denoted by red lines.

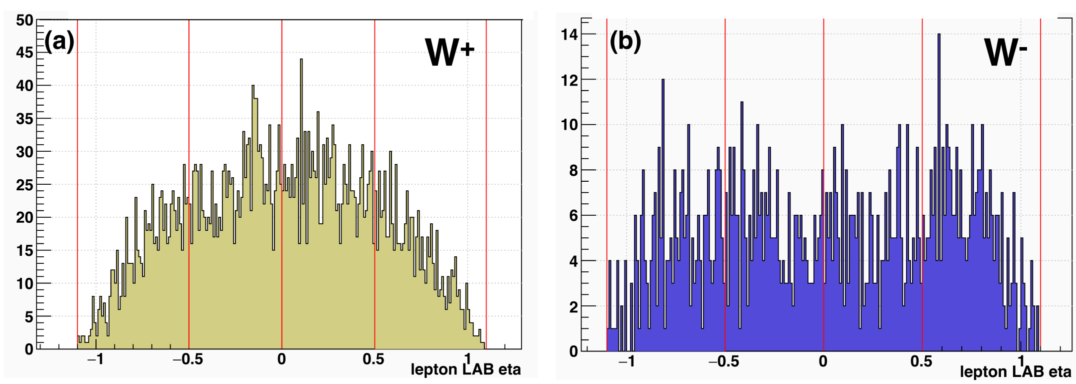

Figure 9.6.: η distributions of e^+ and e^- of spin sorted yields shown in table 9.2 of period I for W^+ (a) and for W^- (b).

---

[1] To calculate $\partial A_L^{raw}(\eta)$, where $A_L^{raw}(\eta)$ is a function of luminosity corrected yields, $M_i^{\eta^{STAR}}$ and polarizations P_1 as shown in equations 9.6, statistical uncertainty of each $M_i^{\eta^{STAR}}$ were considered. The polarization value P_1 were treated as constants and its uncertainty were added as a contribution to the systematic uncertainty.

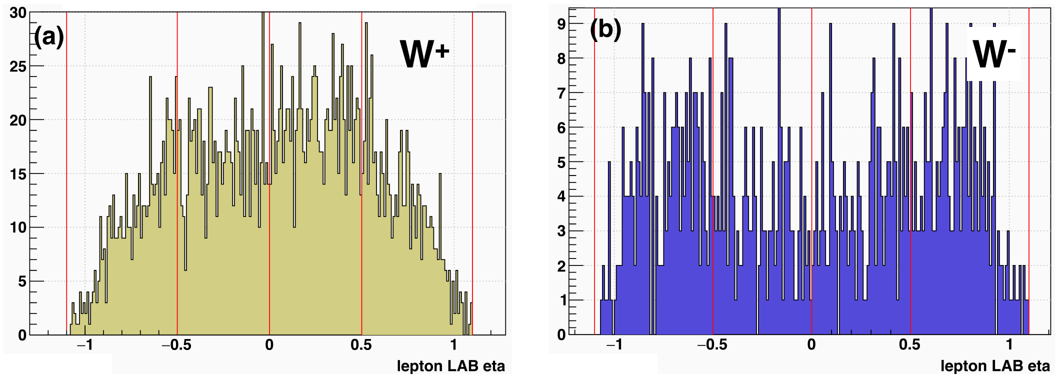

Figure 9.7.: η distributions of e^{+} and e^{-} of spin sorted yields shown in table 9.3 of period II for W^{+} (a) and for W^{-} (b).

9.7 Results and Discussion

In this section, the results of W single-spin asymmetry, A_L and W double-spin asymmetry, A_{LL} are presented along with a evaluation of full systematic uncertainties. The impact of prior STAR W A_L results and expectation from the new results on the helicity PDFs are discussed.

9.7.1 Single-spin Asymmetry

The results of the single-spin asymmetry from the data analyzed in this thesis (labeled as STAR preliminary) are shown in Fig. 9.8 along with several theoretical predictions. The numerical values of A_L are given in the table 9.4 along with respective statistical uncertainties. As noted before, the statistical uncertainty are shown by the vertical error bars. The length of horizontal error bars represent the RMS of the η distribution in each STAR-η bin. The thickness (height) of the horizontal error bars however represent the systematic uncertainty on A_L due to the systematic uncertainty of BEMC absolute energy scale calibration which was discussed in chapter 5. The estimation of the magnitude of this uncertainty and

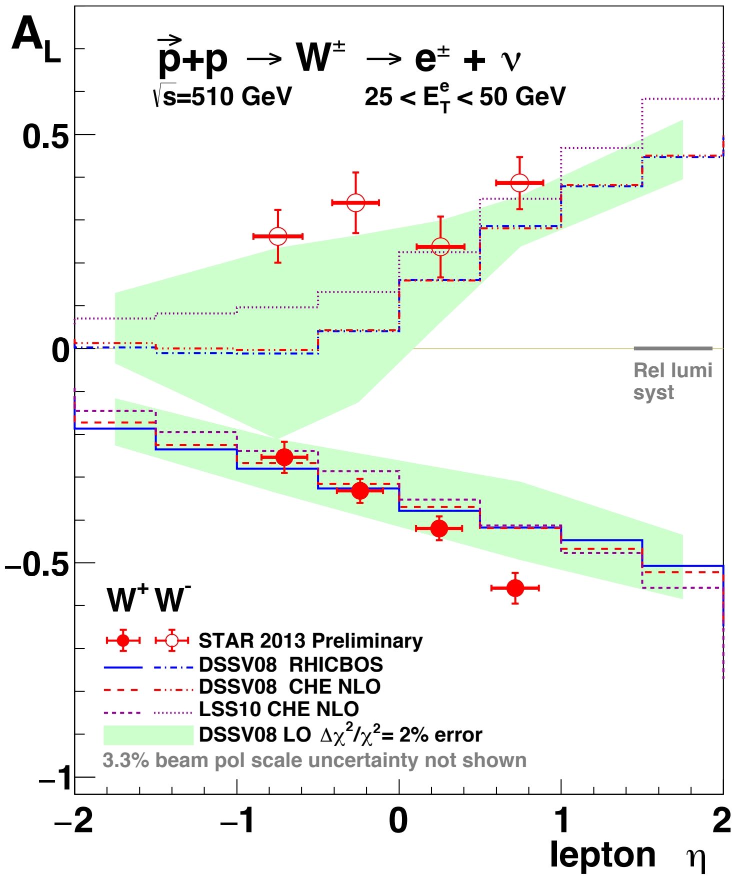

Figure 9.8.: Longitudinal single-spin asymmetry, A_L for $W^{\pm}$ production as a function of $e^{\pm}$ pseudorapidity for STAR 2013 data.

STAR-η bin	$A_L^{W^+} \pm$ stat	$A_L^{W^-} \pm$ stat
1	-0.263±0.038	0.272±0.064
2	-0.344±0.029	0.352±0.073
3	-0.435±0.029	0.245±0.074
4	-0.580±0.037	0.401±0.063

Table 9.4.: The measured $W^{\pm}$ A_L values with their uncertainties.

all other types of systematic uncertainties are discussed in Sec. 9.7.2. The thickness (height) of the grey band represents the systematic uncertainty due to the relative luminosity correction discussed in Sec. 9.2. The common systematic uncertainty on single-spin asymmetries due to the normalization scale uncertainty of the beam polarization of 3.3 % is not shown. The theoretical curves of A_L are calculated using both next-to-leading order (NLO) CHE[1][69] method and NLO RHICBOS[2][71] method. While the RHICBOS calculations are based on sets of helicity PDFs from the DSSV08[3] [56], the CHE calculations are based on both the DSSV08 and the LSS10[4] [54] helicity PDF sets. The green region represent the estimated PDF uncertainty within $\Delta\chi^2/\chi^2 = 2\%$ of the DSSV08 CHE A_L predictions.

As expected the A_L^{W+} was found to be negative and consistent, within uncertainties to the theoretical predictions. As discussed in Sec. 2.5.1, in the mid-rapidity region the A_L^{W+} is sensitive to the combination of both u and anti-d quark polarizations. However it is expected to be dominated by the polarization of the valence quark. In this results, one can see that the asymmetry values begin to deviate from the theoretical prediction towards positive η values, in particular the value in the most forward bin is below the theoretical predictions. Towards the forward region A_L^{W+} is more sensitive to the anti-d quark polarization over the u quark polarization.

The A_L^{W-} is large and positive as expected due to the large negative polarization of the valance d quark. However, A_L^{W-} is deviated from the theoretical prediction towards large negative pseudorapidities. One can see that the measured A_L^{W-} values are significantly larger than the theoretical prediction in the

[1] CHE stands for Collisions at High Energies, and it is a Monte-Carlo like code used to access the full kinematics of the final-state particles.

[2] A method where prediction for W boson production and decay are made based on a calculation for resummation of large logarithmic contributions originating from multiple soft gluon radiation.

[3] PDF sets extracted by performing a global analysis primarily using DIS and SIDIS experimental data all over the world by DSSV collaboration.

[4] PDF sets extracted by performing a global analysis primarily using DIS and SIDIS experimental data all over the world by LSS collaboration.

two backward bins. This behavior is in agreement with the published STAR 2012 W A_L results [100]. The $A_L^{W^-}$ is largely sensitive to the anti-u quark polarization towards large negative pseudorapidity region while in the mid-rapidity it is sensitive to the combination of anti-u and d quark polarization. Therefore, the large measured $A_L^{W^-}$ towards negative pseudorapidity region indicates larger anti-u quark polarization. The impact on the polarization of both anti-u and anti-d quarks had been estimated by extracting their respective helicity PDFs using the STAR 2011+ 2012 W A_L results where this significant deviation was first observed and are discussed in Sec. 9.7.3.

The uncertainty of the measured A_L is dominated by the statistical uncertainty as the systematics uncertainties are well under control and are less than 10% of the statistical uncertainty. The total uncertainty of this result is reduced by 40% in comparison to the STAR 2011+2012 published W A_L results [100] and also significantly smaller than the $W^{\pm} + Z^0$ A_L results[1] [121] published by the PHENIX collaboration at RHIC. This makes the W A_L results measured in this dissertation using the STAR 2013 data, the most precise W A_L results in the world, as of this writing. A significant impact were seen on the extracted helicity PDFs from the previous W A_L results from the STAR experiment. A similar impact on the helicity PDFs that would extracted in the future after inclusion of this results in global analyses is expected, in particular reducing the uncertainties of the helicity PDFs.

Figure 9.9 shows the measured W A_L in this thesis along with published STAR W A_L results [100] (labeled as STAR 2011+2012 data) and published PHENIX W+Z A_L results [121] (labeled as PHENIX 2011+2012 and PHENIX 2013). In STAR 2011+2012 results, A_L measurements were extended into the forward rapidity region in addition to the mid-rapidity region which the 2013

[1] As the results from the PHENIX collaboration are from $W^{\pm} + Z^0$ decays and the STAR results are solely from $W^{\pm}$ decay, a direct comparison between data points cannot be make, however, a comparison can be made through curves which explains in [121]. Nevertheless a qualitative comparison between statistical uncertainties can be made.

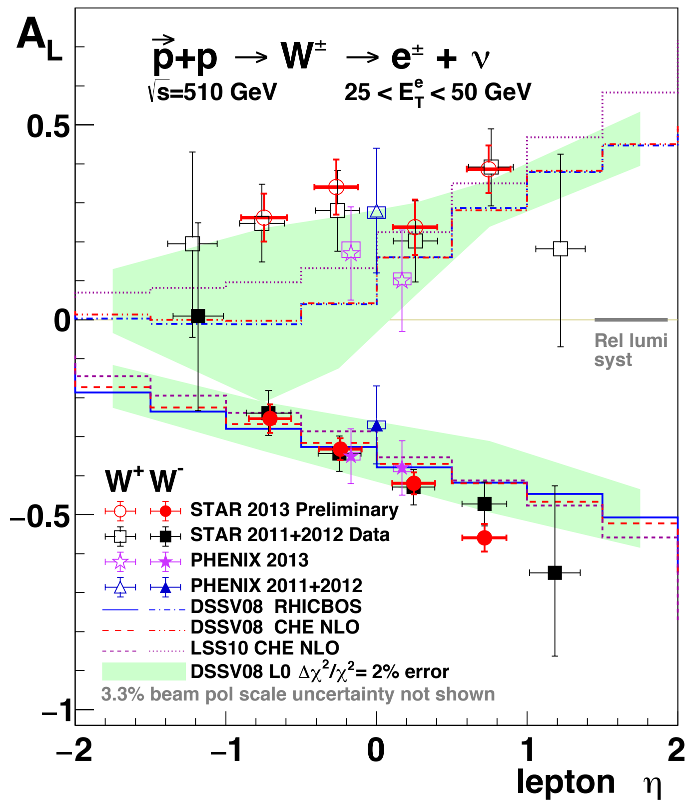

Figure 9.9.: Parity violating longitudinal single-spin asymmetry, A_L for $W^\pm$ production as a function of $e^\pm$ pseudorapidity from STAR and PHENIX collaboration at RHIC.

results are presented.[1] The two data points in $|\eta| > 1$ correspond to A_L in this region. The representation of data points and uncertainties of STAR 2011+2012 follow a similar procedure as was discussed for the STAR 2013 data. The representation of the results from the PHENIX collaboration are quite similar to that of the STAR and are discussed in detail at [121]. However the pseudorapidity coverage of the PHENIX results are smaller than that of the STAR results and their systematic uncertainties of A_L are represented by a small box around each

[1] The corresponding measurements in the forward region using the STAR 2013 data are being analyzed as the time of this writing.

data point. By comparing these data points one can clearly see that the results obtained in this thesis yield the smallest uncertainties.

9.7.2 Systematic Uncertainty of A_L

As mentioned before, the systematic uncertainty on the measured A_L due to the background dilution factor β were included in the total statistical uncertainty of the A_L that were listed in the table 9.4 and are on the order of 5% of the total statistical uncertainty.

The systematic uncertainty on A_L due to the relative luminosity correction discussed in Sec. 9.2 was estimated. This was accomplished by selecting an another statistically independent set of QCD background sample, similar to the one used to obtain the relative luminosity correction factors themselves. Similarly, these QCD events were selected from the same sample that was triggered for W and high-p_T track requirements. However, the conditions of isolation requirements discussed in Sec. 7.3.3 and signed-Pt balance requirement discussed in Sec. 7.4.1 were oppositely imposed in order to select only QCD type events. Next, only the events in the E_T range of 25 to 50 GeV from this sample was used and their single-spin asymmetries, $A_L^{QCD\pm}$ were calculated in a single bin by combining all 4 STAR-η bins together. This $A_L^{QCD\pm}$ was calculated in the same way where W A_L was calculated except β obviously was set to zero. The values are given in the table 9.5 along with their statistical uncertainties. As

$A_L^{QCD^+}$ ± **stat**	$A_L^{QCD^-}$ ± **stat**
-0.002±0.006	-0.001± 0.007

Table 9.5.: The measured A_L^{QCD} values with their uncertainties.

expected these value are consistent with zero. Half of the statistical uncertainty in each case, which is equal to 0.004 was taken as the systematic uncertainty on

A_L due to the relative luminosity corrections.

In chapter 5 a systematic uncertainty of 3.0% was obtained as the BEMC absolute energy scale calibration procedure. In order to calculate the systematic uncertainty on A_L due to the calibration scale uncertainty, A_L was calculated twice additionally in the full barrel region (by combining all four STAR-η bins into a one) by increasing and decreasing BEMC tower gains by 3.0% from the nominal tower gains. The difference between resulted A_L^{up} and A_L^{down} was estimated and half of the difference between two asymmetries, was taken as the systematic uncertainty on A_L due to the uncertainty of BEMC absolute scale. The values are tabulated in Table 9.6.

	A_L^{up}	A_L^{down}	$\lvert A_L^{up} - A_L^{down}\rvert$
W^+	-0.383	-0.388	0.005
W^-	0.302	0.31	0.008

Table 9.6.: The measured $A_L^{up(down)}$ values by scaling up (down) the BEMC tower gains.

9.7.3 Impact on helicity PDFs from STAR W A_L results

The published STAR 2011+2012 results [100] were used by the recent global analyses, NNPDFpol1.1 [122] performed by the NNPDF collaboration [55] and the DSSV++[1] [124] performed by the DSSV group. Figure 9.10 shows the extracted helicity PDFs of $\Delta\bar{u}$ and $\Delta\bar{d}$ by the NNPDF group[2] before (green) and

[1] For the DSSV++ global analysis the STAR 2011+2012 preliminary results [123] was used.

[2] In contrast to the global analysis [69] by the DSSV group, the NNPDF group does include neither SIDIS data nor the pion production data from the various experiments around the world in the process of extracting their PDFs sets, [122]. Therefore, their uncertainties are larger in comparison to the DSSV.

after (red) the inclusion of the STAR 2011+2012 W A_L data into their global analysis. The corresponding absolute uncertainties are given in the distributions in the right. One can clearly see a significant change in the central value of

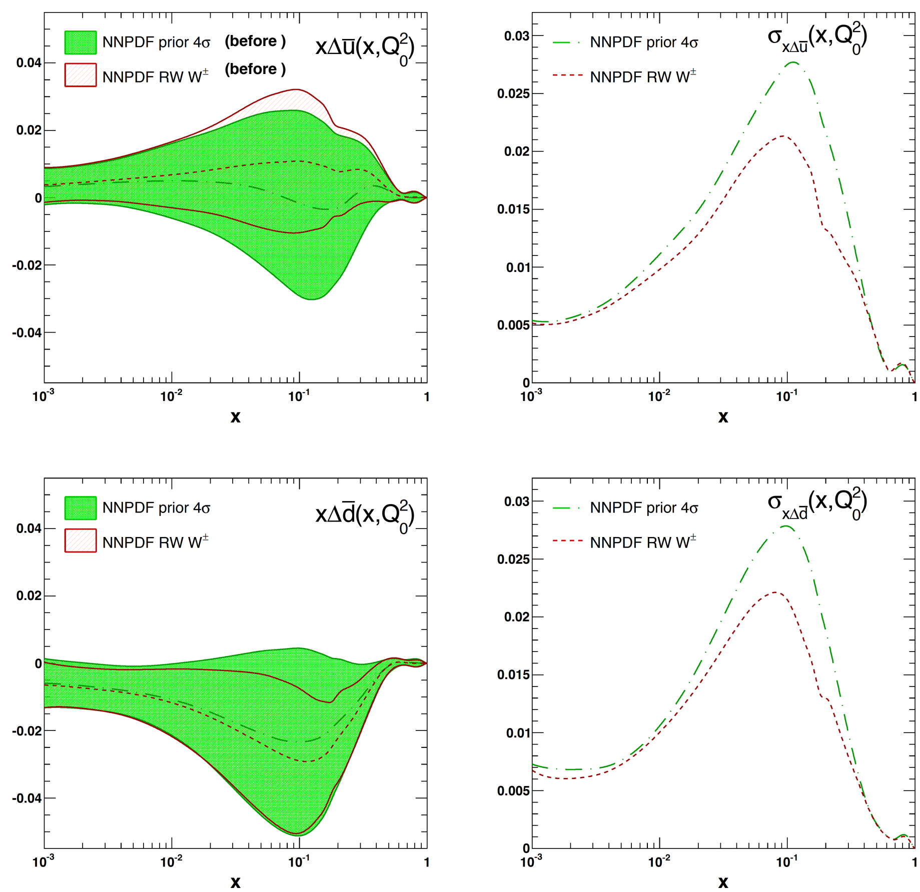

Figure 9.10.: NNPDFpol1.1 [122] helicity PDFs of $\Delta\bar{u}$ and $\Delta\bar{d}$ before(green) and after(red) the inclusion of STAR 2011+2012 W A_L published results [100]. The shaded area indicate the uncertainty bands of 4σ ensemble of the respective prior distributions.

the PDFs, in particular the $\Delta\bar{u}$ changed from negative to positive with in the kinematic range available at the RHIC, $0.05 < x < 0.2$. This clearly indicate a significant impact on the light antiquarks helicity PDFs from the W asymmetry results in comparison to the DIS/SIDIS results. The uncertainties as well are largely reduced. Thus, one can expect the STAR 2013 W A_L results presented in this thesis work will reduce the uncertainty and further constrain these helicity PDFs.[1]

The χ^2 profiles for the $\Delta\bar{u}$ and the $\Delta\bar{d}$ in the range of $0.05 < x < 0.1$ of the DSSV++ [124] global analysis are shown in Figure 9.11. The DSSV++

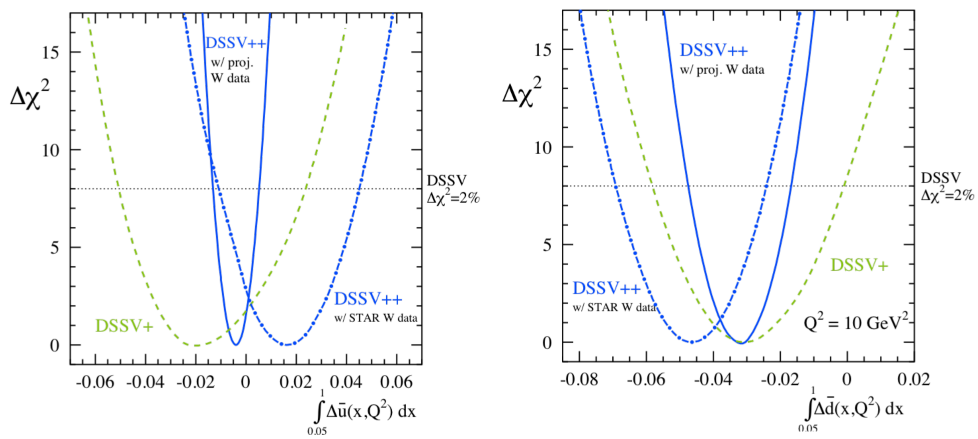

Figure 9.11.: The χ^2 profiles for the truncated integral for $\Delta\bar{u}$ and $\Delta\bar{d}$ in the range of 0.05< x <0.1 of DSSV++ [124] (dashed blue) helicity PDFs, which include STAR W A_L data in comparison to the that of DSSV+ (dashed green) which only include DIS and SIDIS data.

curve (dashed blue) which include the STAR W A_L data (from 2009 [104] to 2012 [100]) is compared to the DSSV+ curve (dashed green) which include only the DIS and the SIDIS data. A clear improvement of the helicity PDFs of the two antiquarks can be seen with uncertainties reduced from without to with STAR W A_L data. In particular for $\Delta\bar{u}$ a significant shift from negative to positive can be seen indicating a sizable anti-u quark polarization similar to what was witnessed from the global analysis of NNPDFpol1.1. The solid blue curve represent the

[1] A proceeding published in the arXiv journal by the one of the authors in the NNPDF group as of this writing, shows the preliminary set of helicity PDFs [125] after the inclusion of the STAR 2013 preliminary W A_L results (the results presented in this thesis).

same DSSV++ curve but with expected uncertainties[1] from the RHIC W A_L data from 2013. Both STAR 2013 and the PHENIX 2013 W A_L results are now available with STAR 2013 results being most precise. Therefore, a future global analysis from the DSSV group is expected to yield significant reduction of the uncertainty of light antiquark helicity PDFs.

9.7.4 Double-spin Asymmetry

The parity conserved double-spin asymmetry, A_{LL} for the W boson production was calculated using the formula given in equation 9.8. The A_{LL} was corrected for backgrounds similar to that of A_L as discussed in the Sec. 9.4 and was expected to be consistent with zero as the A_{LL} for W boson should conserved the parity in contrast to the A_L. Figure 9.12 shows the measured A_{LL} from this analysis (red) along with the STAR 2011+2012 published results [100] (black). Similar to the case of A_L the vertical error bars represent the statistical uncer-

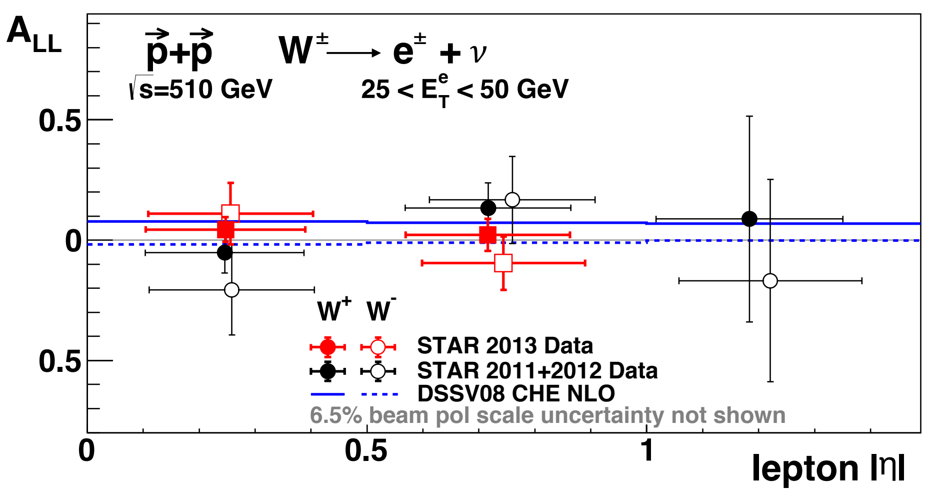

Figure 9.12.: Parity conserving longitudinal double-spin asymmetry, A_LL for $W^\pm$ production as a function of $e^\pm$ pseudorapidity.

[1] By the time of these [124] global analysis the RHIC 2013 W A_L data was not available.

tainty and the horizontal error bars represent the RMS of the η distribution in the bin. A common 6.5% beam polarization scale uncertainty which associated with all double-spin asymmetries due to the uncertainty in the measured beam polarization is not shown. One can clearly see that, the two results agree between each other within the given statistical uncertainties and the run 13 results yield smaller uncertainties in comparison to the published results. In addition, the asymmetries are consist with the theoretical prediction, DSSV08 CHE NLO [56] which is indicated by blue lines. It must also be noted, both the DSSV and the NNPDF[122] theoretical calculations predict positive bounds for particular combinations[1] of A_L and A_{LL} as a function of W rapidity, y_W. The positive bounds for these combinations are expected to be satisfied when ever the A_{LL} is positive. One can see that these results have a tendency of being positive and thus satisfy these arguments within the given statistical uncertainties.

[1] A combination such as $1+A_{LL}(y_{W^+}) - |A_L(y_{W^+}) + A_L(-y_{W^+})|$ for W^+[122].

CHAPTER 10
CONCLUSION AND OUTLOOK

The analysis presented in this dissertation is motivated by one of the fundamental questions in nuclear physics, How do the underlying quarks, gluons and their dynamics carry the spin of proton? The focus of the analysis was to measure the single spin asymmetries, A_L, for $W^{\pm}$ boson production using the longitudinally polarized proton-proton collisions at RHIC at a center of mass energy of 510 GeV. The measured asymmetries can be used to extract the helicity-dependent distribution functions of up and down quarks and antiquarks (Δu, Δd, $\Delta\bar{u}$, $\Delta\bar{d}$) and the difference between antiquarks distributions ($\Delta\bar{u} - \Delta\bar{d}$).

The results presented in this thesis from the data collected at the STAR experiment provide the most precise measurement of $W^{\pm}$ A_L to date in the word. Combined with all prior STAR W A_L (RHIC results) results in a future global analysis, this results will provide the most precise constraints of Δu, Δd, $\Delta\bar{u}$, $\Delta\bar{d}$ in the range of partonic momentum fraction, x, of $0.01 < x < 0.27$.

The results shown here are compared to the existing theoretical predictions based on DIS / SIDIS, and one can see that the measured W^{-} asymmetry in the negative paseudorapidity region is deviated from the predictions. This region is largely sensitive to the anti-up quarks, thus this results indicate a larger positive anti-up quark polarization than the theoretical predictions. A similar deviation from the theoretical prediction was first observed during the STAR 2012 W single-spin asymmetry measurement. This implies that the results presented in this thesis further confirm the observed deviation. Here, one could conclude that in the kinematic region of $0.01 < x < 0.27$, the anti-up sea quark shows a large positive polarization and thus, add a positive spin contribution to the spin of the proton.

With the suggestive larger positive $\Delta\bar{u}$ than DIS / SIDIS extraction and slightly more negative $\Delta\bar{d}$ as seen from the results presented in this thesis, one can expect to extract large positive $\Delta\bar{u} - \Delta\bar{d}$ than what was predicted from DIS / SIDIS. In addition, based on the recent extraction of $\Delta\bar{u}$ and $\Delta\bar{d}$ using STAR 2012 data as shown in Figure 9.11, 9.10 one can also further predict that the results presented in this thesis together with prior STAR W A_L results to show a impact on the difference between the polarized and unpolarized sea, ($|\Delta\bar{u} - \Delta\bar{d}| > |\bar{u} - \bar{d}|$) as expected by the chiral quark soliton model than what is predicted based on DIS / SIDIS. The reduction of uncertainty in these results will further help to analyze the similarities and differences between various non-perturbative model predictions and NLO calculations of the flavor asymmetry of the sea.

The natural question that comes to my mind is then, can we do better?. The systematic uncertainty of the results obtained in this thesis is less than 10% of the total statistical uncertainty, which implies that the ratio between statistical to systematic uncertainty is still large. This tells me that, we can further improve this results by asking two questions. How much can we improve the results with existing resources (existing data), and if additional resources are to be available, how could these results be improved? Regarding the former, one can see that the total W bosons that were reconstructed in this thesis using data set of total integrated luminosity of 246.6 pb^{-1}, is $\sim$ 10000. Can we increase the reconstruction efficiency of W bosons by further optimizing the W selection algorithm as discussed in Chapter 7? During the analysis, analysis cuts based on the calorimeter were optimized to larger extent. However, I tend to suggest that one can further improve the selection cuts related to tracking in the TPC by improving the software algorithms that were used for the track reconstructions in this analysis. Yet again, one could not expect a significant impact on the final asymmetry results through further improvements on systematic uncertainties based on existing resources. However, the expected larger uncertainties in the W A_L analysis at forward and backward regions could largely benefit from such studies of reducing systematic uncertainties.

On the other hand a possible future longitudinally polarized protons+protons runs at RHIC could certainly have a significant impact. More data would indeed reduced the statistical uncertainty. I would suggest that roughly the integrated luminosity similar to the data set used in this analysis can reduced the statistical uncertainty of W A_L significantly once combined with the the data used in this analysis. In addition, further data taking and analyses in the extended kinematic coverage using the STAR detectors EEMC[1] and FGT[2] would provide constraint on the helicity-dependent distribution at low x region. Forward and backward rapidity regions are sensitive to further smaller and larger x values and provide a cleaner separation of $\Delta\bar{u}$ and $\Delta\bar{d}$. Another aspect that one could consider is, an increase in the center of mass energy, $\sqrt{s}$ of RHIC collisions. An increase in $\sqrt{s}$ would result in an increase in W production cross section. However, one must also pay attention to the increase in depolarizing effects with increasing energy and thus the impact on maintaining stable polarization. Nevertheless, this would certainly be an option to be considered in order to increase the statistics by increasing W production cross section. By considering the above facts, I believe a future run on longitudinally polarized proton+proton collision at RHIC would provide advantages to further and precisely understand the role of individual anti-quarks polarization to the proton and the nature of the polarized nucleon sea.

As of this writing, no plans have been made to offer longitudinally polarized proton proton collisions at the RHIC in the near future. Thus the work done in this thesis will remain as the most precise measurements of W asymmetry at

[1] Preliminary results of the analysis using EEMC for the STAR 2013 data has released by the time of this writing.

[2] Analysis is ongoing in the very forward region using FGT for the STAR 2013 data by the time of this writing.

the RHIC. Combined with two prior year's W asymmetry measurements (2009, 2011+2012) at the STAR and all the same measurements at the PHENIX (2009, 2011+2011, and 2013) would provide the most precise constrain to up and down quarks and antiquarks polarization in the RHIC kinematic range ($0.05 < x < 0.2$). The future EIC facility will probe these distribution at a lower x region than the RHIC by means of DIS and SIDIS [126].

BIBLIOGRAPHY

[1] P. V. Pobylitsa, M. V. Polyakov, K. Goeke, T. Watabe, and C. Weiss. Isovector unpolarized quark distribution in the nucleon in the large-N_c limit. *Phys.Rew.D*, 59(3):034024, February 1999.
Cited on page(s): 3, 32

[2] J. J. Thomson M.A. F.R.S. *Philosophical Magazine Series 5*, 44:293–316, 1897.
Cited on page(s): 6

[3] H. Geiger and E. Marsden. "lxi. the laws of deflexion of a particles through large angles". *Philosophical Magazine Series 6*, 25:604, 1913.
Cited on page(s): 6

[4] Physics at the British Association. *"nature"*, 106:357–358, November 1920.
Cited on page(s): 7

[5] J. Chadwick. "the existence of a neutron". *Proceedings of the Royal Society of London A: Mathematical, Physical and Engineering Sciences*, 136(830):692–708, 1932.
Cited on page(s): 8

[6] N. Kemmer. "hideki yukawa. 23 january 1907-8 september 1981". *Biographical Memoirs of Fellows of the Royal Society*, 29:660–676, 1983.
Cited on page(s): 8

[7] V. D. Hopper and S. Biswas. Evidence Concerning the Existence of the New Unstable Elementary Neutral Particle. *Physical Review*, 80:1099–1100,

December 1950.
Cited on page(s): 9

[8] T. D. Lee and C. N. Yang. Question of Parity Conservation in Weak Interactions. *Physical Review*, 104:254–258, October 1956.
Cited on page(s): 10

[9] Murray Gell-Mann. Symmetries of baryons and mesons. *Phys. Rev.*, 125:1067–1084, Feb 1962.
Cited on page(s): 10, 11

[10] V. E. Barnes, P. L. Connolly, D. J. Crennell, B. B. Culwick, W. C. Delaney, W. B. Fowler, and et.al.
Cited on page(s): 11

[11] Murray Gell-Mann. A Schematic Model of Baryons and Mesons. *Phys. Lett.*, 8:214–215, 1964.
Cited on page(s): 11

[12] G. Zweig. An SU_3 model for strong interaction symmetry and its breaking; Version 1. (CERN-TH-401), Jan 1964.
Cited on page(s): 11

[13] G. Zweig. An SU_3 model for strong interaction symmetry and its breaking; Version 2. (CERN-TH-412):80 p, Feb 1964.
Cited on page(s): 11

[14] G. Zweig. Memories of Murray and the Quark Model. *International Journal of Modern Physics A*, 25:3863–3877, 2010.
Cited on page(s): 11

[15] S. Sakata. On a Composite Model for the New Particles. *Progress of Theoretical Physics*, 16:686–688, December 1956.
Cited on page(s): 12

[16] J. D. Bjorken and S. L. Glashow. Elementary Particles and SU(4). *Phys. Lett.*, 11:255–257, 1964.
Cited on page(s): 12

[17] S. L. Glashow, J. Iliopoulos, and L. Maiani. Weak interactions with lepton-hadron symmetry. *Phys. Rev. D*, 2:1285–1292, Oct 1970.
Cited on page(s): 12

[18] Richard P. Feynman. Very high-energy collisions of hadrons. *Phys. Rev. Lett.*, 23:1415–1417, Dec 1969.
Cited on page(s): 12, 22

[19] E. D. Bloom, D. H. Coward, H. DeStaebler, J. Drees, G. Miller, L. W. Mo, R. E. Taylor, M. Breidenbach, J. I. Friedman, G. C. Hartmann, and H. W. Kendall. High-energy inelastic $e{-}p$ scattering at 6^0 and 10^0. *Phys. Rev. Lett.*, 23:930–934, Oct 1969.
Cited on page(s): 13, 21

[20] J. D. Bjorken and E. A. Paschos. Inelastic electron-proton and γ-proton scattering and the structure of the nucleon. *Phys. Rev.*, 185:1975–1982, Sep 1969.
Cited on page(s): 13

[21] J. E. Augustin, A. M. Boyarski, M. Breidenbach, F. Bulos, J. T. Dakin, G. J. Feldman, G. E. Fischer, D. Fryberger, G. Hanson, B. Jean-Marie, R. R. Larsen, V. Lüth, H. L. Lynch, D. Lyon, C. C. Morehouse, J. M. Paterson, M. L. Perl, B. Richter, P. Rapidis, R. F. Schwitters, W. M. Tanenbaum, F. Vannucci, G. S. Abrams, D. Briggs, W. Chinowsky, C. E. Friedberg, G. Goldhaber, R. J. Hollebeek, J. A. Kadyk, B. Lulu, F. Pierre, G. H. Trilling, J. S. Whitaker, J. Wiss, and J. E. Zipse. Discovery of a narrow resonance in e^+e^- annihilation. *Phys. Rev. Lett.*, 33:1406–1408,

Dec 1974.

Cited on page(s): 13

[22] J. J. Aubert, U. Becker, P. J. Biggs, J. Burger, M. Chen, G. Everhart, P. Goldhagen, J. Leong, T. McCorriston, T. G. Rhoades, M. Rohde, Samuel C. C. Ting, Sau Lan Wu, and Y. Y. Lee. Experimental observation of a heavy particle j. *Phys. Rev. Lett.*, 33:1404–1406, Dec 1974.

Cited on page(s): 13

[23] L. Clavelli and T. C. Yang. Phenomenology of the ψ (3105) and the hypothesis of charm. *Physics Letters B*, 57:83–86, June 1975.

Cited on page(s): 14

[24] M. L. Perl, G. S. Abrams, A. M. Boyarski, M. Breidenbach, D. D. Briggs, F. Bulos, W. Chinowsky, J. T. Dakin, G. J. Feldman, C. E. Friedberg, D. Fryberger, G. Goldhaber, G. Hanson, F. B. Heile, B. Jean-Marie, J. A. Kadyk, R. R. Larsen, A. M. Litke, D. Lüke, B. A. Lulu, V. Lüth, D. Lyon, C. C. Morehouse, J. M. Paterson, F. M. Pierre, T. P. Pun, P. A. Rapidis, B. Richter, B. Sadoulet, R. F. Schwitters, W. Tanenbaum, G. H. Trilling, F. Vannucci, J. S. Whitaker, F. C. Winkelmann, and J. E. Wiss. Evidence for anomalous lepton production in $e^+ - e^-$ annihilation. *Phys. Rev. Lett.*, 35:1489–1492, Dec 1975.

Cited on page(s): 14

[25] S. W. Herb, D. C. Hom, L. M. Lederman, J. C. Sens, H. D. Snyder, J. K. Yoh, J. A. Appel, B. C. Brown, C. N. Brown, W. R. Innes, K. Ueno, T. Yamanouchi, A. S. Ito, H. Jöstlein, D. M. Kaplan, and R. D. Kephart. Observation of a dimuon resonance at 9.5 gev in 400-gev proton-nucleus collisions. *Phys. Rev. Lett.*, 39:252–255, Aug 1977.

Cited on page(s): 14

[26] F. Abe, H. Akimoto, A. Akopian, M. G. Albrow, S. R. Amendolia, D. Amidei, J. Antos, C. Anway-Wiese, S. Aota, G. Apollinari, and et al. Observation of Top Quark Production in p$\bar{p}$ Collisions with the Collider Detector at Fermilab. *Physical Review Letters*, 74:2626–2631, April 1995.
Cited on page(s): 14

[27] David J. Griffiths. INTRODUCTION TO ELEMENTARY PARTICLES. *NEW YORK, USA: WILEY (1987) 392p*, 1987.
Cited on page(s): 15, 16, 18

[28] A. Pich. The Standard Model of Electroweak Interactions. *ArXiv High Energy Physics - Phenomenology e-prints*, February 2005.
Cited on page(s): 15, 17

[29] https://sciencenode.org/spotlight/go-particle-quest-first-cern-hackfest.php.
Cited on page(s): xv, 17

[30] J. Bernstein. Spontaneous symmetry breaking, gauge theories, the higgs mechanism and all that. *Rev. Mod. Phys.*, 46:7–48, 1974. [Erratum: Rev. Mod. Phys.46,855(1974)].
Cited on page(s): 18

[31] A. D. Martin. Proton Structure, Partons, QCD, DGLAP and Beyond. *Acta Physica Polonica B*, 39:2025, September 2008.
Cited on page(s): 19, 23, 25

[32] J. D. Bjorken. Asymptotic sum rules at infinite momentum. *Phys. Rev.*, 179:1547–1553, Mar 1969.
Cited on page(s): 21

[33] M. Breidenbach, J. I. Friedman, H. W. Kendall, E. D. Bloom, D. H. Coward, H. DeStaebler, J. Drees, L. W. Mo, and R. E. Taylor. Observed

behavior of highly inelastic electron-proton scattering. *Phys. Rev. Lett.*, 23:935–939, Oct 1969.
Cited on page(s): 21

[34] Richard E. Taylor. Deep inelastic scattering: The early years. *Rev. Mod. Phys.*, 63:573–595, Jul 1991.
Cited on page(s): 22

[35] Henry W. Kendall. Deep inelastic scattering: Experiments on the proton and the observation of scaling. *Rev. Mod. Phys.*, 63:597–614, Jul 1991.
Cited on page(s):

[36] Jerome I. Friedman. Deep inelastic scattering: Comparisons with the quark model. *Rev. Mod. Phys.*, 63:615–627, Jul 1991.
Cited on page(s): 22

[37] C. G. Callan and David J. Gross. High-energy electroproduction and the constitution of the electric current. *Phys. Rev. Lett.*, 22:156–159, Jan 1969.
Cited on page(s): 22

[38] Julius Kuti and Victor F. Weisskopf. Inelastic lepton-nucleon scattering and lepton pair production in the relativistic quark-parton model. *Phys. Rev. D*, 4:3418–3439, Dec 1971.
Cited on page(s): 22

[39] Frank Wilczek. QCD made simple. *Phys. Today*, 53N8:22–28, 2000.
Cited on page(s): 22

[40] K. A. Olive et al. Review of Particle Physics. *Chin. Phys.*, C38:090001, 2014.
Cited on page(s): xv, 23, 24

[41] J. W. Negele. Understanding parton distributions from lattice QCD: present limitations and future promise. *Nuclear Physics A*, 711:281–290,

December 2002.

Cited on page(s): 24

[42] J. C. Collins, D. E. Soper, and G. Sterman. Factorization of Hard Processes in QCD. *ArXiv High Energy Physics - Phenomenology e-prints*, September 2004.

Cited on page(s): 24

[43] A. D. Martin, W. J. Stirling, R. S. Thorne, and G. Watt. Parton distributions for the LHC. *European Physical Journal C*, 63:189–285, September 2009.

Cited on page(s): xv, 25, 26

[44] S. D. Bass. The Proton Spin Puzzle:. where are we Today? *Modern Physics Letters A*, 24:1087–1101, 2009.

Cited on page(s): 27

[45] John Ellis and Robert Jaffe. Sum rule for deep-inelastic electroproduction from polarized protons. *Phys. Rev. D*, 9:1444–1446, Mar 1974.

Cited on page(s): 27

[46] M. J. Alguard, W. W. Ash, G. Baum, J. E. Clendenin, P. S. Cooper, D. H. Coward, R. D. Ehrlich, A. Etkin, V. W. Hughes, H. Kobayakawa, K. Kondo, M. S. Lubell, R. H. Miller, D. A. Palmer, W. Raith, N. Sasao, K. P. Schüler, D. J. Sherden, C. K. Sinclair, and P. A. Souder. Deep inelastic scattering of polarized electrons by polarized protons. *Phys. Rev. Lett.*, 37:1261–1265, Nov 1976.

Cited on page(s): 27

[47] G. Baum, M. R. Bergström, P. R. Bolton, J. E. Clendenin, N. R. DeBotton, S. K. Dhawan, Y. N. Guo, V. R. Harsh, V. W. Hughes, K. Kondo, M. S. Lubell, Z. L. Mao, R. H. Miller, S. Miyashita, K. Morimoto, U. F. Moser, I. Nakano, R. F. Oppenheim, D. A. Palmer, L. Panda, W. Raith, N. Sasao,

K. P. Schüler, M. L. Seely, P. A. Souder, S. J. St. Lorant, K. Takikawa, and M. Werlen. New measurement of deep-inelastic $e{-}p$ asymmetries. *Phys. Rev. Lett.*, 51:1135–1138, Sep 1983.
Cited on page(s): 27

[48] J. Ashman et al. An Investigation of the Spin Structure of the Proton in Deep Inelastic Scattering of Polarized Muons on Polarized Protons. *Nucl. Phys.*, B328:1, 1989.
Cited on page(s): 27, 28, 29

[49] R. L. Jaffe and A. Manohar. The g_1 problem: Deep inelastic electron scattering and the spin of the proton. *Nuclear Physics B*, 337:509–546, June 1990.
Cited on page(s): 29

[50] Daniel de Florian, Rodolfo Sassot, Marco Stratmann, and Werner Vogelsang. Evidence for polarization of gluons in the proton. *Phys. Rev. Lett.*, 113:012001, Jul 2014.
Cited on page(s): 30

[51] A. Airapetian, Akopov, and et al. Quark helicity distributions in the nucleon for up, down, and strange quarks from semi-inclusive deep-inelastic scattering. *Phys. Rev. D*, 71:012003, Jan 2005.
Cited on page(s): 30

[52] Daniel de Florian, Rodolfo Sassot, and Marco Stratmann. Global analysis of fragmentation functions for pions and kaons and their uncertainties. *Phys. Rev. D*, 75:114010, Jun 2007.
Cited on page(s): 30

[53] M. Soleymaninia, A. N. Khorramian, S. M. Moosavi Nejad, and F. Arbabifar. Determination of pion and kaon fragmentation functions including spin asymmetries data in a global analysis. *Phys. Rev. D*, 88(5):054019,

September 2013.
Cited on page(s): 30

[54] Elliot Leader, Aleksander V. Sidorov, and Dimiter B. Stamenov. Determination of polarized parton densities from a qcd analysis of inclusive and semi-inclusive deep inelastic scattering data. *Phys. Rev. D*, 82:114018, Dec 2010.
Cited on page(s): 31, 172

[55] https://nnpdf.hepforge.org.
Cited on page(s): 31, 176

[56] Daniel de Florian, Rodolfo Sassot, Marco Stratmann, and Werner Vogelsang. Global analysis of helicity parton densities and their uncertainties. *Phys. Rev. Lett.*, 101:072001, Aug 2008.
Cited on page(s): xv, 31, 32, 42, 172, 180

[57] E. A. Hawker, T. C. Awes, and et.al. Measurement of the light antiquark flavor asymmetry in the nucleon sea. *Phys. Rev. Lett.*, 80:3715–3718, Apr 1998.
Cited on page(s): 32

[58] J. C. Peng, G. T. Garvey, T. C. Awes, M. E. Beddo, and ph/9804288. 58(9):092004, November 1998.
Cited on page(s): 32

[59] A. E. Dorokhov and N. I. Kochelev. Instanton induced asymmetric quark configurations in the nucleon and parton sum rules. *Phys. Lett.*, B304:167–175, 1993.
Cited on page(s): 32

[60] R. S. Bhalerao. Statistical model for the nucleon structure functions. *Physics Letters B*, 380:1–6, February 1996.
Cited on page(s): 32

[61] M. G. Alekseev, V. Y. Alexakhin, Y. Alexandrov, G. D. Alexeev, A. Amoroso, A. Austregesilo, B. Badełek, F. Balestra, J. Barth, G. Baum, and et al. Quark helicity distributions from longitudinal spin asymmetries in muon-proton and muon-deuteron scattering. *Physics Letters B*, 693:227–235, October 2010.
Cited on page(s): xv, 33

[62] M. Wakamatsu. Light-flavor sea-quark distributions in the nucleon in the su(3) chiral quark soliton model. i. phenomenological predictions. *Phys. Rev. D*, 67:034005, Feb 2003.
Cited on page(s): xv, 33

[63] S. Kumano and M. Miyama. Polarized light-antiquark distributions in a meson-cloud model. *Phys. Rev. D*, 65:034012, Jan 2002.
Cited on page(s): xv, 33

[64] C. Bourrely, J. Soffer, and F. Buccella. A statistical approach for polarized parton distributions. *European Physical Journal C*, 23:487–501, April 2002.
Cited on page(s): xv, 33

[65] G. Bunce. The First RHIC Spin Run - at PHENIX and PP2PP. *ArXiv High Energy Physics - Experiment e-prints*, July 2002.
Cited on page(s): 34

[66] Claude Bourrely and Jacques Soffer. Parton distributions and parity violating asymmetries in W+- and Z production at RHIC. *Phys. Lett.*, B314:132–138, 1993.
Cited on page(s): 34

[67] Gerry Bunce, Naohito Saito, Jacques Soffer, and Werner Vogelsang. Prospects for spin physics at RHIC. *Ann. Rev. Nucl. Part. Sci.*, 50:525–575, 2000.
Cited on page(s): xv, 34, 35

[68] Edmond L. Berger and Pavel M. Nadolsky. Longitudinal parity-violating asymmetry in hadronic decays of weak bosons in polarized proton collisions. *Phys. Rev. D*, 78:114010, Dec 2008.
Cited on page(s): 35, 40

[69] Daniel de Florian and Werner Vogelsang. Helicity parton distributions from spin asymmetries in W-boson production at RHIC. *Phys. Rev. D*, 81:094020, May 2010.
Cited on page(s): xvi, 38, 40, 41, 42, 43, 44, 164, 172, 176

[70] STAR Collaboration, L. Adamczyk, J. K. Adkins, G. Agakishiev, M. M. Aggarwal, Z. Ahammed, I. Alekseev, A. Aparin, D. Arkhipkin, E. C. Aschenauer, and et al. Measurement of the transverse single-spin asymmetry in $p^{\uparrow} + p \rightarrow W^{\pm}/Z^0$ at RHIC. *ArXiv e-prints*, November 2015.
Cited on page(s): 39

[71] P. M. Nadolsky and C.-P. Yuan. Single-spin physics with weak bosons at RHIC. *Nuclear Physics B*, 666:31–55, August 2003.
Cited on page(s): 40, 42, 172

[72] D. de Florian, S. Frixione, A. Signer, and W. Vogelsang. Next-to-leading order jet cross sections in polarized hadronic collisions. *Nuclear Physics B*, 539:455–476, February 1999.
Cited on page(s): 42

[73] I et al. Alekseev. Polarized proton collider at RHIC. *Nuclear Instruments and Methods in Physics Research A*, 499:392–414, March 2003.
Cited on page(s): xvi, 45, 46, 50, 51, 52, 54, 55

[74] A et al. Zelenski. Optically pumped polarized H ion source for RHIC spin physics. *AIP: Review of Scientific Instruments*, 73:888, February 2002.
Cited on page(s): 45, 46

[75] A et al. Zelenski. The RHIC polarized source upgrade. *BNL-102509-2013-IR*, October 2013.
Cited on page(s): 46, 48

[76] A et al. Zelenski. The RHIC polarized source upgrade. *Presented at the 19th International Spin Physics Symposium (SPIN 2010)*, October 2013.
Cited on page(s): 48

[77] J.G et al. Alsssi. PERFORMANCE OF THE NEW AGS RFQ PREINJECTOR. *Proceedings of the IEEE Particle Accelerator Conference*, March 1989.
Cited on page(s): 48

[78] J.F. et al. SHEEHAN. THE RF SYSTEM FOR THE AGS LINAC INJECTOR*. *IEEE TRANSACTIONS ON NUCLEAR SCIENCE*, 1967.
Cited on page(s): 48

[79] Thomas Roser. High Intensity Beam Operation of the Brookhaven AGS*. *Workshop on Instabilties of High Intensity Hadron Beams in Rings*, 1999.
Cited on page(s): 48

[80] H. et al. Huang. POLARIZED PROTON ACCELERATION AT THE BROOKHAVEN AGS -AN UPDATE*. *Submitted to: EPAC 02, Paris France, 6/2-7/02*, 2002.
Cited on page(s): 49

[81] T. et al. Roser. Accelerating and Colliding Polarized Protons in RHIC with Siberian Snakes. *Proceedings of EPAC 2002, Paris, France*, 2002.
Cited on page(s): 49

[82] N. Tsoupas, M. Bai, H. Huang, and T. Roser. Transferring Polarized Proton Beam from AGS to RHIC at energies below the Spin Resonance $G = 36_\gamma$=36+v_y of AGS. *Collider-Accelerator Department*, October 1999.
Cited on page(s): 49

[83] J. Claus and H. Foelsche. Beam Transfer from AGS to RHIC. *Accelerator Development Department RHIC Technical Note 47, BROOKHAVEN NATIONAL LABORATORY*, December 1988.
Cited on page(s): 49

[84] W. W. MacKay et al. Spin Dynamics in AGS and RHIC. *Conf. Proc.*, C030512:405, 2003.
Cited on page(s): 51

[85] M. Harrison, Stephen G. Peggs, and T. Roser. The RHIC accelerator. *Ann. Rev. Nucl. Part. Sci.*, 52:425–469, 2002.
Cited on page(s): 51, 54

[86] H. Okada, I. G. Alekseev, A. Bravar, G. Bunce, S. Dhawan, R. Gill, W. Haeberli, O. Jinnouchi, A. Khodinov, Y. Makdisi, A. Nass, N. Saito, E. J. Stephenson, D. N. Svirida, T. Wise, and A. Zelenski. Measurement of the Analyzing Power A_N in *pp* Elastic Scattering in the CNI Region with a Polarized Atomic Hydrogen Gas Jet Target. *ArXiv High Energy Physics - Experiment e-prints*, December 2006.
Cited on page(s): 55

[87] Absolute polarized H-jet polarimeter development, for RHIC. *Nucl. Instrum. Meth.*, A536:248–254, 2005.
Cited on page(s): 55, 57, 58

[88] K. H. Ackermann et al. STAR detector overview. *Nucl. Instrum. Meth.*, A499:624–632, 2003.
Cited on page(s): 59

[89] K. Adcox et al. PHENIX detector overview. *Nucl. Instrum. Meth.*, A499:469–479, 2003.
Cited on page(s): 59

[90] M. Anderson et al. The Star time projection chamber: A Unique tool for studying high multiplicity events at RHIC. *Nucl. Instrum. Meth.*, A499:659–678, 2003.
Cited on page(s): 61

[91] F. Bergsma et al. The STAR detector magnet subsystem. *Nucl. Instrum. Meth.*, A499:633–639, 2003.
Cited on page(s): 61

[92] L. Kotchenda, S. Kozlov, P. Kravtsov, A. Markov, M. Strikhanov, B. Stringfellow, V. Trofimov, R. Wells, and H. Wieman. STAR TPC gas system. *Nuclear Instruments and Methods in Physics Research Section A: Accelerators, Spectrometers, Detectors and Associated Equipment*, 499, December 2003.
Cited on page(s): 62

[93] M. Anderson, F. Bieser, R. Bossingham, D. Cebra, E. L. Hjort, S. R. Klein, S. Kleinfelder, C. Q. Vu, and H. Wieman. A readout system for the STAR time projection chamber. *Nuclear Instruments and Methods in Physics Research A*, 499:679–691, March 2003.
Cited on page(s): 62

[94] J. Abele et al. The laser system for the STAR time projection chamber. *Nucl. Instrum. Meth.*, A499:692–702, 2003.
Cited on page(s): 63

[95] M. Shao, O. Barannikova, X. Dong, Y. Fisyak, L. Ruan, P. Sorensen, and Z. Xu. Extensive particle identification with TPC and TOF at the STAR experiment. *Nuclear Instruments and Methods in Physics Research*

A, 558:419–429, March 2006.
Cited on page(s): 64, 83

[96] Beddo, M. and others. The STAR barrel electromagnetic calorimeter. *Nucl. Instrum. Meth.*, A499:725–739, 2003.
Cited on page(s): 64, 65

[97] C. W. Fabjan and F. Gianotti. Calorimetry for particle physics. *Rev. Mod. Phys.*, 75:1243–1286, 2003.
Cited on page(s): 64, 76

[98] C. E. Allgower et al. The STAR endcap electromagnetic calorimeter. *Nucl. Instrum. Meth.*, A499:740–750, 2003.
Cited on page(s): 66

[99] R Reed, J Balewski, L. S. Barnby, A. Ogawa, and J van Leeuwen M. Lauret. Vertex finding in pile-up rich events for p+p and d+Au collisions at STAR. *Journal of Physics: Conference Series*, 219:032–020, 2010.
Cited on page(s): 73

[100] STAR Collaboration, L. Adamczyk, J. K. Adkins, G. Agakishiev, M. M. Aggarwal, Z. Ahammed, I. Alekseev, J. Alford, C. D. Anson, A. Aparin, and et al. Measurement of longitudinal spin asymmetries for weak boson production in polarized proton-proton collisions at RHIC. *ArXiv e-prints*, April 2014.
Cited on page(s): xxi, 78, 173, 176, 177, 178, 179

[101] F.S. Bieser, H.J. Crawford, J. Engelage, G. Eppley, L.C. Greiner, E.G. Judd, S.R. Klein, F. Meissner, R. Minor, Z. Milosevich, G. Mutchler, J.M. Nelson, J. Schambach, A.S. VanderMolen, H. Ward, and P. Yepes. The STAR Trigger. 499:766–777, 2003.
Cited on page(s): 80, 83, 97, 98

[102] T. M. Cormier, A. I. Pavlinov, M. V. Rykov, V. L. Rykov, and K. E. Shestermanov. STAR barrel electromagnetic calorimeter absolute calibration using "minimum ionizing particles" from collisions at RHIC. *Nuclear Instruments and Methods in Physics Research A*, 483:734–746, May 2002.
Cited on page(s): 80

[103] R. Brun, R. Hagelberg, M. Hansroul, and J. C. Lassalle. Geant: Simulation Program for Particle Physics Experiments. User Guide and Reference Manual. 1978.
Cited on page(s): 84, 104

[104] M. M. Aggarwal, Z. Ahammed, A. V. Alakhverdyants, I. Alekseev, J. Alford, B. D. Anderson, C. D. Anson, D. Arkhipkin, G. S. Averichev, J. Balewski, and et al. Measurement of the Parity-Violating Longitudinal Single-Spin Asymmetry for W Boson Production in Polarized Proton-Proton Collisions at s=500GeV. *Physical Review Letters*, 106(6):062002, February 2011.
Cited on page(s): 95, 164, 178

[105] L. Adamczyk, G. Agakishiev, M. M. Aggarwal, Z. Ahammed, A. V. Alakhverdyants, I. Alekseev, J. Alford, B. D. Anderson, C. D. Anson, D. Arkhipkin, and et al. Measurement of the W$\rightarrow$eν and Z/$\gamma^*\rightarrow$e$^+$e$^-$ production cross sections at mid-rapidity in proton-proton collisions at s=500GeV. *Physical Review D*, 85(9):092010, May 2012.
Cited on page(s): 95, 136

[106] http://www.agsrhichome.bnl.gov/RHIC/Runs/index.html.
Cited on page(s): xvii, 95, 96

[107] P. R. et al. Cameron. The RHIC wall current monitor system. *18th IEEE Particle Accelerator Conference*, page 21462148, 1999.
Cited on page(s): 103

[108] A. Drees, Zhangbu Xu, B. Fox, and Haibin Huang. Results from vernier scans at rhic during the pp run 2001-2002. *Proceedings of the 2003 Particle Accelerator Conference*, 3:1688–1690 vol.3, May 2003.
Cited on page(s): 103

[109] S van der Meer. Calibration of the effective beam height in the ISR. (CERN-ISR-PO-68-31. ISR-PO-68-31), 1968.
Cited on page(s): 103

[110] R. Corliss. Measurement of absolute luminsotiy for STAR BHT3 trigger for p+p collisions at sqrt of 500 GeV in 2009 (Internal STAR note, 533).
Cited on page(s): 103

[111] T. Sjöstrand, S. Mrenna, and P. Skands. PYTHIA 6.4 physics and manual. *Journal of High Energy Physics*, 5:026, May 2006.
Cited on page(s): 104

[112] Peter Z. Skands. Tuning monte carlo generators: The perugia tunes. *Phys. Rev. D*, 82:074018, Oct 2010.
Cited on page(s): 104

[113] P. Golonka, B. Kersevan, T. Pierzchała, E. Richter-Was, Z. Was, and M. Worek. The tauola-photos-F environment for the TAUOLA and PHOTOS packages, release II. *Computer Physics Communications*, 174:818–835, May 2006.
Cited on page(s): 104

[114] Matteo Cacciari, Gavin P. Salam, and title= Gregory Soyez.
Cited on page(s): 119

[115] STAR Collaboration, L. Adamczyk, J. K. Adkins, G. Agakishiev, M. M. Aggarwal, Z. Ahammed, I. Alekseev, J. Alford, C. D. Anson, A. Aparin,

and et al. Precision Measurement of the Longitudinal Double-spin Asymmetry for Inclusive Jet Production in Polarized Proton Collisions at $\sqrt{s} =$ 200 GeV. *ArXiv e-prints*, May 2014.
Cited on page(s): 119

[116] J. Beringer and et.al Arguin. Review of particle physics. *Phys. Rev. D*, 86:010001, Jul 2012.
Cited on page(s): 132

[117] Elliot Leader. Spin in particle physics. *Camb. Monogr. Part. Phys. Nucl. Phys. Cosmol.*, 15:pp.1–500, 2011.
Cited on page(s): 158

[118] OPAL Collaboration, K. Ackerstaff, and et al. Measurement of the Michel parameters in leptonic tau decays. *European Physical Journal C*, 8:3–21, March 1999.
Cited on page(s): 163

[119] Justin Stevens Jan Balewski and Jinlong Zhang.
Cited on page(s): 163

[120] RHIC polarization for Runs 9-15. *RHIC polarimetry group.*
Cited on page(s): 165

[121] A. Adare, C. Aidala, N. N. Ajitanand, Y. Akiba, R. Akimoto, J. Alexander, M. Alfred, K. Aoki, N. Apadula, Y. Aramaki, and et al. Measurement of parity-violating spin asymmetries in W production at midrapidity in longitudinally polarized p +p collisions. *Phys. Rev. D*, 93(5):051103, March 2016.
Cited on page(s): 173, 174

[122] E. R. Nocera, R. D. Ball, S. Forte, G. Ridolfi, and J. Rojo. A first unbiased global determination of polarized PDFs and their uncertainties. *Nuclear*

Physics B, 887:276–308, October 2014.
Cited on page(s): xxi, 176, 177, 180

[123] J. R. Stevens and for the STAR Collaboration. The STAR W Program at RHIC. *ArXiv e-prints*, February 2013.
Cited on page(s): 176

[124] E. C. Aschenauer, A. Bazilevsky, K. Boyle, K. O. Eyser, R. Fatemi, C. Gagliardi, M. Grosse-Perdekamp, J. Lajoie, Z. Kang, Y. Kovchegov, J. Koster, I. Nakagawa, R. Sassot, R. Seidl, E. Sichtermann, M. Stratmann, W. Vogelsang, A. Vossen, S. W. Wissink, and F. Yuan. The RHIC Spin Program: Achievements and Future Opportunities. *ArXiv e-prints*, March 2013.
Cited on page(s): xxi, 176, 178, 179

[125] E. R. Nocera. Impact of Recent RHIC Data on Helicity-Dependent Parton Distribution Functions. *ArXiv e-prints*, February 2017.
Cited on page(s): 178

[126] A. Accardi, Albacete, and el. Electron Ion Collider: The Next QCD Frontier - Understanding the glue that binds us all. *ArXiv e-prints*, December 2012.
Cited on page(s): 184

APPENDIX

APPENDIX A
LIST OF STAR RUNS

A.1 Period I runs

R14076033 R14076042 R14076043 R14076044 R14076047 R14076048 R14076055 R14076060 R14076067 R14076068 R14076071 R14076072 R14076073 R14076075 R14076081 R14076082 R14076083 R14076084 R14076085 R14076086 R14076087 R14076088 R14077001 R14077004 R14077005 R14077006 R14077007 R14077008 R14077009 R14077011 R14077012 R14077013 R14077015 R14077016 R14077017 R14077018 R14077019 R14077020 R14077021 R14077042 R14077043 R14077044 R14077045 R14077046 R14077047 R14077048 R14077051 R14077055 R14077058 R14077059 R14077060 R14078016 R14078017 R14078018 R14078019 R14078021 R14078022 R14078023 R14078037 R14078038 R14078039 R14078042 R14078044 R14078045 R14078046 R14078049 R14078051 R14078052 R14078053 R14078054 R14078055 R14079001 R14079002 R14079003 R14079004 R14079007 R14079008 R14079010 R14079011 R14079013 R14079014 R14079015 R14079016 R14080009 R14080017 R14080018 R14080019 R14080036 R14080037 R14080038 R14080044 R14080045 R14081004 R14081005 R14081006 R14081007 R14081009 R14081010 R14081013 R14081014 R14082029 R14082030 R14082031 R14082033 R14082034 R14082036 R14082037 R14083005 R14083006 R14083007 R14083008 R14083009 R14083019 R14083020 R14083021 R14083022 R14083034 R14083036 R14083038 R14083039 R14083041 R14083043 R14083044 R14083045 R14083047 R14083051 R14083055 R14083056 R14083057 R14084005 R14084008 R14084009 R14084010 R14084013 R14084014 R14084015 R14084018 R14084019 R14084020 R14084021 R14084057 R14084058 R14084059 R14084061 R14085006 R14085007 R14085008 R14085009 R14085012 R14085014 R14085016 R14085017 R14085018 R14085019

R14085022 R14085023 R14085024 R14085034 R14085035 R14085063 R14085069
R14086001 R14086013 R14086016 R14086018 R14086019 R14086020 R14086022
R14087004 R14087005 R14087019 R14087022 R14087024 R14087033 R14087035
R14087036 R14087037 R14088002 R14088003 R14088007 R14088009 R14088010
R14088027 R14088105 R14088108 R14088135 R14088136 R14088138 R14088140
R14088141 R14088142 R14089001 R14089002 R14089003 R14089004 R14089008
R14089010 R14089011 R14089012 R14089014 R14089015 R14089022 R14089023
R14089029 R14089030 R14089032 R14089033 R14089034 R14089035 R14089036
R14089037 R14089041 R14089042 R14089043 R14089044 R14089059 R14089074
R14090004 R14090005 R14090006 R14090007 R14090008 R14090010 R14090011
R14090013 R14090014 R14090015 R14090016 R14090018 R14090032 R14090033
R14090034 R14090035 R14090036 R14090037 R14090040 R14090041 R14090042
R14090045 R14090046 R14090047 R14090049 R14090050 R14090051 R14090052
R14090053 R14091002 R14091003 R14091004 R14091005 R14091006 R14091008
R14091013 R14091016 R14091017 R14091018 R14091019 R14091020 R14091021
R14091022 R14091023 R14091026 R14091027 R14091028 R14091029 R14091030
R14091033 R14091034 R14091062 R14091064 R14091065 R14092001 R14092002
R14092004 R14092005 R14092010 R14092011 R14092015 R14092024 R14092030
R14092057 R14092058 R14092061 R14092062 R14092063 R14092065 R14092067
R14092068 R14092071 R14092087 R14092090 R14092091 R14092092 R14092093
R14092097 R14092098 R14092099 R14092100 R14092101 R14092104 R14092105
R14092106 R14092107 R14092108 R14092109 R14092110 R14093001 R14093005
R14093006 R14093007 R14093008 R14093009 R14093010 R14093014 R14093015
R14093016 R14093017 R14093018 R14093019 R14093020 R14093021 R14094005
R14094006 R14094007 R14094008 R14094020 R14094022 R14094024 R14095012
R14095019 R14095020 R14095022 R14095023 R14095024 R14095025 R14095027
R14095029 R14095030 R14095034 R14095035 R14095038 R14095039 R14095044
R14096010 R14096011 R14096013 R14096014 R14096077 R14096078 R14096082
R14096083 R14096084 R14096085 R14096098 R14096099 R14096100 R14096101

R14096102 R14096104 R14096105 R14096106 R14096107 R14096108 R14097005 R14097006 R14097014 R14097018 R14097019 R14097020 R14097021 R14097022 R14097023 R14097026 R14097028 R14097030 R14097031 R14097033 R14097036 R14097037 R14097038 R14097039 R14097061 R14097062 R14097063 R14097064 R14097065 R14097066 R14097067 R14097068 R14097070 R14098004 R14098015 R14098016 R14098017 R14098026 R14098027 R14098028 R14098029 R14098031 R14098032 R14098033 R14098039 R14098044 R14098045 R14098046 R14098047 R14098048 R14098049 R14098050 R14098051 R14098052 R14098053 R14099013 R14099014 R14099015 R14099016 R14099017 R14099018 R14099020 R14099024 R14099025 R14099027 R14099029 R14099030 R14099031 R14099032 R14099033 R14099047 R14099048 R14099049 R14099050 R14099089 R14099090 R14100004 R14100009 R14100014 R14100018 R14100021 R14100022 R14100027 R14101044 R14101046 R14101048 R14101050 R14101051 R14101052 R14101053 R14101054 R14101055 R14101060 R14101061 R14101062 R14101063 R14101064 R14101065 R14101066 R14101067 R14101068 R14102029 R14102030 R14102031 R14102032 R14102034 R14102035 R14102036 R14102037 R14102041 R14102042 R14102043 R14102047 R14102049 R14104015 R14104017 R14104018 R14104021 R14104025 R14104026 R14104039 R14104040 R14104041 R14104042 R14104044 R14104046 R14104047 R14104049 R14104050 R14104051 R14104052 R14104059 R14104060 R14104061 R14104062 R14104063 R14105001 R14105002 R14105006 R14105007 R14105008 R14105009 R14105011 R14105013 R14105014 R14105015 R14105016 R14105019 R14105020 R14105021 R14105022 R14105024 R14105025 R14105029 R14105031 R14105032 R14105033 R14105034 R14105036 R14105037 R14105038 R14105039 R14105043 R14106002 R14106003 R14106004 R14106005 R14106007 R14106035 R14106036 R14106037 R14106041 R14106042 R14106043 R14107017 R14107018 R14107133 R14107134 R14107139 R14107141 R14107144 R14108001 R14108002 R14108003 R14108005 R14108006 R14108007 R14108013 R14108014 R14108015 R14108017 R14108019 R14108059 R14108075 R14108077 R14108078 R14108079 R14108080 R14108081 R14108083 R14108084 R14108085 R14108091

R14108092 R14108093 R14108095 R14108096 R14108097 R14109013 R14109014 R14109018 R14109020 R14109021 R14109022 R14109023 R14109025 R14109026 R14109027 R14109028 R14109030 R14109046 R14109047 R14109052 R14109080 R14109082 R14110004 R14110012 R14110018 R14110020 R14110021 R14110022 R14110024 R14110025 R14110026 R14110027 R14110044 R14110045 R14110046 R14110048 R14110050 R14110051 R14110052 R14110053 R14110054 R14110055 R14110056 R14110058 R14110059 R14110060 R14110061 R14110062 R14110064 R14110065 R14110072 R14110073 R14110074 R14111001 R14111003 R14111004 R14111009 R14111011 R14111013 R14111014 R14111015 R14111018 R14111020 R14111036 R14111038 R14111046 R14111047 R14111048 R14111051 R14111052 R14111053 R14111055 R14111056 R14111057 R14111058 R14111060 R14111062 R14111063 R14111064 R14111066 R14111067 R14111070 R14111071 R14112001 R14112023 R14112024 R14112027 R14112031 R14112032 R14112034 R14112035 R14112038 R14112040 R14112041 R14112042 R14112044 R14112094 R14112096 R14112098 R14113001 R14113003 R14113004 R14113006 R14113007 R14113008 R14113009 R14113010 R14113011 R14113012 R14113015 R14113016 R14113017 R14113018 R14113019 R14113035 R14113036 R14113037 R14113038 R14113039 R14113061 R14113062 R14113065 R14113066 R14113067 R14113076 R14113078 R14113093 R14113096 R14114002 R14114004 R14114005 R14114006 R14114007 R14114008 R14114011 R14114012 R14114013 R14114014 R14114015 R14114016 R14114018 R14114019 R14114020 R14115007 R14115008 R14115010 R14115011 R14115012 R14115013 R14115015 R14115017 R14115018 R14115019 R14115020 R14115022 R14115023 R14115024 R14115060 R14115062 R14115064 R14115065 R14115067 R14115068 R14115069 R14115070 R14115072 R14115073 R14115074 R14115075 R14116001 R14116002 R14116011 R14116014 R14116015 R14116016 R14116019 R14116020 R14116043 R14116044 R14116047 R14116048 R14116051 R14116055 R14116056 R14116057 R14116059 R14116060 R14116065 R14117002 R14117012 R14117013 R14117014 R14117015 R14117020 R14117021 R14117022 R14117023 R14117024 R14117025 R14117026 R14117027 R14117028 R14117047

R14117048 R14117052 R14117054 R14117055 R14117056 R14117058 R14117059
R14117061 R14117063 R14117064 R14117069 R14118014 R14118015 R14118016
R14118017 R14118018 R14118020 R14118021 R14118022 R14118023 R14118028
R14118030 R14118032 R14118033 R14118034 R14118035 R14118048 R14118049
R14118050 R14118051 R14118052 R14118056 R14118059 R14118060 R14118061
R14118063 R14118064 R14119007 R14119008 R14119009 R14119010 R14119014
R14119017 R14119018 R14119019 R14119022 R14119024 R14119026 R14119027
R14119052 R14119053 R14119059 R14119060 R14119061 R14120011 R14120017
R14120018 R14120019 R14120025 R14120026 R14120112 R14120113 R14120114
R14120115 R14120116 R14120118 R14120119 R14120120 R14120121 R14121001
R14121002 R14121004 R14121009 R14121010 R14121013 R14121014 R14121017
R14121018 R14121019 R14121020 R14121021 R14121022 R14121023 R14122006
R14122008 R14122009 R14122013 R14122014 R14122015 R14122017 R14122018
R14122019 R14122020 R14122021 R14122024 R14122025 R14122058 R14122060
R14122061 R14122062 R14123001 R14123002 R14123004 R14123005 R14123008
R14123009 R14123010 R14123015 R14123016 R14123024 R14123025 R14123026
R14123028 R14123029 R14123030 R14123031 R14123032 R14123033 R14123034
R14123035 R14123037 R14123039 R14123040 R14123053 R14123054 R14123056
R14123057 R14123059 R14123060 R14123061 R14123076 R14123077 R14123078
R14124001 R14124003 R14124004 R14124005 R14124006 R14124007 R14124009
R14124013 R14124014 R14124016 R14124017 R14124018 R14124019 R14124025
R14124026 R14124027 R14124028 R14124029 R14124030 R14124033 R14124034
R14124035 R14124036 R14124037 R14124038 R14125002 R14125003 R14125004
R14125056 R14125060 R14126003 R14126004 R14126005 R14126006 R14126008
R14126009 R14126011 R14126012 R14126013 R14126014 R14126015

A.2 Period II runs

R14129022 R14129023 R14129024 R14129026 R14129028 R14129029 R14130033
R14130034 R14130035 R14130036 R14130037 R14130039 R14130041 R14130042
R14130043 R14130068 R14130069 R14130070 R14130072 R14130073 R14130074
R14130076 R14130077 R14130079 R14130080 R14131001 R14131003 R14131013
R14131014 R14131016 R14131020 R14131022 R14131024 R14131025 R14131026
R14131028 R14131029 R14132006 R14132007 R14132011 R14132018 R14132019
R14132021 R14132023 R14132024 R14132026 R14132039 R14132040 R14132041
R14132042 R14132044 R14132046 R14132047 R14132057 R14132058 R14132059
R14132060 R14132061 R14132062 R14132064 R14132065 R14132066 R14132067
R14132068 R14132076 R14132077 R14132078 R14132079 R14132080 R14132082
R14133002 R14133004 R14133005 R14133014 R14133016 R14133019 R14133020
R14133025 R14133026 R14133027 R14133028 R14133029 R14133030 R14134007
R14134008 R14134010 R14134011 R14134012 R14134013 R14134014 R14134016
R14134017 R14134018 R14134033 R14134034 R14134036 R14134037 R14134038
R14134039 R14134040 R14134042 R14134043 R14134044 R14134045 R14134046
R14134047 R14134049 R14134050 R14134062 R14134063 R14134065 R14135001
R14135002 R14135003 R14135004 R14135007 R14135009 R14135014 R14135015
R14135016 R14135017 R14135018 R14135019 R14135021 R14135022 R14136002
R14136003 R14136004 R14136005 R14136006 R14136007 R14136010 R14136012
R14136014 R14136030 R14136031 R14136032 R14136035 R14136036 R14136037
R14136047 R14136048 R14136049 R14136053 R14136054 R14136055 R14136056
R14136057 R14136059 R14136060 R14136061 R14137001 R14137002 R14137003
R14137004 R14137005 R14137009 R14137010 R14137011 R14137012 R14137013
R14137017 R14137019 R14137020 R14137021 R14137046 R14137049 R14137055
R14137058 R14137059 R14137060 R14137064 R14137067 R14137084 R14137086
R14137090 R14138002 R14138003 R14138004 R14138005 R14138006 R14138007
R14138011 R14138012 R14138018 R14138020 R14138021 R14138022 R14138023

R14138024 R14138026 R14138027 R14138028 R14138029 R14138030 R14138032
R14138033 R14138034 R14138040 R14138041 R14138043 R14138044 R14138045
R14138047 R14138048 R14138049 R14138050 R14138051 R14138052 R14138060
R14138061 R14138062 R14138063 R14138065 R14138066 R14139011 R14139012
R14139015 R14139016 R14139017 R14139018 R14139019 R14139021 R14139022
R14139023 R14139043 R14139044 R14139046 R14139047 R14139049 R14139050
R14139052 R14139058 R14139059 R14139060 R14139062 R14139063 R14139064
R14139065 R14139067 R14139068 R14139069 R14140002 R14140006 R14140007
R14140008 R14140014 R14140016 R14140020 R14140021 R14140022 R14140023
R14140024 R14140025 R14140026 R14140028 R14140029 R14140030 R14140043
R14140044 R14140045 R14140046 R14140047 R14140048 R14140050 R14140054
R14140055 R14140056 R14140057 R14140058 R14140060 R14140061 R14140062
R14141011 R14141013 R14141015 R14141016 R14141018 R14141019 R14141020
R14141021 R14141022 R14141023 R14141025 R14141045 R14141046 R14141050
R14141052 R14141057 R14141069 R14141070 R14141071 R14141072 R14142002
R14142004 R14142007 R14142009 R14142011 R14142012 R14142014 R14142016
R14142017 R14143111 R14143112 R14143113 R14143114 R14143115 R14143116
R14143118 R14143119 R14143120 R14143121 R14144006 R14144007 R14144008
R14144021 R14144022 R14144024 R14144025 R14144026 R14144027 R14144028
R14144030 R14144032 R14144035 R14144036 R14144037 R14144115 R14144117
R14144118 R14144119 R14144120 R14144121 R14144125 R14144126 R14144127
R14144128 R14145009 R14145010 R14145011 R14145021 R14145022 R14145023
R14145024 R14145025 R14145028 R14145029 R14145030 R14145031 R14145032
R14145033 R14145034 R14145036 R14145038 R14145039 R14145068 R14145070
R14145072 R14145073 R14145075 R14145076 R14145077 R14145080 R14145081
R14145082 R14145084 R14145085 R14145090 R14146006 R14146007 R14146008
R14146010 R14146011 R14146012 R14146014 R14146015 R14146016 R14146017
R14146018 R14146019 R14146020 R14146021 R14146022 R14146023 R14146024
R14146025 R14146026 R14146027 R14146028 R14146050 R14146051 R14146052

R14146053 R14146054 R14146055 R14146056 R14146057 R14146059 R14146060
R14146065 R14146066 R14146067 R14146068 R14146069 R14146072 R14146073
R14146074 R14146084 R14146085 R14147001 R14147002 R14147003 R14147004
R14147005 R14147007 R14147008 R14147009 R14147011 R14147012 R14147014
R14147016 R14147017 R14147049 R14147050 R14147051 R14147053 R14147054
R14147055 R14147056 R14147057 R14147061 R14147062 R14147063 R14147066
R14147067 R14147068 R14147074 R14147075 R14147077 R14148011 R14148012
R14148017 R14148018 R14148020 R14148022 R14148023 R14148024 R14148025
R14148026 R14148029 R14148030 R14148033 R14148034 R14148057 R14148058
R14148059 R14148065 R14148066 R14148067 R14148069 R14148070 R14148071
R14148072 R14148073 R14148074 R14148075 R14148077 R14148078 R14148079
R14148080 R14148081 R14148082 R14149017 R14149020 R14149021 R14149022
R14149024 R14149025 R14149027 R14149028 R14149032 R14149033 R14149034
R14149131 R14150002 R14150004 R14150005 R14150011 R14150013 R14150014
R14150015 R14150045 R14150046 R14150048 R14150057 R14150058 R14150126
R14150130 R14150131 R14150132 R14150133 R14150135 R14150136 R14150137
R14150138 R14150139 R14151009 R14151012 R14151013 R14151014 R14151019
R14151023 R14151024 R14151031 R14151032 R14151033 R14151034 R14151035
R14151037 R14151038 R14151039 R14151042 R14151085 R14151089 R14151090
R14151095 R14151098 R14151100 R14151101 R14151102 R14151103 R14151104
R14151105 R14151106 R14151109 R14152001 R14152002 R14152006 R14152008
R14152009 R14152011 R14152012 R14152014 R14152015 R14152017 R14152018
R14152019 R14152020 R14152022 R14152023 R14152047 R14152048 R14152049
R14152050 R14152051 R14152053 R14152054 R14152057 R14152058 R14152059
R14152060 R14152065 R14152067 R14152068 R14153003 R14153008 R14153009
R14153010 R14153011 R14153013 R14153014 R14153015 R14153016 R14153017
R14153018 R14153022 R14153023 R14153024 R14153037 R14153038 R14153039
R14153040 R14153045 R14153047 R14153048 R14153049 R14153053 R14153054
R14153055 R14153060 R14153061 R14153062 R14153071 R14153072 R14153073

R14154001 R14154002 R14154003 R14154006 R14154008 R14154009 R14154011 R14154013 R14154016 R14154017 R14154018 R14154035 R14154037 R14154038 R14154039 R14154041 R14154042 R14154045 R14154048 R14154049 R14154052 R14154056 R14154057 R14154059 R14155004 R14155005 R14155006 R14155007 R14155010 R14155011 R14155016 R14155017 R14155019 R14155035 R14155036 R14155037 R14155042 R14155048 R14155049 R14155051 R14155056 R14155057 R14155058 R14155059 R14155060 R14155062 R14155087 R14155092 R14155093 R14155094 R14155096 R14155097 R14156003 R14156015 R14156016 R14156094 R14157002 R14157003 R14157005 R14157006 R14157007 R14157009 R14157010 R14157011 R14157014 R14157016 R14157017 R14157018 R14157020 R14157022 R14157024 R14158001 R14158003 R14158005 R14158016 R14158017 R14160010 R14160011 R14160012 R14160014 R14160016 R14160017 R14160019 R14160020 R14160021 R14160028 R14160029 R14160030 R14160031 R14160033 R14160042 R14160045 R14160046 R14160047 R14160048 R14160050 R14160051 R14160052 R14160053 R14160054 R14160055 R14160056 R14160058 R14161001 R14161002 R14161003 R14161004 R14161006 R14161007 R14161008 R14161009 R14161010 R14161011 R14161013 R14161018

APPENDIX B
JET FINDING PARAMETERS

```
// TPC cuts
anapars12->addTpcCut(new StjTrackCutFlag(0));
anapars12->addTpcCut(new StjTrackCutNHits(12));
anapars12->addTpcCut(new StjTrackCutPossibleHitRatio(0.51));
anapars12->addTpcCut(new StjTrackCutDca(3));
anapars12->addTpcCut(new StjTrackCutTdcaPtDependent);
anapars12->addTpcCut(new StjTrackCutPt(0.2,200)) ;
anapars12->addTpcCut(new StjTrackCutEta(-2.5,2.5)) ;
anapars12->addTpcCut(new StjTrackCutLastPoint(125)) ;

  // BEMC cuts
anapars12->addBemcCut(new StjTowerEnergyCutBemcStatus(1));
anapars12->addBemcCut(new StjTowerEnergyCutAdc(4,3));
anapars12->addBemcCut(new StjTowerEnergyCutEt(0.2));
anapars12->addBemcCut(new StjTowerEnergyCutTowerId(1237));
anapars12->addBemcCut(new StjTowerEnergyCutTowerId(1176));
anapars12->addBemcCut(new StjTowerEnergyCutTowerId(4595));

// EEMC cuts
anapars12->addEemcCut(new StjTowerEnergyCutBemcStatus(1));
anapars12->addEemcCut(new StjTowerEnergyCutAdc(4,3));
anapars12->addEemcCut(new StjTowerEnergyCutEt(0.2));
```

```
// Jet cuts
anapars12->addJetCut(new StProtoJetCutPt(3.5,200));
anapars12->addJetCut(new StProtoJetCutEta(-100,100));

    // Set anti-kt R=0.6 parameters

StFastJetPars* AntiKtR060Pars = new StFastJetPars;
AntiKtR060Pars->setJetAlgorithm(StFastJetPars::antikt-algorithm);
AntiKtR060Pars->setRparam(0.6);
AntiKtR060Pars->setRecombinationScheme(StFastJetPars::E-scheme);
AntiKtR060Pars->setStrategy(StFastJetPars::Best);
AntiKtR060Pars->setPtMin(3.5);
```